Mgr inż. Sylwia Pawłowska

Instytut Podstawowych Problemów Techniki PAN

# Dynamics of nano objects suspended in liquids: experimental analysis

Eksperymentalna analiza dynamiki nano-obiektów zawieszonych w cieczy

Rozprawa doktorska przedłożona

Radzie Naukowej

Instytutu Biocybernetyki i Inżynierii Biomedycznej

im. Macieja Nałęcza

Polskiej Akademii Nauk

Promotor rozprawy:

Prof. dr hab. Tomasz Kowalewski, IPPT PAN

Promotor pomocniczy:

Dr Filippo Pierini, IPPT PAN

Warszawa 2018

*Składam serdeczne podziękowania mojemu promotorowi Prof. Tomaszowi Kowalewskiemu za poświęcony mi czas, opiekę naukową oraz ogromną cierpliwość i cenne wskazówki, dzięki którym ta praca mogła powstać.*

*Serdeczne podziękowania kieruję do mojego promotora pomocniczego dr Filippo Pierini za przekazaną mi wiedzę, nieocenioną pomoc i wsparcie podczas prowadzonych przeze mnie badań.*

*Serdecznie dziękuję Prof. Piotrowi Garsteckiemu za wprowadzenie mnie w zagadnienia mikroprzepływów, dzięki czemu moja przygoda z tą tematyką mogła się dalej rozwinąć.*

*Serdecznie dziękuję dr inż. Pawłowi Nakielskiemu, Krzysztofowi Zembrzyckiemu oraz dr inż. Izabeli Piechockiej za ogromną pomoc i wszelkie rady podczas prowadzonych przeze mnie badań.*

*Dziękuję także koleżankom i kolegom z Instytutu oraz wszystkim, którzy przyczynili się do powstania niniejszej pracy.*

*Szczególne słowa podziękowania kieruję do moich ukochanych Rodziców i Brata oraz wspaniałych Przyjaciół za ich ogromne wsparcie, motywację oraz bezgraniczną wiarę we mnie.*

Sylwia Pawłowska was supported by the National Science Centre under grants no. 2011/03/B/ST8/05481 and 2015/17/N/ST8/02012.

The experiments were performed using apparatus available thanks to the EC structural funds in framework of the Centre for Preclinical Research and Technology (CePT), POIG Nr. 02.02.00-17-024/08-00. The computational resources were made available thanks to the EC structural funds in framework of the Biocentrum Ochota, POIG.02.03.00-00-003/09-00

# Streszczenie

**Eksperymentalna analiza dynamiki nano-obiektów zawieszonych w cieczy**

Przedmiotem pracy jest eksperymentalna analiza dynamiki nanoobiektów zawieszonych w cieczy. Celem przeprowadzonych zadań jest ocena roli oddziaływań hydrodynamicznych, chemicznych i fluktuacji brownowskich na dynamikę i parametry transportu w mikro i nanoskali dla obiektów sferycznych, silnie deformowalnych filamentów i makromolekuł.

W pierwszym etapie pracy przeprowadzono analizę ruchów brownowskich sferycznych nanocząstek (polistyrenowych, barwionych rodaminą) zawieszonych w elektrolitach. W pracy przedstawiono wyniki przeprowadzonych badań dotyczących wpływu siły jonowej medium oraz bliskości ścianki na wielkość średnicy hydrodynamicznej tychże sferycznych nano-obiektów (efektywnego oporu lepkiego). Wykazano istnienie znacznych rozbieżności miedzy danymi tabelarycznymi a faktycznymi współczynnikami oporu, reprezentowanymi przez tzw. średnicę hydrodynamiczną cząstki. Uzyskane wyniki wskazują na to, że średnica hydrodynamiczna nanocząstek sferycznych jest silnie zależna od siły jonowej medium, w którym cząstki zostały zawieszone, a także, że w zakresie niskich stężeń soli jej wartość spada wraz ze wzrostem siły jonowej. Pokazano również, iż na wielkość średnicy hydrodynamicznej ma wpływ zarówno wartościowość soli, jak i wielkość tworzących je jonów. Znajomość średnicy hydrodynamicznej nanocząstek bądź makrocząstek biologicznych w określonym środowisku jest niezbędna do określenia ich dyfuzji w badanym środowisku (np. środowisku wnętrza komórki, płynów ustrojowych). Stanowi to bardzo ważną informację na etapie projektowania układów nanocząstek jako obiektów w zastosowaniach biomedycznych.

Drugi etap badań dotyczył ruchliwości deformowalnych nano-obiektów o strukturze analogicznej do długich makromolekuł. Są to wytworzone z materiału hydrożelowego nanofilamenty. Opracowano oryginalną metodę ich wytwarzania, wykorzystującą technikę elektroprzędzenia współosiowego. Technika ta pozwala na fabrykację włókien typu core-shell (rdzeń-otoczka), których to rdzeń stanowią hydrożelowe nanofilamenty. Nowością w prowadzonych badaniach jest zamknięcie w polimerowej otoczce hydrożelowego materiału w postaci filamentów charakteryzujących się wysoką elastycznością. Tenże hydrożelowy rdzeń stanowi mieszanina dwóch komponentów: akrylamid (AAm) bądź N,N-izopropyloakrylamid (NIPAAm) oraz czynnika sieciującego N,N'-metyleno bisakrylamidu (BIS-AAm).

Przedstawiona została metoda ewaluacji właściwości mechanicznych badanych filamentów poprzez analizę ruchów Browna. Istotą tych badań jest wyznaczenie wartości długości persystentnej analizowanego obiektu, która skorelowana jest z modułem Younga. Uzyskane wyniki pokazują, że nasze hydrożelowe nanofilamenty charakteryzują się wysoką elastycznością, zbliżoną do typowych materiałów biologicznych, wynoszącą poniżej 10 kPa. Dodatkowo, zmieniając proporcje pomiędzy komponentami tworzącymi hydrożel, możemy również sterować tą elastycznością. Jest to bardzo istotna właściwość materiału z punktu widzenia zastosowania takich wydłużonych obiektów w biomedycynie jako transporterów leków czy materiału implantu tkanki.

Po pełnej charakterystyce morfologicznej oraz właściwości mechanicznych, hydrożelowe nanofilamenty poddane zostały analizie ich zachowania w przepływie. Zbudowany układ eksperymentalny, bazujący na układach mikroprzepływowych, posłużył do analizy dynamiki deformacji oraz zjawiska migracji nanofilamentów w przepływie oscylacyjnym, symulującym przepływy międzykomórkowe i międzytkankowe w żywych organizmach. Zbadane zostało zjawisko migracji tych obiektów w poprzek kanału. To zagadnienie jest istotne dla opisu transportu deformowalnych makromolekuł w kapilarach. Wykazano, iż kierunek migracji zależy od charakterystyk przepływu, położenia w kanale i deformacji filamentu. Obserwacja zachowania badanych nanofilamentów w przepływie oscylacyjnym pozwoliła na wydzielenie trzech grup tych obiektów: „bent-like", „U-shaped buckled", „U-shaped stretched", wykazujących pewne różnice pod kątem właściwości zginania, orientacji w przepływie i kierunku migracji. Obserwacje te pozwalają nam wnioskować, że „bent-like" nanofilamenty mogą symulować zachowanie elastycznych biomolekuł takich jak DNA lub białka, podczas gdy nanofilamenty należące do dwóch pozostałych grup bardziej przypominają zachowaniem semi-elastyczne makromolekuły, jak filamenty aktynowe. Wyniki te wykazały słuszność postawionej tezy mówiącej o dużym potencjale wykorzystania przepływu oscylacyjnego w badaniu mikro- i nano-obiektów do zastosowań w inżynierii biomedycznej.

Przeprowadzone badania dynamiki nanofilamentów stwarzają możliwość ich wykorzystania jako modeli wydłużonych cząstek biologicznych, takich jak białka i DNA, co stanowi potwierdzenie tezy trzeciej niniejszej pracy. Analiza ich przemieszczania i deformacji w przepływie wspomoże weryfikację istniejących już modeli teoretycznych, jak również pomoże w zrozumieniu zjawisk fizycznych odpowiedzialnych za fałdowanie

i dynamikę zginania biomolekuł. Kolejnym bardzo ważnym celem pracy jest możliwość wykorzystania takich silnie deformowalnych obiektów, charakteryzujących się właściwościami fizycznymi bliskimi żywym tkankom, w zastosowaniach biomedycznych, jako systemy kontrolowanego uwalniania leków, transportery substancji leczniczych w konkretne miejsce w organizmie, systemy do regeneracji tkanek. Podjęto próbę scharakteryzowania profili uwalniania substancji symulującej lek z hydrożelowych nanofilamentów. Obiekty takie mogą stanowić nanotransportery substancji o działaniu leczniczym, które w sposób kontrolowany i ukierunkowany uwalniają lek do miejsca zaatakowanego chorobą. Przeprowadzone badania wykazały, że zmieniając proporcję pomiędzy komponentami tworzącymi hydrożel, możliwe jest kontrolowanie szybkości uwalniania substancji np. leku. Całościowe zrozumienie dynamiki pojedynczych obiektów jest kluczowe dla ich dalszych zastosowań biomedycznych.

**Słowa kluczowe:** średnica hydrodynamiczna, ruchy Browna, współczynnik dyfuzji, hydrożelowe nanofilamenty, migracja radialna cząstek zawiesiny, dynamika zginania, właściwości mechaniczne.

# Abstract

**Dynamics of nano objects suspended in liquids: experimental analysis**

The subject of this work is an experimental analysis of the dynamics of nanoobjects suspended in a liquid. The research will make it possible to appreciate the role played by hydrodynamic and ionic interactions on the transport properties of Brownian solid spherical objects, as well as strongly deformable nanofilaments and macromolecules.

In the first stage of the work, an analysis of the Brownian fluctuations of spherical nanoparticles suspended in electrolytes was conducted. This thesis presents the results of the research carried out on the influence of the medium ionic strength and the wall on the size of the apparent (hydrodynamic) diameter of these spherical nanoobjects. As the particle size decreased, some significant discrepancies were found between the tabulated data and the measured hydrodynamic diameter of the particle. The hydrodynamic diameter of nanoparticles or biological macromolecules in a given environment must be known in order to determine their diffusion in the environment studied (e.g. the environment of the cell interior, body fluids).

The second stage of the research concerns the mobility of deformable nanoobjects with a structure similar to long macromolecules. These are nanofilaments made of a hydrogel material. The original coaxial electrospinning technique was developed to produce them. This technique allows for the fabrication of core-shell fibres, with a highly elastic hydrogel filamentous core. This hydrogel core is a mixture of two components: acrylamide (AAm) or N, N-isopropylacrylamide (NIPAAm), and a N, N'-methylene bisacrylamide cross-linking agent (BIS-AAm).

The mechanical properties of nanofilaments are evaluated by analysing their Brownian characteristics. The aim of this research is to determine the value of the persistent length of the object analysed, which is correlated with its bending Young's module. After assessing their full morphological characteristics and mechanical properties, the behaviour of hydrogel nanofilaments in the flow was analysed. An experimental system based on microfluidic systems, was used to analyse the dynamics of filament deformation and the migration of nanofilaments in the oscillating flow, simulating intercellular and inter-tissue flows in living organisms. The investigated phenomenon of lateral migration is important for the description of the transport properties of deformable macromolecules in capillaries.

*Abstract*

The basic goal of the analysis of the dynamics of nanofilaments is the possibility to use them as models of elongated biological particles, such as proteins and DNA. The analysis of their movement and deformation in the flow will support the verification of existing theoretical models, and will expand our understanding of the physical phenomena which are responsible for the folding dynamics of long biomolecules. Another very important aim of this work is to offer the possibility of using such highly deformable, biocompatible objects in biomedical applications. Such objects can be used as nanotransporters of substances with therapeutic effects, which – in a controlled and dedicated manner – release the drug to the site affected by the disease. A comprehensive understanding of the dynamics of individual objects is crucial to their eventual further applications.

**Keywords:** hydrodynamic diameter, Brownian motion, diffusion coefficient, hydrogel nanofilaments, cross-flow migration, bending dynamics, mechanical properties.

## Dissertation theses

The main thesis of this work are:

1) *The proper evaluation of spherical nanoparticle mobility involves several size-dependent factors which strongly influence their effective diffusion and transport properties.*
2) *The oscillatory microchannel flow is a promising tool for conveying, sorting, and targeting the nanoobjects used for dedicated drug release, diagnostics or tissue engineering.*
3) *Highly deformable polymer nanofilaments can be used as model objects for studying the dynamics of long biomolecules (DNA, proteins).*

# Contents

# List of symbols

$a$, $b$ – long and short axis of the elongated object (rod, filament) [-]
$a_1$, $\sigma$ – parameters of the matching function [-]
$a_c$ – acceleration [m/s$^2$]
$a_d$ – diffusion factor depending on the problem dimension (= 2, 4, 6) [-]
$d_h$ – hydrodynamic diameter [m]
$A$ – relative flexural stiffness [-]
$A_r$ – cross sectional area of the object [m$^2$]
$A_s$ – cross section area of the rod [m$^2$]
AAm – acrylamide
AFM – Atomic Force Microscope
APS – ammonium persulfate
$b_s$ – relative stiffness [-]
BIS-AAm – N, N'-methylene bisacrylamide
BSA-FITC – Bovine Serum Albumin conjugated with fluorescein
BU – degree of buckling (= $d_c/L$)
$c$ – distance from the channel wall [m]
$C_D$ – drag coefficient [-]
$CHCL_3$ – chloroform
$d$ – particle (filament) diameter [m]
$d_c$ – circle diameter [m]
$d_e$ – short axis of ellipse encircling filament [m]
$d_{ph}$ – physical diameter [m]
$D_a$ – translational diffusion coefficients along principal axis [m$^2$/s]
$D_b$ – translational diffusion coefficients along minor axis [m$^2$/s]
$D_{ex}$ – experimental diffusion coefficients [m$^2$/s]
$D_f$ – flexural diffusivity [m$^2$/s]
$D_{th}$ – theoretical diffusion coefficients [m$^2$/s]
$D_\Theta$ – rotational diffusion coefficient [rad$^2$/s]
$D_\perp$ – diffusion coefficient towards to the wall [m$^2$/s]
$D_\parallel$ – diffusion coefficient parallel to the wall [m$^2$/s]
DMF – N,N-dimethylformamide
DLS – Dynamic Light Scattering
DLVO – Derjaguin-Landau and Verwey-Overbeek
$E$ – flexural Young modulus of filaments [Pa]
$E_r$ – relative elastic modulus [Pa]
$E_x$ – extensional Young modulus of filaments [Pa]
EA1 – AAm:Bis-AAm with mass ratio (w/w) 37.5:1
EA2 – AAm:Bis-AAm with mass ratio (w/w) 20:1
EA3 – AAm:Bis-AAm with mass ratio (w/w) 4:1
EDL – electric double layer
EE – end-to-end distance
EL – degree of elongation (= $d_e/L_e$)
EN1 – NIPAAm:Bis-AAm with mass ratio (w/w) 37.5:1
EN2 – NIPAAm:Bis-AAm with mass ratio (w/w) 20:1

EN3 – NIPAAm:Bis-AAm with mass ratio (w/w) 4:1
$F_d$ – hydrodynamic drag force [N]
$F_e$ – elasticity force [N]
$I$ – moment of inertia of filament cross-section [$m^4$]
IA – inclination angle
$k_B$ – Boltzmann's constant [kg $m^2/s^2$ K]
$k_e$, $k_x$, $k_y$ – elasticity constant, trap stiffness [N/m]
$K$ – relative extensional (Hookonean) stiffness [-]
KCl – potassium chloride
$L_e$ – long axis of ellipse encircling filament [m]
$L$ – object (filaments) contour length [m]
$\underline{L}$ – length-to-diameter ratio [-]
$L_p$ – persistence length [m]
LiCl – lithium chloride
$m$ – mass of the rod [kg]
$m_s$ – the space dimension [-]
*MSD*, $\langle x^2 \rangle$, $\langle (\Delta x(t))^2 \rangle$ – mean square displacement of particles [$m^2$]
$NiCl_2$ – nickel chloride
NIPAAm – N, N-isopropylacrylamide
NTA – Nanoparticle Tracking Analysis
OT – Optical Tweezers
$P$ – the force applied [N]
*Pe* – Peclet number [-]
PCL – polycaprolactone
PDMS – polydimethylsiloxane
PLCL – Poly(L-lactide-co-caprolactone)
PLLA – polylactic acid
$Q$ – flow rate through the channel [$m^3/s$]
$R$ – radius of object [m]
$R_e$ – the equivalent radius for a spherical intender [m]
$R_t$ – the tip radius of curvature [m]
*Re* – Reynolds number [-]
$\langle Rn^2 \rangle$ – mean square of the end-to-end distance of object (filament, rod) [$m^2$]
*Sp* – Sperm number [-]
SDS – sodium dodecyl sulfate
SEM – Scanning Electron Microscope
$t$ – interval time [s]
$\Delta t$ – time interval between images [s]
$T$ – absolute ambient temperature [K]
TEMED – N,N,N',N'- tetramethylethylenediamine
$U_r$ – average lateral migration velocity [m/s]
$U_s$ – absolute slip velocity, ratio of translational velocity of particle (filament) to the calculated local fluid flow velocity [ - ]
$W$ – channel width [m]
WLC – worm-like-chain model
$V(x,y,z,t)$ – flow velocity of liquid in the channel [m/s]
$V_{max}$ – maximum absolute flow velocity at the channel axis [m/s]

$V_r$ – absolute relative migration velocity, ratio of averaged over observation time lateral velocity of particle (filament) to the maximum flow velocity $V_{max}$ [ - ]
$V_x$ *and* $V_y$, – voltages, proportional to X and Y position of the incident beam [V]
$V_A$ – attractive van der Waals potential [V]
$V_R$ – electrostatic repulsion potential [V]
$V_T$ – total potential [V]
$x$ – distance from the channel center line [m]
$\underline{x}$ – relative distance from the channel center line [-]
$x_0$, $y_0$ – displacement of the fitting window [m]
$x(t)$, $y(t)$ – frame coordinates [-]
$\Delta x$ – displacement of object [m]
$\kappa$ – bending rigidity [$Nm^2$]
$\delta$ – the indentation depth [-]
$\theta(t)$ – orientation of filament [rad]
$\Theta$ – tangent angle [rad]
$v_f$ – Poisson's ratio of the hydrogel [-]
$\eta$ – dynamic viscosity of the carrier fluid [Pa s]
$\rho$ – density of the carrier fluid [$kg/m^3$]
$\omega$ – angular oscillation frequency of the flow [rad/s]
$\gamma$ – shear rate for the channel flow [1/s]

# List of figures and tables

# Chapter 1: Introduction

Transport processes in biological systems are based on laminar, creeping flows supported by molecular diffusion. The intercellular and cellular transport of molecules, subcellular organelles, and cells immersed in an aqueous environment is based on “stochastic” transport phenomena. Molecular diffusion becomes very efficient over short distances. While typical biomolecules need hours to be transported a few centimetres by diffusion, such transport takes less than 1 s at subcellular distances. Therefore, the random movement of nanoobjects driven by intermolecular interactions initiates all living processes, whereas hydrodynamic interactions mainly play the role of a drag force, modifying species mobility.

The thermal fluctuations generated by molecules are not only noises. It has been demonstrated that such fluctuations are fundamental to the function of biological systems. Several results are possible with the same probability, unlike in a mechanical system where there is a deterministic result. In ensemble measurements, the obtained values – which are the average values of many molecules – have usually been wrongly interpreted as deterministic values. In biological systems, however, the average values are not necessarily effective, but the values of individual molecules play a decisive role [1, 2]. The biomolecular system may spontaneously fluctuate, and one of the two states occurs alternately. The preferential binding of ligands to one of the spontaneously fluctuating protein structures leads to their activation or deactivation. This mechanism appears essential for a long-scale evolutionary development of living species, and for the short-time creation of signalling paths for the early immune response of individual cells [3, 4].

To evaluate the role of diffusion in microsystems, we must discriminate between two specific configurations. The idealistic model is a free-moving spherical particle. Its mobility is well described at least in terms of physical geometry and displacements of its centre of mass. On other hand there are long molecules, described as strongly deformable chains of complex shape with different mobility. In the following chapter I will attempt to describe some of the problems connected with the interpretation of the behaviour of such objects and share the following it observations and conclusions.

## 1.1 Solid spherical particles

Particle size is a very important parameter in such branches of science and technology as materials science, medicine, pharmacology, biology, energy technology, and others. This

size, understood as a linear length measure (measured in SI units [m]), can be uniquely defined only for spheres, and is referred to as the radius or diameter. In the case of shapes other than spheres, it is important to clearly define what the measured particle size is [5]. The hydrodynamic diameter is the apparent size representing a sphere having mobility of the physical object analysed. For large particles it will be quite close to the physical size of the sphere, whereas in micro- and nano-scales it may diverge very noticeably. The phenomenon of the significant differences between hydrodynamic diameters, determined on the basis of the diffusion coefficient of nanoparticles, varies, and its physical value is fairly well known in literature. It is mainly based on effects related to the influence of the solvent. Such factors as the ionic strength or the distance from the wall, and the effect of a size, will be discussed in this thesis. Other effects such as the surface structure of nanoparticles (associated with the presence of surfactants), agglomeration, and particle concentration are described in the Appendix 1.

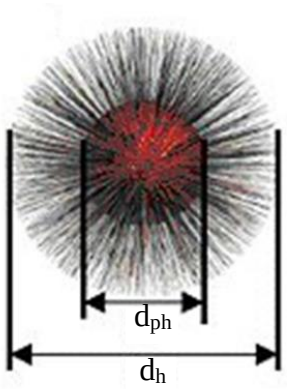


Fig. 1.1. Hydrodynamic (steric) and physical diameter of nanoparticle: $d_h$ – hydrodynamic diameter; $d_{ph}$ – core physical diameter) [6].

The hydrodynamic diameter provides information on the core, coating material, and the solvent layer attached to the particle as it moves under the influence of Brownian motion (Fig. 1.1). When the physical diameter of the particle is known, the effect of solvent ions, attached steric macromolecules can be partly estimated from its mobility (diffusion coefficient). On other hand, the physical radius of the particle core estimated based on the observation of its mobility is plagued by errors, due to difficulties in estimating the role of surface effects. The Stokes-Einstein equation can be used for calculating a hydrodynamic size from the diffusivity, although this ignores the influence of the ion cloud surrounding each particle and the relevant surface charge [7].

It is commonly known that the values of the hydrodynamic diameter ($d_h$) obtained are usually higher than the diameters obtained from microscopic measurements (e.g. TEM, AFM), and change when suspension conditions are changed. The most common theoretical models link these differences to the presence of the electric double layer [8, 9] surrounding the particles suspended in aqueous solutions. In scientific literature there are numerous reports on problems related to the unequivocal determination of the physical size of particles based on their hydrodynamic size. Typically, the reported value of the latter was significantly higher than the physical size of the particles analysed (Table 1.1).

Table 1.1. Comparison of physical and hydrodynamic size of nanoparticles.

| **Sample** | **Technique of analysis** | **Physical diameter of particle [nm]** | **Analysis technique** | **Hydrodynamic diameter of particle [nm]** | **Ref.** |
|---|---|---|---|---|---|
| Sulfate latex nanoparticles | Transmission Electron Microscopy | 265 | Dynamic Light Scattering | 260-335 | [10] |
| Sulfate polystyrene latex particles | Transmission Electron Microscopy | 33.5 | Static Light Scattering | 37.27 | [11] |
| Surfactant-free sulfate polystyrene latex particles | Transmission Electron Microscopy | 55 | Static Light Scattering | 64.5 | [11] |
| Polystyrene latex particles | Transmission Electron Microscopy | 156 | Dynamic Light Scattering | 158-180 | [7] |
| Polystyrene nanoparticles | Transmission Electron Microscopy | 600 | Nanoparticle Tracking Analysis | 595-660 | [12] |

There are many useful methods for determining the value of the hydrodynamic size of micro- and nanoparticles suspended in liquid. A description of several of them is provided in Appendix 2.

### 1.1.1 Ionic strength of medium effect

An electric double layer (EDL) is a diffuse layer of charges which surrounds the particles dispersed in liquid. It is created by the dissociation of the surface ions and the redistribution and adsorption of the ions from the solution near the particle surface. When the suspension is diluted, the characteristic double-layer thickness is associated with the ionic strength of the solution. The particle displacement – as a result of either the Brownian motion or another type of motion – induces the motion of the attached charged layers of the solvent [8]. The charged liquid layer surrounding the particle is made up of

two parts: (i) an inner region (Stern layer), where ions are strongly bound; (ii) an outer layer, defined as the diffuse region (Gouy Chapman layer), where ions are not so strongly attached as in the inner layer. A notional inner boundary is present within the diffuse layer. In this layer, particles and ions form a stable structure. The motion of a particle causes the simultaneous movement of ions within this boundary, but ions beyond the boundary do not travel with the particle. This boundary defines the particle's electrokinetic property and is called the "slipping plane" or "hydrodynamic shear surface". The particle charge (zeta potential) corresponds to the potential that exists at this boundary [13]. It can be measured and used to evaluate the EDL thickness.

The thickness of the electrical double layer can be described by two characteristic lengths: (i) the distance where the excess of counterions drops to a chosen fraction of its initial value, and (ii) the distance that contains a chosen fraction of all the excess counterions. It has been shown that the effective thickness of the electrical double layer increases whenever the counterion size increases and the bulk concentration of ions decreases. The increased surface charge may cause either an increase or a decrease in the effective double layer thickness [14]. The electric double layer surrounding the suspended particles plays an important role in the hydrodynamic motion of particles [8].

In polymer systems, the electrolyte concentration determines the electric double layer interaction. Adsorbed ions modify the polymer surface charge and potential, but on the other hand, the free ion density in the solution determines the exponential decay length of the electric double layer interaction (Debye length) [15].

The magnitude of the zeta potential determines the stability of the colloidal system. It is based on the DLVO (Derjaguin-Landau and Verwey-Overbeek) theory [16] which assumes that the interaction between two particles is due to the addition of two opposing forces: the attractive van der Waals potential ($V_A$) and the electrostatic repulsion potential ($V_R$), which exist among particles when the latter approach each other due to the Brownian motion (Fig. 1.2) [13, 17].

The total potential ($V_T$) is described by the equation:

$$V_T = V_A + V_R \tag{1}$$

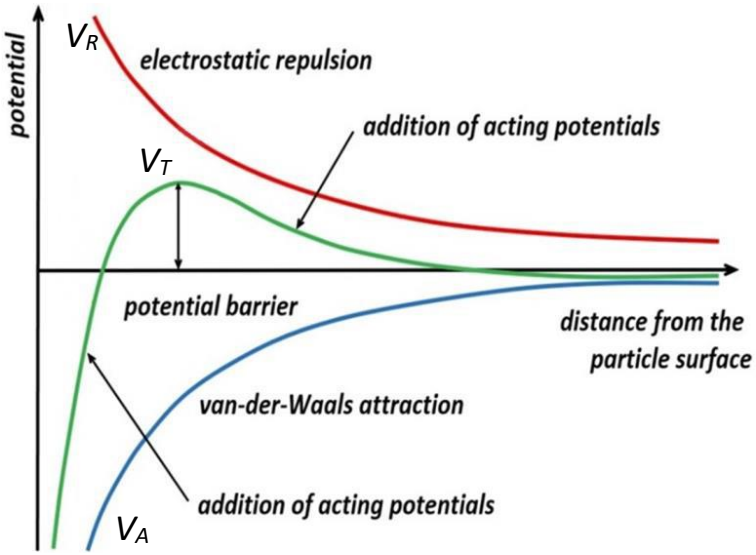


Fig. 1.2. DLVO potential energy as a function of the particle distance from the surface.

In situations when all particles in suspension have a very high positive or negative zeta potential they will not show a tendency to flocculate, but rather will tend to repel each other. However, if particles have low zeta potential values, they come together and flocculate. The range of zeta potential between +30 mV and -30 mV is regarded as the general range between stable and unstable suspensions. In a case where the particle zeta potentials are either above +30 mV or below -30 mV, the particle suspension is defined as very stable [13].

Numerous studies have shown relationships between the zeta potential of the particles suspended in liquid and the electrolyte concentration of the suspension. For spheroidal particles, the zeta potential is defined as a function of the surface structure, surface charge density, and shear plane location. Any changes in the electrolyte concentration can induce changes in the shear plane location: something that may be caused by changes in either the surface morphology or the double layer thickness and polarization. The presence of the shear layer significantly affects the stability of the colloidal systems and, primarily, the hydrodynamic motion of the suspended particles [8].

Hence, when there is a low concentration of salt in the solvent, the repulsion of the double layer is sufficiently strong, thus causing the stability of the single particles. An increased ionic strength causes electrostatic repulsion. When the saline concentration is increased, the stability of the colloid system starts to decrease because the van der Waals attraction then becomes higher than the repulsive electrostatic barrier [10].

The type of ions in the medium and the total ionic concentration can both affect the particle diffusion by changing the thickness of the electric double layer, known as the Debye length (Fig. 1.3) [13].

- Low conductivity media will produce an extended double layer of ions around the particle, thus reducing the diffusion and resulting in a larger, apparent hydrodynamic diameter.
- A higher media conductivity will suppress the electrical double layer and, consequently, the measured hydrodynamic diameter.

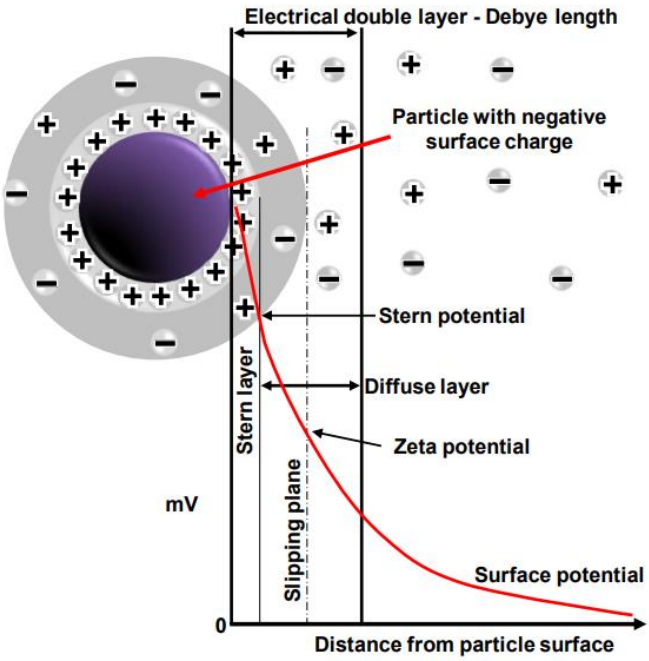


Fig. 1.3. The electric double layer [13].

Some standards have been defined to take into account the EDL layer by measuring the particle size: for example, for polystyrene particles the standard solvent should be 10 mM NaCl. This concentration of salt will ensure that the suspension of particles remains stable.

Table 1.2. Typical electric double layer EDL of different types of electrolytes (pH = 7.5; T = 25$^{o}$C) [18].

| **Ionic strength [mM]** | 2.393 | 15.481 | 55.573 | 95.616 | 145.648 |
|---|---|---|---|---|---|
| **EDL [nm]** | 6.277 | 2.468 | 1.302 | 0.993 | 0.805 |

Table 1.2 gives some examples of the theoretical values of the thickness of the electric double layer which were calculated for different ionic strengths of the medium [18]. In the experimental practice, an excessively high concentration of salt ions leads to the

collapse of the electrical double layer, while particles start to aggregate. Several studies have been devoted to finding a relationship between the hydrodynamic diameter of particles and the ionic strength of the solvent. This dependency becomes evident as an increased hydrodynamic diameter based on the electric double layer thickness can be seen. In a case of very low ionic concentration, the apparent particle size enlargement can reach 20 nm. Such a size variation (between physical and hydrodynamic diameter) is independent of the sphere size but dependent on the solution conductivity (ionic strength) [8].

Chassagne et al. [10] investigated the effect of the ionic strength on the steric ("hairy") diameter of polystyrene sulphate latex particles with a physical radius – confirmed by TEM images – of 265 nm. Two commercial devices were used to measure the hydrodynamic diameter and electrophoretic mobility of samples for different ionic strengths of the suspending solution. At low ionic KCL concentration, the apparent (hydrodynamic) radius measured was about 300 nm, nearly 25% higher than the physical radius. By increasing the ionic strength of the solvent it was found that the hydrodynamic radius of particles decreases, most probably due to the reorganization of steric "hairs" on the polymeric particle surface. With the increased ionic strength, the observed aggregation rate also decreased.

Numerous other data can be found in literature either with the estimation of nanoparticle mobility from statistical experiments (like DLS), or even using single-particle tracking methods. Difficulties arise in properly evaluating wall effects and the environmental factors responsible for the apparent increase or decrease in particle mobility as the particle size decreases. This research area – which is important for recent applications of nanocarriers for targeted drug delivery – appears to be still open for further studies.

### 1.1.2 Wall effect

An interesting study was presented by Jurney et al. [19], who investigated the effect of the size of nanoparticles on their tendency to adhere to the microchannel wall. They found that, for small nanoparticles (below 100 nm), due to the competition between the Brownian force and the electrostatic force, no clear diameter dependence on the volume of the particles that adhered to the channel wall can be seen. Their finding underscores the importance of the zeta potential on particle and wall surface interactions.

Hydrodynamic slip is usually considered on the basis of the averaged flow properties over all the liquid molecules near the solid boundary, and is expressed as the slip length. It is defined by extrapolating the velocity profile beyond the channel wall. Obviously, the slip

or no-slip boundary condition affects the mobility of Brownian particles by modifying the hydrodynamic drag force and the particle-channel wall interaction. Hence, the stochastic motion of Brownian particles changes depending on fluid properties, molecular size ratio, or spatial constraints. Its detailed analysis makes it possible to estimate the value of the hydrodynamic slip.

Due to the hydrodynamic interactions, the mobility of Brownian particles changes in the vicinity of the wall. It affects the measured diffusion coefficients, since these changes depend on the particle motion in relation to the wall. The diffusion coefficients ($D_\perp$; $D_\parallel$) for a single particle which is located close to the wall can be defined by the equations [20]:

$$D_\perp = \beta_\perp D \qquad D_\parallel = \beta_\parallel D \qquad D = \frac{k_B T}{3\pi\eta d_{ph}} \tag{2}$$

where: $D_\perp$ and $D_\parallel$ are diffusion coefficients towards and parallel to the wall; $\beta_\perp$ and $\beta_\parallel$ are scaling coefficients for the perpendicular and parallel diffusion; $D$ is a bulk diffusion coefficient; $T$ and $\eta$ are the absolute temperature and viscosity of the medium; $k_B$ is the Boltzman constant; $d_{ph}$ is the physical particle diameter.

Lauga and Squires [21] evaluated the hydrodynamic mobility of particles close to the wall, by taking into account the hydrodynamic slip boundary condition. The effect depends on the relative distance of the particle from the wall to its diameter. For nano- and micrometric particle this change of mobility becomes measurable [20].

## 1.2 Deformable elongated particles

The characterization of the flexibility or stiffness of biomolecules and polymers is essential for describing their structure and dynamics. Complex molecular interactions are usually described in a reduced way with spherical subunits (e.g. as in the case of model spherical proteins or bead-models of flexible polymers). Their dynamic structure may be regarded as stiff or semiflexible chains. Observing by optical means the dynamics of the flexible molecules suspended in a liquid one may evaluate their main mechanical properties, which are responsible for their complex behaviour, like folding-unfolding sequences of DNA chains. The description of such phenomena at a molecular scale, however, is still limited to very short length and time scales. At such scales it is difficult or nearly impossible to answer basic questions about potential effects of hydrodynamic interactions, initiating or even causing some complex behaviours of long biological molecules. Our aim is to introduce micro-scale models of flexible objects, where length scale allows for precise optical measurements and the application of simple

hydrodynamic models. Hence, it became necessary to develop techniques permitting the production of highly flexible fibres, with deformability and elasticity resembling long DNA chains.

In the following chapter the unique method for the fabrication of short nanofibres using the core-shell electrospinning technique is discussed. The proposed electrospinning method of producing gel-like fibres made it possible to obtain highly deformable hydrogel nanofilaments with a diameter of around 200 nm. The understanding of the behaviour of these highly flexible objects allows for the verification of existing theoretical models and can help to elucidate physical phenomena which are responsible for the folding and bending dynamics of long molecular objects.

### 1.2.1 Nanofibres

Nanofibres and nonwovens made of them are unique nanostructures with an extraordinary potential in both technical and medical areas. Filter applications, functional textiles, fibre reinforcement, catalysis, drug delivery, wound healing, and tissue engineering are just a few examples of their potential applications. The term nanofibre commonly applies to a fibre with a diameter of less than 1 micron. The manufacture of objects characterized by such a small size requires the use of special techniques.

Electrospinning is a process that forms nanofibres through an electrically charged jet of polymer solution or polymer melt. This technique provides a simple and versatile method for producing ultrathin fibres from a wide range of materials that include polymers, composites, and ceramics. Electrospun fibre diameters usually range from tens of nanometres to a few micrometres [22, 23].

The electrospinning of polymers was invented by Formalas [24] in 1934. He described an apparatus using electrostatic forces to draw down polymer solutions. However, it took over 50 years until the method was rediscovered for the production of nanofibres [25].

The basic setup for electrospinning consists of three major components: a high-voltage power supply (usually in the range of 1 to 30 kV), a nozzle (a metal needle), and a collector (a grounded conductor). The nozzle is connected to a syringe filled with a polymer solution. When a high voltage is applied, the pendent drop of the polymer solution at the nozzle becomes highly electrified and the induced charges are evenly distributed over the surface [25-27]. Finally, the drop is subjected to two major types of electrostatic forces: the electrostatic repulsion between the surface charges, and the coulombic force exerted via the external electric field. Under the influence of these electrostatic interactions, the liquid drop is distorted into a conical object, generally

known as the Taylor cone [25, 28, 29]. As the liquid jet is continuously drawn out and the solvent evaporates, its diameter becomes significantly reduced from hundreds of micrometres to tens of nanometres. Being attracted by the grounded collector placed under the pipette, the charged fibres are often deposited as a nonwoven mat [25]. The collector has a significant impact on the arrangement and productivity of nanofibres and their final structure. This is due to its effect on the ability of the charges on fibres to be brought to ground which, in turn, affects the amount of fibres that are collected on the substrate [30]. The collector orientation influences the fibre alignment. Different collector models also affect the properties and morphology of the produced nanofibre [31]. There are several different collectors used to produce aligned nanofibres in electrospinning experiments: plane plate collector, drum rotatory collector, grid type collector, etc. [32]. The surface area can be increased to enable the faster evaporation of residual solvent molecules by using a porous collector plate. Compared to a non-porous collector plate, the porous collector yields fibres with lower packing density. A rotating collector is useful in obtaining dry fibres as it ensures more time to allow the solvent to evaporate [31]. Electrospinning combined with blow spinning is considered the technique with the most potential for scaling to commercial production [22].

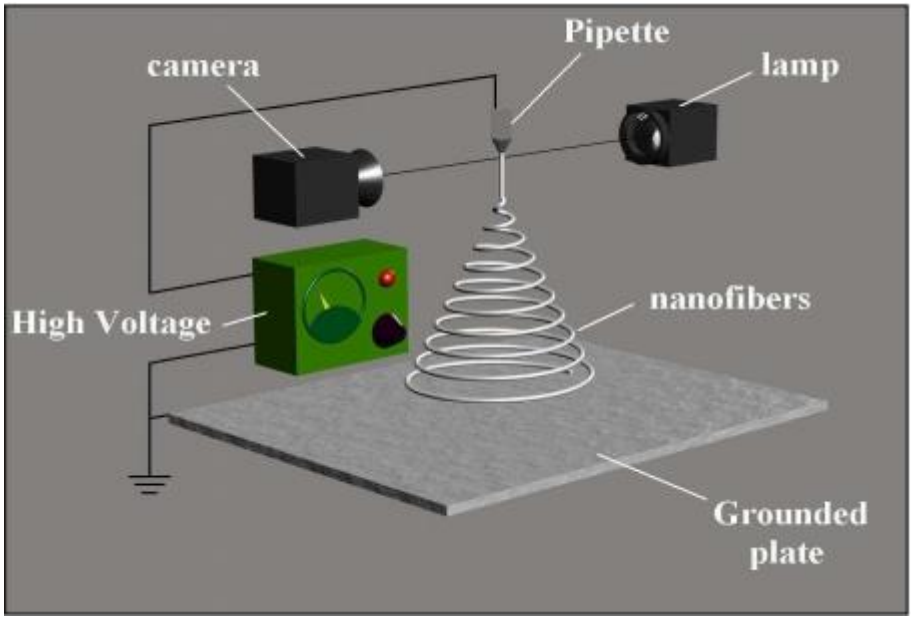


Fig. 1.4. Schematic of an electrospinning setup [28].

For electrospun polymer fibres and nonwovens there are several applications: filters, smart textiles, protective clothing, templates, catalysis process, sensors, functional materials, composite reinforcement, cosmetics, in medicine (tissue engineering, transport

and release of drugs, cancer treatment, wound healing, artificial blood vessels, inhalation therapy), and electronics (batteries/cells and capacitors) [22, 23, 25, 26, 28, 33, 34].

Electrospinning allows mixing or encapsulating different components of spun material. One of such methods, applied to the present work, offers a core-shell system with a special co-axial nozzle. The nozzle consists of two co-axial cylinders (e.g. needles) supplied with two different solutions. As in the conventional electrospinning process, the two-component jet is simultaneously pulled, stretched, elongated, and bent via electric forces [35, 36]. During the core-shell electrospinning, two different solutions are dosed at the same time through the inner and outer needles, and charged in the same way as in the classic single nozzle. The resulting core-shell fibre consists of two material structures in which one is surrounded by the other. The coaxial electrospinning depends on the same parameters as those in conventional electrospinning [37-39]. Using precisely controlled syringe pumps, the flow rate of each component can be varied to control the dimensions of the core and shell material [35, 36], as well as the overall nanofibre diameter [40]. For proper encapsulation of the core material, the flow rates of both components should be carefully matched. If the core-to-shell flow rate ratio is too small, an insufficient outflow of core solution cannot ensure a continuous smooth core phase, and only a chain of small droplets is encapsulated [37].

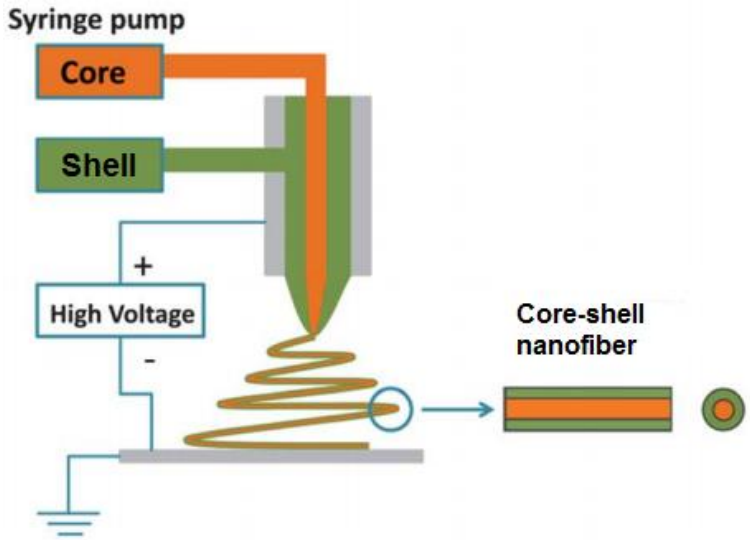


Fig. 1.5. Coaxial electrospinning setup for core-shell fibres [37].

In this work core-shell electrospinning is used to fabricate hydrogel nanofilaments; in our opinion this is the only technique that enables obtaining soft hydrogel filaments by encapsulating them in a mechanically stable polymeric shell [27].

## 1.3 Dynamic characterization of nanoobjects suspended in liquid

The characterization of suspended micro- and nanoobjects depends mainly on their geometry and material parameters. In the case of spherical particles, their geometry is described by a single dimension, usually defined by their physical diameter. Deformable droplets or solid rods are characterized by three dimensions: height, width, and length. In addition, for droplets, the viscosity ratio characterizes their deformability in a shear flow. In the case of more complex structures, such as elongated and deformable fibres, apart from the dimensional parameters, their deformability is characterized by the fibres' material elasticity. The knowledge of these parameters is essential for describing the mobility of Brownian objects suspended in liquid.

### 1.3.1 Brownian diffusion

Thermal energy causes random movements of molecules or small particles suspended in fluids. A particle suspended in a fluid kept at absolute temperature $T$ has, on average, a kinetic energy $k_bT/2$ associated with movements along each coordinate, where $k_b$ is the Boltzmann's constant. Such chaotic movements of particles (micro- and nanoobjects) are due to their collisions with molecules of the fluid in which they are suspended. This phenomenon was discovered by the Scottish biologist Robert Brown (1827). He observed, under a microscope, an incessant movement in random directions of the pollens suspended in water. Einstein (1905) and Smoluchowski (1906) contributed with their independent work to a complete understanding of this phenomenon and a determination of its mathematical description. They discovered the relationship of the chaotic pollen motion found by Brown with the thermal fluctuations of the molecules in the solvent (water). Water molecules bombarding particles of pollen initiate their random movements. This is a manifestation of the thermal energy: the temperature is a measure of the intensity of the pollen movements observed. According to Smoluchowski, this can be interpreted as stochastic fluctuations of particle density, responsible for diffusion processes. It is worthwhile to note that diffusion processes, which are relatively slow at macro scales, are the most effective mechanisms for the small-scale material transport within the fluid. By observing the Brownian motion of suspended objects and evaluating their trajectories, it is possible to obtain detailed information about the environment in which the analysed objects are suspended [41].

Brownian movement is responsible for a diffusion phenomenon, i.e. the spontaneous spreading of molecules or particles in space. Depending on the scale of the phenomenon, we consider two basic types of diffusion:

1) Molecular diffusion (the phenomenological approach) – this process comprises the macroscopic quantities of matter (or energy) usually referring to diffusion equation, and leads to the equalization of the concentration (or temperature) of each of the diffusible substances in the whole system. This kind of process is typically described mathematically by using Fick's law of diffusion [42].
2) Tracer diffusion (from the atomistic standpoint) – this process relies on the microscopic chaotic motion of single particles (Brownian motion), depending on their mobility tensor [43].

Diffusion coefficients for these two types of dispersion are generally different because the diffusion coefficient for molecular dispersal is binary and includes the effects of the movement of different diffusing species. In this work, we concentrated on the second type of the phenomenon, analysing the particle mobility to evaluate the diffusion process. A single-particle tracking method, based on optical techniques, is used to record the trajectory of a moving microparticle [44].

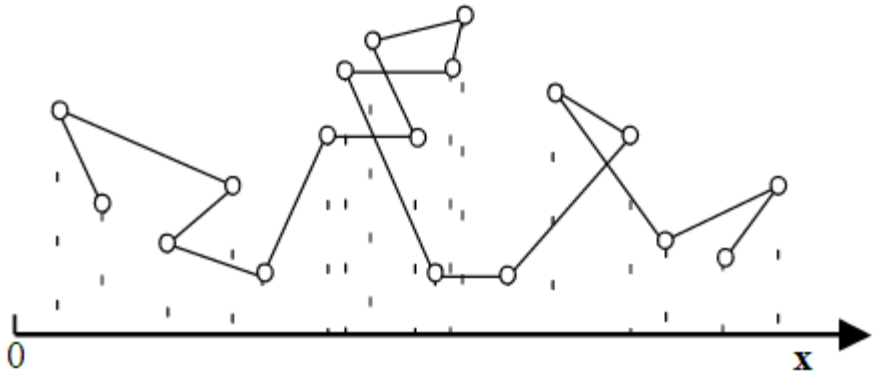


Fig. 1.6. Brownian random displacement of particles along the x axis at time t.

Einstein and Smoluchowski concluded that the observed Brownian movement of the particles suspended in a liquid is a direct proof of its molecular structure. They suggested that the study of the mobility of Brownian particles permits the detailed analysis of solvent properties. Their work proved the direct relation between the mean square displacement of the observed particles ($<x^2>$, MSD) and the diffusion coefficient *D*, which can be measured applying following formula:

$$MSD = <(\Delta x(t))^2> = 2a_d Dt \quad (3)$$

where: $\Delta x(t)$ = abs(x(t) – x(0)), the particle displacement during an interval time *t*; $a_d$ – the space dimension [44]. The MSD value is evaluated as a time or space average over a large number of observed displacements.

For the spherical particles suspended in a homogeneous liquid, the diffusion is determined by the translational diffusion coefficient and the usually neglected, rotational diffusion coefficient. In the case of asymmetric particles (elongated shape objects), non-isotropic translational diffusion coefficients are possible: along the main axis ($D_a$) and along the minor axis ($D_b$). Here, also the rotational diffusion coefficient $D_\Theta$[44,45] is not negligible. Within the limit of small Reynolds numbers and long-time scales, the Brownian diffusion coefficient for the translational motion of isolated spherical particles can be evaluated using a simple formula derived by Einstein:

$$D = \frac{k_b T}{6\pi\eta R} \tag{4}$$

where: $6\pi\eta R$ is the friction (drag) coefficient given by Stokes law for a sphere moving in a viscous liquid; $T$ is the absolute temperature of the liquid; $k_b$ is the Boltzmann constant [44]. $R$ is the radius of the particle, and $\eta$ is the dynamic viscosity of surrounding media. Stokes-Einstein equations for rotational diffusion are given as [46]:

$$D_\theta = \frac{k_B T}{8\pi\eta R^3} \tag{5}$$

The translational diffusion is anisotropic for non-spherical particles. For stiff elongated particles (rods, spheroids) we can distinguish six individual diffusion coefficients. Three coefficients are responsible for random particle displacements in each of the *x*, *y*, *z* directions:

$$dx(t_n) = x(t_{n+1}) - x(t_n), \tag{6}$$

and other three rotational coefficients are defined for particle rotation along each axis:

$$d\theta(t_n) = \theta(t_{n+1}) - \theta(t_n). \tag{7}$$

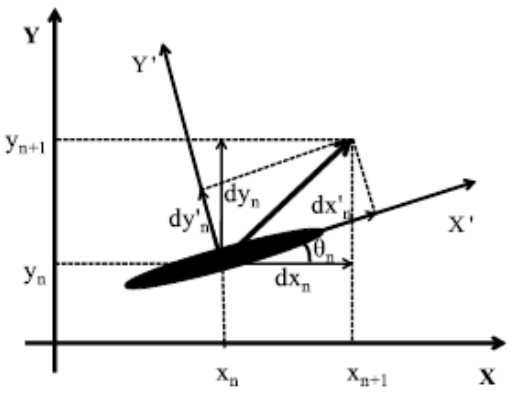


Fig. 1.7. Coordinates for the planar rotation of a spheroid [44].

An experimental evaluation of these complex displacements is not an easy task. The observation of displacements in space must be accomplished by means of a more difficult analysis of object rotation. One of the methods used to determine the rotational diffusion is static or dynamic fluorescence anisotropy [47]. In this work we limit our observations to in-plane displacements, while rotational motions are analysed only for the axis perpendicular to this plane.

The theoretical evaluation of drag forces for ellipsoidal objects moving in viscous liquid makes it possible to calculate the corresponding diffusion coefficients of long, thin ellipsoids [41]. Using such approximation, three basic diffusion parameters of rods can be evaluated according to the following formulas:

$$D_a = \frac{k_B T[\ln\left(\frac{L}{R}\right) - 0.5)]}{2\pi\eta L} \tag{8}$$

$$D_b = \frac{k_B T[\ln\left(\frac{L}{R}\right) - 0.5]}{4\pi\eta L} \tag{9}$$

$$D_\theta = \frac{3k_B T[\ln\left(\frac{L}{R}\right) - 0.5]}{\pi\eta L^3} \tag{10}$$

where: $D_a$, $D_b$ denote translational diffusion coefficients along and perpendicularly to the rod main axis; $D_\theta$ is the rotational diffusion perpendicular to the main axis of the rod; $L$, $R$ denote length and radius of the rod $(L >> R)$; $\eta$ is the dynamic viscosity of surrounding media.

The above approximation will be used in the present work as the first test for evaluating the behaviour of the long microobjects we observed under a microscope.

The problems of characterizing the diffusion of flexible objects, such as nanofilaments or long molecular chains, can be solved only on a statistical basis due to the large number of degrees of freedom. There are not just translational and rotational motions of the object to be analysed. The main response of thermal fluctuations is transformed to the multifunctional shape variation of the object analysed. There is no unique method for characterizing the diffusivity of such objects. The diffusivity of flexible objects depends not only on their geometry and shape, but also on a large number of parameters characterizing the constraints of the internal and external mechanical interactions. Hence, it is necessary to introduce several simplifications. In the most common approach, proposed by Kratky and Porod [48], the complex shape variations of such an object are

described in a reduced way as that of a chain of spherical subunits. Its dynamic structure may be regarded as a stochastic behaviour of randomly moving chain elements connected by flexible springs. The statistics of chain deformations can be described by the persistence length, being a measure of the chain stiffness or flexibility; the stiffer the chain, the larger the persistence length [49]. As will be shown in the following chapter, such an approach allows for a relatively straightforward interpretation of the observed shape variations in terms of basic mechanical parameters.

### 1.3.2 Mobility of elongated, deformable nanoobjects in a flow

Predicting the behaviour of deformable objects carried by the flowing fluid is necessary for a full understanding of the physics of macromolecules, bioliquids, and filaments suspensions. The investigation of the nature of the biomolecule and polymer flexibility is essential for determining their structure and dynamics, and is crucial for the interpretation of effective reaction rates in cellular signal transduction and amplification. Here, we assume that by investigating the dynamics of the elastic objects suspended in a liquid it is possible to gain knowledge about the role of the mechanical properties responsible for the complex behaviour of biological molecules (e.g. the folding of DNA). Theoretical assumptions, especially in the field of polymer physics, use coarse-grained models to study the folding process of DNA and proteins. However, to describe this phenomenon on a molecular scale, such an analysis must still be limited to very small length and time scales.

Moreover, the transport properties of elongated and deformable objects suspended in liquids are still far from being completely understood. Despite recent progresses in this field, there is still a paucity of experimental investigations for a validation of the assumptions of numerous theoretical and numerical models. The mathematical description of mobility for stiff objects is already characterized by several serious limitations, being generally based on their shape simplifications. The simplest models of rod-like shaped particles are based on elongated ellipsoids, or chains of interconnected spheres, which are easier to accommodate to a Stokesian set of equations. Even for such relatively simple geometry, however, only the general description of their mobility properties is validated experimentally. In the case of flexible objects – mainly investigated as elements of polymer science – the details of mobility for individual molecular chains are deduced only from the available statistically averaged bulk flow data. The lack of experimental studies is mainly due to the absence of good model systems that can make it possible to determine and control the elasticity and geometry of the

objects analysed.

**Theoretical models**

Most of the current models describing the dynamics and properties of flexible objects use complex systems of interconnected identical spherical particles. Many studies focusing on the phenomenon of object migration show that, in general, the flow properties of flexible objects (e.g. hydrogel fibres) are strongly influenced by hydrodynamic interactions [50]. However, presently available experimental data are mainly qualitative and not sufficiently precise for the verification of numerical models. In addition, it is very difficult to directly model microbial processes that require complex molecular interactions [51, 52].

The microscale experimental model of elastic objects introduced here enables us to perform accurate optical measurements and limit the description of its mobility to hydrodynamic interactions only. It should help in verifying the role of hydrodynamic interactions in modelling the dynamics of elastic bio-objects such as DNA or proteins.

The flexibility of rubber-like, elongated elastic objects is usually described by two parameters: stretching and bending. Such an approach makes it possible to adopt the already-mentioned warm-like-chain (WLC) approximation, which is widely used for modelling polymer chains in different simulation methods [50, 53, 54]. Another approach used in polymer science is a dumbbell model. In this model, two particles that represent two ends of the object (e.g. a filament) are connected by a spring (Fig. 1.8). The spring represents entropic forces. The end-to-end mobility vector describes stretching and orientation (conformation) of the dumbbell, thus representing the mechanics of the deformable object. The mobility vector of the centre-of-mass describes the translational transport of a dumbbell in a flow field [55, 56].

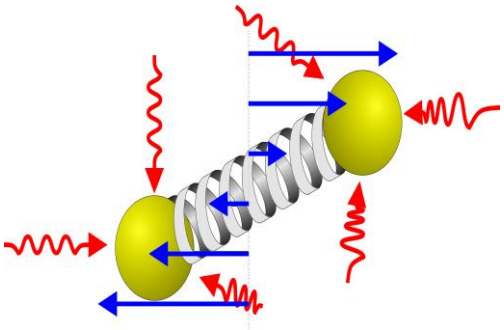

Fig. 1.8. Dumbbell model in shear flow.

One of the most common approximations used for describing the behaviour of long objects in a fluid flow is the slender-body theory. Using the slenderness ratio, this theory makes use of the large aspect ratio of long objects. Tornberg and Shelley [57] used the slender-body theory to construct a numerical method for simulating the dynamics of single or multiple flexible filaments in a shear flow. These authors show that, in a plane shear flow, flexible fibres have a tendency to become unstable to bucking when the shear rate is high enough, while a stiff fibre will rotate around its centre when conveyed by the fluid flow. Delmotte and co-workers [58] proposed a numerical model based on interconnected beads for the simulation of flexible fibre dynamics at low Reynolds number. In general, in the bead model, the fibre is formed by chains of spherical balls, connected together by an inextensible linker (Fig. 1.9). Its aim is to describe a complex flexible object (e.g. a fibre) by the elastic assembly of rigid ones [57, 58].

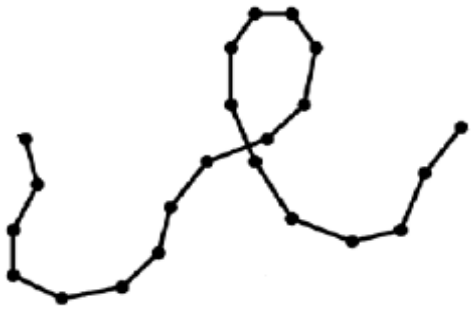

Fig.1.9. Interconnected beads model.

A similar study was presented by Reddig and Stark [59] and Khare et al. [60]. They simulated a cross-streamline migration of semiflexible polymer modelled by a bead-spring chain in a low Reynolds number regime.

Recent advances, mainly in micro-fabrication and microfluidic techniques, greatly expanded experimentally accessible flow configurations. In particular, microfabrication techniques made it possible to: (i) obtain a precise control of the fibre orientation and deformation, and (ii) analyse their interactions with well-defined micro obstacles. Proposed for this study flexible hydrogel nanofilaments cover effects of mechanical properties of complex molecular structures, whereas simplify mobility description by allowing to neglect short range molecular effects, screening potentials, hydrophobicity, steric effects, and van der Waals interactions. Therefore, one of our main goals is to use flexible nanofilaments as model objects to systematically investigate the influence of their mechanical properties on hydrodynamic interactions and the resulting macroscopic

transport properties. Such data should help validate the essential assumption of typical models, such as "worm-like-chains", commonly used in polymer science.

**Experimental models**

There are numerous experiments focusing on the study of long bio-molecule dynamics, mostly devoted to DNA dynamics. Doule et al. [61] investigated individual tethered DNA chains in a shear flow and compared them with numerical simulations. These authors conducted an experiment involving the observation of the dynamics of several DNA molecules, which had been attached to the substrate at one end and subjected to shear flow. They analysed the chain extension by varying the flow strength, and demonstrated that the elongation of the DNA chain depends on the flow rate and has a linear behaviour. This confirmed the earlier results of Smith and co-workers [62]. However, they could not find a correlation of the chain dynamics with DNA conformations. Another experimental study on DNA chains as an object was conducted by Jo et al. [63]. The authors experimentally investigated the behaviour of a DNA conveyed by an oscillatory shear flow and migrating towards the central microchannel part. They reported intriguing performances of the DNA chains. It appeared to be more coiled near the central part of the channel and stretched near the channel walls. It was found that the conformation of DNA molecules is very dynamic, and this can be visible in continuous cycles of relaxed and stretched forms. As the ends of DNA chains are mostly relaxed, usually the central part of the molecule is completely stretched, i.e. polymer ends show more freedom than the internal segments.

The dynamics of the actin filament – another long and deformable biostructure – in fluid flow were also investigated. Actin filaments are much stiffer than DNA molecules, considered as semi-flexible objects. Harasim and co-workers studied the complex conformational dynamics of individual actin filaments in a shear flow [64]. In his work Steinhauser [55] also focused on actin filaments and their configuration and orientation in a flow. Due to their relatively large diameter (7 nm) and length of several micrometres, the dynamics of the actin filaments conveyed by a fluid flow resembles that of worm-like-chain models.

### 1.3.3 Cross flow migration of particles, droplets, and deformable nanoobjects (DNA, biomolecules)

The microfluidic systems developed for focusing and sorting cells and biological objects are based on the hydrodynamic interactions responsible for the cross-flow migration of selected objects suspended in the carrier liquid. This effect has long history of

investigations, initiated by the intriguing redistribution of red blood cells in capillaries observed by the pathologist Fåhræus (comp. [65]). Some early experiments conducted by Segre and Silberberg [66, 67] on the spherical particles observed in a tube flow confirmed the existence of lateral hydrodynamic forces which redistribute the suspended particles across the channel to the equilibrium position between the tube wall and its centre. As a solid spherical particle is obviously a very coarse approximation of highly deformable blood cells, the liquid droplets suspended in the flow were used as models of erythrocytes [68]. These preliminary studies indicated the presence of cross-flow migration and paved the way for a chain of studies devoted to elucidating the role of shear stresses, wall interactions, droplet deformability, and viscosity ratios in the migration process [69-72]. One of the important messages originating from these studies is that the inertial forces, usually neglected in microfluidics, play an important role for the proper interpretation of the cross-flow migration of particles and droplets [73]. The presence of residual inertial forces and the breakup of the flow symmetry in the case of suspended deformable objects lead to irreversible hydrodynamics, imposing a limited use of the so called Stokesian approximation of theoretical models. This became evident in microfluidic experiments on the lateral migration of droplets [74, 75].

In 1956, Starkey [76] was the first to demonstrate that – under appropriate conditions – neutrally rigid spheres in Poiseuille flow could migrate across streamlines. Very interestingly, many studies observed that the spheres eventually attained an equilibrium position at approximately 0.6 of the tube radius from the tube centre. Segre and Silberberg called it "tubular pinch effect" [66]. This effect was confirmed in the following years by other researchers [77, 78].

Suspension behaviour is one of the fundamental challenges of modern rheology [50, 53]. There are numerous experimental reports on the migration of solid spherical particles [66] and droplets [70]. They confirm the presence of a radial migration, but the theoretical interpretation of this phenomenon is still a subject of controversy. Ho and Leal [79] presented the lateral migration velocity of spherical particles in two-dimensional Poiseuille. The main outcome of the model is that there is, in fact, an effective cross-flow migration of the solid sphere, even for the low, but finite, Reynolds number flow regime. For deformable objects the most cited work by Chan and Leal [69] showed that deformable droplets migrate across the flow streamlines. Their model demonstrated that even in the creeping flow regime the particle (droplet) deformation creates the conditions for irreversible cross-flow migration. Recent numerical simulations [75] performed for

oscillatory flow, indicated that cross-flow migrating droplets follow some complex spiral-like paths with parameters additionally depending on the frequency and phase lag of imposed flow. The migration may change direction depending on the viscosity ratio, while droplets can migrate either into the flow axis or to the channel wall. To some extent, the elongated viscous liquid threads could be treated as a model configuration of polymer filaments. However, as we find in the following section, their mechanical properties are quite different.

The cross-flow migration problem already starts to be complex in the case of elongated objects (e.g. rod-like particles, molecules). In most cases, microscale migration effects of elongated objects are simplified to an ellipsoidal model introduced by Jeffrey [80, 81], and possibly applied to stiff fibres.

Most of the theoretical models describing the behaviour of particles in a microflow are based on the reversible, creeping flow approximation. Creeping (Stokesian) flow models, however, can be misleading in the case of deformable objects and complex flow structures. Thus, despite the widespread belief in the creeping flow reversibility, irreversible hydrodynamics are commonly present for deformable objects and in curved microchannels [82]. Therefore, we may expect irreversible hydrodynamic interactions even for the creeping flow of flexible filaments observed in a microchannel. One of the most common effects of such interactions is the cross-flow lift force exerted on suspended objects, which is due to the wall and velocity profile interactions and depends on a number of factors. Depending on the geometry ratio, physical properties of suspended objects, and degree of shape deformation, the cross-flow migration may lead to the uneven distribution of suspended objects across the channel, and their consequent collection at one or more equilibrium radial positions [68, 69, 71]. The migration problem is quite complex in the case of long flexible objects (e.g. filaments, molecules). Without a doubt, this phenomenon is affected by changes in conformation, object elongation, or tumbling. The cross-flow migration of fibres or other long objects in a channel flow is one of the fundamental issues of modern lab-on-chip techniques, being important in a variety of biological, medical, and industrial contexts (e.g. Brownian dynamics of proteins, DNA or biological polymers, cell movement, movement of microbes, and drug delivery). The existing simulations conducted for long objects suspended in a flow suggest that stiff fibres tend to accumulate near the channel wall, while flexible fibres undergo great deformations and accumulate far from the wall [51, 53]. A detailed experimental validation is still unavailable for such data.

Simulations have shown that long biopolymers (e.g. filaments) have a tendency to accumulate near the wall and bend only slightly [50, 51]. On the other hand, the flexible fibres conveyed by the flow tend to accumulate rather far from the wall, where they bend significantly [53]. Other studies on the self-organization of semi-flexible long objects (actin filaments) along the channel cross-section depending on different flow velocities show the tendency to elongate or bend fibres in a microflow. The fibre elongation increases as the flow rate increases. In addition, the flow rate also affects the equilibrium position of fibres across the channel. At a high flow speed, there is a little chance of finding fibres near the centre of the channel. Fibres may migrate from the centre of the channel to the walls, and modify the shear rate of the flow near the wall [55]. Such an effect is known for polymers used to damp development of the turbulent boundary layer at a channel wall [83].

### 1.4 Mechanical properties of elongated particles (persistence length)

The knowledge of the mechanical properties of polymers is important in the context of their applications (e.g. medicine, industry). It is especially important that they have a suitable strength, stiffness, and toughness. For the correct determination of their mechanical properties, it is crucial to understand the relationships among molecular structure, morphology of the materials, and their final mechanical properties [84]. The strength reveals the material resistance to a damage caused by breakage or excessive deformation, while stiffness is a measure of the load required to cause a deformation in the material. Stiffness is determined by measuring the deformation resulting from the application of a given load (force), which does not damage the object. Stiffness is the rigidity of an object; it carries shape information of the sample. A complementary definition of stiffness is material flexibility; the more flexible an object is, the less stiff it is. The dependence of Hooke's law on stiffness and Young's modulus (elastic modulus) results is given by:

$$P = k_e \delta \ , \tag{11}$$

where $P$ is the load, $k_e$ is the stiffness, and $\delta$ is the deformation. The Hookean $k_e$ stiffness is given by the linear relationship between Young modulus $(E)$, the cross sectional area of the object $(A_r)$, and its length $(L)$:

$$k_e = \frac{A_r E}{L} \tag{12}$$

A common method for determining the stiffness of polymers is the use of the value defined as the persistence length ($L_p$). This may be any value, even greater than the contour length of the sample. As a matter of fact, it does not describe any physical distance in the material structure. It refers, instead, to the ability of the sample to independently deform under the influence of thermal fluctuations when its segments are at distances above $L_p$. Generally speaking, the pieces of polymers that are shorter than their persistence length behave like flexible elastic rods, while the deformability of the pieces of polymers that are much longer than their persistence length can only be described statistically as a three-dimensional shape fluctuation. In other words, it is the length after which the polymer chain loses its initial orientation [85]. The value of $L_p$ varies from 0 to ∞. Bending rigidity – a fundamental parameter used to describe the conformation of long polymeric objects – is related to persistence length. It determines the object bending deformation due to the applied external forces [85].

The first model defining persistence length for molecular chains was offered by Frenkel and Bressler [86]. Ten years later Kratky and Porod [48] evaluated it in the better known form of worm-like chain of small segments. They proposed that the bending potential $U(\Theta)$ of the elastic rod (contour length $L$) which bends at an angle $\Theta$ in the first approximation must be proportional to the square of that angle. With an increased contour length of the rod, its bending potential decreases [87]. The effective parameter determining the deformability of the molecular chain is the ratio of the persistence length ($L_p$) to the contour length ($L$). This parameter is called relative stiffness ($b_s$):

$$b_s = \frac{L_p}{L} \tag{13}$$

There are three methods commonly used to evaluate the persistence length:

1) Cosine correlation – this method is based on the analysis of the two-dimensional cosine correlation of the tangent angle $(\Theta)$ along segments $(s)$ of the long object with a contour length $L$. It uses the fitting function:

$$cos\Theta(s) = < \cos[\Theta(s) - \Theta(0)] >= e^{-L/2L_p} \tag{14}$$

where $\Theta(0)$ is an initial reference angle. The symmetry of cosine function ($\pm \Theta(s) - \Theta(0)$) is not convenient for fitting it to the experimental data. Thus, for the evaluation of the persistence length, data are fitted to an exponential function [85, 88, 89].

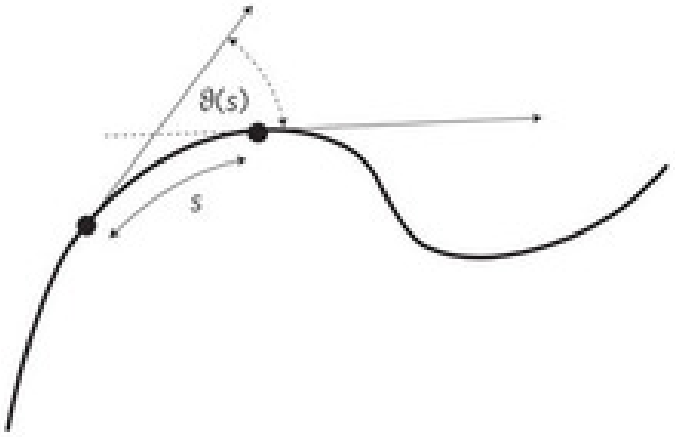


Fig. 1.10. Principle of defining the deformation of elongate objects by the cosine correlation method.

2) End-to-end distance analysis – this method uses the mean square of the end-to-end distance ($<R_n^2>$) as a function of the contour length ($L$) and persistence length:

$$< R_n^2 > = 2{L_p}^2(e^{-L/L_p} - 1 + L/L_p) \qquad (15)$$

It permits the direct determination of the persistence length, but it is less accurate than the cosine correlation method. Each object is represented as a single data point, so this method shows the global geometry of an individual object. Therefore, from a statistical standpoint, it requires the analysis of a large number of samples [85, 88].

3) Bending mode analysis – this method is used to analyse the shape fluctuations of single elongated objects [88]. It determines object angular bending modes through the Fourier analysis of the object shape. Persistence length is calculated using the amplitude of several bending modes and taking their weighted average. The method was found particularly useful for analysing the flexural stiffness of the microtubules responsible for driving the mitosis of eukaryotic cells [90, 91]. There, the single microtubule fixed at one end changes its shape due to the thermal fluctuations damped by the hydrodynamic drag. Usually the contribution of up to ten bending modes is necessary to estimate the microtubule flexural rigidity.

Short molecules characterized by low relative stiffness behave – in terms of conformations – in the same way as the long, very stiff molecules. If the value of the relative stiffness $b_s$ is below 0.05, the macromolecule is treated as a flexible object ($L >> L_p$).

The chain of molecules may be considered as a system of freely connected segments (e.g. long DNA fragments). If the value of $b_s$ is in the range $0.05 < b_s < 5$ – the molecule is characterized by a reduced stiffness (semi-flexible, since $L \cong L_p$). Actin filaments are examples of semi-flexible biomolecule structures [55]. Molecules with a relative stiffness higher than *5* are identified as rigid and non-deformable $(L << L_p)$.

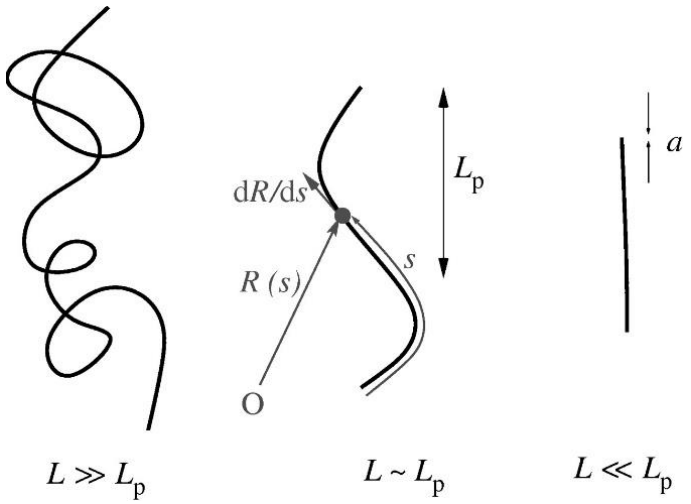


Fig. 1.11. Ratio of elongate object contour length $(L)$ to persistence length $(L_p)$ [89].

Physically speaking, the persistence length of nanofilaments may be described as the ratio of the bending rigidity $(\kappa)$ and thermal energy ($k_bT$). Bending rigidity depends on the Young's modulus $E$ and also on the moment of inertia $(I)$ based on the filament cross-section [92, 93]:

$$L_p = \frac{\kappa}{k_b T} = \frac{EI}{k_b T} \tag{16}$$

where $I = \pi R^4/4$. $T$ is the absolute temperature, $k_b$ is the Boltzmann's constant, and $R$ is the radius of the filament. This relation will be used in the following chapter to evaluate the mechanical properties of our nanofilaments.

Shape fluctuations of the flexible filament suspended in a viscous liquid are damped according to the Stokes law. Assuming that the persistence length represents an elementary unit of such a flexible chain, we may define the flexural diffusivity $D_f$, which represents the ratio of kinetic thermal energy of the environment $k_bT$ to the Stokesian drag exercised on the "free" fragment of the chain represented by its persistence length $L_p$:

$$D_f = \frac{k_b T}{8\pi\eta L_p} \tag{17}$$

## 1.5 Dissertation overview

The current dynamic development of nanotechnologies contributes to numerous new products in various sectors of science and industry. Nano-scale objects became prevalent among theoreticians and experimentalists from several disciplines (chemistry, biology, engineering, and medicine). Their small size creates new opportunities for the application of spherical and elongated nanoobjects as targeted drug carriers. Such systems make it possible to deliver drugs to specific organs, tissues, and cells within the body in order to obtain the targeted action. An important issue is the construction of proper nanocarriers, allowing for their controllable transport within tissue and cell environments.

The micro- and nano-scale motion is coupled to, or sometimes mainly driven by, the molecular diffusion, a direct effect of the molecular structure in our environment. The diffusion governed by Brownian motion is an efficient transport mechanism on short time and length scales. Even a highly organized system like a living cell relies on the random Brownian motion of its constituents to perform complex functions. The observation of the Brownian motion of micro-objects is a classical basis for particle size measurements, the evaluation of liquid properties (viscosity, microrheology), particle-wall interactions, and much more. Nevertheless, such a seemingly simple problem creates a plethora of uncertainties. The equilibrium state and the hydrodynamic properties of many colloid systems in aqueous media are affected by several environmental parameters. The ionic nature of water solutions necessitates, in addition to the analysis of the hydrodynamic friction (the well-known Stokes formulae), the evaluation of surface-liquid interactions. In practice, surface charges, ionic streams, and the creation of the electrostatic double layer are expressed by a nonphysical “hydrodynamic diameter”. The proper prediction of such effects is crucial to an understanding of transport processes at the single-cell level and, consequently, to possible applications of nanoparticles for diagnostic or medication proposes. In my thesis, some of these aspects will be evaluated with the aim of identifying problems, providing a proper interpretation of micro- and nanoparticle mobility.

Moreover, the transport properties of elongated objects, such as long molecules, are complicated by additional degrees of freedom due to their changes in shape. Here, I have explored this problem by constructing long, elastic nanocarriers, with yet-unexploited applicability in biology and medicine. This study could even help expand our knowledge of the physical phenomena which are responsible for the behaviour of long biological particles, such as long proteins or nucleic acids in the cellular environment.

The experiments performed in transparent microchannels permitted the precise, microscopic analysis of examined objects, i.e. nanoparticles and hydrogel nanofilaments. Understanding the relationship between particle or filament microstructure and macroscopic flow properties opens the door to designing nanoobjects, which could be transported by body fluids for dedicated drug release and/or local tissue regeneration. It should be noted that, at the present time, the analytical/numerical modelling of such processes is difficult and not sufficiently credible, thus leaving experiments as the only alternative.

The dissertation is organized as follows. In Chapter 2 we will present the list of all materials used in the experiments, basic apparatus, descriptions of electrospun core-shell nanofibers preparation, and microfluidic devices preparation. In the next chapter (Chapter 3) full analysis of Brownian diffusion of spherical polystyrene particles will be given. We check influence of ionic strength of medium and wall effect on the value of nanoparticle hydrodynamic diameter. Experiments with lateral migration of nanoparticle under the influence of an oscillatory flow will also be performed. In Chapter 4 we will focus on highly deformable hydrogel nanofilaments. After morphological and mechanical characterisation, we will analyse their behaviour in Brownian fluctuations and oscillatory flow conditions. Especially we focus on changes of filament conformation and lateral migration as a result of oscillatory flow. Finally, in Chapter 5 we present short introduction about the potential applications of the studied nanoobjects in biomedicine and we show the results of analyses of our highly deformable hydrogel nanofilaments as controlled drug delivery systems.

# Chapter 2: Materials, preparation, and apparatus

Below we summarize the main data on materials and methods used in the experiments conducted within the framework of this study.

## 2.1 Materials

### 2.1.1 Solid spherical particles

Three different types of solid spherical particles were used for Brownian motion analysis. Fluorescent polystyrene particles (emission wavelength of 550 nm and physical sizes 48 nm, 63 nm, 100 nm, 300 nm, 600 nm, 1000 nm, 3200 nm, dispersed in 1% (w/w) aqueous solution [Fluoro-Max Red Aqueous Fluorescent Particles – Thermo Scientific™]), carboxylate-modified polystyrene particles (95 nm, 200 nm, 328 nm, Fluoro-Max Dyed Carboxylate- Modified Microparticles – Thermo Scientific™), and gold particles (60 nm, 100 nm, Aldrich) were studied. Nanoparticles were suspended in water or salt (KCl, LiCl and $NiCl_2$ (Sigma-Aldrich)) solutions with different concentrations.

### 2.1.2 Polymer filaments

Hydrogel filaments were produced using the following chemical components: Poly(L-lactide-co-caprolactone) (PLCL, 70% L-lactyde and 30% caprolactone unit, Corbion Purac, Netherlands), chloroform ($CHCl_3$, POCh, Poland), N,N-dimethylformamide (DMF, POCh, Poland), Bovine Serum Albumin conjugated with fluoresceine (BSA-FITC, Sigma Aldrich, Poland), acrylamide (AAm, Sigma Aldrich, Poland), N,N-isopropylacrylamide (NIPAAm, 97%, Sigma Aldrich, Poland), N,N'-methylene bisacrylamide (BIS-AAm, 99.5%, Sigma Aldrich, Poland), ammonium persulfate (APS, 98%, Sigma Aldrich, Poland), N,N,N',N'- tetramethylethylenediamine (TEMED, 99%, Sigma Aldrich, Poland), and photoinitiator (2-Hydroxy-4′-(2-hydroxyethoxy)-2-methylpropiophenone) (Irgacure 2959, 98%, Sigma Aldrich, Poland).

## 2.2 Preparation methods

### 2.2.1 Electrospun core-shell nanofibre preparation

The electrospinning shell solution was prepared by dissolving 1 g of PLCL polymer in 10 g of mixture of DMF and $CHCl_3$ 1:9 (w/w). The core solution (10 wt.% AAm/BIS-AAm or NIPAAm/BIS-AAm) was prepared by dissolving 2.24 g of AAm (or NIPAAm) and 0.06 g of BIS-AAm in 20.7 g of deionised water in the ratio of 37.5:1 of AAm or NIPAAm and BIS-AAm, respectively. Mixtures of core polymer AAm (or NIPAAm) and BIS-AAm with mass ratio of 20:1 and 4:1 were also prepared (Table 2.1). PLCL polymer

solution and core mixture were prepared one day before nanofibre fabrication. Before electrospinning, 10 μl of APS and 0.007 g of BSA-FITC were mixed with 1 ml of NIPAAM (or AAm) / BIS-AAm solution. The addition of a small amount of BSA-FITC made it possible to use fluorescence for image acquisition and to study protein release dynamics [94]. Lastly, a suitable amount of TEMED (1 μl) was added to the solution of AAm/ BIS-AAm/APS which was then vigorously shaken. The addition of TEMED triggered hydrogel polymerization (Fig. 2.1 (a)).

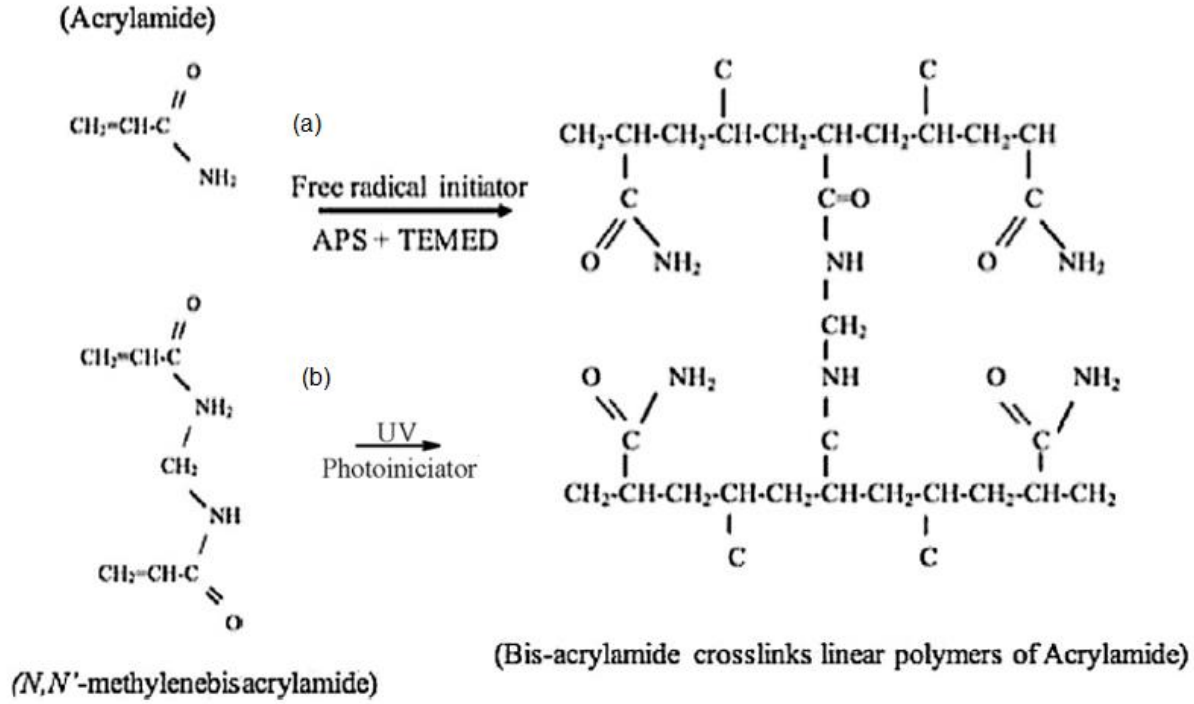


Fig. 2.1. Polymerization process of AAm-BIS-AAm hydrogel: (a) with a free radical initiator; (b) with photoinitiator and UV light [95, 96].

To improve the control of the polymerization process an alternative method for preparing the hydrogel core was tested using a photoinitiator (Irgacure 2959) instead of APS and TEMED as the molecule that triggers the polymerization reaction under the influence of UV irradiation (Fig. 2.1 (b)). This procedure made it possible to control the polymerization of the core-forming solution inside the PLCL shell accurately and easily. Based on bibliographical data [97-99], the used here proportion of polymeric components forming the hydrogel core (NIPAAm/AAm and BIS) and the photoinitiator (PhIn) is given in Table 2.1.

Table 2.1. Concentration of components for core-shell fibre preparation.

| | | (a) | | | (b) |
|---|---|---|---|---|---|
| | | **37.5:1** | **20:1** | **4:1** | **37.5:1** |
| Core (10%) | **AAm / NIPAAm** | 100 [mg/mL] | 100 [mg/mL] | 100 [mg/mL] | 100 [mg/mL] |
| | **BIS-AAm** | 2,67 [mg/mL] | 5 [mg/mL] | 25 [mg/mL] | 2,67 [mg/mL] |
| | **BSA-FITC** | 7 [mg/mL] | | | |
| | **TEMED** | 1 [μL/mL] | | | - |
| | **APS** | 10 [μL/mL] | | | - |
| | **PhIn** | - | | | 5 [mg/mL] |
| Shell (9%) | **PLCL** | 1 [g] | | | |
| | **$CHCl_3$** | 9 [g] | | | |
| | **DMF** | 1 [g] | | | |

Monomers and photoinitiator were dissolved in deionized water no later than one day before the electrospinning process. Before starting the electrospinning process, the core mixture solution must be degassed by bubbling argon for half an hour. Degassing is important for removing oxygen from the core solution, thus avoiding the formation of radicals through a reaction that competes with the hydrogel polymerization. Another method for removing oxygen involves the use of low pressure (20 mbar environment) for degassing. However, it will reduce the volume of the mixture by the solvent evaporation and the concentration of polymer components becomes different from at the initial one and difficult to estimate.

The polymerization process (with a photoinitiator as the initiator of this process) was carried out using a UV lamp (density of power 225 $mW/cm^2$) for 1 minute under a cooling bath. The average temperature of the bath was between $2^oC$ and $4^oC$.

The cooling of hydrogel during the polymerization process is necessary to prevent any change due to overheating in the structure of the hydrogel. The temperature of hydrogel after irradiation should be not higher than $32^oC$, in order to ensure that the sample does not lose water, the concentration of polymers does not change, and – most importantly – to avoid inhomogeneity during the formation of the polymer cage. Acrylamide is much less sensitive to high temperatures during a polymerization process. Its Lower Critical Solution Temperature (LCST) is higher (above $50^oC$) than in the case of NIPA ($32^oC$) [98-101].

### 2.2.2 Preparation of microfluidic devices

The first step in microfluidic device fabrication includes the design of the microchannel architecture by producing a mask. The mask is a film made using the CtF (Computer to Film) exposure method, on which the areas presenting the microstructure scheme are transparent. It is necessary for the UV light to pass through these areas in the next step of photolithography. Therefore, the mask is a negative of the design of the microfluidic system. Then the film is used to prepare matrices using the negative lithography technique. This technique, called soft lithography, is commonly used in the fabrication of PDMS microfluidic chips. The essential materials for the fabrication of the matrices are a backplate (silica wafers) and a suitable photoresist (Su-8 2075, MicroChem). Su-8 is a group of epoxy-based negative photoresists which, during exposure to UV, become crosslinked. Only non-illuminated areas of photoresists are removed from the silicon wafer by the developer solvent. This procedure requires the use of specific laboratory equipment as a spin coater (SCS G3 Spin Coater Series) and an UV lamp (DYMAX Flood Lamp 5000). The prepared matrices are used to achieve a proper microchannel architecture, by stamp the thermoscuring elastomer of poly(dimethylsiloxane) (PDMS, Dow Corning), which perfectly reflects the convex elements of the matrix. The fabricated PDMS microchannel is then sealed with a microscope glass cover slip (joining method using oxygen plasma) used for the observation of the phenomena studied under a microscope. A typical scheme for the production of PDMS microfluidic systems is shown in Fig. 2.2:

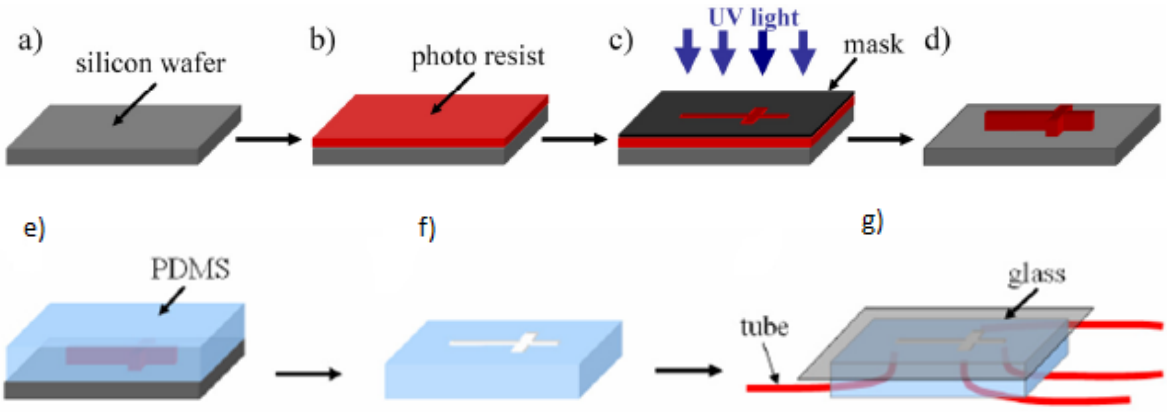


Fig. 2.2. Photolithography and fabrication of a PDMS microfluidic system [55].

## 2.3 Apparatus

The experiments described in this thesis were conducted using apparatuses available at the IPPT Laboratory of Bio- and Microfluidics, mostly purchased thanks to POIG

structural funds CePT [POIG No. 02.02.00-17-024/08-00]. The basic microscopes used for imaging are a Nikon Eclipse E-50i epi-fluorescent microscope with double-shutter CCD camera and double-pulsed Nd:YAG laser, a Leica AM TIRF system based on inverted fully automated microscope Leica DMI6000 with AFC, an environmental chamber, a set of lasers and 120 W mercury metal halide lamps, and a confocal microscope Leica TCS SP5 X with environmental chamber. For image recording three different cameras were used: EM-CCD Hamamatsu C9100-02 (1000x1000 pix, monochrome, cooled, high EM gain, 256 fps), Leica DFC365FX (1391x1040 pix, monochrome, cooled, 122 fps), and Leica DFC295 (2048x1536 pix, colour, 12 fps). For the analysis of mechanical properties (in the case of filaments) and micro-object morphology, an atomic force microscope (AFM, Ntegra Spectra, NT-MDT, Limerick, Ireland) and portable scanning electron microscope JSM-6010PLUS/LV were used.

An innovative device used to analyse the interaction of spherical particles with the wall of the microchamber (wall effect evaluation) was Optical Tweezers, developed at IPPT PAN and based on the inverted microscope (IX71, Olympus Optical Co. Ltd, Tokyo, Japan) which is part of a commercial AFM (Ntegra Spectra, NT-MDT, Limerick, Ireland).

In order to be able to produce hydrogel nanofilaments for further analyses the environmental chamber for electrospinning built at IPPT PAN was used. The electrospinning chamber is equipped with a polymer dosing pump system, a high voltage generator, and a grounded collector. Another important apparatus created at IPPT for the purposes of the present study is a pulsating pump for generating an oscillatory flow. Its operation principle is based on the use of a rotating disk, which is mounted eccentrically on the stepper motor. The disk presses the pushing arm and, consequently, closes and opens the cross-section of the elastic tube filled with the working liquid, thus generating a flow in the microchannel connected to it. The apparatus used and its operation principle are described in the Appendix 5 with more details.

# Chapter 3: Mobility of spheroidal particles

Over one hundred sets of single-particle tracking experiments were performed to evaluate the role played by the particle size and ionic strength of the suspension liquid on mobility the particle. These experiments aimed to elucidate the background of reported discrepancies between physical and measured hydrodynamic diameters in nano- and microscale experiments with colloidal suspensions.

## 3.1 Morphological characteristics of solid particles

The morphology of commercially available spherical particles was tested using SEM and AFM microscopies. These measurements were necessary to confirm the physical size of the particles used in experiments, in order to determine the hydrodynamic size of the particles tested. A detailed description of the sample preparation method of morphological characteristic is given in Appendix 6.

## 3.2 Experiments on Brownian diffusion

### 3.2.1 Sample preparation

The tables below summarize the parameters of the particles and experimental conditions used for Brownian motion analysis. Particle concentration is given as a volume concentration.

Table 3.1a. Spherical polystyrene particles.

| Physical particle size [nm] | Solution | Concentration of solution | Concentration of particles* |
|---|---|---|---|
| **63** | $H_2O$ | - | 1:500000 |
| | KCl | 0.1 mM; 1 mM; 10 mM | 1:500000 |
| **100** | $H_2O$ | - | 1:100000<br>1:250000<br>1:500000 |
| | KCl | $10^{-9}$ mM; $10^{-8}$ mM; $10^{-6}$ mM; $10^{-5}$ mM; $10^{-4}$ mM; $10^{-3}$ mM; 0.005 mM; 0.01 mM; 0.05 mM; 0.1 mM; 1 mM; 10 mM; 40 mM; 80 mM; 100 mM | 1:100000<br>1:150000<br>1:250000 |
| | LiCl | $10^{-9}$ mM; $10^{-8}$; mM; $10^{-6}$ mM; $10^{-5}$ mM; $10^{-3}$ mM; 0.1 mM; 10 mM | 1:150000<br>1:250000 |
| | $NiCl_2$ | $10^{-9}$ mM; $10^{-7}$; mM; $10^{-6}$ mM; $10^{-5}$ mM; $10^{-3}$ mM; 0.1 mM; 10 mM | 1:200000<br>1:250000 |
| **300** | $H_2O$ | - | 1:150000 |
| **600** | $H_2O$ | - | 1:100000 |
| **1000** | $H_2O$ | - | 1:50000 |

* Concentration obtained by diluting 1% solids initial value.

Table 3.1b. Carboxylate-modified polystyrene particles.

| Physical particle size [nm] | Solution | Concentration of particles* |
|---|---|---|
| **100** | $H_2O$ | 1:1000 |
| **200** | $H_2O$ | 1:1000 |
| **300** | $H_2O$ | 1:1000 |

* Concentration obtained by diluting 1% solids initial value.

Table 3.1c. Gold particles.

| Physical particle size [nm] | Solution | Concentration of particles* |
|---|---|---|
| **40** | $H_2O$ | 1:10000 |
| **60** | $H_2O$ | 1:10000 |
| **100** | $H_2O$ | 1:10000 |

* Concentration obtained by diluting 1% solids initial value.

### 3.2.2 Observation methods

In the case of gold particles (not fluorescent), the PDMS chamber was illuminated on one side with a laser, while a camera recorded images perpendicularly to the reflection of the light wave on the surface of particles. To avoid the impact of the bottom wall, which could change the movement dynamics of particles, the focal plane of the microscope was set at the middle of the channel. Images were taken at specific time intervals (0.5-2 fps) and exposition time (100 ms), which was adjusted to obtain the greatest possible brightness of the particles. Over 1,000 images were taken for each sequence.

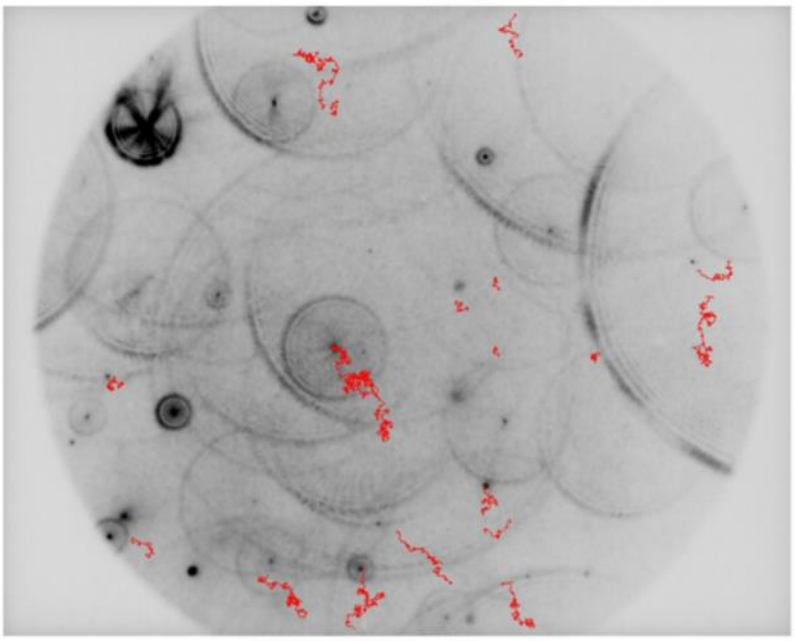

Fig. 3.1. Trajectories of 100 nm gold particles dispersed in water and observed under the microscope (red tracks). Several circles indicate diffraction rings from immobile disturbances, mostly particles settled at the bottom wall.

### 3.3 Diffusion coefficient evaluation (Brownian)

Before analysing the Brownian motion (particle displacements), the raw experimental images had to be filtered to detect the positions of particles. A denoising Wiener filter built in Matlab software was used. For each detected particle the image brightness *f(x,y)* was fitted using the equation:

$$f(x,y) = a_1 exp\left(\frac{-(x-x_0)^2}{2\sigma_x^2} - \frac{(y-y_0)^2}{2\sigma_y^2}\right) \tag{18}$$

where:

$x_0$, $y_0$ – displacement of the fitting window;
$a_1$, $\sigma$ – parameters of the matching function.

Knowing the position of the particle in each picture, time interval between frames, and scale of the microscope-camera system, we were able to calculate the trajectory of the particle in a series of photos (Fig. 3.1). The measured diffusion coefficient was calculated for each particle track obtained from such analysis, using the following equation:

$$D_{ex} = \frac{< MSD >}{a_d \Delta t} \tag{19}$$

where:

<*MSD*> – mean square displacement;

$a_d$ = 2, 4, 6 – factor based on the problem dimension (for 2D analysis $a_d$ = 4);

$\Delta t$ – time interval between images.

Experimental results were compared with the theoretical diffusion coefficient calculated as (4):

$$D_{th} = \frac{k_B T}{3\pi\eta d_{ph}}$$

where:

$k_B$ – Boltzmann constant;

$T$ – temperature inside the channel;

$\eta$ – dynamic viscosity of the fluid;

$d_{ph}$ – diameter of the particle (physical value).

For each series, the calculated arithmetic mean and standard deviation for experimental diffusion coefficient ($D_{ex}$) were compared with the theoretical diffusion coefficient ($D_{th}$) and represented as the ratio of diffusion coefficients $D_{ex}/D_{th}$.

For a few experimental runs, the diffusion coefficients, determined on the basis of particle tracking experiments, were compared with the data obtained from the commercially available Malvern NanoSight NTA hardware, which is described in Appendix 6.

### 3.4 Hydrodynamic diameter

The experimentally determined particle diffusion coefficient made it possible to determine its hydrodynamic diameter. The following formula was used to calculate this value:

$$d_h = d_{ph} \frac{D_{th}}{D_{ex}} \tag{20}$$

where: $d_h$ – hydrodynamic diameter; $d_{ph}$ – physical diameter, $D_{th}$ – theoretical diffusion coefficient calculated from the Stokes-Einstein equation (4); $D_{ex}$ – experimental diffusion coefficient.

### 3.5 Wall effect evaluation

To investigate the impact of the microchannel wall on the mobility of solid particles, we used the Optical Tweezers (OT) system developed at IPPT PAN (see Appendix 5). For this purpose, polystyrene particles (1μm diameter) suspended in pure deionized water and in four different potassium chloride solutions were used. In the experiment, the particle suspension was obtained by a 1:100 volume dilution of 1% particle solution samples.

The experiments were performed inside a PDMS microfluidic chip (Fig. 3.2) with 60 μm deep channels filled with water or salt solutions. The temperature of the experimental chamber was set to 295 K. Before each experiment microchannels were degassed under a vacuum pump (20 mbar) for one hour, and then they were placed for several minutes into water or KCl solution.

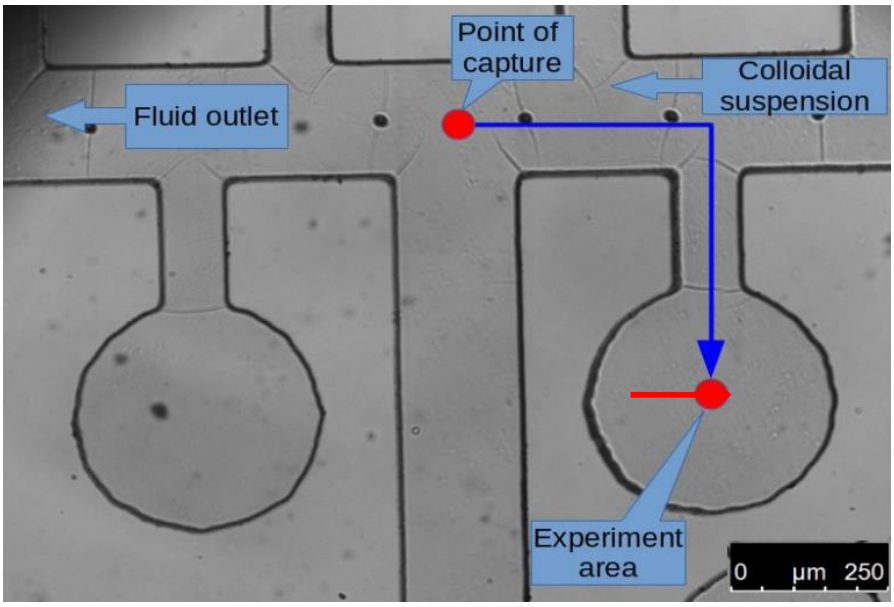


Fig. 3.2. Microchannels with round wells designed for experiments with optically trapped particles. Circle chambers had a diameter of 200 μm and depth of 60 μm. The red arrow indicates the direction in which the wall moves as a result of the microscopic table moving [102].

Round wells have only one way-in which helps provide a flow-free chamber. Once the Optical Tweezers catched the particle we transferred it to the chamber by moving the microscopic table with microchannels. Than the measurement of particle displacements starts (Fig. 3.3). Thanks to multiple wells we were able to conduct several experiments in the same microchannel.

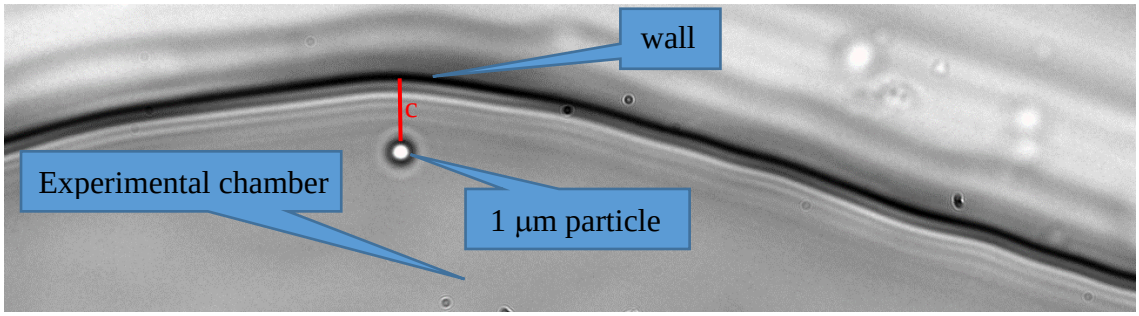


Fig. 3.3. Starting position of 1 μm particle trapped by OT during a single experiment inside the chamber. The red line indicates the direction of the particle motion tagged by OT into the wall; *c* is the shortest distance from the wall. The black contour in the image indicates the wall.

Particles were set at an average distance of 3-8 μm from the wall, and then tagged into it. The particle distance from the bottom of the chamber was 5μm. The speed of the table movement was 500 μm/s, the size of the movement step was 50 nm in the direction of the y axis. After each movement, the microscopic table stopped and the particle-wall interactions measurement was started. At each position of the particle its Brownian motion was indicated by OT signal fluctuations. The mean displacement of the particle position within OT focus indicated the net force due to the particle-wall interactions. The recording speed of the particle Brownian motion was equal to 1 kHz. A single recording lasted 2 seconds. The first 0.2 seconds of measurement were used to stabilize the system. The average for a given measurement point was calculated from the next 1.8 seconds (average value from 1800 time points). Each series consisted of 50-200 measuring stop points. Laser power was set to 10% of the maximum, which is equal to 9 mW. The moment of contact between the particle and the wall was determined as the time step when the particle falls out from the optical trap area and the amplitude of its vibrations rapidly decreases.

### 3.6 Lateral migration

As discussed in Chapter 1.3.5, cross-stream migration is a phenomenon that has been investigated – over many decades – for micro- and nanoobjects under the influence of the fluid flow in which they are suspended. In presented here experiments that investigated the migration process an oscillatory flow was used for two reasons. Firstly, it allows for a long time analysis without the need to create very long channels or a complex tracking measuring setup. Secondly, such an oscillatory (pulsatile) flow simulates the intracellular fluid motions in the human body.

Fluorescent polystyrene particles with a diameter of 1 μm, suspended in a 10 mM KCl solution, were used. This salt concentration was chosen in order to obtain the conditions in which the double electric layer is most compressed and the values of physical and hydrodynamic particle diameters are similar. To avoid particle-particle interactions, it was important to obtain a low concentration of particles in the liquid. For this reason, a particle solution with a concentration of 1:20000 (from 1% solids) was used.

Microfluidic channels with a rectangular cross-section (200 μm x 60 μm) and a length of 30 mm were used in experiments. Microchannels were fabricated by soft lithography from polydimethylsiloxane (PDMS). At one end, the channel was connected by a steel capillary to a home-built pulsatile pump, at the other end with a syringe filled with a

suspension of spherical particles (Fig. 3.4). The same experimental setup was used to investigate the lateral migration of elongated hydrogel nanofilaments, which will be discussed in Chapter 4.

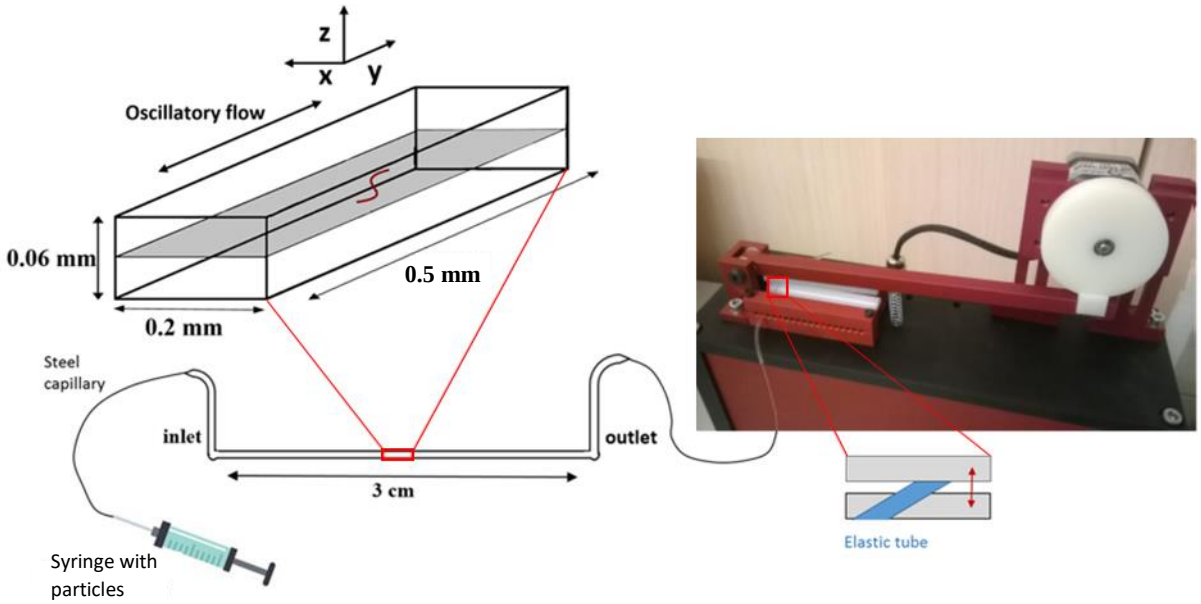


Fig. 3.4. Experimental set up for the analysis of nanoobject dynamics. The experimental channel and pulsatile pump were connected with the reservoir (syringe) by a steel capillary.

An inverted epifluorescence microscope (Leica AM TIRF MC) with a 20x/0.40 NA microscopic lens, an appropriate set of filter, and a mercury lamp (Leica EL6000) as a source for fluorescence excitation were used for particle observation. For recording particle displacements (from 500 to 2,000 individual images for each series), a high-gain EM-CCD camera (C9100-2, Hamamatsu) was used. Particles were observed at 15 mm from the channel inlet and 30 μm above the bottom wall of the microchannel. Experiments were performed inside the environmental chamber of the microscope with a stabilized temperature of 302 K.

The maximum flow velocity amplitude (Vmax) used for the experiments was between 0.06 mm/s and 0.27 mm/s, while the forcing frequency varied between 0.26 Hz and 0.59 Hz. The flow of Newtonian liquid through the microchannel with a rectangular cross-section was characterized by a small Reynolds number *Re* ($= V_{max} W \rho / \eta$) based on the channel width *W*, which varied in the range of 0.01 to 0.07.

The variation in the distance between the position of the analysed particle and the microchannel centreline was measured. This distance changed periodically during each oscillatory flow cycle, hence the instantaneous lateral migration velocity periodically

varied. The absolute value of the particle migration velocity $U_r$ was defined as the ratio of the average total lateral displacement of particles and the total observation time.

### 3.7 Evaluation of the focal depth

The evaluation of the particle lateral migration is based on the assumption that particles remain within the plane of observation defined by the microscope focal depth. This was distinguished by analysing only sharp, fully bright images of particles. To determine the range of distances in which the objects observed by the optical device appear sharp, the focal depth was experimentally determined. For this purpose, we immobilised 1 μm fluorescent particles suspended in the experimental channel and recorded their images by changing the vertical position of the microscope table. Results of this experimental evaluation are presented in Fig. 3.5.

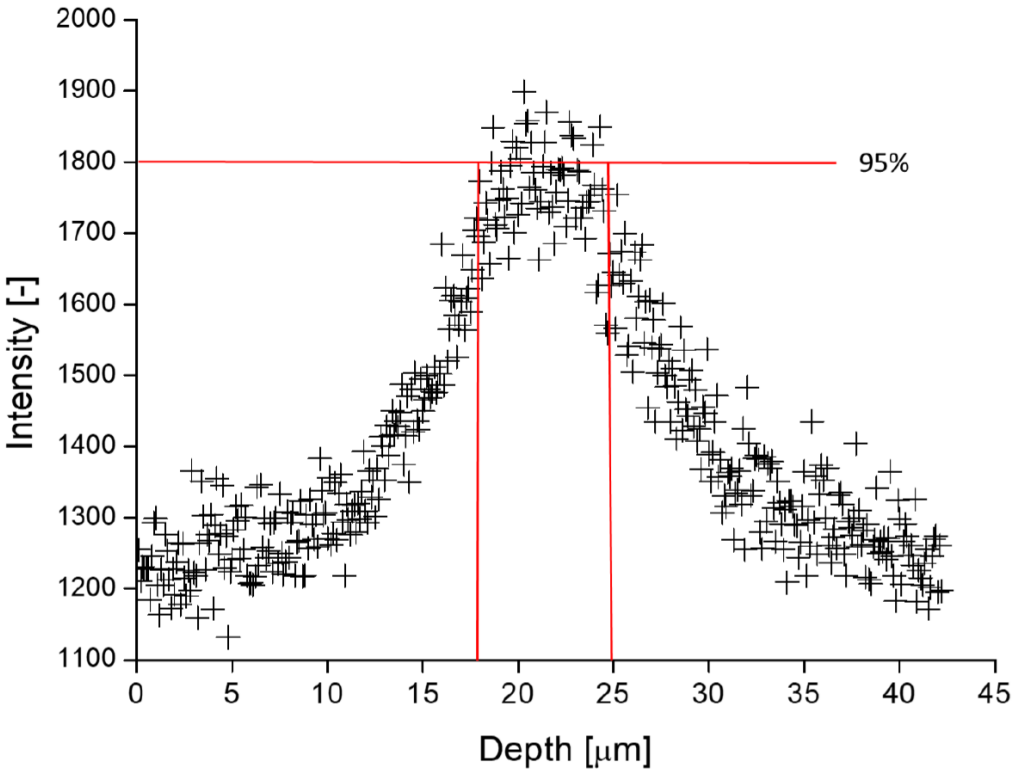


Fig. 3.5. Graph indicating the focal depth of the experimental system. The intensity of the fluorescent particle was recorded for 400 steps of the microscope table moved from the top wall to the bottom wall of the channel, where the distance between steps was equal to 100 nm. The evaluated focal depth is about 10 μm.

A graph of the intensity of the particles' brightness based on depth (Fig. 3.5) made it possible to estimate the thickness of the focal plane for the microscope lens 20x / 0.40 NA used in the experiments. This value depends on factors such as lens magnification and aperture, therefore it will vary when these parameters are changed.

## 3.8 Results and discussion

### 3.8.1 Particle morphology

The analysis conducted using AFM and SEM microscopes confirmed the physical size of the tested particles (Fig. 3.6). Sample preparation for solid particle morphology characterization is described in Appendix 6.

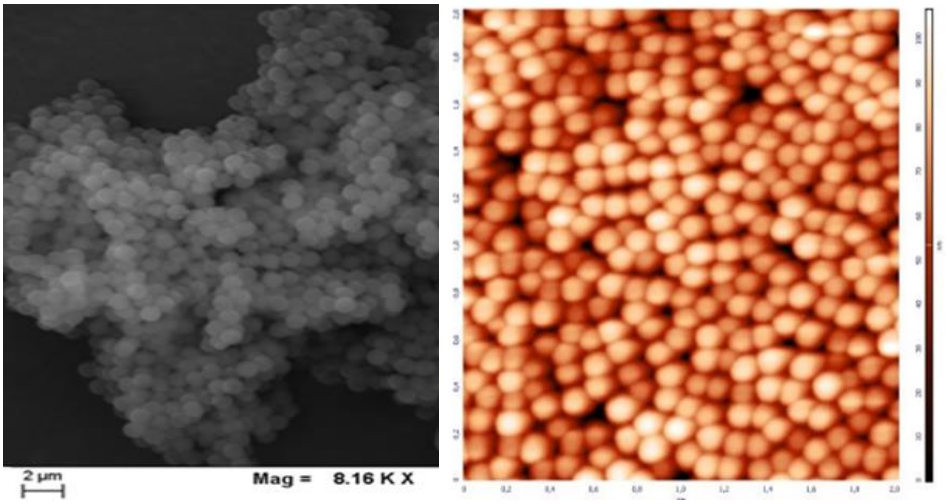


(a) (b)

Fig. 3.6. (a) 1 µm polystyrene particles observed by SEM; (b) AFM image of 100 nm polystyrene particles, substrate: silicon.

It is worthwhile to note that some interesting honeycomb structures were observed during the imaging of the particle layer previously suspended in a mixture of Triton X-100 / methanol (Fig. 3.7), demonstrating the attempt at self-organization which is typical in building biological tissues.

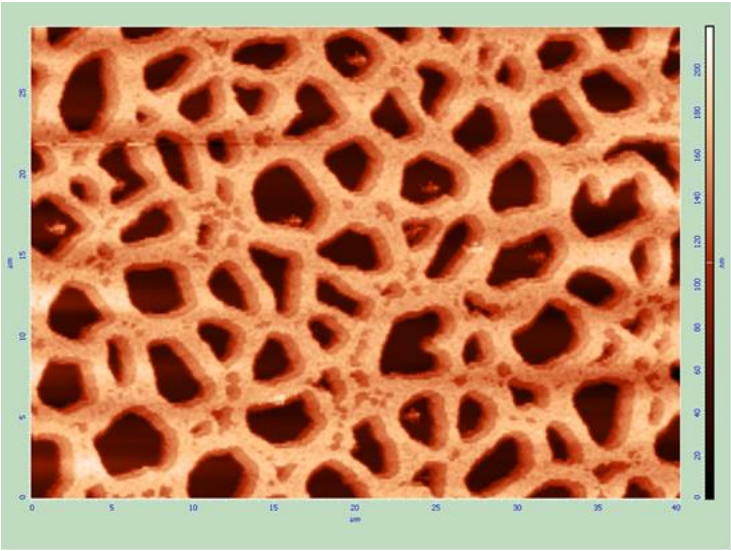

Fig. 3.7. AFM surface topography of 100 nm polystyrene particles immersed in Triton X-100/Methanol (1:1); particles concentration 1:100, poured onto the silicon substrate.

Similar structures were not observed with other surfactants in methanol (SDS and Tween). In addition, it was noted that the hole sizes varied with different Triton X-100 to the evaporated methanol ratios. This was probably related to the evaporation of methanol, because large amounts of evaporated methanol leave large spaces between the particle aggregates. In practice, this phenomena could be used to modify the pattern of such structures according to needs, for example by building appropriate matrixes for cell culture proliferation.

### 3.8.2 Hydrodynamic diameter for different types of particles

Polystyrene particles, carboxylate-modified polystyrene particles, and gold particles of various sizes were suspended in deionized water and their Brownian motion analysed. Following the procedure outlined earlier in this chapter, the diffusion coefficients determined were used to calculate the hydrodynamic diameter of the investigated particles. The final results, based on a series of thousands of measurements, each of which consisted of 500 to 1,000 frames, are shown in Table 3.2.

Table 3.2. Experimental data obtained as hydrodynamic diameter ($d_h$) for polystyrene particles of different physical diameters suspended in deionized water.

| **Physical diameter [nm]** | **Hydrodynamic diameter [nm]** |
|---|---|
| **63** | 186±11 |
| **100** | 132±65 |
| **300** | 409±61 |
| **600** | 639±127 |
| **1000** | 960±149 |

The results obtained for polystyrene particles show that the largest differences between hydrodynamic diameter and physical diameter occur in the case of small particles (up to 300 nm). This difference can arrive at over 100% (as in the case of 63 nm particles). In the case of larger particles (at least 600 nm), both sizes are comparable. In comparison with the results obtained by other researchers [10, 11, 12], mainly using the DLS method, our results indicated the existence of quite large differences between physical and measured diameter (compared with Table 1.1 in Chapter 1).

By analysing the diffusion coefficients of polystyrene particles of various sizes (from 63 nm to 1000 nm), we were able to observe a remarkable relationship (Fig. 3.8). When decreasing the particle sizes, there was a very visible systematic decrease in their relative diffusion coefficients.

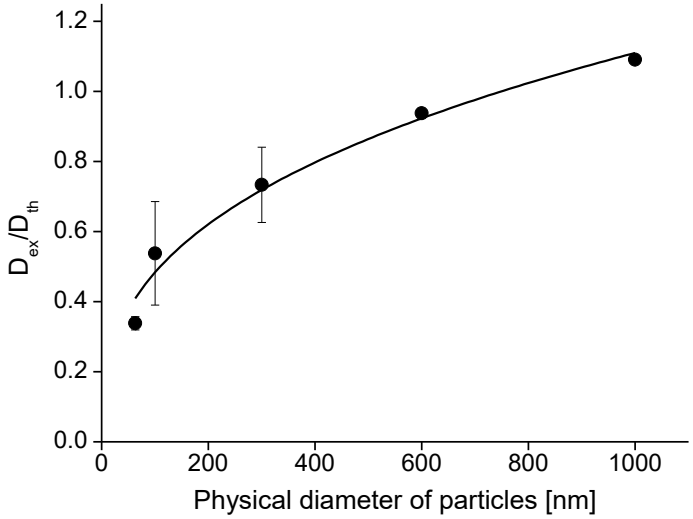


Fig. 3.8. Dependence of the relative diffusion coefficient (ratio of experimental to theoretical diffusion coefficients) on the physical diameter for polystyrene particles suspended in deionized water.

This effect may be related to the thickness of the electric double layer (EDL), characteristic of any given medium, in which the tested particles were suspended. Its thickness (typically from 5 nm to 100 nm) is negligible for large-diameter particles, hence the value of the measured hydrodynamic diameter is close to the value of the physical diameter. By decreasing the particle size, the effect of the EDL increases, and its thickness may even approach the particle diameter. To the best of my knowledge, this phenomenon has not been observed by other researchers and requires a more detailed analysis.

In an indirect way, low colloidal stability can cause a significant discrepancy between the hydrodynamic and physical diameters of the particles examined. The particles in most colloidal dispersions in aqueous media carry an electric charge. The stability of such dispersions is very sensitive to the addition of electrolytes. Surfaces can become electrically charged by the ionisation of surface groups [17]. For this reason, we investigated another particle type with a carboxylate-modified surface. Colloidal stability requires a minimum amount of surface charge. For particle materials containing acidic groups, their dissociation gives rise to a negatively charged surface. The negative charge causes a repulsive electrostatic force to counteract the inherent attractive van der Waals force [103]. Such polystyrene particles with a modified surface were suspended in deionized water and their hydrodynamic size was estimated using our tracking procedure. The experimental results averaged for nearly thousand series are shown in Table 3.3.

Table 3.3 Experimental data obtained for carboxylate-modified polystyrene particles suspended in deionized water. Physical diameter versus hydrodynamic diameter.

| **Physical diameter [nm]** | **Hydrodynamic diameter [nm]** |
|---|---|
| **100** | 845±430 |
| **200** | 1262±462 |
| **300** | 1457±930 |

As we may find, the measured hydrodynamic diameter is much higher than expected. In all three cases it is several times higher than the physical particle size. The simple explanation of particle agglomeration was ruled out. Observing the traces of individual particles, we were unable to detect any unexpected changes in their image spots or brightness. Therefore, since the results for this particle type, obtained in numerous repeated series, were significantly different every time from the expected values, we decided to discontinue this investigation. An interpretation of the observed phenomenon has yet to be formulated.

The third particle type studied, by tracking their trajectories, were gold particles. Due to the lack of a fluorescent factor in the structure of the particles, we recorded the light scattered on their surface. One of the shortcomings of this strategy is the fact that the air bubbles present in the solution also scatter light, which is then recorded and analysed as originating from the examined particles, thus negatively affecting the final result. The obtained results for gold particles are shown in Table 3.4. As can be seen, the hydrodynamic diameter of the particles is up to 60% greater than their physical size.

Table 3.4. Experimental data obtained for gold nanoparticles suspended in deionized water. Physical versus hydrodynamic diameter.

| **Physical diameter [nm]** | **Hydrodynamic diameter [nm]** |
|---|---|
| **40** | 65±19 |
| **60** | 102±17 |
| **100** | 162±33 |

By applying gold particles we expected to minimize the effects of the EDL layer or chemical deposits on their mobility. It seems that this is not the case. Similarly to polystyrene particles, the differences between physical and measured particle diameters are significant. Hence, to evaluate the correctness of our analysis performed with the particle tracking scripts developed at IPPT, 63 nm and 100 nm polystyrene particles and 100 nm gold particles suspended in water were tested using a commercially available NanoSight device. The description of the operating principle and the parameters used can

be found in Appendix 5. The images recorded during the NanoSight measurement were extracted from the device and used by IPPT script for analysing Brownian motion. The results obtained by the commercial NanoSight software and our own software are compared in Fig. 3.9.

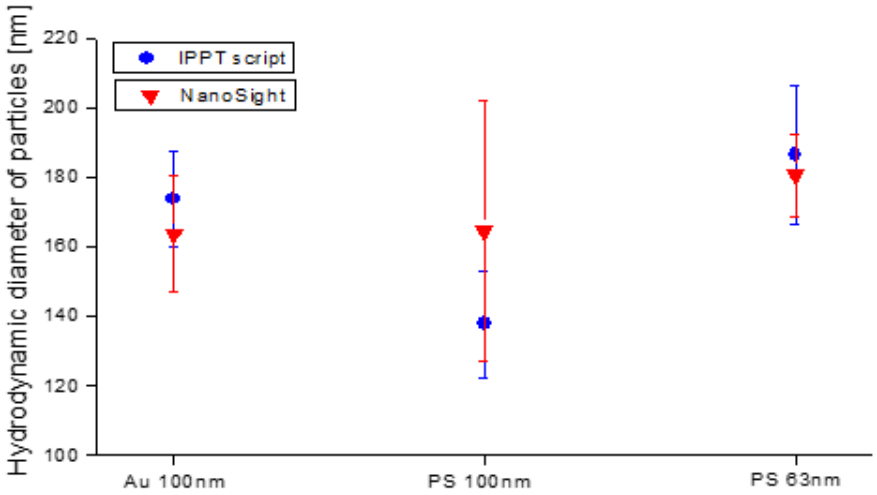


Fig. 3.9. Comparison of hydrodynamic diameter results obtained for three particle types: Au100nm – 100 nm gold particles, PS100nm – 100 nm polystyrene particles, PS63nm – 63 nm polystyrene particles. Experiments performed in deionized water. Red dots – Nanosight results, blue dots – IPPT particle tracking scrip.

In the case of 100 nm gold particles and 63 nm polystyrene particles, the resulting hydrodynamic diameters partly overlap. For 100 nm polystyrene particles the differences are greater. Even taking into account relatively large standard deviations of the results obtained with both methods, the averaged hydrodynamic diameter obtained using NanoSight is almost 20% greater than that determined using IPPT script. Nevertheless, it can be concluded that the results obtained by the two methods used (IPPT and NanoSight scripts) overestimate the physical diameter of particles in a similar way. It seems that only using a special calibration procedure and the correction factors included in the commercial software is it possible for users to obtain values corresponding to the physical diameter of the investigated colloids.

### 3.8.3 Ionic strength effect

To analyse the influence of the ionic strength of the medium on the value of the hydrodynamic diameter of particles, two types of solutions were prepared using a monovalent (KCl) and a divalent salt ($NiCl_2$). The range of salt concentrations ranged from $10^{-9}$ mM to 100 mM, depending on the type of salt. The results were based on thousands of experimental series conducted, each consisting of 500-1,000 camera frames.

Fig. 3.10 shows how the changed KCl concentration affects the measured hydrodynamic diameter. Looking at the chart, we can see that at a 10 mM salt concentration the EDL thickness reaches its minimum, while increasing again at a higher salt concentration. At this salt concentration the measured hydrodynamic diameter is closest to the physical diameter. This conclusion is confirmed by the guidelines of the International Standard on DLS, which state that the salt concentration suppresses the electrical double layer. Similar results have been obtained by other researchers [10]. Below the 10 mM salt concentration, hydrodynamic values are higher and fluctuate, while the corresponding hydrodynamic diameter is about 30% to 45% greater than the physical size of the tested particles.

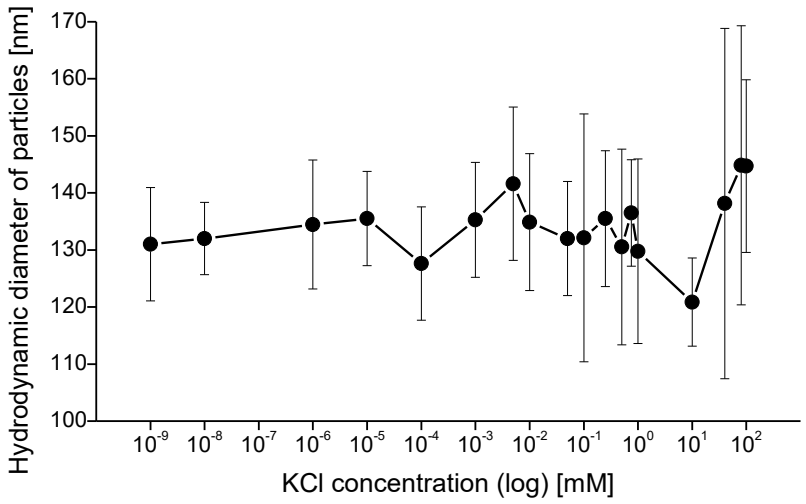


Fig. 3.10. Hydrodynamic diameter of 100 nm polystyrene particles obtained at different concentrations of KCl.

On the basis of the results obtained by us, it is difficult to state clearly whether the hydrodynamic diameter decreases or increases with the increased salt concentration (ionic strength of the medium). Therefore I cannot confirm the results obtained by Xu [8], Chassahne [10], and Gittings [7], stating that the hydrodynamic diameter continuously decreases with increasing ionic strength.

We confirm, however, that when the concentration of a monovalent salt exceeds 10 mM, the hydrodynamic diameter significantly increases. This could be related to the formation of particle aggregations, the size of which increases when the salt concentration increases. In short, my investigation indicates that the hydrodynamic diameter of spherical nanoparticles depends strongly on the ionic strength of the liquid in which they are suspended.

In the case of a divalent salt ($NiCl_2$), the situation is slightly different. Fig. 3.11 compares the impact of KCl and $NiCl_2$ salt concentrations on the hydrodynamic diameter of the analysed particles. At low salt concentrations, in both cases, waveforms are similar – the value of the hydrodynamic size does not change much with the increased ionic strength. The situation begins to change when the salt concentration reaches 10 mM. Unfortunately, in the case of $NiCl_2$, we were unable to obtain results for samples with a concentration higher than 10 mM, because we observed only large aggregates (even several times larger than single particles) over this value, thus hampering the performance of our particle tracking analysis. However we can guess that, as in the case of a monovalent salt, particles have a great tendency to group themselves in salt concentrations above 10 mM: a result also reported by other researchers [10] for this type of salt.

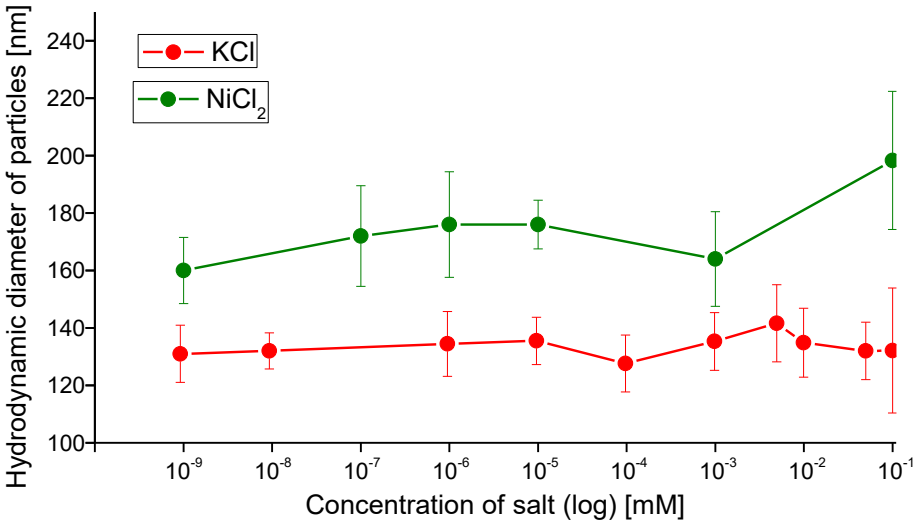


Fig. 3.11. Hydrodynamic diameter of 100 nm polystyrene particles obtained at different concentrations of monovalent (KCl) and divalent ($NiCl_2$) solutions.

On the basis of the results I obtained, it is difficult to determine unequivocally in which divalent salt concentration the hydrodynamic particle size is closest to its physical value. According to the research presented by Chassagne [10], this value should be similar to that of a monovalent salt, and equal to around 10 mM. As already mentioned, the waveform of the curves look similar at lower concentrations of the salts tested (below 10 mM). However, it is clearly visible that in the case of a divalent salt, the hydrodynamic diameter values obtained are higher than the corresponding values for a monovalent salt at the same concentrations. This is most likely related to the different packing of ions forming the double electric layer.

As in the case of the particles suspended in deionized water, polystyrene particles (63 nm and 100 nm) suspended in potassium chloride solution at various concentrations (0.1 mM, 1 mM, 10 mM) were examined using a commercially available device (NanoSight) to determine their hydrodynamic particle size. The images of the particles recorded over the course of NanoSight measurements were extracted and used to analyse the Brownian motion by IPPT script. The results obtained by these two programs are compared in Fig. 3.12 and Fig. 3.13.

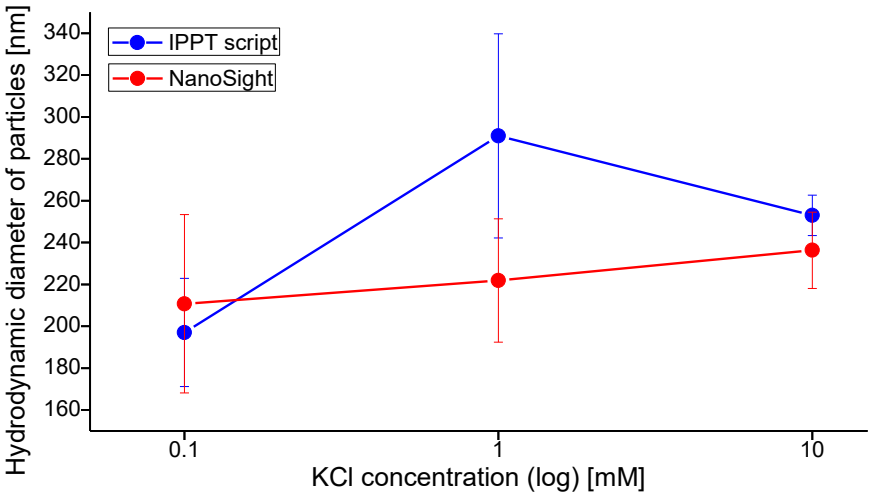


Fig. 3.12. Hydrodynamic diameter of 100 nm polystyrene particles as a function of the potassium chloride concentration evaluated by IPPT script (blue dots) and a commercial NanoSight instrument (red dots).

In the case of 100 nm particles, except for those suspended in the 1 mM KCl solution, the results are very similar. An even greater convergence of results was obtained for 63 nm particles. In both cases, the values obtained were higher (in the case of 63 nm particles a few times higher) than the physical particle size. On the basis of this analysis and a similar analysis for particles suspended in water, I can conclude that the program we developed for the analysis of Brownian motion makes it possible to determine the hydrodynamic diameter of nanoparticles with an accuracy comparable to that of commercially available devices.

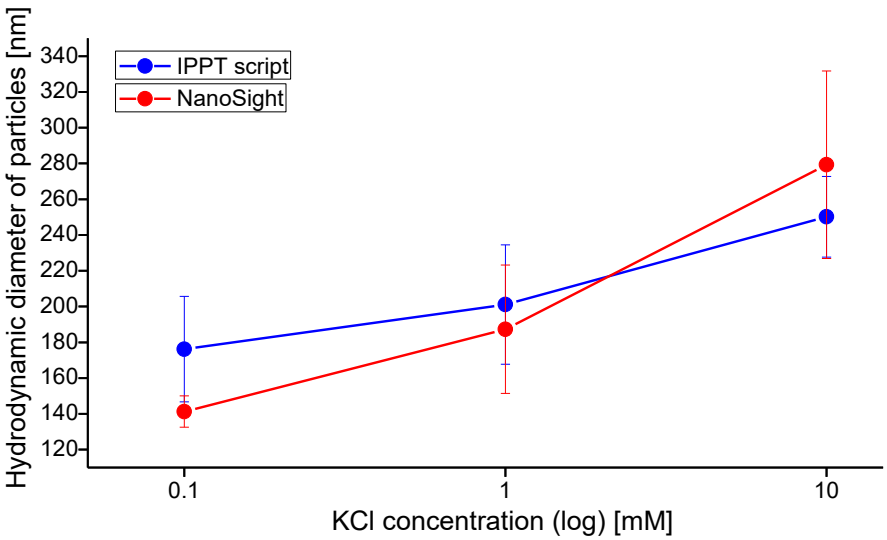


Fig. 3.13. Hydrodynamic diameter of 63 nm polystyrene particles as a function of the potassium chloride concentration evaluated by IPPT script and the commercial NanoSight instrument.

### 3.8.4 Effect of ion size

It is worthwhile to remember that the interpretation of the diffusion coefficients (hydrodynamic diameter) measured for unknown biological particles may be very difficult, because it requires information on the ionic structure of the particle environment and details on the physical and chemical properties of an underlying biological system. For example, the difference in ionic sizes of solvent molecules can noticeably affect the measured mobility of nucleic acids [104].

For this reason an interesting factor was the effect exerted by the size of ions forming the medium on the size of the electrical double layer, and thus on the hydrodynamic size of the investigated particles. An experiment was therefore conducted in which particles were suspended in two different salt solutions with significantly different sizes of cations (KCl and LiCl). Polystyrene particles with a physical size of 100 nm were used for this experiment. The results obtained for a wide range of concentrations of both salts are shown in Fig. 3.14.

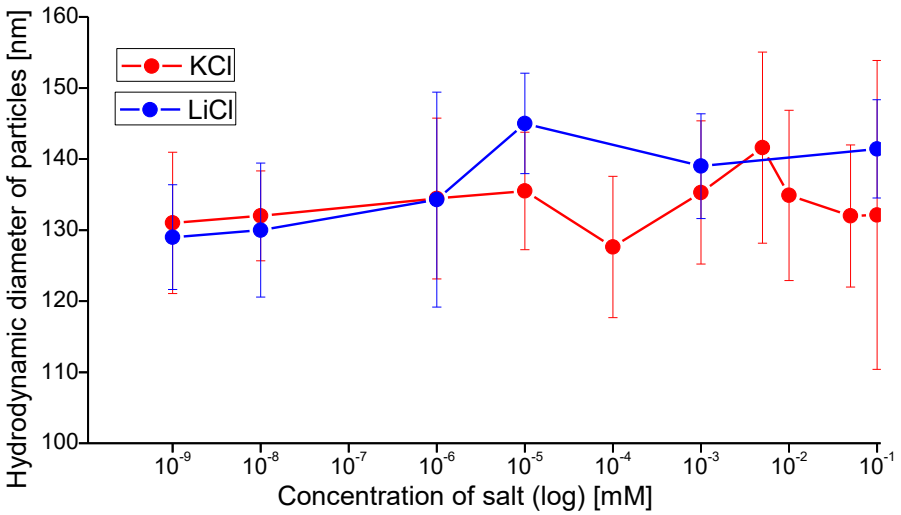


Fig. 3.14. Hydrodynamic diameter of 100 nm polystyrene particles measured for different concentrations of KCl and LiCl solutions.

Since both salts have the same type of anion ($Cl^-$), the cation is the element that differentiates them. The $Li^+$ and $K^+$ ions have a radius of 0.06 nm and 0.133 nm, respectively. In addition to the radius of the ion the hydrated radius is also an important datum: 0.34 nm for $Li^+$, and 0.232 nm for $K^+$ [105]. The ion size translates into the thickness of the double electric layer surrounding the particle in a given medium, which in turn is reflected in the hydrodynamic diameter of the nanoparticle in question.

The two graphs in Fig. 3.14 have a very similar shape. Both have a clear maximum. The graph showing the results for KCl has a maximum of hydrodynamic size shifted towards a higher concentration (around 0.8 $10^{-2}$ mM). For LiCl, the maximum is $10^{-5}$ mM. At low salt concentrations, hydrodynamic diameter values were comparable. After reaching a salt concentration of $10^{-5}$ mM, the values of the hydrodynamic diameters obtained in both cases started to differ more and more. The higher salt concentration caused particles to be surrounded by a larger amount of ions. If the radius of these ions is larger, the thickness of the double electric layer also correspondingly increases. On the basis of the results obtained, I cannot confirm unambiguously that the effective thickness of the electrical double layer decreases as the counterion size decreases, as postulated by Bohinc et al. [14]. It is worthwhile to note that, according to the Poisson–Boltzmann theory, a continuously decreasing electrical double layer is observed as the surface charge density increases.

### 3.8.5 Wall effect

The optical tweezers system was used to analyse the interaction of 1 μm spherical particles, suspended in four different concentrations of KCl salt, with the microchannel wall (comp. Fig. 3.2). The experiment allowed us to demonstrate the possibility to obtain unperturbed measurements of the forces acting between the channel wall and the particles suspended near-by. Here, we limit our interest mainly to the electrostatic interactions of the ionic layer attached to the wall (EDL) and approaching it micro particle with its own EDL.

The experiment is conducted by stepwise approaching the trapped polystyrene particle in the wall at a constant 500 μm/s velocity (for single step equal 50 nm) and recording its displacement in the optical tweezers focus. This displacement was later calculated to be the force responsible for wall-particle interactions. In order to make the measurement as accurate as possible, first the calibration of the trap stiffness *k* (depending on the laser power k(P)) and detection system (quadrant photodiode response) were performed. The linear regression coefficients for the x and y axes were determined to be 0.0091 and 0.0093, respectively. So for 10% of the laser power, the trap stiffness was: $k_x$ = 0.091 pN/nm and $k_y$ = 0.093 pN/nm (comp. Fig. 3.15).

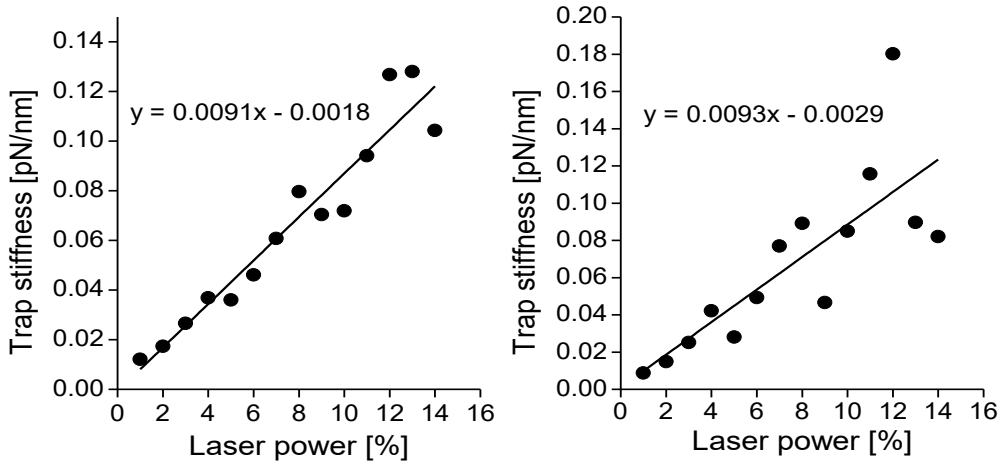


(a) (b)

Fig. 3.15. The stiffness of the optical trap in X (a) and Y (b) direction as a function of the trapping laser power.

As the output from the measurement we received values of signal power P [V] and the voltages ($V_x$ and $V_y$, proportional to X and Y position of the incident beam) generated by the four photodiode amplifiers ($V_1$, $V_2$, $V_3$, $V_4$). This data were then further analyzed using a special Matlab script to determine the force of particle-wall interaction , as well as effective viscosity change as a results of decreasing distance between surface of the

particle and the wall. For each measurements set, consisting of 1800 time points, we evaluated such parameters as:

- distance from the wall [nm], where 0 is the surface of the wall;
- mean force acting on particle [pN] in X (parallel) and Y (perpendicularly) direction to the wall;
- mean X and Y position of particle in trap [nm];
- mean square displacement amplitude [$nm^2$], calculated separately for two half of peak-to-peak distance;
- mean quadrant photodiode laser power [V] – parameter important for controlling the stability of the laser power, and thus the stability of the measurement system.

For further analysis a component perpendicular to the wall (Y) was used. The parallel component (X) was burdened with an additional error resulting from the fact that displacements are not exactly parallel to the surface of the wall. This component is very sensitive to the roughness of the wall surface and the imperfection of setting the trap in relation to the surface plane.

The results of the measurements obtained for X and Y force acting on particle are shown in Fig. 3.16. The differences between both measured force components X and Y are worth noting that strongly depends on salt concentration, with the smallest differences in the case of 1 mM KCl concentration (Fig. 3.16 (c)). The experimental runs started when particles were relatively far from the wall (about 3-8 particle diameters). At such a distance both electrostatic and molecular forces between the particle and the wall should be very small. Nevertheless, even at such a distance we recorded non-negligible particle displacements from the trap centre. The values of the particle-wall interaction forces were in the range of -8.0 pN to 7.0 pN. Depending on the salt concentration, the shapes of the force curves appeared different. At low salt concentration (from 0.1 mM to 10 mM) the interacting forces (in the Y direction) change with the distance from the wall uniformly without sudden jumps. Sudden jumps in the curves of force appear at a distance below 1500 nm from the wall. These irregularities of the force curves are shifting towards smaller distances from the wall as the salt concentration increases. Surprisingly, with the increased KCl concentration to 100 mM (Fig. 3.16 (e)), the waveform of graphs becomes more and more irregular. The smallest changes of force with the decreasing distance of the particle from the wall were observed when the particle was suspended in deionized water ( Fig. 3.16 (a)). It is evidently difficult to see a clear, uniform relationship between

the salt concentration and the levels of force recorded close to the wall. This puzzling behaviour recalls the observations obtained from the Brownian mobility, where several up-and-down variations in the ionic interactions are present (comp. Fig. 3.10).

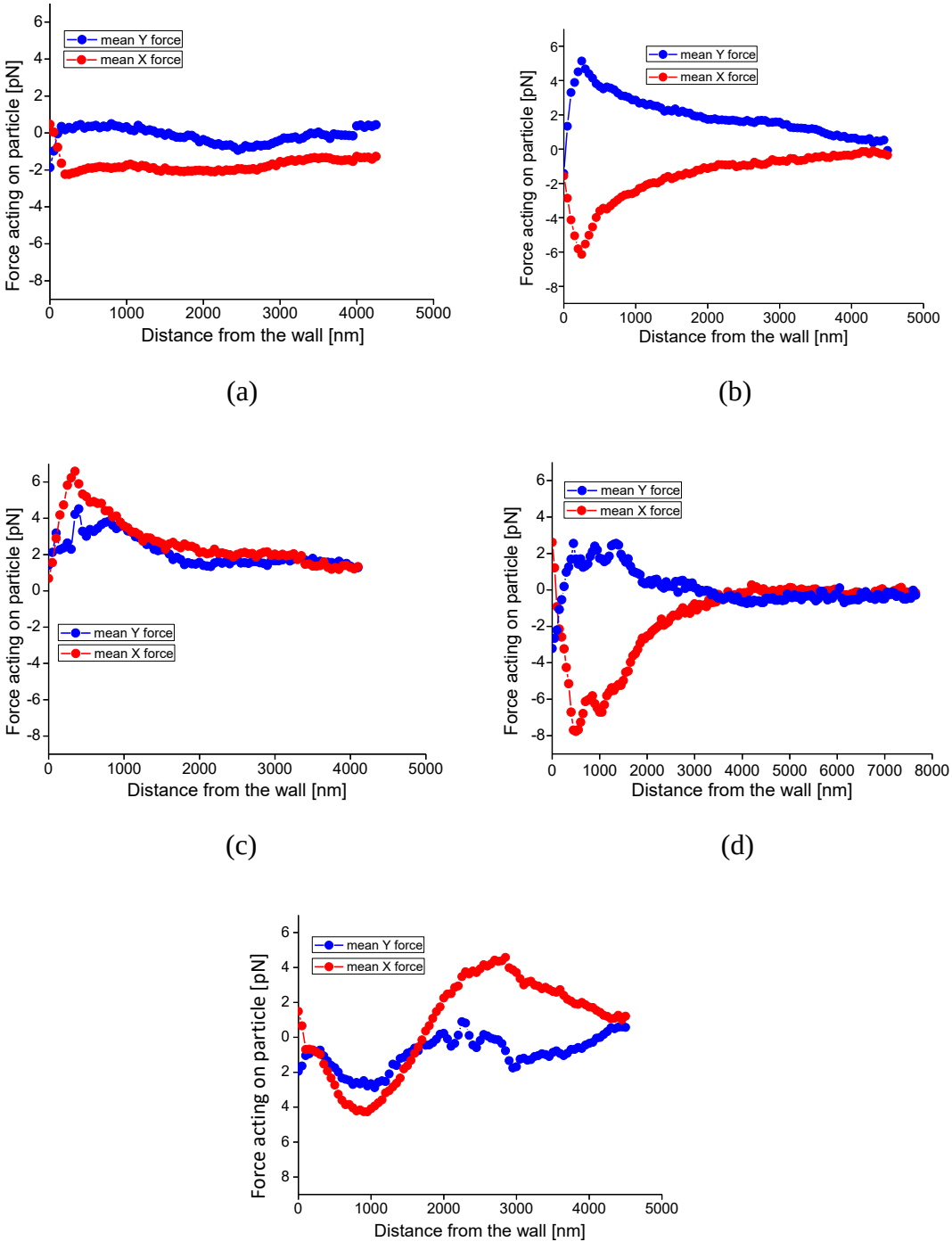


Fig. 3.16. The force of the interaction between 1 μm polystyrene particle and PDMS wall in deionized water (a) and different KCl concentrations: (b) 0.1 mM; (c) 1 mM; (d) 10 mM; (e) 100 mM.

Fig. 3.17 shows normalized force for particles in deionized water and three KCl concentrations. The obtained values of force components were normalized firstly to the value of force at the infinity (set as 0) and next normalized to unity, which corresponded to the highest particle-wall interaction force for all investigated salt concentrations (in this case equal to 0.135 pN, for 1 mM KCl). The data obtained for 100 mM KCl concentration appeared difficult to be correctly interpreted for us.

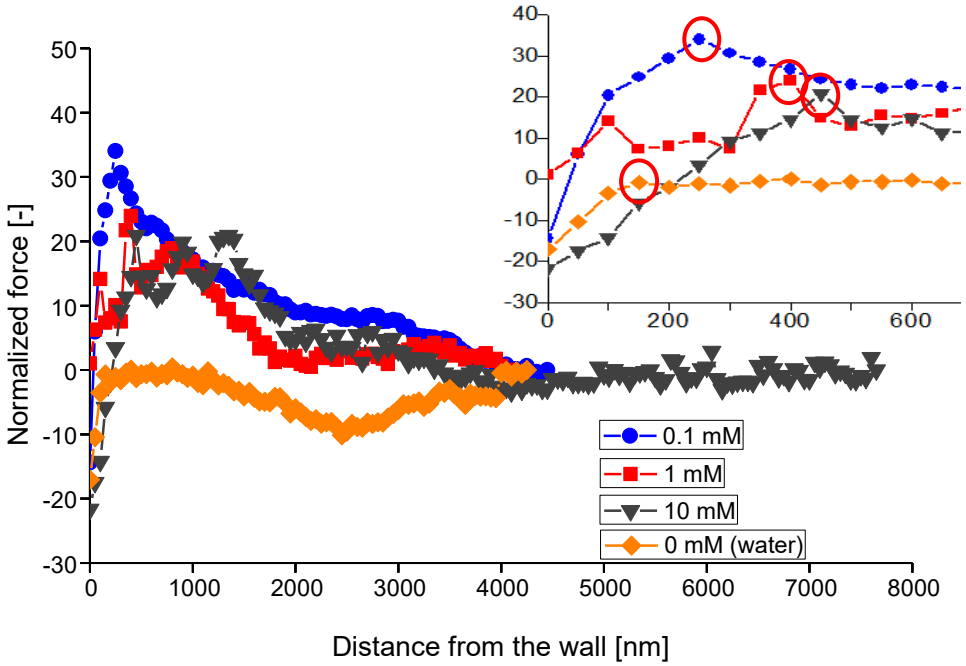


Fig. 3.17. The force of the interaction between 1 μm polystyrene particle and PDMS wall in deionized water and in different KCl concentration.

For low concentrations, independently of the medium used in which the test particle was suspended, the force values only slightly deviate from the neutral value equal to 0, in the initial stage of observation (above 4 μm from the wall). As we approach the wall, the values of the forces recovered increase tendency (repulsion a particle-wall), obtaining a maximum value in the range from 100 to 500 nm from the wall. The location of this maximum is clearly dependent on the salt concentration – it is closer to the wall when the ionic strength of the medium is lower. It is 150 nm, 250 nm, 400 nm and 450 nm for deionized water, 0.1 mM, 1 mM and 10 mM KCl, respectively ( Fig. 3.17, the top right section of the chart, inside red circles). This may be probably related to the thickness of the double electrical layer focused around the analyzed particle and the ionic layer adjacent to the wall to which we approach the particle. We could predict that the higher the ionic strength, the stronger the layers are and then more strongly they interact. However, after crossing a certain distance limit, we observe a decrease in the particle-

wall interaction force associated with the presence of attractive forces. The observed phenomenon is contrary to the DLVO theory. However, Larsen and Grier made similar observations to ours [106] and showed that the effective pair potential between two like-charged polystyrene spheres in water electrolyte includes a long-range attraction, when they put this spheres near a charged glass wall.This phenomenon is particularly visible at low salt concentration and large screening lengths. The classical DVLO theory neglects any effect that a charged sphere has on the screening ion density in the vicinity of other spheres [107].

If we look at the level of the obtained maximum of repulsive interactions (Fig. 3.17, the top right section of the chart), then we also observe its dependence with the concentration of KCl salt. The highest value of the repulsive force between the particle and the wall is observed at the lowest KCl concentration (0.1 mM). This force decreases as the concentration of ionic strength increases. For comparison, the results of Assemi et al. with regard to force measurements between carboxylate-modified polystyrene sphere and glass in different NaCl concentrations using an atomic force microscope showed that the maximum repulsive force decreases as the salt concentration increases [108]. A similar relationship was also observed in our previous investigations with KCl salts and interaction between two particles [109].

As we may see in Fig. 3.17 the lowest force values were obtained for the particle suspended in deionized water. In a distance not greater than the particle diameter (1 μm) it was close to 0, then after reaching a small maximum, it dropped to a relative value of - 17 (equal to -2.3 pN).

The data collected during the measurement also allowed to study how the relative viscosity (interpreted as the inverse of diffusion change and determined from the amplitude of vibrations) changes as the particle approaches the wall surface. The obtained effective viscosity values (component Y) were normalized to the value of viscosity in the infinity (set as 1).

We show that the relative viscosity increases with the decrease of the ionic strength of the medium. As seen in Fig. 3.18, at a distance above about 1-1.5 μm from the wall, we observe a significant decrease of the apparent viscosity as particle approaches the wall. Below this distance there is an increase, and then a sudden jump of viscosity associated with the touch of the particle to the wall, and thus the inhibition of the particle vibrations.

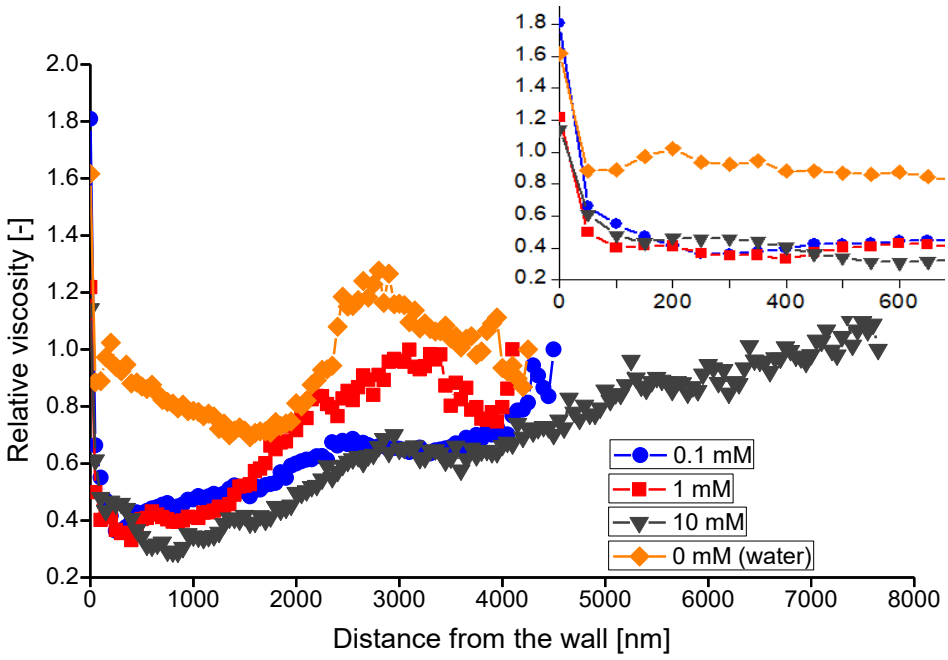


Fig. 3.18. The effective viscosity as a function of distance between wall and approaching to it particle, for water and different concentrations of salt.

The present preliminary results show that using Optical Tweezers opens possibilities for detailed studies of particle-wall hydrodynamic interactions with unavailable ever before femtonewton accuracy and spatial resolution of tens of nanometer. What is also very important, is that during one such measurement we can collect information about three parameters: (i) force interaction between objects; (ii) the apparent liquid viscosity, indicated by damping of Brownian fluctuations; (iii) the flow resistance, when we collect data also when the particle moves towards the wall.

### 3.8.6 Lateral migration of spherical particle

As mentioned earlier, the cross-flow migration of spheroidal objects such as particles, droplets, and red blood cells has been the subject of numerous studies [67-70, 73, 79]. This thesis compares the results concerning the migration of spherical particles and our experimental results obtained in the oscillating flow.

Before the experimental runs started, we observed that the distribution of the investigated particles across the whole plane of observation was rather uniform, except in the wall region (Fig. 3.19).

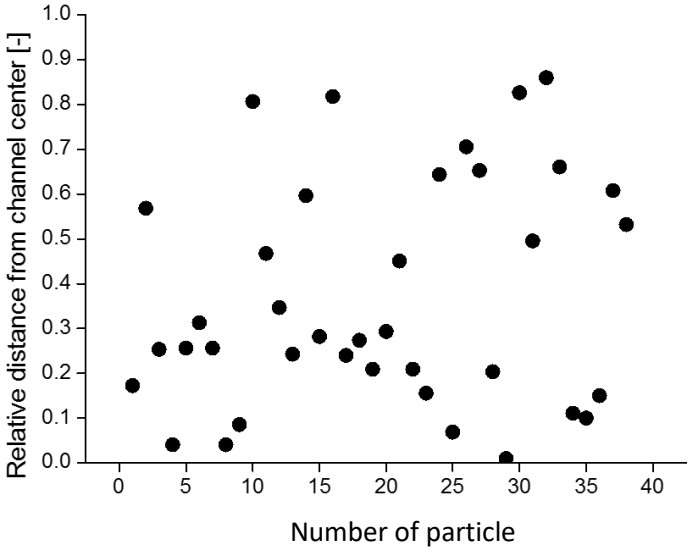


Fig. 3.19. Initial position of each examined particle in the microchannel; the relative distance [0,1] denotes the microchannel centre and the wall, respectively.

During each experimental run the position of the observed fluorescent particles conveyed by the oscillating flow was recorded and analysed. Depending on the particle's initial location, its cross-flow trajectory changed, and the particles tended to move either to the side wall or in the opposite direction, into the channel axis.

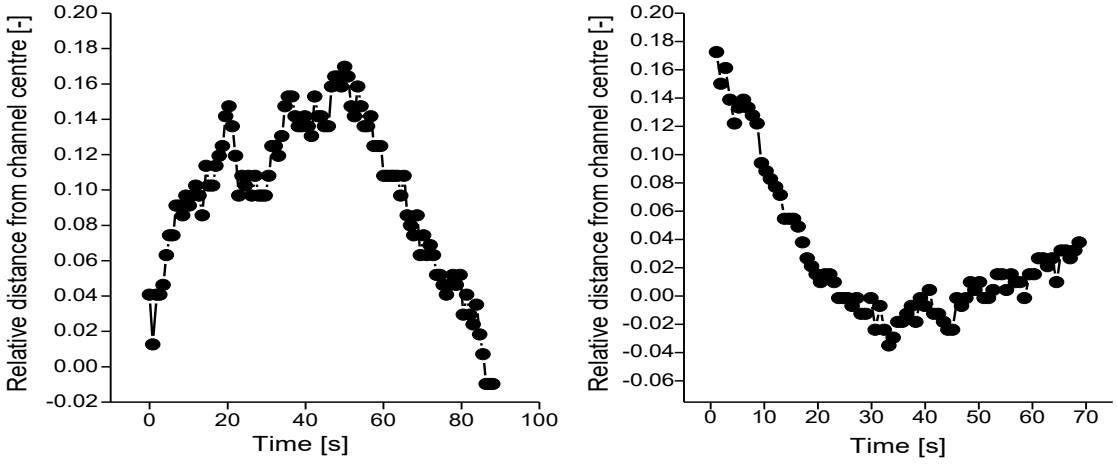


(a) (b)

Fig. 3.20. Cross-flow migration of 1 μm spherical particles in the oscillatory flow: (a) maximum flow velocity $V_{max}$ = 259 μm/s; Reynolds number $Re$ = 0.063; relative migration velocity $V_r$ = 7.7 $10^{-6}$; (b) $V_{max}$ = 255 μm/s; $Re$ = 0.062; $V_r$ = 2.2 $10^{-6}$.

When the particle's initial position is relatively far from the channel centre, the migration direction is clearly into the flow axis (comp. Fig. 3.20 (a)). After approaching the flow axis, the particle position fluctuates around this axis. For the particle starting its track

already close to the channel axis, its final (equilibrium) position appears to continue fluctuating across the channel axis (comp. Fig. 3.20 (b)).

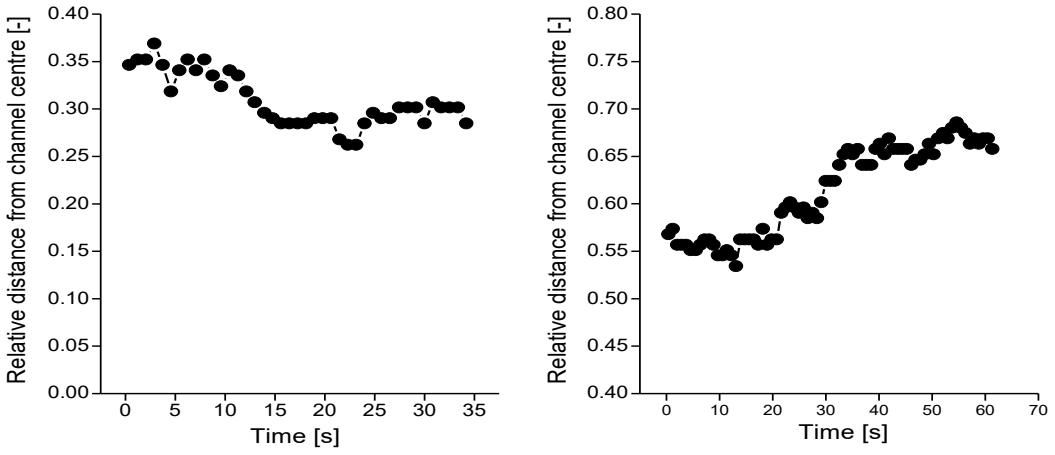


(a) (b)

Fig. 3.21. Cross-flow migration of 1 μm spherical particles in the oscillatory flow: (a) maximum flow velocity $V_{max}$ = 252 μm/s; Reynolds number *Re* = 0.061; relative migration velocity $V_r$ = 7.2 $10^{-6}$; (b) $V_{max}$ = 228 μm/s; *Re* = 0.060; $V_r$ = 6.5 $10^{-6}$.

Fig. 3.21 shows the cross flow migration of the particles located closer to the side wall. At still relatively great distances from the channel wall (Fig. 3.21 (a)), particles slowly move into the flow axis. Closer to the wall, however (Fig. 3.21 (b)), particles seem to reach a weak equilibrium position, being close to the theoretical value reported in the literature ($\underline{x}$ = 0.6).

When comparing present observations with the reported data obtained for steady, creeping flow [79], some important differences can be seen. Our particles are Brownian particles, the cross-flow velocity magnitude is comparable in magnitude with the stochastic jumps of a Brownian particle. For the oscillatory flow, this effect is magnified at periodically repeated changes in the flow direction. When the flow ceases out before changing its direction, any stochastic change in the particle position creates its new cross-flow trajectory, to be continued during the next flow oscillation period. This effect is especially evident close to the channel axis, where the amplitude of the sudden changes in the flow direction is greatest. This may induce the strong fluctuation observed of the particle position across the flow axis. We do not see such strong fluctuations at greater distances from the centre line (more than 0.2). In any case, it is worthwhile to note that even in the case of low Reynolds number flows, where one could expect the reversibility of particle tracks, there is obviously a net cross-flow particle migration.

Undoubtedly, this particle migration is influenced by many factors. To see how the flow velocity determines the direction of migration, we tested different values of the maximum velocity of the oscillating flow. The first group was characterized by an average maximum flow velocity of 251 μm/s (Fig. 3.22 (a)), while that of the second group was 90 μm/s (Fig. 3.22 (b)). Fig. 3.22 shows the frequency distribution of 1 μm polystyrene particles across the microchannel width, before the application of a hydrodynamic force (grey bars) and after around 40 oscillatory cycles (dashed-contour bars).

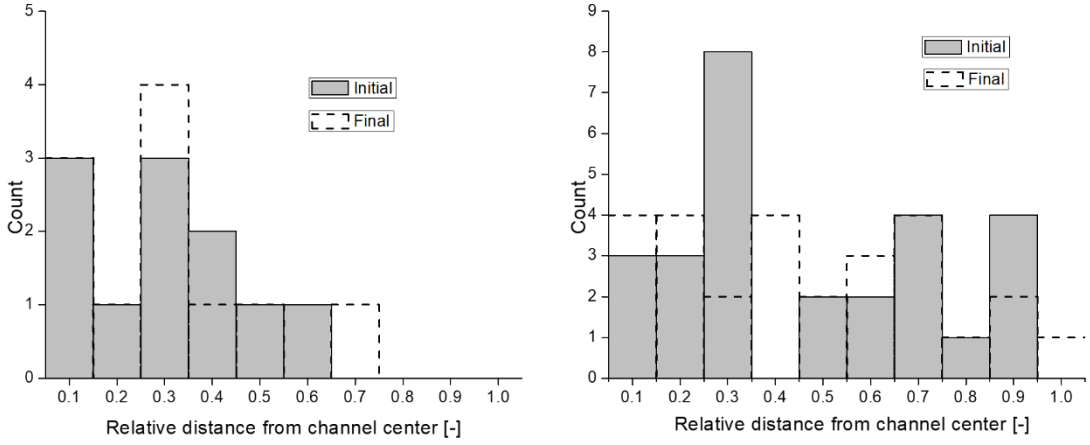


(a) (b)

Fig. 3.22. Lateral migration of spheroidal polystyrene 1 μm particles depending on flow rate: (a) average Vmax = 251 μm/s; (b) average Vmax = 90 μm/s.

As we can see, the results are inconclusive, even though the influence of the flow velocity on the location of the equilibrium position is small. Both oscillating flow and Brownian diffusion seem to similar the equilibrium position of particles. According to the low Reynolds number model given by Ho and Leal [79] also confirmed by other researchers [66, 77, 78], this equilibrium for steady flow is close to $\underline{x} = 0.6$.

An interesting factor is the magnitude of the averaged lateral migration velocity $U_r$. This value referring to the maximum amplitude of the flow velocity, marked as $V_r$, is between $1.12\ 10^{-6}$ and $3.48\ 10^{-5}$. We compared this lateral migration velocity with the results calculated by Ho and Leal [79] for spherical particles in a two-dimensional Poiseuille flow. For the corresponding two-dimensional steady flow, the relative migration velocity predicted by the model is in the range of $7.40\ 10^{-7}$ to $2.02\ 10^{-4}$. The obtained values of experimental lateral migration velocity and those from Ho and Leal equation are not completely similar. The results obtained from the Ho and Leal model have a wider range of values. The lowest values obtained are almost three orders of magnitude lower than in the experiment described. It must be remembered, however, that the equation used in the

model refers to the translational motion, whereas in our case we are referring to the oscillatory motion. Secondly, the model practically ignores any inertial effects. This is not the case of our oscillatory flow, where the velocity direction changes periodically at a relatively high frequency. The relatively high values of the migration velocity indicate that, for the investigated range of experimental conditions, the oscillating flow may be treated as the efficient method for sorting particles or directing them into desired locations in capillaries.

# Chapter 4: Mobility of highly deformable hydrogel nanofilaments

## 4.1 Morphology of core-shell nanofibres and hydrogel nanofilaments

The morphology of collected core-shell nanofibres was tested by SEM (Nova NanoSEM 450 model, FEI, USA). Before the analysis, nanofibres were sputtered with gold (using a Polaron model SC7620 mini sputter coater, Quorum Technologies Ltd., Ashford, UK). ImageJ [110] software was used for the calculation of the nanofibre average diameter using about 100 manually selected nanofibres. The hydrogel nanofilaments extracted from nanofibres were examined by fluorescent microscopy and AFM. AFM (Ntegra, NT-MDT), equipped with a closed liquid cell. A rectangular silicon cantilever (CSG01, NT-MDT) was used to evaluate sample surface topography. The mechanical resonance and cantilever spring constant were in the range of 4-17 kHz and 0.003–0.13 N/m, respectively. Measurements were carried out in aqueous solutions at 25°C, in the contact mode.

## 4.2 Experiments on diffusion and channel flow

### 4.2.1 Brownian motion experiment

Extracted from nanofibres, the suspension of hydrogel nanofilaments in DMF solution was prepared and placed between two sealed microscope slides, at a distance of about 50 μm from each other (Fig. 4.1).

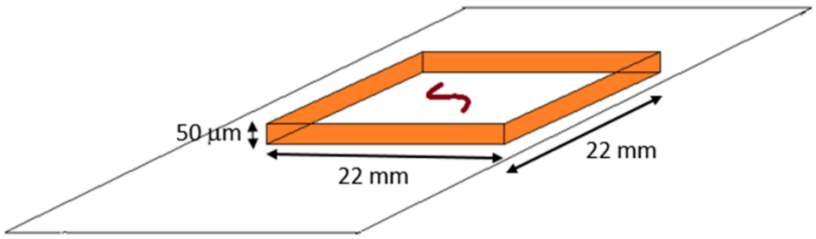


Fig. 4.1. Scheme of the experimental microchannel.

The Brownian motion of nanofilaments was recorded by an electronic camera (C9100-2, Hamamatsu, Japan) coupled with a Leica AM TIRF MC epifluorescence microscope. For observing single nanofilaments, a 63x 0.70 NA objective lens were used. The sampling was at approximately 10 frames per second, with 1,000 frames recorded in one experimental sequence. A Matlab [111] script was developed to evaluate filament displacements; it was used to locate the filament centre in frame coordinates [x(t); y(t)], as well as the orientation of filaments θ(t) with respect to the *x* axis of the frame. The rotation matrix was used to calculate the incremental displacement of every analysed

nanofilament. This displacement was observed between two time steps in the object frame ($\delta a_n$; $\delta b_n$) longitudinally and perpendicularly to the long axis of the fibre. Resulting displacements were evaluated from the laboratory frame incremental displacement ($\delta x_n$, $\delta y_n$) using a rotation matrix [112]:

$$\begin{pmatrix} \delta a_n \\ \delta b_n \end{pmatrix} = \begin{pmatrix} cos\theta_n & sin\theta_n \\ -sin\theta_n & cos\theta_n \end{pmatrix} \begin{pmatrix} \delta x_n \\ \delta y_n \end{pmatrix} \quad (21)$$

To obtain translational diffusion coefficients along the *a* and *b* axes of the fibre, long sequences of images (~1000) were evaluated. Diffusion coefficients were calculated using the mean square displacement related to the known time interval *t* between frames [112]:

$$\langle [\Delta a(t)]^2 \rangle = 2D_a t \quad (22)$$

$$\langle [\Delta b(t)]^2 \rangle = 2D_b t \quad (23)$$

To calculate the rotational diffusion coefficient, the mean square angular displacement was evaluated [112]:

$$\langle [\Delta \theta(t)]^2 \rangle = 2D_\theta t \quad (24)$$

We compared the results of our experimental diffusion coefficients of short filaments and the theoretical diffusion coefficients obtained for long, thin spheroids, where a >> b [41, 112]:

$$D_a = \frac{k_B T[\ln\left(\frac{L}{R}\right) - 0.5)]}{2\pi\eta L} \quad D_b = \frac{k_B T[\ln\left(\frac{L}{R}\right) - 0.5]}{4\pi\eta L} \quad D_\theta = \frac{3k_B T[\ln\left(\frac{L}{R}\right) - 0.5]}{\pi\eta L^3}, \quad (8 - 10)$$

where: $k_B$ – Boltzmann's constant, $T$ – absolute temperature, $\eta$ – the water viscosity, and $R$ and $L$ – filaments' radius and length.

### 4.2.2 Filament flexibility measurements

#### 4.2.2.1 Atomic Force Microscopy nanoindentation method

AFM nanoindentation analysis is a helpful method for directly measuring the Young modulus of hydrogel nanofilaments immersed in water. Stiffness was measured at 302 K in a closed liquid cell. This procedure was necessary in order to keep the hydrogel hydrated, minimise the thermal drift influence, and prevent contamination. We used a silicon nitride cantilever (CSG01, NT-MDT) with nominal 6 nm tip radius. The cantilever with spring constant equal to 0.040 N/m was calibrated by the thermal method [113]. We selected and then analysed different zones of a few hydrogel nanofilaments collecting

several series of force curves (Fig. 4.2) [113]. By fitting the Hertz model into the collected data, the filament Young's modulus was calculated using the following equation:

$$E = E_r\left(1 - \nu_f^2\right) \tag{25}$$

where $\nu_f$ is the Poisson's ratio of hydrogel and $E_r$ is relative elastic modulus. The swollen hydrogel material $\nu_f$ may be considered similar to rubber-like materials, which have a Poisson ratio of around 0.5 [114]. The relative elastic modulus is evaluated using the following formula [113]:

$$E_r = \sqrt{\frac{9P^2}{16R_e\delta^3}} \tag{26}$$

where $P$ is the force applied, $\delta$ is the indentation depth, and $R_e$ is the equivalent radius for a spherical intender, defined as [113]:

$$R_e = \sqrt{\frac{R_t^2 R}{R_t + R}} \tag{27}$$

where $R_t$ is the tip radius of curvature and $R$ is the radius of the nanofilament.

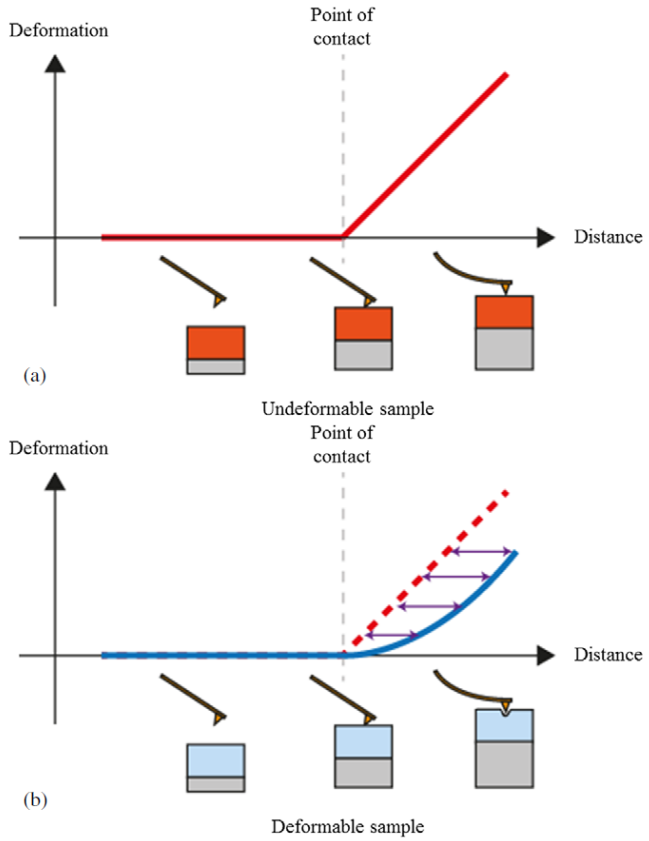


Fig. 4.2. Scheme of force-distance evaluation for AFM indentation of a hard sample (a) and a soft sample (b). The curve of indentation can be obtained by subtracting one curve from the other, as indicated by the violet arrows [115].

The method has its limitations. It may be expected that when a surface is pushed by a conventional AFM probe, the cantilever bending and applied force will be linearly dependent. This is true when the sample is hard and the probe does not deform it.

#### 4.2.2.2 Thermal fluctuation method

The second method used to evaluate the mechanical properties of flexible nanofilaments is based on the observation of the shape dynamics due to their thermal fluctuations [90, 92, 116]. Using this method, the mechanical properties of polymers such as microtubules or DNA can be evaluated in terms of persistence length, as described in Chapter 1.4.

In the procedure for determining the persistence length, the prepared hydrogel nanofilaments were injected into a chamber formed by microscope slides sealed with a grease and observed using a fluorescent microscope. Only nanofilaments longer than 1 μm were analysed. The images of the nanofilaments to be analysed were prepared according to the recommendations of Ott et al. [88, 92]. Briefly, grayscale images were cleaned from short objects and smoothed. Nanofilament positions were enhanced and the conversion to binary images was performed. A Matlab script was written to connect the filament structure gaps caused by the low fluorescence intensity and to process these images. About 500 to 700 images of skeletonised filaments were analysed with the cosine correlation method implemented in Matlab. Equation (16) given in Chapter 1 was used for the calculation of the flexural Young modulus *E*. To verify our methodology, several of our calculation results were compared with the persistence length obtained using the software developed by the De La Cruz group [88].

#### 4.2.2.3 Hydrodynamic interactions method

The last method we used to determine the filament Young modulus is based on the interaction of the fluid flow with the filament fixed to the channel wall at one end. This technique is based on the analysis of the nanofilament bending as a result of the fluid force exerted on a deformable cylinder [116]. As a first step, fibres were electrospun on a piece of PDMS with an elongated structure of 5 mm width and 3 mm depth. We were able to obtain a perpendicular arrangement of the fibres relative to the wall of this structure. Two identical pieces of PDMS (one with and one without fibres) were then glued together to form the channel. The attached fibres were placed in the middle of the channel. Then the PDMS channel was placed under an epifluorescence microscope and connected at one end by a PTFE tube to a syringe pump (neMESYS, Cetoni GmbH). After gradually filling the channel with DMF solvent, nanofibre shells dissolved, revealing hydrogel filaments in the form of short rods. After initiating the fluid flow, the

hydrogel rod started to bend due to exerted hydrodynamic drag force. Once the flow stopped, the bending elasticity of the nanorod returned it to its original position. The evaluation of its deformation rate and exerted hydrodynamic forces allowed us determine the elastic properties of the rod. To minimise the uncertainties of estimating the magnitude of very low flow rates applied, the nanorod elasticity was determined during the return phase of the bending process. Hence, the rod displacement in time (velocity) determined the hydrodynamic drag balancing the elastic force of returning it back to the initial position (Fig. 4.3).

The balance of elasticity force and hydrodynamic drag force is equal:

$$F_e - F_d = m\, a_c \tag{28}$$

where $a_c$ and $m$ are the acceleration and mass of the rod, respectively. Elasticity force is described by:

$$F_e = k_e\, \Delta x \tag{29}$$

$k_e$ – elasticity constant, and $\Delta x$ – displacement. Generally speaking, the hydrodynamic drag force for the rod moving with velocity $V$ relative to a fluid is given by:

$$F_d = C_D \frac{\rho V^2}{2} A_s \tag{30}$$

where $\rho$ – density of the fluid, $V$ – speed of the filament relative to the fluid velocity, $A_s$ – cross-section area of the rod, and $C_D$ – drag coefficient for the rod.

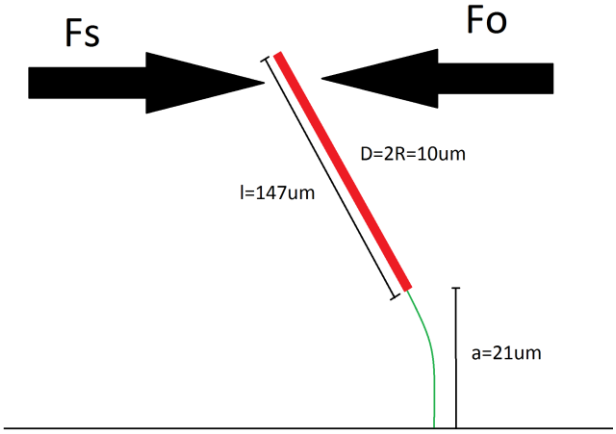


Fig. 4.3. Scheme presenting forces acting on the deformed hydrogel rod.

At a low Reynolds number regime, neglecting inertial effects, the hydrodynamic drag force is given by the simplified formula obtained for an elongated ellipsoidal obstacle, characterized by a radius $R$ and length $L$ [41]:

$$F_d = \frac{4\pi\eta VL}{\ln(L/R)} \quad (31)$$

where $\eta$ is fluid viscosity.

Recording the speed of the returning rod attached to the channel wall, this formula enabled us to calculate the bending Young modulus of the hydrogel filament.

### 4.2.3 Channel flow analysis

For experiments with hydrogel nanofilaments in a flow, the same measurement setup as for the lateral migration of spherical particles was used (Chapter 3.6). Before each experimental run, a suspension of fluorescently labelled hydrogel nanofilaments was manually injected into the PDMS microchannel. Then the solution was subjected to an oscillatory shear flow using a pulsatile pump. Very short hydrogel debris (L ~ 1 μm), always present in the solution after the removal of the polymer shell, were used to estimate the local flow velocity around the nanofilaments. The maximum amplitude of the flow velocity ($V_{max}$) used during the experiments varied between 0.05 mm/s and 0.95 mm/s, while the range of the forcing frequency was between 0.12 Hz and 0.64 Hz. We considered a flow of Newtonian liquid through the microchannel with a rectangular cross-section. The flow was characterized by a small Reynolds number *Re* ($= V_{max}W\rho/\eta$) based on the channel width *W*. It varied from 0.01 to 0.18.

Nanofilaments were observed by using an inverted epifluorescence microscope (Leica AM TIRF MC) with a 20x/0.40 NA microscopic lens, and an appropriate set of filters for fluorescence imaging. As a source for fluorescence excitation, a mercury lamp (Leica EL6000) was used. The high-gain EM-CCD camera (C9100-2, Hamamatsu) was used to record nanofilament displacements, with a typical frame rate of 10 Hz. Each series consisted of 500 to 2,000 individual images. Nanofilaments were observed and recorded at 15 mm from the channel inlet within the 500 μm-long and 200 μm-wide section of the horizontal central plane located 30 μm above the bottom wall of the microchannel. If filaments were above or below the focal plane of the microscope they were not used in further analyses. Moreover, filaments were also excluded from the analysis if they clearly changed their contour length during an experimental run, i.e. when its variations exceeded 10%. Such apparent length changes indicated their out-of-plane shape deformations. All experiments were conducted by using the microscope environmental chamber at a stable temperature of 302 K. The working liquid density $\rho$ and dynamic viscosity $\eta$ measured at that temperature were 984 kg/m$^3$ and 7.5 10$^{-4}$ kg m/s, respectively.

### 4.3 Filament mechanical properties evaluation

The hydrogel nanofilaments obtained by the electrospinning technique had a typical contour length in the range from 1 μm to over 500 μm. In this experiment, we used nanofilaments with a contour length of 20 μm to 90 μm, which was evaluated using microscopic images and the ImageJ program [110]. The long sequences of filament images taken in the channel before the oscillating flow started provided the opportunity to obtain their average value of contour length along with the corresponding persistence length.

Before each experimental run, the geometry of the selected nanofilaments was evaluated. For this purpose, the selected object was conveyed by a micro-pump into the observation area of the microscope and its fluorescent images were analysed in stop-flow conditions with the help of the image processing Matlab software. The evaluation procedure of the geometry and persistent length of the filaments is described in detail in Chapter 1.

The dynamics of the filaments carried by the flow depends both on their mechanical properties (flexural and extensional modules, *E*, *Ex*) and on their geometry (diameter and contour length). The mechanical properties of a hydrogel material depend on its composition. As described before, the fabricated nanomaterials were characterized by nanoindentation, hydrodynamic bending, and thermal fluctuation analysis. The obtained mean value of the flexural Young modulus (*E*) was equal to 2 kPa. Its approximate result was obtained by the method of the direct bending of the sample filament in a shear flow (hydrodynamic interaction method) and the AFM indentation method. The accuracy of this estimation depends significantly on the proper evaluation of the filament geometry.

The extensional Young modulus (*Ex*) was obtained from macro-scale stretching experiments with a hydrogel beam of 4 mm diameter and 1.8 cm length. The asymptotic value of *Ex* obtained at the limit of small stretching forces was equal to 20 kPa. This value appears to be an order of magnitude higher than flexural rigidity, thus confirming the relatively high extensional stiffness of our filaments.

Young modulus, once established for the sample material, is used to obtain the filament diameter *d* from the evaluated persistence length $L_p$, according to the formula:

$$E = (64 k_B T L_p)/(\pi d^4). \qquad (32)$$

This procedure provides better results than the analysis of microscopic images. Determined that way diameter of filaments used in the experiment are in the range of 110 nm to 180 nm, which is in agreement with the AFM measurements of single samples.

For analysis of the filament deformations, we determined two non-dimensional parameters to characterize the mechanical properties of our hydrogel filaments: relative flexural stiffness (*A*), and relative extensional (Hookonean) stiffness (*K*). Relative flexural stiffness describes the ratio of filament bending stiffness related to the hydrodynamic force. A high value of *A* indicates a stiffer (less flexible) filament. For A = 0, the fibre bends freely without recovering its initial shape. The definition used to evaluate the relative flexural stiffness is [51]:

$$A = Ed/(32\,\eta V_{max}) \tag{33}$$

where: $V_{max}$ is the absolute maximum flow velocity in the centre of the microchannel, and $\eta$ is the dynamic viscosity of the carrier fluid.

The relative extensional stiffness describes the ratio of the extensional filament deformation force related to the hydrodynamic force of the flow amplitude. It is defined as:

$$K = E_x d^2/(4L\,\eta V_{\max}) \tag{34}$$

For our highly deformable objects suspended in a fluid flow, one of the significant degrees of deformational freedom is bending/buckling. This behaviour is due to the flow-induced viscous forces characterized by the local flow shear rate, and to the thermal fluctuations characterized by persistence length. Following the approach of Kanstler and Goldstein [117], and Li et al. [118], we introduced two additional non-dimensional numbers characterizing the dynamics of the analysed filaments. The first parameter, Sperm number (*Sp*), characterizes the relative magnitudes of viscous and elastic forces for deformable objects conveyed by a steady flow [119]. It is given as:

$$Sp = 32\pi\,\eta V_{max}\underline{L}^4/(EW) \tag{35}$$

where: *W* is the channel width, and $\underline{L}$ is the length-to-diameter ratio (= *L/d*).

For $Sp \leq 1$, thermal modes dominate over the flow-induced viscous friction, and a flexible filament oscillates transversely and symmetrically. For $Sp >> 1$, thermal bending shape fluctuations are damped by the flow-induced viscous stresses, while the free filament ends are motionless [58]. We must remember, however, that at each oscillating cycle there is a short dwell time. At that moment, thermal fluctuations are dominant and could slightly modify the position and deformation of tangled filaments. For the analysed configuration this effect appears to be residual, as the elastic relaxation time of filaments is over 100 s, much longer then the stopped flow time.

As the position of the filaments conveyed by the flow is perturbed by thermal fluctuations, the significance of this effect can be evaluated by correlating the flow-induced convection time to the characteristic time of Brownian diffusion. The latter depends on the shape, configuration, and local deformations of filaments, something that is generally difficult or impossible to describe by a simple formula. Hence, we estimated the diffusion relaxation time from our experimental data collected for the measured translational displacements. The corresponding Peclet number becomes:

$$Pe = LV_{max}/D \tag{36}$$

where $D$ is the longitudinal diffusion.

For Peclet numbers lower than 1, we have to assume the dominating Brownian diffusion over the flow-induced longitudinal translation of the filament. However, for typical values in our experiments, with the Peclet number over $10^2$, we may conclude that the translational diffusion has negligible effects, again except the short time intervals of stop flow of oscillating periods.

### 4.4 Orientation, elongation, and bending analysis methods

Because of the large number of degrees of freedom, the problem of characterizing the mobility of flexible objects, such as nanofilaments or long molecular chains, can be solved only on a statistical basis. It is not only that the translational and rotational motions of objects must be analysed. The main response to thermal fluctuations and shear stresses is transformed into a multifunctional shape variation. There is no single method of characterizing the dynamics of such objects, because they depend on geometry and shape, as well as on a large number of parameters characterizing the constraints of the filaments the internal and external mechanical interactions.

To quantify the deformation properties of filaments during several periods of the oscillating flow, we define four basic parameters. The first is the degree of buckling or looping (BU) measured as the ratio of the smallest circle diameter ($d_c$) binding an object to the filament contour length (Fig. 4.4). Hence BU ≤ 1, where BU = 1 corresponds to a straight rod.

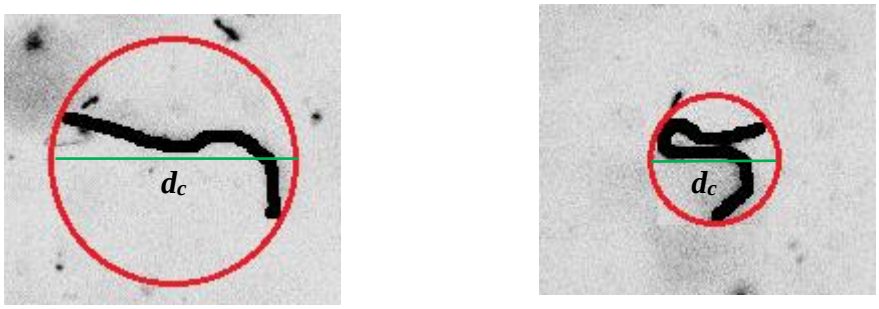


(a) (b)

Fig. 4.4. Degree of buckling, example of BU evaluation: (a) BU = 0.84; (b) BU = 0.42.

The second shape parameter is the degree of elongation (EL), which is quantified by relating the short ($d_e$) to the long ($L_e$) axis of the ellipse encircling filament (Fig. 4.5). Obviously, for rod-like objects EL << 1, while for regularly coiled filaments it approaches 1.

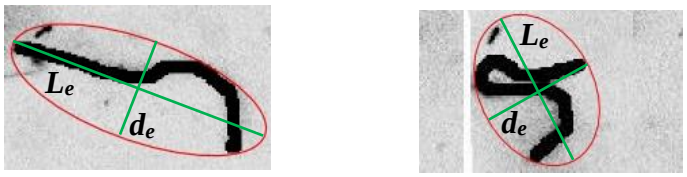


(a) (b)

Fig. 4.5. Degree of elongation, example of EL evaluation: (a) EL = 0.42; (b) EL = 0.60.

For the same encircling ellipse the third quantifier is defined, namely the inclination angle IA of the long ellipse axis in relation to the channel axis (Fig. 4.6). It changes from -π/2 to +π/2 for object orientation directed either into the channel inlet or from the inlet.

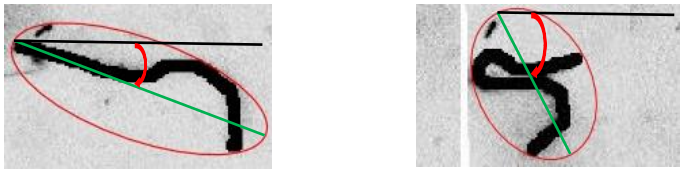

(a) (b)

Fig. 4.6. Inclination angle, example of IA evaluation: (a) IA = -24.25°; (b) IA = -73.84°.

The end-to-end distance (EE) related to the filament contour length is selected as the fourth shape characteristic (Fig. 4.7). It depicts the bending degree for relatively short filaments.

(a) (b)

Fig. 4.7. End-to-end distance, example of EE evaluation: (a) EE = 0.84; (b) EE = 0.38.

## 4.5 Cross-flow migration analysis

The observation of hydrogel nanofilaments during the oscillatory flow allowed us to analyse their cross-flow migration. The distance of the centre of mass of the observed filament from the microchannel centre was chosen. This distance changed during every cycle of the oscillatory flow. The absolute value of the migration velocity $U_r$ was defined as the ratio of the averaged total lateral displacement of the filament mass centre to the time in which the filament oscillated. Due to the hydrodynamic interactions and deformations observed, the filament longitudinal velocity lags slightly behind the fluid flow velocity. Its value related to the local fluid velocity is marked as a *slip* velocity $U_s$.

## 4.6 Results and discussion

### 4.6.1 Nanofilament morphology

Fig. 4.8 confirms the presence of a core structure in electrospun fibres. Micrographs indicate core segments in fibres, although the dissolution of the PLCL shell showed that many short nanofilament objects were released together with long hydrogel nanofilaments.

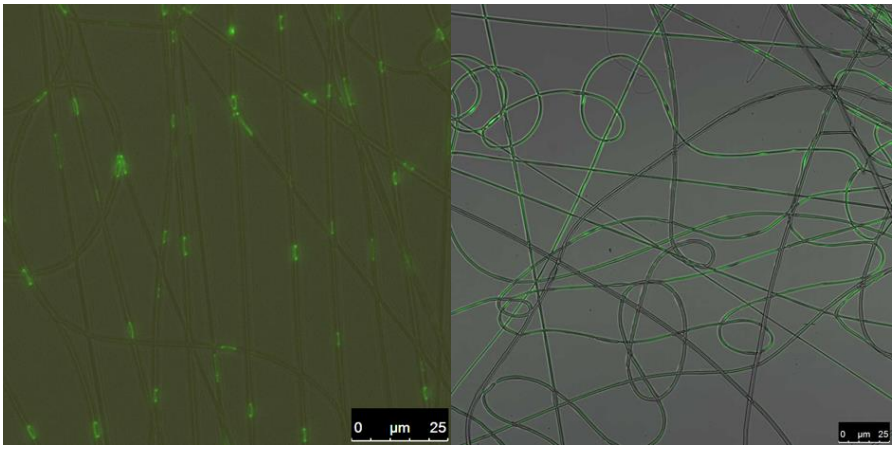


(a) (b)

Fig. 4.8. Images of core-shell nanofibres from fluorescence microscope (TIRF). Fluorescent parts (core) of fibres indicate (a) short and (b) long hydrogel nanofilaments inside a shell (PLCL) structure.

We found that the hydrogel core pieces differed in length. Depending on the changes in the parameters of the electrospinning process, they formed short (Fig. 4.8 (a)) or long (Fig. 4.8 (b)) hydrogel filaments.

The nanofilaments of AAm:Bis-AAm with a mass ratio (w/w): 37.5:1, 20:1 and 4:1 were labelled as EA1, EA2, and EA3, respectively. The nanofilaments of NIPAAm:BIS-AAm with a mass ratio (w/w): 37.5:1, 20:1 and 4:1 were labelled as EN1, EN2, and EN3, respectively.

The averaged diameters obtained from the SEM images of PLCL/PNIPAm and PLCL/AAm core-shell nanofibres with a hydrogel core of NIPAm:Bis-AAm with a mass ratio of 37.5:1, 20:1, and 4:1 are shown in Table 4.1. The corresponding diameters of the extracted hydrogel filaments are also shown.

Table 4.1. Diameter of core-shell fibres and extracted hydrogel nanofilaments.

| **AAm/NIPAm : BIS mass ratio** | Diameter of PLCL core-shell fibres and extracted hydrogel filaments | | | |
|---|---|---|---|---|
| | **PLCL/AAm: Bis-AAm** | **PLCL/NIPAm: Bis-AAm** | **AAm:Bis-AAm** | **NIPAm:Bis-AAm** |
| **37.5:1** | 1980 ± 210 nm | 1350 ± 380 nm | 96 ± 24 nm | 126 ± 36 nm |
| **20:1** | 2100 ± 450 nm | 710 ± 310 nm | 112 ± 47 nm | 170 ± 65 nm |
| **4:1** | 1270 ± 180 nm | 790 ± 150 nm | 290 ± 209 nm | 257 ± 207 nm |

It is rather difficult to control the nanofilament diameter in experiments. This may be achieved by changing the monomer ratio. An increase in the filament diameter was observed when the amount of BIS-AAm was increased. During electrospinning, nanofibres falling onto the collector are thicker as result of the fast core polymerization, which prevents further fibre elongation.

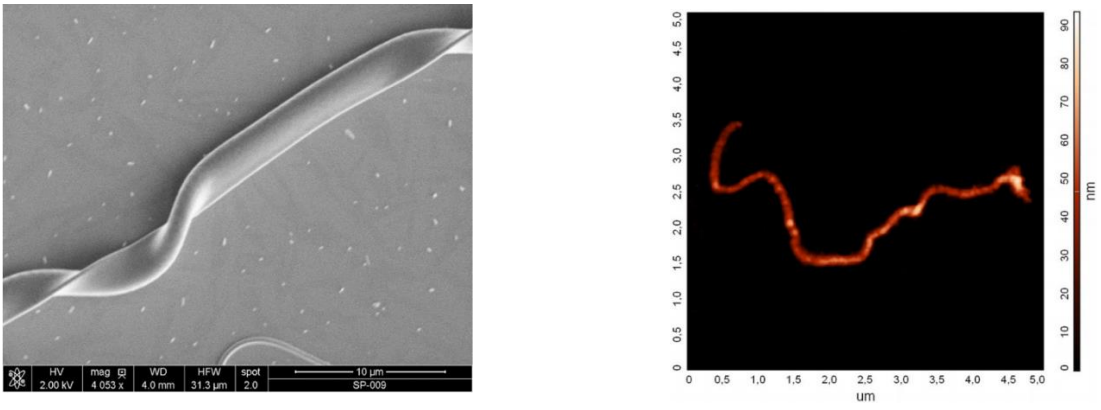


(a) (b)

Fig. 4.9. (a) Micrograph of a ribbon-like core-shell PLCL/PAAm nanofibre (EA3) observed under SEM (b) Topography of a ribbon-like nanofilament (EA1) observed by AFM (width 128 nm, contour length 7 μm, height 39 nm, equivalent diameter 80 nm).

We also observed ribbon-like nanofilaments (Fig. 4.9 (a)). The ratio of height to width for the investigated nanofilaments varied from about 5 to over 20 (Fig. 4.10).

We may find some correlation between this size variation and crosslinker concentration. Additionally, it is very likely that the faster polymerization cause nanofibres not to have enough time for the relaxation of their shape when they leave the nozzle.

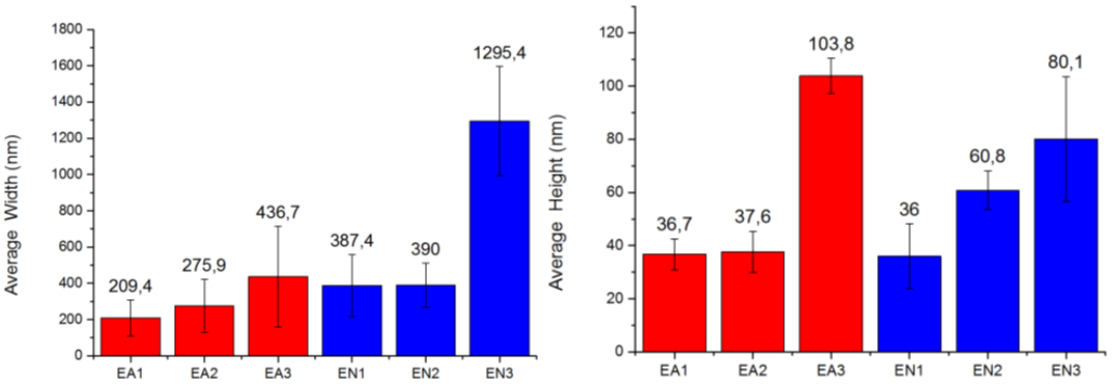


(a) (b)

Fig. 4.10. Average width (a) and height (b) of the analysed hydrogel nanofilaments.

It is worthwhile to note that the hydrogel nanofilaments observed under AFM have a typical height in the range of 30 nm to 60 nm, therefore their expected bending direction is most likely anisotropic. A proper diameter evaluation is necessary for the proper estimation of the elasticity. Furthermore, the quantitative theoretical analysis of nanofilament flow-induced deformations is challenging, due to the possible non-uniformity of their shape. Such a non-uniform shape, however, is typical in the case of biological objects such as proteins.

### 4.6.2 Brownian motion of flexible nanofilaments

The Brownian motion of hydrogel nanofilaments was measured in DMF solution at temperature T = 302 K and viscosity $\eta = 1.02 \cdot 10^{-3}$ Pa s. The typical traced path of a short nanofilament suspended in a fluid, the resulted displacements, and the rotation due to collisions with fluid molecules are shown in Fig. 4.11.

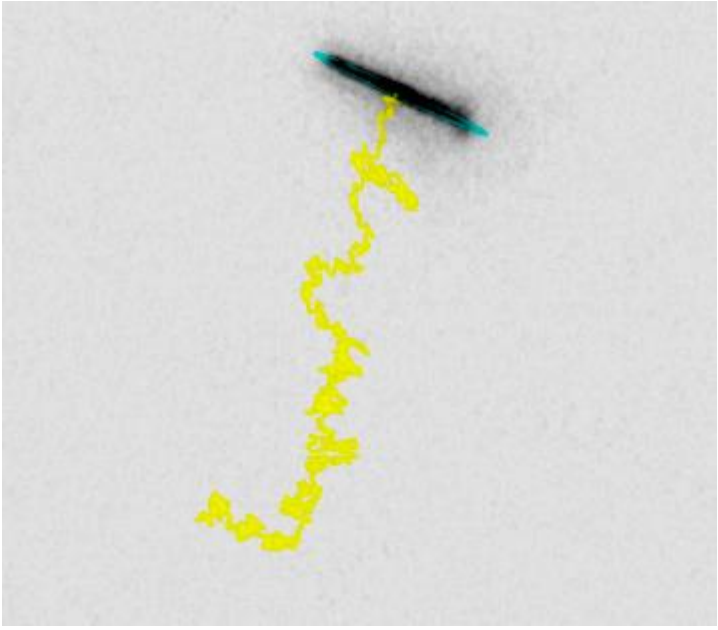

Fig. 4.11. Diffusion path (yellow) of a filament with contour length 15.6 μm (Table 4.2, nanofilament no 5). The ellipse outlines the filament and indicates the rotation angle of the filament.

The diffusion coefficients for hydrogel nanofilaments shown in Table 4.2, were calculated as mean square displacements (eqs. 8-10). We analysed only nanofilaments which were far away from the surface of the cover glass (more than 10 μm). The surface proximity could constrain one end of the hydrogel and yield unrealistic results. Diffusion coefficients were measured by tracking analysis.

In the case of short nanofilaments (no 1-5, Table 4.2) we observed that diffusion coefficients are, on average, two times smaller than the theoretical ones calculated for the oblate ellipsoid (eqs. 8-10). For long nanofilaments (no 6-9, Table 4.2), average diffusion coefficients are two times larger than the theoretical values for an ellipsoid. Theoretical diffusion coefficients are obtained using the length and radius of the observed filaments as a virtual ellipsoid. Obviously these theoretical values should be used only as a reference for the very simplified model of filaments shape.

The figures in Table 4.2 show the typical shapes of the examined nanofilaments. In the first nanofilament there is possibly some narrowing, which could affect the bending dynamics results. In the second flexible filament, we mainly observed a rotation along its main axis (no 2, Table 4.2). All three diffusion coefficients were about two times smaller than the theoretical values for a long, thin prolate spheroid. The third filament was moving along the main (*a*) axis at a slower rate than in the perpendicular direction (along the *b* axis). In contrast to the two previous cases, the diffusion coefficient along the b axis was

even greater than the model value for a straight, non-deformable ellipsoid. This may suggest the presence of an additional factor affecting the diffusion between parallel microscope slides. As in previous experiments, the rotational diffusion was lower than its theoretical value.

Table 4.2. Comparison between experimental and theoretical diffusion coefficients of highly deformable hydrogel nanofilaments suspended in DMF. $D_f$ – flexural diffusion (from persistence length $L_p$).

| No | | L/2R | $D_f$ [μm²/s] | $D_a$ [μm²/s] | $D_b$ [μm²/s] | $D_\theta$ [rad²/s] | L [μm] | $L_p$ [μm] | Motion | Shape |
|---|---|---|---|---|---|---|---|---|---|---|
| 1 | exper. | 43.0 | 0.0018 | 0.052 | 0.035 | 0.0006 | 21.5 | 93 | Bending | 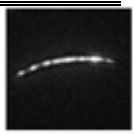 |
| | theor. | 43.0 | | 0.144 | 0.090 | 0.0019 | | | | |
| 2 | exper. | 31.2 | 0.0056 | 0.093 | 0.067 | 0.0025 | 15.6 | 29 | Rotation |  |
| | theor. | 31.2 | | 0.182 | 0.116 | 0.0045 | | | | |
| 3 | exper. | 29.8 | 0.0005 | 0.059 | 0.140 | 0.0029 | 14.9 | 339 | Rotation |  |
| | theor. | 29.8 | | 0.189 | 0.121 | 0.0051 | | | | |
| 4 | exper. | 47.8 | 0.0008 | 0.231 | 0.053 | 0.0005 | 23.9 | 211 | Bending |  |
| | theor. | 47.8 | | 0.133 | 0.083 | 0.0014 | | | | |
| 5 | exper. | 31.4 | 0.0003 | 0.266 | 0.070 | 0.0023 | 15.6 | 598 | Rotation |  |
| | theor. | 31.4 | | 0.182 | 0.116 | 0.0044 | | | | |
| 6 | exper. | 48.4 | 0.0326 | 0.112 | 0.105 | 0.0026 | 24.2 | 5 | Bending |  |
| | theor. | 48.4 | | 0.132 | 0.082 | 0.0013 | | | | |
| 7 | exper. | 104.8 | 0.0326 | 0.054 | 0.070 | 0.0005 | 52.4 | 5 | Bending |  |
| | theor. | 104.8 | | 0.072 | 0.044 | 0.0002 | | | | |
| 8 | exper. | 171.0 | 0.0053 | 0.039 | 0.150 | 0.00005 | 85.5 | 31 | Bending |  |
| | theor. | 171.0 | | 0.049 | 0.029 | 0.00004 | | | | |
| 9 | exper. | 105.6 | 0.0109 | 0.029 | 0.087 | 0.0002 | 52.8 | 15 | Bending |  |
| | theor. | 105.6 | | 0.072 | 0.043 | 0.0002 | | | | |

The fourth filament analysed showed a detectable bending of its arms, and had a higher diffusion coefficient along the *a* axis compared to the theoretical model, but we found a comparable diffusion coefficient along the *b* axis. As in the previous cases, its rotational diffusion was about half that predicted by the equation (8-10). The fifth nanofilament had the same contour length as nanofilament no 2. The two nanofilaments discussed differ in shape, as shown by the figures in Table 4.2. The experimental diffusion coefficient along the main axis *a* is one and half times higher than the theoretical value. The diffusion path of this nanofilament is shown in Fig.4.11, where we can see its translational dominated motion. The sixth filament had a contour length comparable to that of the fourth nanofilament but with a different shape, and was observed to bend during the experiment. Both translational diffusion coefficients in the *a* and *b* axis direction were comparable with theoretical values, but its rotational diffusion coefficient was two times greater than in the straight ellipsoid model. This observation may be associated with the shape of nanofilaments. The seventh nanofilament had a contour length of 52.4 μm. It has a much smaller diffusion coefficient than the preceding shorter nanofilaments. The experimental diffusion coefficient in the main axis direction is smaller than to its theoretical value, and – at the same time – the diffusion coefficient along the *b* axis is higher than its theoretical value. As in the preceding C-shaped nanofilament, the rotational diffusion coefficient was approximately two times higher than the theoretical value for the equivalent ellipsoid. The longest nanofilament (no 8), with a contour length of 85.5 μm, showed a rotational diffusion closer to the theoretical value as compared to other nanofilaments. The diffusion coefficient along the *b* axis, however, is nearly five times greater than the theoretical value for the ellipsoid. For the last, ninth, L-shaped nanofilament, we observed smaller experimental diffusion coefficients in both directions, compared to its theoretical model values. Its translational diffusion was almost in agreement with the rotational diffusion coefficient for the equivalent ellipsoid. The typical frames of these filaments exhibiting bending dynamics are shown in Fig. 4.12.

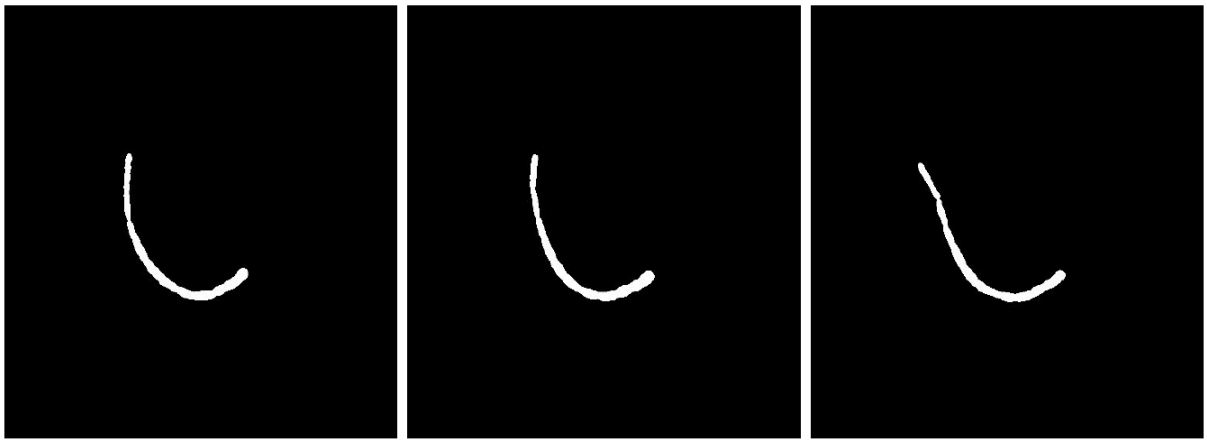

(a) t = 0 s (b) t = 0.5 s (c) t = 1.0 s

Fig. 4.12. Binary images demonstrating the filament bending. These images were used for the calculation of the persistence length. The contour length of the nanofilament was equal to 52.8 μm (Table 4.2, no 9).

Fig. 4.13 (a) shows the nanofilament mean square displacement for translational (along *a* and *b* axes) and rotational diffusion. We can see the more or less linear passage of the curves obtained. Each filament was divided into two segments, and three main points were marked on the object analysed.

The evaluation of bending dynamics as a result of thermal fluctuations was possible thanks to the analysis of the angle between the two arms of the nanofilament (Fig. 4.13 (b)). The nanofilament arms were in the range of 11.8°. Additionally, we measured the distance between arm ends and arm lengths to confirm bending and exclude rotation. For C-shaped nanofilaments, the rotation of the nanofilaments would cause filament ends to go out of focus and, apparently the length of the arms will be shorten. This effect was used to rule out such cases during the bending evaluation. This meant that filaments whose length varied more than 10% during observation were eliminated from further analyses. In the case of the data shown (Fig. 4.13 (c)), we can see that the distance between the arm ends and the variation in their length is around 3%, thus proving the bending of the filaments.

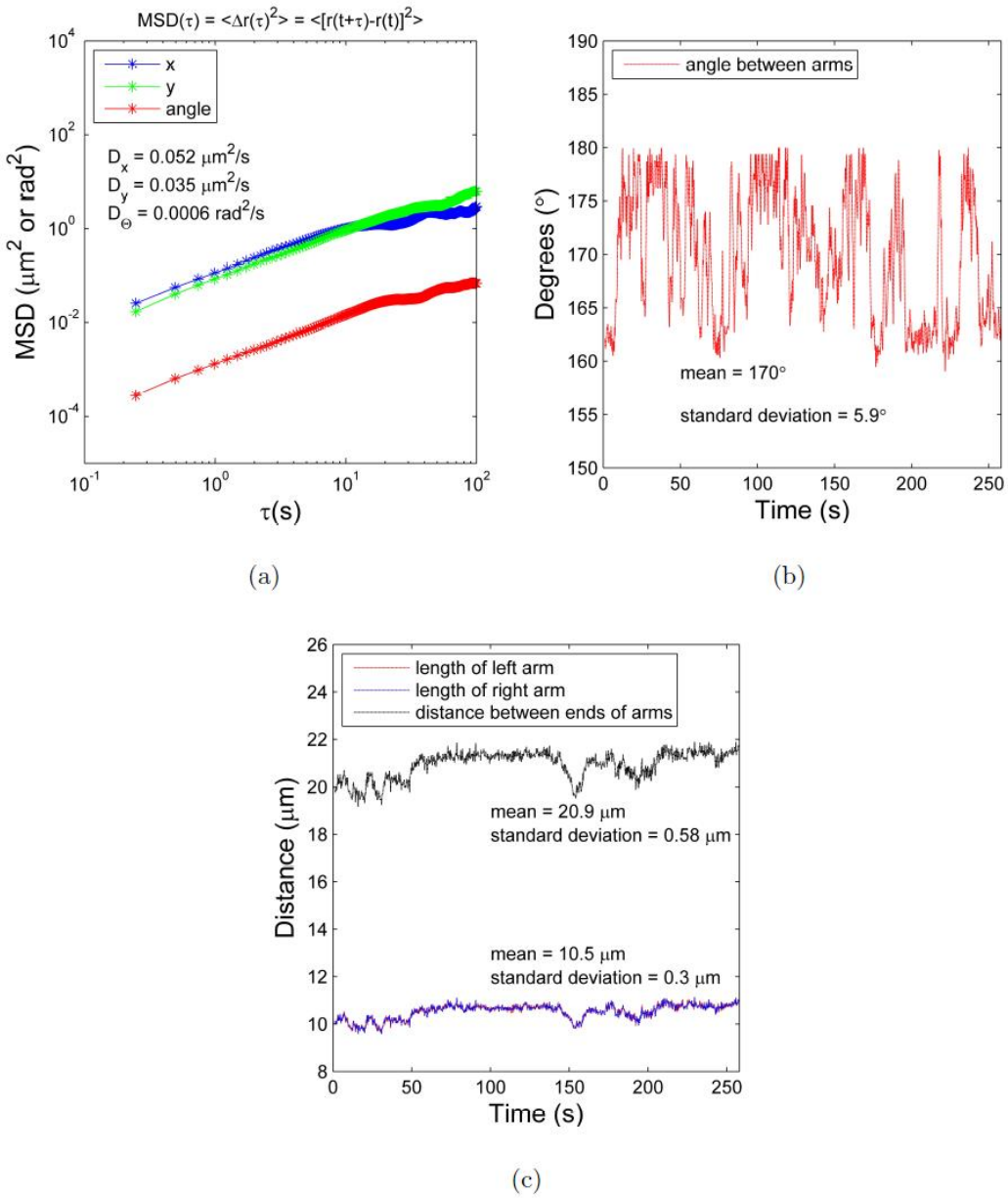


Fig. 4.13. (a) Plot of the mean square displacement of filaments with a 21.5 μm contour length in function of lag time. The upper two plots are MSDs along axes *a* and *b* in terms of $\mu m^2$, whereas the bottom one is the angular MSD in terms of $rad^2$. (b) Angle between arms of the bending filament based on time. (c) Length of left and right arms of the bending filament and length of distance between the arm ends. All plots show calculations for the nanofilament no. 1 from Table 4.2.

An example of frames captured during the bending of the nanofilament is shown in Fig. 4.14.

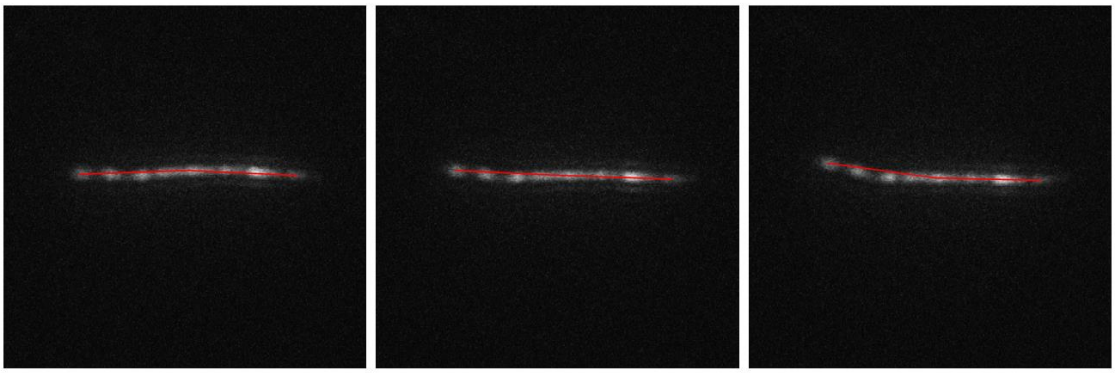

(a) t = 0 s (b) t = 0.25 s (c) t = 0.50 s

Fig. 4.14. Bending dynamics of a nanofilament (Table 4.2, nanofilament no. 1). Red lines indicate the fibre arms starting from its centre of mass. The angle between the red lines was measured to assess flexibility.

### 4.6.3 Evaluation of mechanical properties of hydrogel nanofilaments

In Table 4.3 we summarized the results of three experimental methods aiming to estimate the bending Young modulus of selected samples of the nanofilaments obtained using six different compositions of hydrogels. The three experimental methods used are described in the following subsections. As previously mentioned, each experimental method applied has its pros and cons. Therefore, before selecting the proper hydrogel samples for forthcoming experiments in the channel flow, we found it necessary to gain some fundamental knowledge on the possibility of evaluating their mechanical properties.

Table 4.3. Young modulus evaluated by AFM nanoindentation, cosine correlation, and hydrodynamic interactions methods. We analysed three types of nanofilaments with different AAm:BIS-AAm and NIPAAm:BIS-AAm mass ratios. Only one experiment performed for EN1 material was successfully accomplished for evaluating Young modulus by the hydrodynamic interaction method.

| Experiment | **Young modulus E (kPa)** | | |
|---|---|---|---|
| | **AFM nanoindentation** | **Cosine correlation (Thermal fluctuations)** | **Flow hydrodynamic interactions** |
| **EN1** | - | 4.5 ± 0.4 | 2.3 |
| **EN2** | 8.50 ± 1.19 | 3.1 ± 1.7 | - |
| **EN3** | 18.11 ± 4.85 | 3.8 ± 1.1 | - |
| **EA1** | 4.06 ± 1.18 | 6.1 ± 2.6 | - |
| **EA2** | 15.80 ± 2.77 | 5.0 ± 1.1 | - |
| **EA3** | 55.82 ± 5.64 | 5.8 ± 0.8 | - |

#### 4.6.3.1 Evaluation by AFM nanoindentation

Table 4.3 shows the result of hydrogel filaments Young modulus obtained by several AFM measurements. The average Young modulus obtained for three different nanofilaments was given. It should be noted that the applicability of the AFM nanoindentation method must be limited to extremely soft objects. This is mostly due to the fact that the stiffness of the cantilever is relatively higher, compared to the fluid-like behaviour of the hydrogel. Results were averaged over all recorded measurements. In most cases, the values obtained overlap the data already available for such materials [120]. The wide range of results obtained is a consequence of the non-uniform nanofilament geometry, their environmental interactions, and a problematic procedure for catching the proper part of the filaments. The main problem with AFM nanoindentation is that the stiff substrate contributes a great deal to soft and thin materials. Because of this, nanoindentation outcomes may differ from the actual sample stiffness; therefore, it was decided to compare them with the Young module values obtained using two other methods.

#### 4.6.3.2 Evaluation from thermal fluctuations

For the Young modulus evaluation of nanofilaments made by different monomer ratios, the persistence length with the cosine correlation was found to be the easiest, most direct method. For this method, around 500–700 images were analysed per single nanofilament. The time interval of the image sequence was 0.25 s. All experiments were conducted under the same experimental conditions for the different samples. As we can see in Table 4.3, the results of the Young modulus evaluated by the cosine correlation method do not show an increasing trend with increased crosslinker amounts, in contrast to the AFM nanoindentation results. We also observed that PAAm filaments are slightly less flexible than PNIPAAm filaments. This is consistent with the results presented in the literature.

We compared the data obtained by the persistence length method with the diffusion coefficients of analysed nanofilaments and show them in Fig.4.15. The relation between persistence length (flexibility) and diffusion is very weak. But if we look at filaments no. 4 and no. 5 we can see that a straight filament shape and higher stiffness are correlated with a relatively high longitudinal diffusion. For this reason, it is necessary to include the shape parameterisation in order to find any possible correlation between persistence length and diffusion.

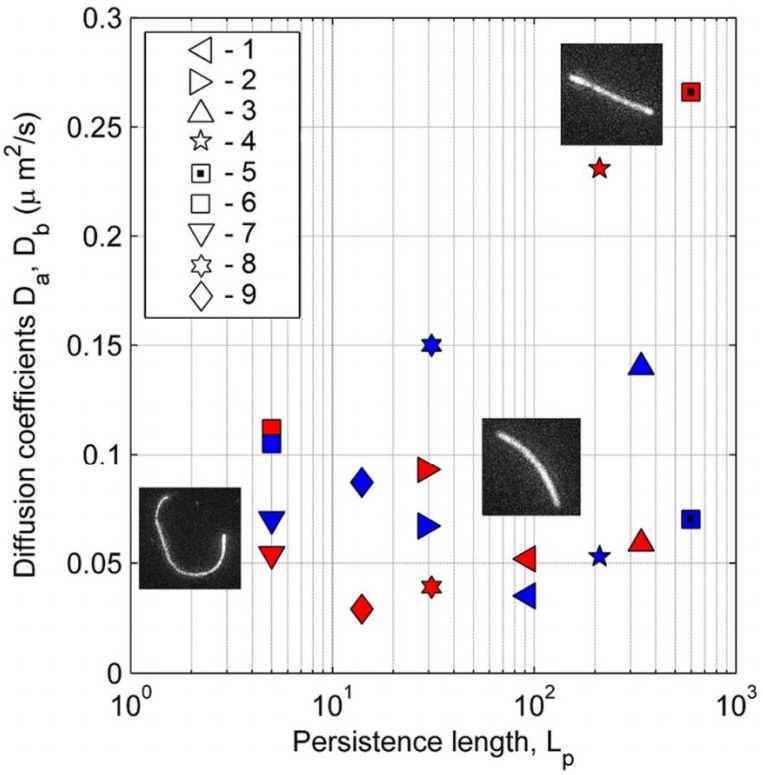


Fig. 4.15. Translational diffusion coefficient $D_a$ (red symbols) and $D_b$ (blue symbols) as a function of persistence length for the analysed filaments shown in Table 4.2.

We should also remember that Young modulus measurements based on the persistence length are evaluated using a theoretical formulation neglecting any hydrodynamic interactions with the environment. It would be interesting to know the damping effect of liquid viscosity on the evaluated persistence length. In Table 4.2 we show flexural diffusivity, a parameter taking into account the viscous damping exerted by the surrounding filament liquid. In the case of bending fluctuations (cases 6 and 7 in Table 4.2), the contribution of flexural diffusivity is evidently dominant over translational or rotational diffusion. This illustrates the difficulty in formulating a single interpretation of the dynamics of long, deformable molecules suspended in a complex, viscous biological environment.

#### 4.6.3.3 Evaluation from hydrodynamic interactions

Data acquired during the recovery of the bent filament five seconds after stopping the flow were used for the Young modulus calculation. Fig. 4.16 shows three images of our experimental procedure.

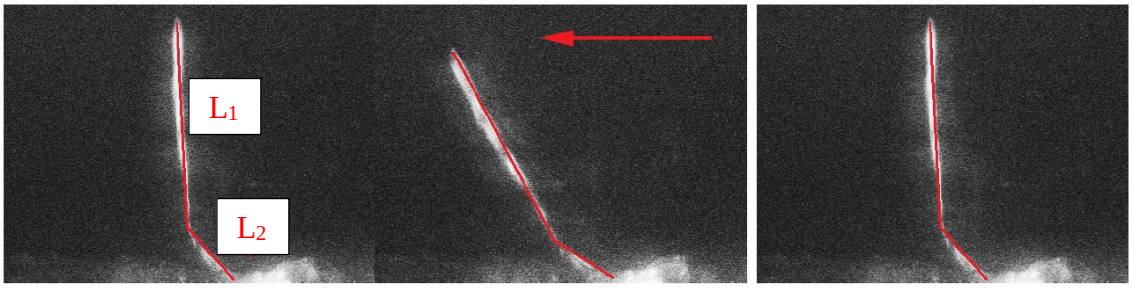


(a) (b) (c)

Fig. 4.16. Bending of a filament in a flow recorded by fluorescence microscopy; (a) – initial position, (b) – bending of the filament triggered by the flow, (c) – returning phase of the filament after the flow was stopped. $L_1$ – stiff part of the filament, $L_2$ – flexible part of the filament attached to the wall.

The flow applied deformed the filament attached to the wall. Only the part attached to the wall seems to be bent, with the upper part responsible for the acting drag force. The phase of recovery of the initial position was analysed to evaluate the mechanical properties of the filament. To calculate the Young modulus of the filament, we used the data on the varying filament position taken during time intervals of about three seconds and recorded five seconds after the flow was paused. During this three-second observation time, the filament was moving back to its original position at an apparently constant angular velocity. Its linear velocity at any point on the filament was equal to V = 1.34 μm/s. The drag force acting on a stiff fibre part ($L_1$ = 145.38 μm) was equal to $4.53 \cdot 10^{-13}$ N. Thus the Young modulus calculated for the flexible part ($L_2$ = 39.14 μm) was found to be equal to 2.34 kPa. The Young modulus value calculated by the hydrodynamic method appeared to be comparable to that obtained by the persistence length method (Table 4.3). The hydrodynamic method appeared to be the most reliable method for evaluating elastic interactions with the environment. On the other hand, it also appeared to be the most difficult to carry out, and not accurate enough to be evaluated. Due to the difficulties encountered in finding additional filaments perpendicular to the channel wall after the dissolution of the fibre shell, only one such experiment was reliable enough to be evaluated. It was difficult to repeat this experiment with other filaments. For this reason, we evaluated the Young modulus by the flow method only for one hydrogel formulation EN1.

### 4.6.4 Filament shape variation under flow interactions

The configuration of the oscillating flow proposed in this study resembles in vivo conditions. Bio-objects are transported by inter-tissue and time-dependent fluctuations of the flow field. It is also important to point out that, the oscillatory flow makes it possible

for us to visualize the dynamics of nanofilaments in one detection regime over a relatively long recording time.

Our pulsate pump allowed to maintain the maximum amplitude of the flow oscillations imposed to remain constant throughout the entire observation period, in the first and in the second half of the cycle, where we applied a reverse flow (Fig. 4.17). The flow velocity gained its maximum value at oscillatory phases ± $n\pi/2$, where $n$ = 1, 3, 5, etc. Numerical and experimental data evidenced that the flow generated in the microchannel was not characterized by any phase lags, thus confirming the low Reynolds number (Re < 0.2) almost purely sinusoidal flow characteristics. Therefore, we may assume that the flow we applied was in a quasi-steady creeping flow regime.

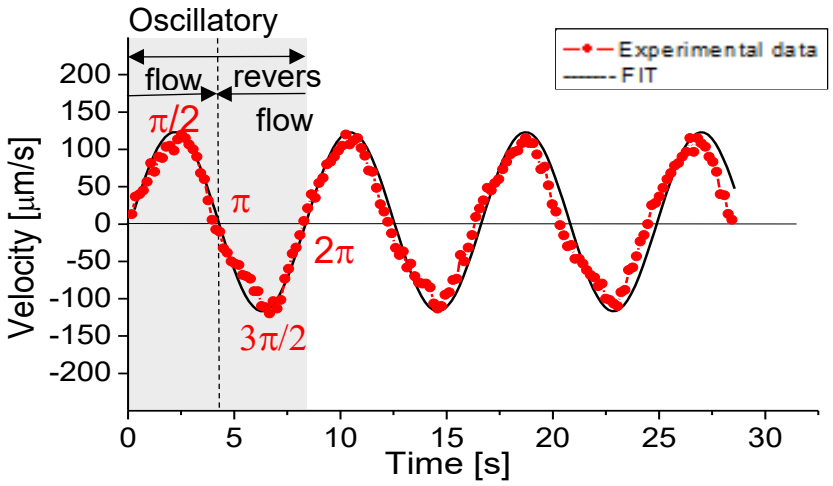


Fig. 4.17. Oscillatory flow waveform generated by our home-built pulsatile pump. The horizontal solid line at $V$ = 0 (for $n\pi$ = 0, 1, 2, etc.) marks cross-points of short stop-flow intervals at which some changes in nanofilament conformation and migration were recorded for each constitutive oscillatory cycle. At $V = n\pi/2$ (for $n$ = 1, 3, 5, etc.), hydrogel nanofilaments experienced the maximum flow velocity, which was used to define nondimensional flow characteristics. Empirical data are compared with the sinusoidal fit function.

In microchannels with rectangular cross-section, and especially in those with a high aspect ratio (e.g. Hele-Shaw configuration), the flow pattern along two main axes is substantially different. In addition, the presence of sharp corner edges generates relatively high local shear stresses that may affect the dynamics and migration behaviour of nanoobjects conveyed into such microchannels. Therefore, to obtain reliable information on local shear rates and velocity flow profile, we performed a finite element simulation of the oscillatory flow inside a rectangular microchannel. As expected, the shape of the velocity profile takes a plug-like shape already at the beginning of the oscillatory cycle

(Fig. 4.18, red line), and not a truly parabolic shape, as in a microchannel with a circular (or squared) cross-section.

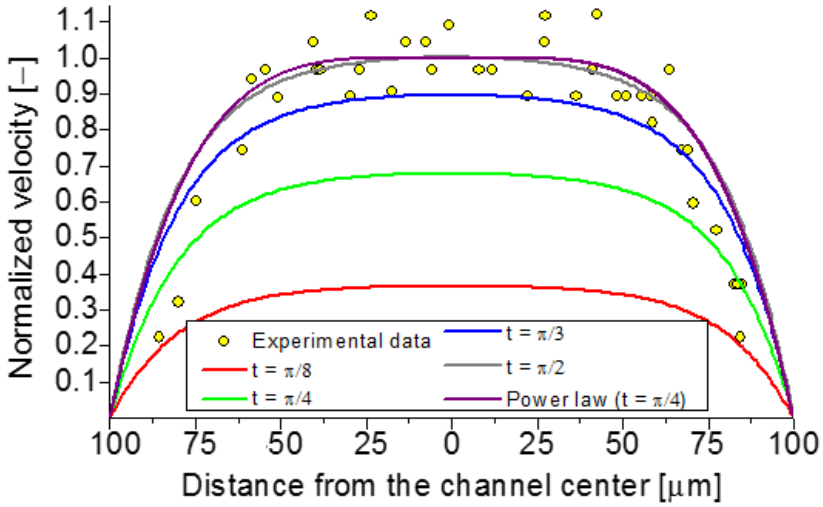


Fig. 4.18. Velocity flow field from finite element method simulations of the oscillatory flow. Yellow dots represent experimental data; the violet line signifies fit by higher order parabola; red, green, blue, and grey lines represent the results of numerical simulations obtained for different time steps.

Experimental data were obtained by calculating the velocity of individual hydrogel debris located at a given distance from the microchannel wall, where 0 and 100 μm denote the microchannel centreline and wall, respectively. They were fitted with a higher order parabola, which offered an easy way to evaluate the local velocity at each position inside the microchannel:

$$V(x,t) = V_{max}\left[1 - \left|\left(\frac{x}{0.5W}\right)^{4.5}\right|\right]\sin(\omega t) \qquad (37)$$

Since the velocity profile in a rectangular geometry is blunted compared to the parabolic distribution in a circular cross-section, shear rates in the centre of rectangular microchannels are expected to be smaller than those in circular tubes (comp. Fig. 4.19).

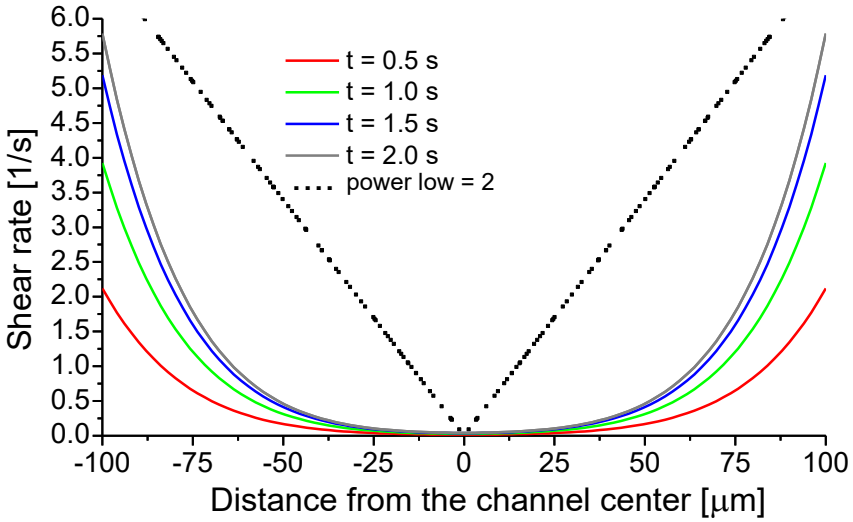


Fig. 4.19. The shear rate distribution across the rectangular microchannel was calculated in a few stages of the oscillatory cycle and compared with theoretical values for parabolic flow profile (dots).

Our computational analysis of the velocity profile inside a rectangular geometry revealed that its plug-like shape in the *x*-*y* dimensions is purely defined by the microchannel aspect ratio. Such a blunted distribution is very similar to the velocity profile typically found in large arteries or arterial tree networks [121].

The observation of hydrogel nanofilaments under the influence of an oscillatory flow helps us understand how this type of flow affects the conformation of elongated objects [122]. For this purpose, we followed the filaments' motion and evaluated the changes in their shape based on time. The behaviour of the nanofilaments during the oscillatory flow helped us select two groups: bent-like filaments and U-shaped filaments. They are represented by different ratios between contour length and diameter ($\underline{L} = L/d$). Long chain nanofilaments ($\underline{L}$ = 500 bent-like) change their shape continuously between uncoiled (bent) and coiled conformations (Fig. 4.20 (a)). The chain coiling always takes place during the first half of the oscillatory cycle. The chain returns to its original uncoiled configuration when the direction of the flow reverses in the second half of the cycle (Fig. 4.20 (b)). These changes in nanofilament shape are not related to any sudden motility changes such as rotation or tumbling. Overall, the degree of chain entanglement progresses with an increasing number of oscillatory cycles over time. At each consecutive forward flow (at $n\pi$, where $n$ = 2, 4, 6, etc.) and reverse flow (at $n\pi$, where $n$ = 1, 3, 5, etc.), the nanofilaments become more compressed.

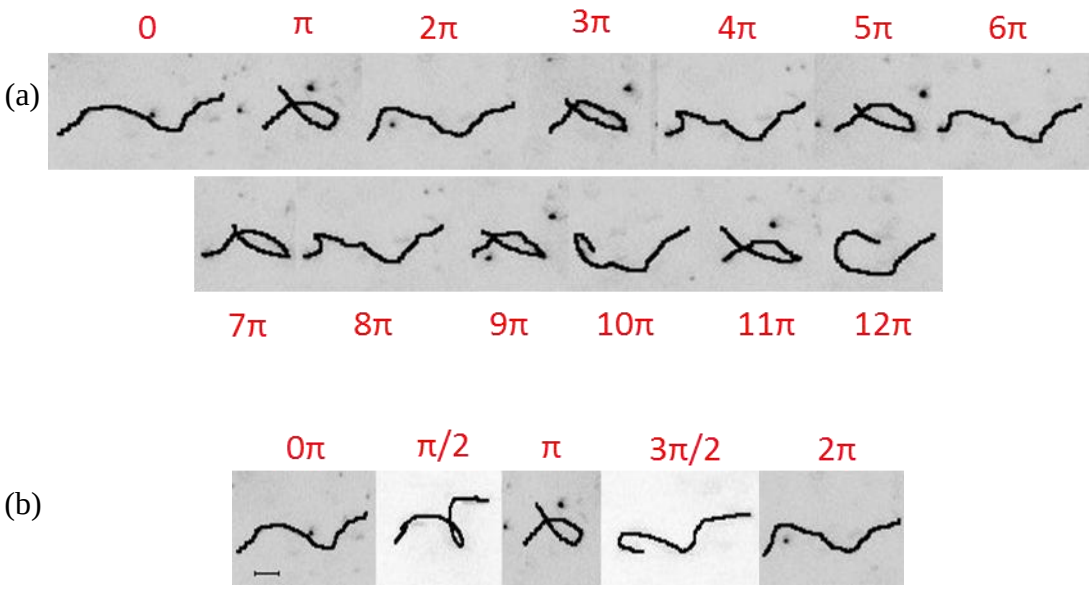


Fig. 4.20. Characteristic bent-like configurations of long hydrogel nanofilaments (L = 500) at different time points over the course of an experiment (a) and during one oscillatory cycle (b).

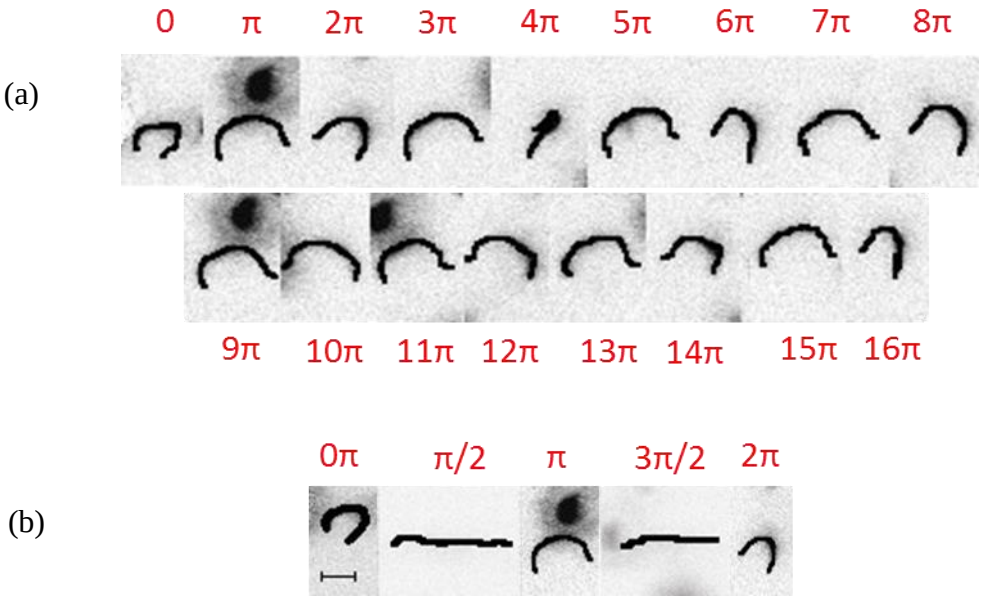


Fig. 4.21. Characteristic U-shaped configurations of short hydrogel nanofilaments (L = 250) at different time points over the course of an experiment (a) and during one oscillatory cycle (b).

Within the limit of short chains (L = 250), hydrogel nanofilaments originally show a U-shaped contour (Fig. 4.21 (a)).

In each oscillatory cycle, we can find two distinct phases which reach the chain: (i) a straightening period, and then the rotation within x-y planes that results in bending in the other direction (at nπ, where n = 1, 3, 5, etc.); (ii) a reverse straightening and rotation period, when the chain goes back to its original conformation (at nπ, where n = 2, 4, 6,

etc.). Over time, at each forward and reverse cycle, the chain straightens slightly with respect to its original configuration (Fig. 4.21 (b)). Consequently, they behave as flexible polymer chains (e.g. DNA), while U-shaped filaments behave as semiflexible objects (e.g. actin) [51, 63, 123, 124].

### 4.6.5 Characteristic parameters of nanofilaments in a flow

Relative extensional (Hookean) stiffness K ~ 120 and relative flexural stiffness A ~ 70 are typical values characterizing hydrogel nanofilaments of high slenderness $\underline{L}$ (Table 4.4). This means that such objects (in our experimental conditions) are characterized by low extensibility and very high bending flexibility. At the same time, the capability of nanofilaments to undergo thermal fluctuations is determined by a very limited bending stiffness of $\kappa = 4 \cdot 10^{-26}\ Nm^2$ and short persistence length ($< 10\ \mu m$). We find that the mechanical properties of nanofilaments with a contour length of less than 40 μm and $\underline{L}$ ~ 250 are similar (Table 4.4). To compare them with elongated biological molecules, the same table also includes some basic parameters from literature data for actin [90] and short DNA [125]. For the evaluation of *A* and *K* as non-dimensional mechanical characteristics for actin and DNA biomolecules, the corresponding values were scaled to our experimental parameters, i.e. the channel width ($200\ \mu m$) and flow velocity ($100\ \mu m/s$).

Table 4.4. Comparison of the mechanical properties of highly deformable hydrogel nanofilaments, (semi)flexible actin filaments, and DNA molecules.

| | **Hydrogel nanofilaments** | | **Actin**[90] | **(λ) DNA**[125] |
|---|---|---|---|---|
| | **$\underline{L}$ ~ 500** | **$\underline{L}$ ~ 250** | **$\underline{L}$ ~ $7 \cdot 10^3$** | **$\underline{L}$ ~ $10^4$** |
| *d* | 109 – 165 nm | 105 – 181 nm | 7 nm | 2 nm |
| *L* | 40 – 83 μm | 26 – 41 μm | < 50 μm | ~ 20 μm |
| *E* | 2 kPa | 2 kPa | 2.6 GPa | 0.3 – 1 GPa |
| $L_p$ | 3 – 18 μm | 3 – 25 μm | 17 μm | 50 nm |
| $\kappa$ | $1 \cdot 10^{-26} – 7 \cdot 10^{-26}$ Nm$^2$ | $1 \cdot 10^{-26} – 10 \cdot 10^{-26}$ Nm$^2$ | $7 \cdot 10^{-26}$ Nm$^2$ | $2 \cdot 10^{-28}$ Nm$^2$ |
| $L_p/L$ | 0.08 – 0.22 | 0.09 – 0.79 | 0.34 | $2.5 \cdot 10^{-3}$ |
| *A* | 13 – 124 | 35 – 161 | $7 \cdot 10^5$ | $9 \cdot 10^4$ |
| *K* | 16 – 343 | 33 – 369 | $6 \cdot 10^3$ | 95 |

Our hydrogel nanofilaments have a very high water content (~ 90%) Therefore, they should be treated as highly flexible and inextensible objects ($L_p / L << 1$). In our flow experiment we analysed their shape deformations. The shape deformations observed seem to mimic the behaviour of long biopolymers (e.g. actin filaments and DNA chains). It can be seen, however, that both the extensional stiffness *K* and the relative flexural

stiffness *A* of hydrogel filaments are much lesser than those of biomolecules (Table 4.4). This indicates an extraordinary deformability of such objects when compared with biopolymers, and – in a similar flow configuration – the expected deformations of DNA and actin filaments would be much smaller.

On the basis of the data showing the similarity of bent-like and U-shaped nanofilaments characterized by a similar diameter and Young modulus, it can be stated that their shape deformations are determined mainly by their length. Additionally, it was found that the Peclet numbers *Pe* of all the investigated configurations showed relatively high values. The approximate values of the Peclet number for bent-like (7000), U-shaped stretched (800), and U-shaped buckled (1600) nanofilaments are shown in Table 4.5. This indicates that the effects of nanofilament translational thermal fluctuations are small compared to hydrodynamic forces. Only during relatively short stop-flow time intervals, when flow reversal takes place, is there a possibility for thermal fluctuations to dominate flow-induced filament deformations, while slight stochastic displacements of their position may occur [126].

At the same time, similar persistence length and bending stiffness of hydrogel nanofilaments rule out the influence of different mechanical properties on the chain shape. This is demonstrated by the great differences in the Sperm number (*Sp*) [119], which has an approximate value of 160 for the bent filaments versus 9 and 6 for U-shaped stretched and U-shaped buckled filaments, respectively. These data may suggest that the viscosity-induced strain plays a dominant role in nanofilament conformations.

Table 4.5. Comparison of the nondimensional numbers for electrospun hydrogel nanofilaments, the bead-spring model of flexible polymers, and biodegradable polymers used in early experiments by Sadlej et al. [51].

| | **Hydrogel nanofilaments** | | | **Bead-spring model[17-19] ($\underline{L}$ = 20)** | **Polymer fibres[51]** | |
|---|---|---|---|---|---|---|
| | **Bent-like ($\underline{L}$ ~ 500)** | **U-shaped buckled ($\underline{L}$ ~ 200)** | **U-shaped stretched ($\underline{L}$ ~ 250)** | | **PCL ($\underline{L}$ ~ 50)** | **PLLA ($\underline{L}$ ~ 50)** |
| *Sp* | 16 – 674 | 3 – 10 | 1 – 20 | $2.4\ 10^3$ | $3 \cdot 10^{-8}$ | $2 \cdot 10^{-8}$ |
| *Pe* | 2080 – 23056 | 1498 – 1844 | 485 – 1240 | - | 22 | 22 |
| *K* | 16 – 343 | 33 – 114 | 77 – 369 | 10 | $2 \cdot 10^{7}$ | $5 \cdot 10^{7}$ |
| *A* | 13 – 124 | 35 – 54 | 62 – 161 | 0.5 | $7 \cdot 10^{7}$ | $2 \cdot 10^{8}$ |
| $U_r$ | $5 \cdot 10^{-6} – 1 \cdot 10^{-3}$ | $2 \cdot 10^{-5} – 1 \cdot 10^{-3}$ | $7 \cdot 10^{-5} – 2 \cdot 10^{-3}$ | $5 \cdot 10^{-4}$ * | - | - |
| $U_s$ | 0.7 – 1 | 0.93 – 0.96 | 0.82 – 0.99 | 0.999 * | - | - |

* mean value for initial fibre position $\underline{x} = 0.6$. [51]

In the presence of the oscillatory flow, hydrogel nanofilament thermal bending fluctuations are very small ($Pe$ >>1). Filament conformations are subjected to some periodic coiling/uncoiling or rotations, depending on their length. At a high Peclet number, the bending of an elastic chain is promoted by hydrodynamic forces. Therefore, the bending probability is expected to be higher for chains of polymers with very high flexibility. The Sperm number *(Sp)* controls the threshold of the flow-induced flexible bending. Filaments with high *Sp* values [117, 127, 128] are easily deformed by the flow. Consistently, U-shaped nanofilaments feature a 17- to 27-times lower Sperm number than bent-like nanofilaments (Table 4.5). The coiling/uncoiling conformations of bent-like nanofilaments are assisted by the compression of length during each next oscillatory cycle. In U-shaped nanofilaments, low values of *Sp* indicate that their conformation is more rigid. This is also visible in a greater $L_p/L$ ratio.

The stretching and coiling of longer nanofilaments resemble the DNA chain flexibility [63, 129]. Such flexibility is believed to be crucial in the formation of gene regulatory complexes [130] and in the transport of macromolecules through nuclear pores [131]. Nanofilament elastic mechanical properties are more similar to those of semiflexible actin filaments than DNA chains (Table 4.4), but hydrogel nanofilaments can mimic the behaviour of both types of biopolymers in response to hydrodynamic forces.

The worm-like chain (WLC) model is commonly used to describe the elastic properties of inextensible and flexible chains of biopolymer [48]. The hydrodynamic interactions of long polymer chains are evaluated mostly on the basis of the WLC bead-spring chain models [50, 51, 53, 59, 132]. Two already-mentioned model parameters, i.e. relative extensional stiffness ($K$) and relative flexural stiffness ($A$), are useful for the characterization of the polymer chain mechanical properties in response to the shear stresses of a viscous flow. In Table 4.5, these model parameters for hydrogel nanofilaments are presented and compared with those for the fibres produced from elastomeric polymers (polycaprolactone (PCL) and polylactic acid (PLLA)), which were used in the experiment of Sadlej et al. [51]. Due to their very low bending probability (low Sp values), low extensibility, and bending deformability (high $K$ and $A$ values), their dynamics may show a lack of compliance with the predictions of the WLC model applied there [51] (comp. with bead-spring model in Table 4.5).

### 4.6.6 Elongation and bending analysis

The analysis of the degree of buckling (BU) and degree of elongations (EL) parameters confirmed the division of hydrogel nanofilaments into two groups, while a more detailed

observation of migration direction and flow velocity made it possible to divide the U-shaped group of buckled filaments into two sub-groups.

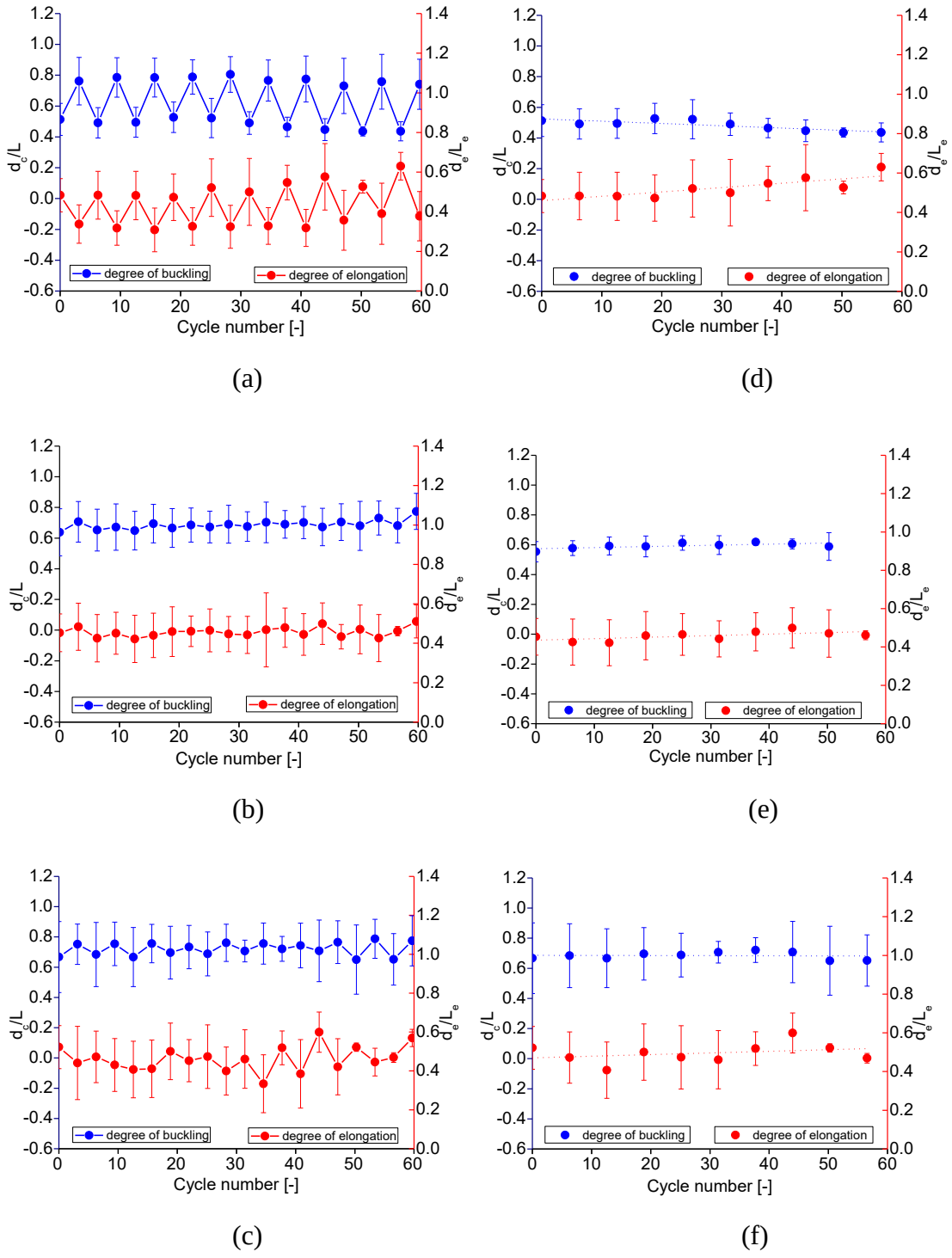


Fig. 4.22. Changes in the degree of buckling and elongation parameters for (a) bent-like filaments, (b) U-shaped stretched filaments, (c) U-shaped buckled filaments in each phase; (d, e, f) – in 2π phase. Left axis – BU, right axis – EL.

Examining the changes in BU and EL values over time (subsequent cycles) for these three classes of filaments (Fig. 4.22 (a), (c), (e)), the different characters of the waveforms were

visible. The first group, referred to as bent-like, is particularly distinguishable. The graphs of BU and EL variations show an approximately sinusoidal nature (Fig. 4.22 (a)). When comparing the graphs for bent-like filaments and U-shaped buckling filaments, it is important to note the differences in the parameter values between the two phases of flow oscillation (0 and π).

For bent-like filaments, the differences are around 0.2. For the filaments of the second group (Fig. 4.22 (c) and (d)), differences are halved. This can be explained by the shape changes in the first group of filaments over a single oscillatory cycle. For example, at 0 phase the filament is coiling (smallest value of $d_c/L$), but at π phase the same filament is uncoiling (increased value of $d_c/L$). Filaments from the second group (Fig. 4.22 (c), (d)) change their shape only slightly with the change of the cycle phase during the oscillatory flow. They mainly rotate or tumble. Consequently, $d_c/L$ and $d_e/L_e$ changes are smaller, and the waveforms of these changes are more regular.

When we look at the changes in the buckling parameter recorded in the same oscillatory phase (0), we can see how the shape of the filaments changes during the oscillatory flow. In the case of bent-like filaments, the $d_c/L$ values are continuously decreasing, i.e. oscillations cause a constantly increasing coiling up of the filament (Fig. 4.22 (b)). The same situation occurs in the π phase of oscillations for uncoiling filaments. In the U-shaped buckling group of filaments, there are two types of behaviour. In the first sub-group, changes recorded in the same phase of each cycle are small, but we see a tendency to increase the $d_c/L$ coiling parameter when the oscillatory time progresses (Fig. 4.22 (e)). The mean velocity value of these U-shaped stretched filaments (145 μm/s) determines their straightening (from U shape to C shape). U-shaped buckled filaments moving at a higher flow velocity (250 μm/s) are only conveyed by the fluid flow. Filament shapes do not significantly change during the oscillatory flow, and the graph of the changes in $d_c/L$ values recorded for each cycle at a phase equal to 0 is flat (Fig. 4.22 (f)).

Bent-like nanofilaments are characterized by an increased compression at each consecutive phase of forward (at $n\pi$, where $n$ = 2, 4, 6, etc.) and reverse (at $n\pi$, where $n$ = 1, 3, 5, etc.) flow cycles (Fig. 4.23 (a), (b)). If we look at the changes in the end-to-end parameters of bent-like filaments over full observation time, we can see that in this type of filaments there was a 2-fold decrease in this distance (Fig. 4.24 left). What is very interesting and worth noting is that – configuration-wise – hydrogel bent-like nanofilaments greatly resemble flexible polymer chains [63, 117, 123, 124]. Conversely, the U-shaped stretched nanofilaments are characterized by a slight straightening of the

chain with respect to its original configuration in each phase of the cycles (forward and reverse) (Fig. 4.23 (c), (d)). In this case, the end-to-end distance increased (Fig. 4.24 middle). In the U-shaped nanofilaments group, there was a chain population that did not change their elongation during the oscillatory flow (Fig. 4.23 (e), (f)). These nanofilaments, called U-shaped buckled, did not change their configuration during entire observation period (Fig. 4.24 right), and responded to the flow by preserving their bulk rotational movement [126]. This type of hydrogel nanofilaments is similar to semiflexible chains of polymers, such as actin filaments [64, 90, 123, 133].

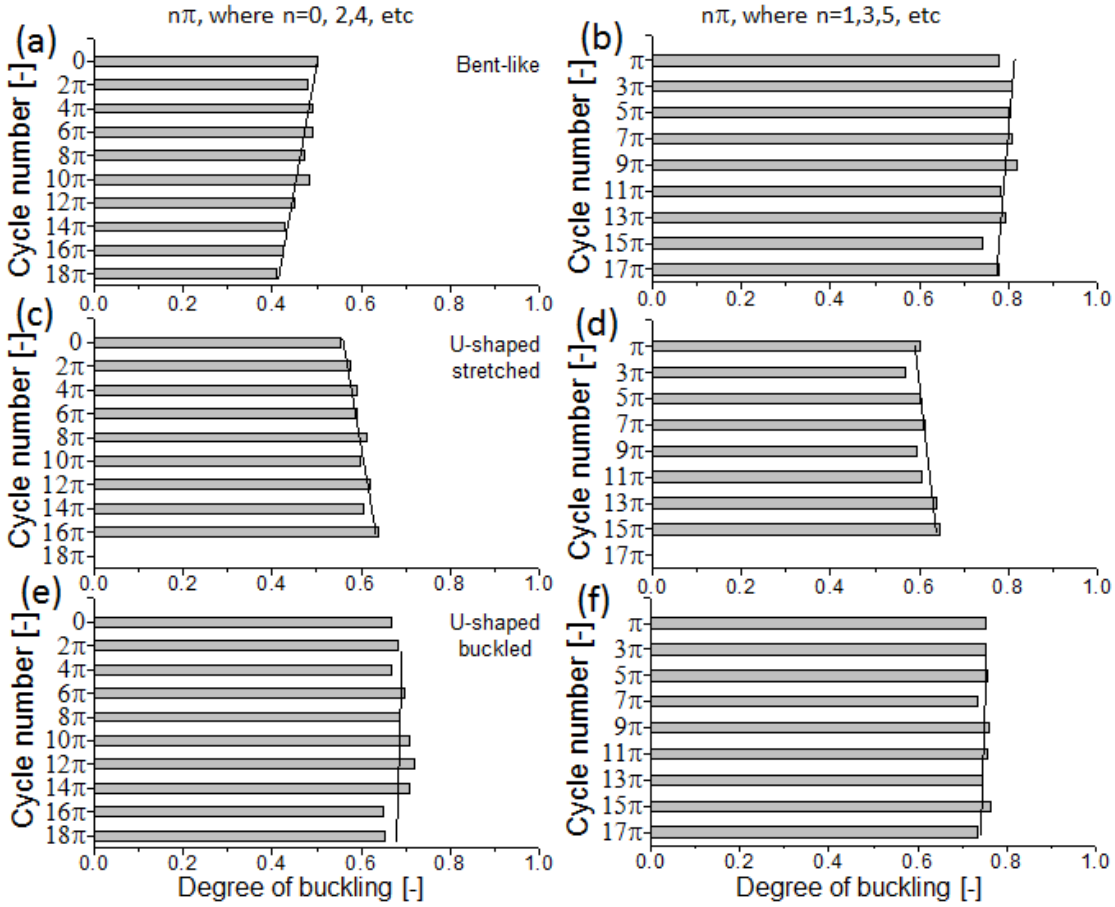


Fig. 4.23. Time-dependent changes in the degree of buckling for bent-like (a, b), U-shaped stretched (c, d) and U-shaped buckled (e, f) hydrogel nanofilaments at each individual forward (left column) and reverse (right column) oscillatory cycle. Nanofilaments were subjected to a maximum of 9-10 consecutive oscillatory runs. Solid lines mark the data trend.

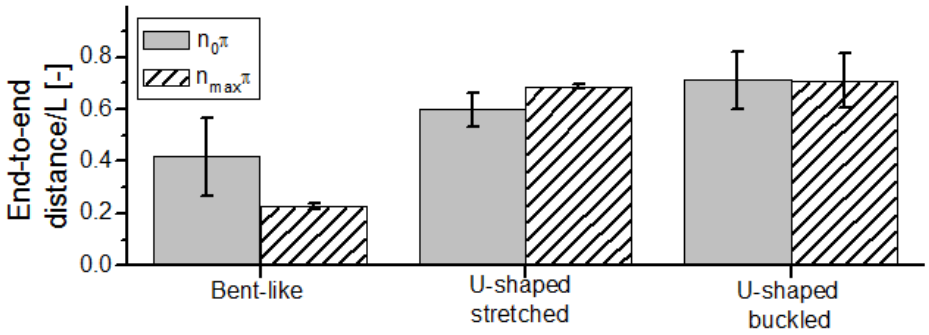


Fig. 4.24. Changes in the end-to-end contour length distribution for the three groups of hydrogel nanofilaments, before the application of a hydrodynamic force (*grey bars*) and after the final 10$^{th}$ oscillatory cycle (*dashed-patterned bars*).

### 4.6.7 Orientation – inclination angle

Differences in the behaviour of two types of filaments and between two groups of filaments classified as U-shaped were also observed when we analysed the change in the filament angle of inclination to the fluid flow in the direction of the x-axis. Fig. 4.25 (a) shows typical changes in the inclination angle of filaments from the bent-like filament group, characterized by coiling and uncoiling depending on the phase of the cycle. The values of the inclination angle corresponding to the same phase (0 or $\pi$) are clearly synchronized. In addition, the filaments in this group tend to be orientated along the flow. Fig. 4.25 (b) shows the typical behaviour of U-shaped buckling filaments. These filaments are characterized by a lower inclination angle values in each phase. Looking at the trend line set for both phases of the cycle we can see (especially in phase 0) that it is parallel to the flow axis. This means that despite the oscillatory flow, this subgroup of filaments do not change their relative orientation, oscillating around the flow axis. We concluded that such filaments, moving with a high average velocity (250 μm/s), are carried by the fluid, without large shape changes and with small changes in the inclination angle.

A different behaviour can be seen in the U-shaped stretched filaments (Fig. 4.25 (c)). Their change in inclination angle is highly stochastic. We were also able to see that the observed filament deviated from the flow axis during the flow time. The main cause for this behaviour is the velocity with which the filaments in this group move (145 μm/s); as we showed in Fig. 4.23 (e), there is a progressive straightening of filaments over time.

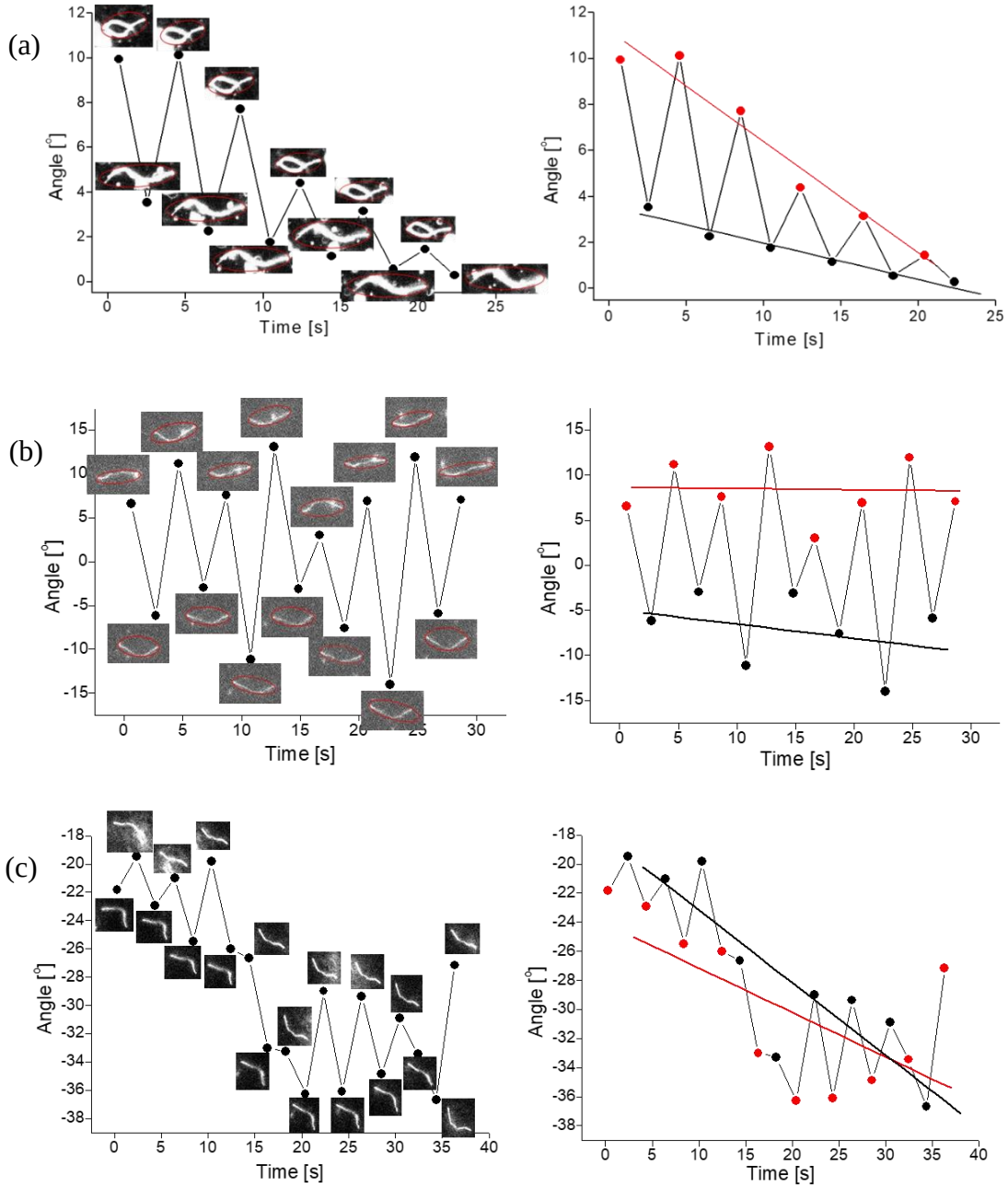


Fig. 4.25. Changes in the inclination angle over time during the oscillatory flow; representative examples for bent-like (a), U-shaped buckled (b), and U-shaped stretched nanofilaments (c).

During the experiment, the U-shaped stretched nanofilaments moved away from their alignment along the flow (Fig. 4.26, centre). At the same time, the orientation angle of the U-shaped buckled nanofilaments decreased over time (Fig. 4.26, right). The bent-like nanofilaments also aligned along the flow (Fig. 4.26, left), even though we applied a flow velocity lower than that of U-shaped buckled nanofilaments.

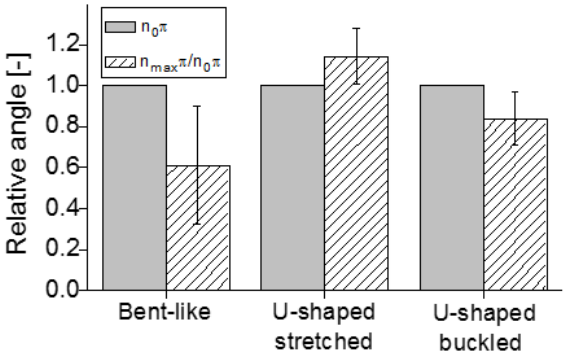


Fig. 4.26. Relative changes of the filament inclination angle after applying a flow: initial status (*grey bars*) and after the final oscillatory cycle (*dashed-patterned bars*). Data are normalized to the initial inclination angle.

Bent-like nanofilaments move to the regions where the value of the local shear rate is minimizing (channel centre). As the velocity of the oscillatory flow in the microchannel centre reaches its maximum value, it can help increase the chain alignment. In the case of U-shaped buckled nanofilaments, the higher flow velocity helps to align filaments, but at the same time it prevents their straightening. In short, a higher flow velocity contributes to increasing the polymer chain orientation along the direction of the flow, and directs the chains closer to the microchannel centre, in accordance with the predictions of the model by Sadlej et al. [51].

### 4.6.8 Lateral migration of highly deformable nanofilaments

Our analysis of the objects suspended in the oscillatory flow also indicates their migratory behaviour across the channel. In the case of elongated objects such as filaments, this behaviour is quite complex and depends on several factors. Initially, the distribution of filaments across the channel geometry was rather uniform (Fig. 4.27), and the typical depletion layer was only observed close to the wall.

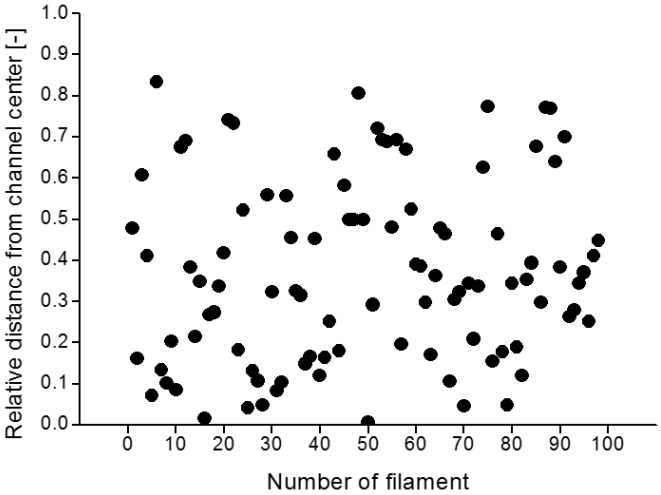


Fig. 4.27. Initial distribution of 100 experimental sequences of investigated nanofilaments across the whole plane of the microchannel.

One of the most important parameters affecting the lateral migration and diffusivity of long polymers is the filament conformation. For this reason, the distribution of the centre-of-mass position for bent and U-shaped hydrogels was observed over time; it was characterized as a change in the relative distance from the channel centre (x), where 0 and 1 denote the microchannel centreline and wall, respectively. The aim of this investigation was to evaluate how the contour length of a nanofilament and its shape determine the cross-flow migration inside the microchannel. Both bent-like and U-shaped nanofilaments show in-phase fluctuations of their centre-of-mass position along the applied flow direction (Fig. 4.28 (a)). When we analysed the slip velocity, we observed that – due to changes in the filament's orientation and shape – the variation of the slip velocity is outside of the oscillation flow phase (Fig. 4.28 (b)).

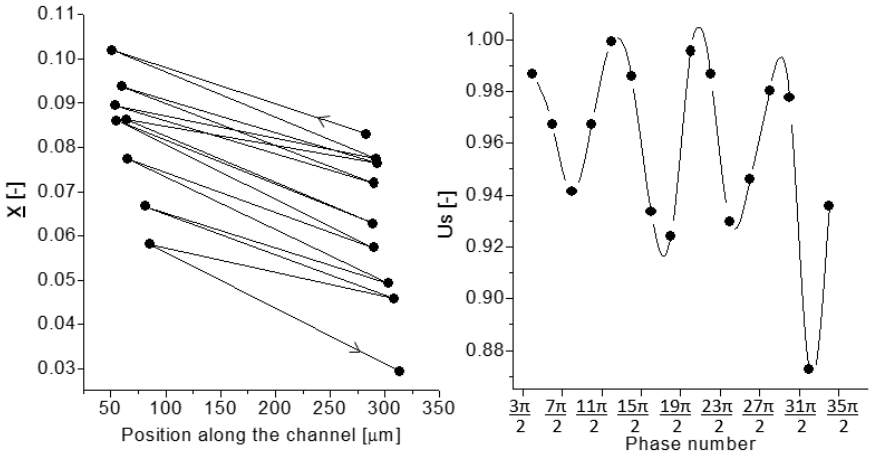


(a) (b)

Fig. 4.28. (a) Path of the cross-flow migration of nanofilament centre-of-mass position towards the axis of the microchannel in each phase of the oscillatory flow (nπ, n = 1,2,3...); (b) Relative longitudinal slip velocity $U_s$ of the nanofilament during each oscillating flow maximum (nπ/2, n = 1,3,5...).

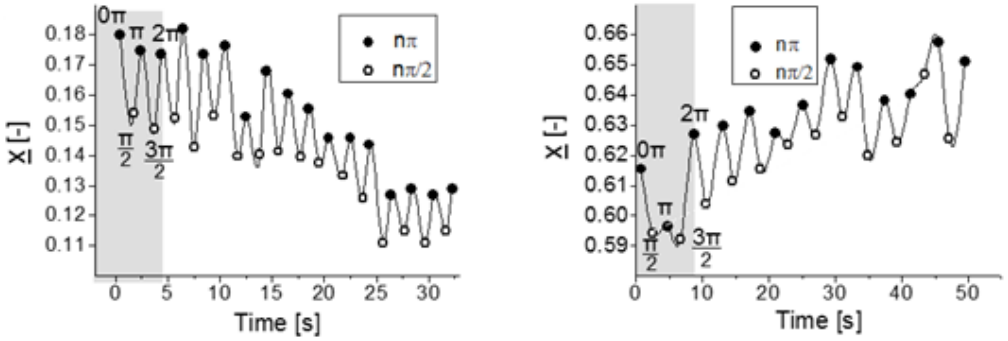


(a) (b)

Fig. 4.29. Trajectories of the centre-of-mass position of nanofilaments in the function of time: (a) towards the channel centre (*d = 105 nm, L = 41 μm, $V_{max}$ = 250 μm/s, $U_r$ = 0.85 $10^{-3}$*; (b) towards the wall (*d = 134 nm, L = 54 μm, $V_{max}$ = 132 μm/s, $U_r$ = 0.6 $10^{-3}$* .

Fig. 4.29 shows two examples of hydrogel nanofilament lateral migration trajectories. As shown in Fig. 4.27, the initial distribution of filaments across the width of the microchannel was roughly uniform. However, in order to provide comparable conditions for analysing how the flow affected on the behaviour of the filaments, most of the experimental data were collected in a central part of the channel at a relative distance from the channel centre of 0.6, where shear forces are relatively uniform and close to zero. Of course, the filaments closer to the wall were also analysed. Fig. 4.30 provides examples of graphs showing the cross-flow migration of the filaments observed near the microchannel wall, with an apparent net cross-flow migration of filaments from the wall.

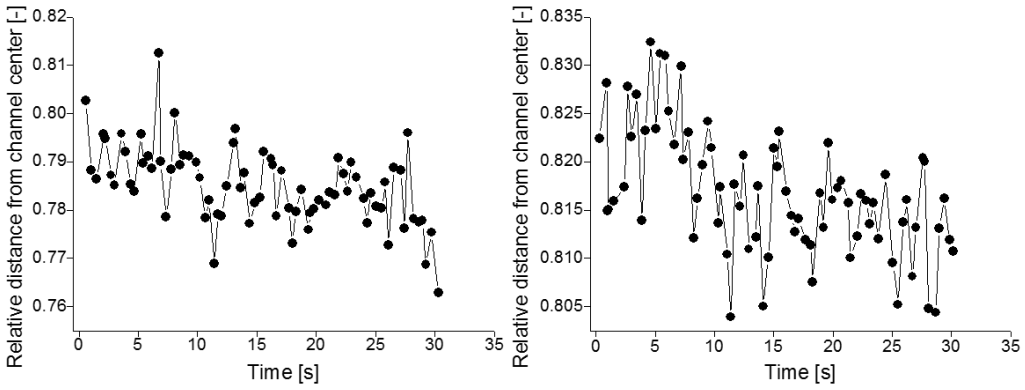


(a) (b)

Fig. 4.30. Lateral migration of nanofilaments conveyed by the oscillating flow, observed close to the microchannel wall. Dots indicate the position of the centre of mass recorded at zero flow velocity (nπ/2), (a) $d = 125$ nm, $L = 27$ μm, $V_{max} = 83$ μm/s, $U_r = 1.34\ 10^{-3}$; (b) $d = 114$ nm, $L = 30$ μm, $V_{max} = 75$ μm/s, $U_r = 0.4\ 10^{-3}$.

The initial distribution of nanofilaments observed across the width of the microchannel after introducing the flow is relatively uniform (Fig. 4.31, grey bars). Later on, in the presence of an oscillatory flow, the nanofilament distribution shifts (i) closer to the centreline of the microchannel in the case of bent nanofilaments, and (ii) further away for the U-shaped stretched nanofilaments (Fig. 4.31 (a), (b), black dotted lines). Both types of U-shaped nanofilaments had a relative migration velocity of similar magnitude. High flow velocity values contributed to the migration of filaments towards the centreline of the microchannel. Such behaviour was visible in the case of the U-shaped buckled nanofilaments (Fig. 4.31, (c)). For comparison, the low magnitude of the flow velocity contributed to the lateral migration towards the wall, as in the case of the U-shaped stretched nanofilaments (Fig. 4.31, (b)). Therefore, it can be inferred that the direction of

migration within the group of nanofilaments with a similar conformation is determined by the applied flow magnitude.

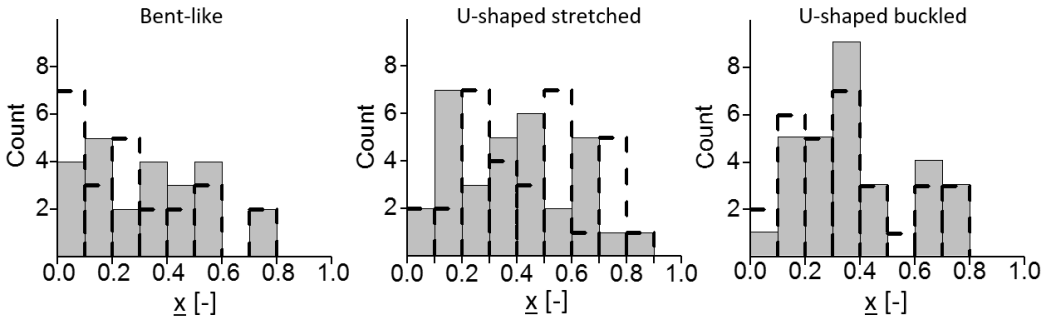


(a) (b) (c)

Fig. 4.31. The centre-of-mass distribution of hydrogel nanofilaments across the microchannel width $\underline{x}$ (0 and 1 denote the microchannel centreline and wall, respectively), before the application of the oscillating hydrodynamic force (*grey bars*), and after over 40 oscillatory cycles (*dashed-contour bars*).

The relative velocity of this migration, however, seems to be marginally dependent on the magnitude of the oscillating flow applied. The same goes for the "slip velocity", the velocity of the filament related to the local flow velocity: for all the configurations analysed, it appeared to be very similar (Fig. 4.32).


Fig. 4.32. The relative slip velocity $U_s$ of three different types of hydrogel nanofilaments.

The tendency of the chain to equilibrate its conformation in the presence of hydrodynamic forces determines the cross-flow migration. In the case of hydrogel nanofilaments, this depends both on the magnitude of the flow applied and on the initial shape. Bent-like nanofilaments are characterized by a cross-flow migration towards the microchannel centreline (Fig. 4.31 (a)). In this region, local shear rates are minimized and the chain conformations are not influenced by any additional deformations. In the case of migration towards the wall, this behaviour may induce the stretching of bent-like nanofilaments, owing to the increasing shear rate. It is also interesting that, in the case of U-shaped stretched nanofilaments, the same flow value velocity caused that migration in the

opposite direction (towards the wall) (Fig. 4.31 (b)). When filaments migrate towards higher gradients, the alignment of the U-shaped stretched nanofilaments is not induced and filaments are tilted with respect to the flow direction. As de Pablo et al. suggested [134], in the case of limited by the wall geometry and at the high values of shear rates which are typical for DNA experiments, migration towards the wall can be weak. The reason for this is that the hydrodynamic migration effects of the two walls are cancelled, and also because the chain, which is stretched in the flow direction, is actually compacted in the wall-normal direction, making it possible for its mass centre to come closer to the wall. Therefore, it seems necessary to conduct some additional studies to obtain further details on: (i) the complex interactions induced by the shear stress of the oscillatory flow, (ii) filament deformability as a result of the flow, (iii) their Brownian diffusivity, and (iv) filaments' tendency to cross-flow migrate.

# Chapter 5: The biomedical applications and prospects of nanoparticles

## 5.1 Biomedical application of nanoobjects

### 5.1.1 Spherical particles biomedical applications

In recent years, the development of medicine and biology research has relied more and more on the development of nanotechnologies. Polymer-based micro- and nanoparticles have been the subject of intense research and development in the pharmaceutical sector in recent decades [135, 136].

Nanomedicine is defined as the application of nanotechnologies in medicine; it includes targeted drug delivery, diagnostics, biosensing, and imaging [135, 137, 138]. Thanks to the application of nanotechnologies, new achievements have become possible [139]:

1) improved delivery of poorly water-soluble drugs;
2) targeted delivery of drugs in a cell- or tissue-specific manner;
3) drug transcytosis through tight endothelial and epithelial barriers;
4) delivery of large macromolecular drugs to intracellular action sites;
5) simultaneous delivery of two or more drugs, as well as different treatments for combination therapy;
6) visualization of drug delivery sites by combining imaging modalities with agents of therapeutic;
7) real-time monitoring of the in vivo efficacy of a therapeutic agent.

Currently, nanotechnology products approved for clinical use are relatively simple. As a whole, there is a lack of active targeting and triggered drug release components. Despite numerous studies, this technology has still not achieved a significant clinical impact on human health. The reason for this is complex and depends on the type of application [139]. Undoubtedly, the development of nanomedicine is an important factor in the search for new applications of nanotechnologies [135].

Nowadays nanoparticles are widely used in medicine as agents of therapeutic drug delivery. They have the ability to target specific areas, such as inflammation sites or tumours. The small size of the particles makes it possible for them to be delivered at the systemic level and transported along the cardiovascular system through the blood flow. This gives them the potential to reach any tissue and organ in the body [140].

The use of nanoparticles in a targeted drug delivery system could definitely increase treatment efficacy and prevent systemic toxicity [139]. It is necessary to know the

pharmacodynamics of nanoparticles in the circulatory system, and also how nanoparticles at the molecular level interact temporally with the targeted tissues, before nanoparticle drug carriers can be directed to living organisms (like animals or humans) [137]. For this purpose, the colloidal particles characterized by a nanometre size range, made primarily of lipids, metals, or polymers, should be used with their associated therapeutics.

Nanoparticles can be designed to provide for the site-specific delivery of drugs, as soon as they are injected into the lymphatic or general circulatory system. Crucial factors in targeting are the surface and size of particles. In order to enhance the specific recognition of the biological target, the surface of particles can be joined to ligand molecules and antibodies [140]. The cell-specific ligand attachment can be useful to increase their selectivity [141].

There are several reasons why drug delivery systems have a definite future as pharmaceuticals. One of them is the passive-targeting effect. This effect is related to the possibility of increasing the drug amount delivered to the disease site (e.g. tumours, inflammation, and infection). Another important aspect is the improvement of the therapeutic index of already-established drugs, thus preventing some of the high risks associated with the development of new pharmaceuticals [142]. Particles for pharmaceutical purposes have to meet authority regulations, especially those relating to safety concerns [137].

In recent years, many expectations have been placed on colloidal carriers because of their potential use as vectors for diagnostics and therapeutics in cancer treatment [19, 140, 141]. The medical procedures which use nanocarriers are considered promising for avoiding the side effects associated with traditional cancer treatments [143]. Particle delivery systems for targeting cancer therapeutics to solid tumours can be used thanks to their ability to avoid the phagocytic clearance through the reticuloendothelial system. The assumption of such systems is that the drug is delivered exclusively within the tumour, while the accumulation of the drug in healthy organs is greatly reduced. Consequently, the relative efficacy and safety of a cancer treatment may increase when using delivery systems [144]. More information about application of nanoparticle as a drug delivery systems is present in Appendix 7.

It is worthwhile to remember that drug delivery systems do not normally cross the blood-brain barrier, even though in some pathological states a limited penetration may occur. In such cases, the application of delivery systems to the central nervous system is usually limited to the intracerebral or intraspinal administration [145]. Nanomedicines can

interact hydrodynamically with neighbouring cell membranes after their injection into the blood flow [146]. The basic feature of such nanoparticles for medical benefit should be their ability to cross through the blood vessel barrier [147].

Surface-targeted nanoparticles have also been applied to the monitoring of gene expression following gene therapy. Very small superparamagnetic nanoparticles have demonstrated to be useful for mapping the topography and monitoring the transfected gene expression level [148]. It has also been proposed to use such particles as specific markers of the fate of transplanted cells [136]. Non-viral vectors based on nanoparticles have been developed for use in human gene therapy [135]. As an alternative non-viral delivery system for plasmid DNA, chitosan has been proposed. It has been found that selective chitosan polymers and chitosan oligomers effectively condense plasmid DNA and transfect several different cell types in vitro [149].

### 5.1.2 Biomedical applications of polymeric fibres

Spherical nanoparticles are not the only nanoscale objects commonly used for biomedical applications. Currently, the interest of researchers is focused on polymer fibres. In the case of these elongated micro- and nanoobjects, research is focused on three main issues [150, 151]:

1) drug delivery systems;
2) scaffolds for tissue engineering;
3) immobilization of enzymes for faster reaction rates in biological reactions.

In contrast to spherical particles, fibres have many more biomedical applications, not only as drug delivery systems, but also as scaffolds and dressings, as will be described in more detail later in this chapter. For example, fibres of an elongated shape, while having a diameter comparable to that of spherical objects, have a larger surface area and bulk that can carry large doses of drugs.

One of the most popular fabrication techniques of fibres for biomedical application is electrospinning. This is one of the most effective methods for manufacturing tissue scaffolds, making it possible to produce a nonwoven mesh with micron- and nanofibers [152, 153]. Such scaffolds ensure support for cells to regenerate a new cellular matrix after the original one has been damaged by injury, disease, or congenital defect. These mats are highly porous and behave like the extracellular matrix in the body [150]. The nanofibres used for scaffolding must be characterized by: high porosity, large surface area, uniform dimension, structural integrity with tissue, biocompatibility, biodegradability, appropriate mechanical properties, and nontoxicity for cells [151].

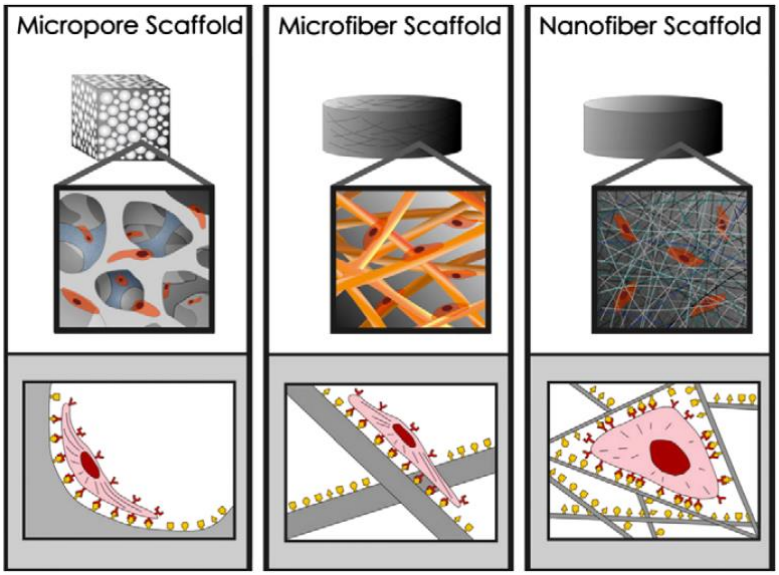


Fig. 5.1. Scaffold architecture built by microspore structures and micro- and nanofibres [154].

The four most important types of scaffolds for tissue engineering include tissue scaffolds for cartilage, bone tissue, nerves, and artificial blood vessels. Cellular scaffolding based on structured scaffolds is one of the most effective ways to repair damaged cartilage tissue [155].

A major concern was that of being able to deliver drugs or other pharmaceutical agents to patients in the most physiologically acceptable manner.

In this thesis I focus on application of polymeric fibres as a drug delivery system. Descriptions of another biomedical applications of such objects are present in Appendix 7. A very important principle for the use of polymer nanofibres for drug delivery is that drug particulate dissolution rates increase when the drug concentration and corresponding carrier surface area are increased. Polymer nanofibres for controlled drug delivery are characterized by several advantages, such as, for example, large surface area to volume ratio [156]. The possibility of delivering topical drugs opens up a number of application opportunities. The potential advantages of this delivery method include the possibility of doing so in a targeted manner, thus reducing the total drug dose and, consequently, its toxicity for non-target sites, also preventing the need for other systemic treatments, such as oral administration [157]. In drug delivery systems for biomedical application, the electrospun fibres help encapsulate the therapeutic agent [158]. To be properly controlled, drug release is usually dependent on such parameters as porosity, surface area, and degradation of polymer fibres. In the case of high-porosity fibres, their

surface area is much larger, which is beneficial for drug release, as the number of drug-binding sites is greater [151].

Drug release methods use biodegradable or non-degradable materials. These materials, which are characterized by specific features obtained by tissue engineering, release numerous drugs in a controlled way, including: antibiotics [159, 160], anticancer drugs [161], proteins [162, 163], and DNA [162, 164]. It would be desirable to succeed in designing a drug delivery device capable of releasing the desired agent in a controlled way, but that would be difficult when the material begins degrading at the time of drug release. In a biodegradable system, the drug can be released by diffusion or the material degradation. In some cases, this last method leads to dose dumping, causing drug concentrations to reach toxic levels locally. That's why it is crucial to tailor the release rate and degradation rate (if using degradable materials) [165].

In addition to the standard electrospinning method of nanofibre fabrication for biomedical applications, to encapsulate drugs or biological active substances in polymer nanofibres, an alternative is coaxial electrospinning. As mentioned in Chapter 1, this enables the formation of two-component core-shell fibres [27, 166, 167]. One of the best advantages of this technique is the effective protection of the biological agents which are easily denatured, and the potential to close all substances within the core, regardless of polymer-drug interactions. Thanks to this behaviour it is possible to incorporate drugs, proteins, and even genes into nanofibres, by dissolving them in the core solutions [159].

In this study we focus on the possibility to use electrospun core-shell nanofibres and hydrogel nanofilaments as a drug delivery system. The first preliminary studies on this topic are discussed below.

## 5.2 Experimental analysis of the possible use of hydrogel nanofilaments as controlled drug release systems

Hydrogel nanofilaments are ideal materials for biomedical use, thanks to their material properties (no toxicity, their physical properties being close to those of living tissues) and shape parameters. Their small size, large surface area, and high flexibility make them ideal for use both as vehicles to carry drugs to specific places in the body, and as systems for the controlled release of drugs. For this reason, we have conducted a series of experiments which have confirmed the possibility to use hydrogel nanofilaments as systems for the controlled release of drugs.

### 5.2.1 Samples preparation

For a protein release study, we analysed six samples of PNIPAAm (EN1–EN3): three samples of hydrogel nanofilaments, and three samples of mats obtained using core-shell nanofibres (with hydrogel core). Each of them contained 7 mg/ml BSA-FITC (Bovine Serum Albumin conjugated with fluorescein) as indicators of the drug release process [168]. Results were then compared with the material of core-shell nanofibres without hydrogel in their core structure. For testing one type of hydrogel nanofilaments, the 3 $cm^2$ piece of nanofibre mat was weighed to determine its BSA-FITC content. Then, to extract the nanofilaments, the polymer shell of fibres was dissolved in 1 ml of DMF. The nanofilament solution was diluted with 2.5 ml deionised water. After vigorously shaking the vial, we transferred three samples of 1 ml each into plastic vials. For the first sample ($1^{st}$ vial) we waited 1 hour for the BSA-FITC release from nanofilaments (in an incubator with a 37$^o$C temperature), and then we centrifuged the sample for 10 minutes at 10,000 rpm. This process was necessary to separate the nanofilaments from the supernatant. We then transferred this liquid to clean plastic vials. This procedure was applied to the next two samples (in two other vials) after 6 and 24 hours from release, respectively.

To study the release from the nanofibre mat, we used 1 $cm^2$ of core-shell nanofibre material, weighed it, immersed it in 1 ml of deionised water, and incubated it at 37°C. After 1, 6, and 24 hours the supernatant fluid was replaced by fresh water.

Fluorescein conjugated with BSA served as a marker to determine the concentration of the released factor. To measure the fluorescent intensity by a fluorimeter (Fluoroskan AscentTM Microplate Fluorometer, Thermo Scientific, USA), 300 μl of each collected supernatant were placed in a 96-well microplate. The calibration curve which had been prepared earlier was used to calculate the concentration of the protein released. Additionally, we employed the Fluorescence Recovery After Photobleaching (FRAP) method, using a Leica TCS SP5 microscope, to evaluate the diffusion coefficient of BSA-FITC in EN1 hydrogel (37°C).

### 5.2.2 Results and discussion

The following two charts show the results for the release kinetics of BSA-FITC from (i) the hydrogel material trapped in the core of nanofibres (Fig. 5.2) and (ii) from the nanofilaments extracted (Fig. 5.3). We compared them with the results obtained for simple nanofibre materials with BSA-FITC. Such materials had been previously used for the drug release modelling by Nakielski et al. [169]. There was a substantial increase in the proteins released from the nanofilaments still trapped in the core of the nanofibre mat,

compared to the proteins released from nanofilaments alone. The reason for this result is probably that the shell polymer precipitates after the addition of water to dissolved materials and after nanofilament absorption, thus preventing the access to the fluid.

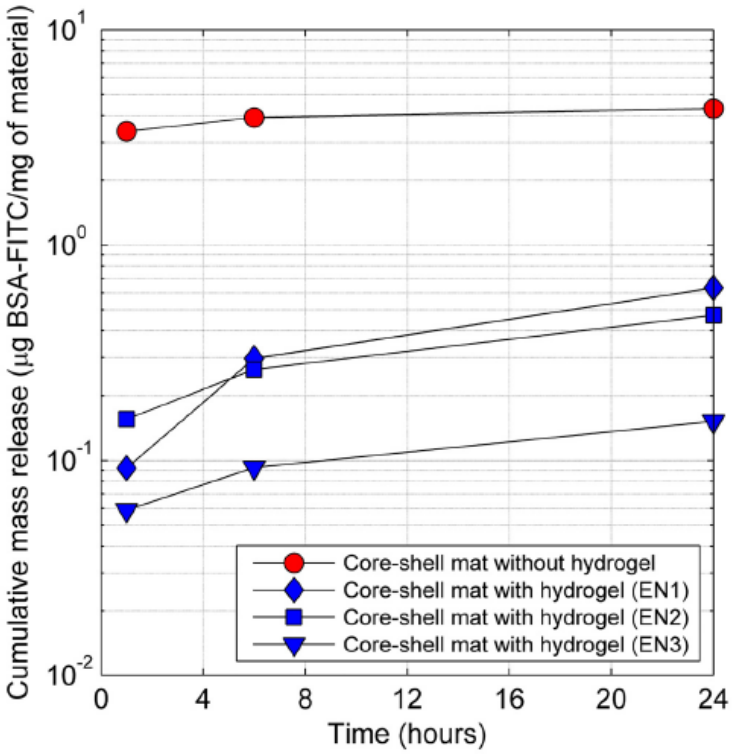


Fig. 5.2. Cumulative release of BSA-FITC from: core-shell mat with NIPA hydrogel in the core (EN1-EN3), and core-shell mat with protein water solution in the core (without hydrogel). For a better visibility of results, the y-axis is in a logarithmic scale. Standard deviation was less than 5%.

After 24 hours, we observed an almost seven-times-lower protein release profile from the material with PNIPAAm hydrogel in the core (EN1) than in the case of the material without hydrogel in the core structure. Similar results were observed by Nakielski et al. [29, 169].

When we look at the characterization of the protein release kinetics for different compositions of materials (Fig. 5.2), we see the lowest release for nanofibre mats with the highest degree of hydrogel crosslinking (EN3), and the highest release for the lowest degree of the hydrogel crosslinking (EN1) after 24 hours. When nanofilaments were extracted from core-shell nanofibres after 24 hours, the release rate for EN1 nanofilaments was the highest (Fig. 5.3).

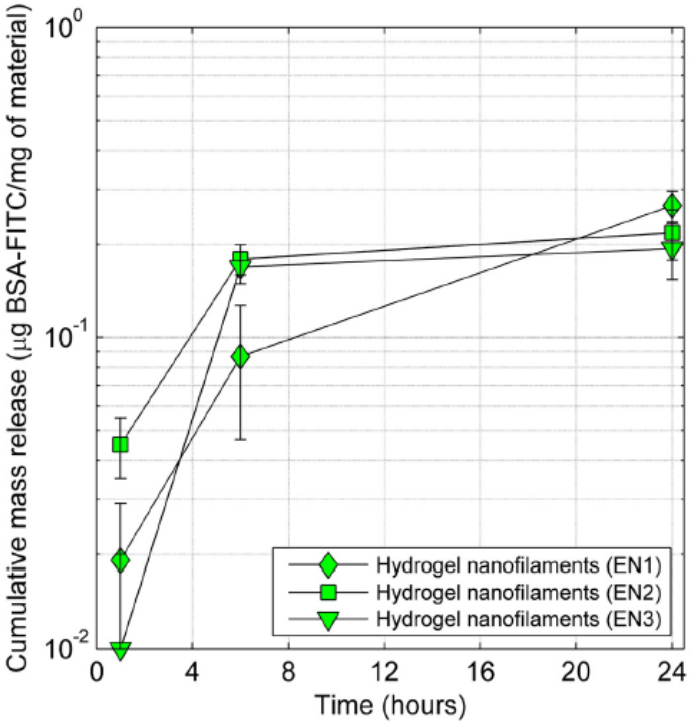


Fig. 5.3. BSA-FITC cumulative release from three different compositions of hydrogel nanofilaments. The y-axis is in a logarithmic scale.

The absence of hydrogel in the core led to a burst release, probably caused by a protein solution leakage through some nano ruptures in the nanofibre shell. It should be remembered that the BSA-FITC diffusion coefficient in hydrogel EN1 ($D_{BSA\text{-}FITC}$ = 7.3 ± 3.7 $\mu m^2/s$) is three orders of magnitude smaller than its diffusion coefficient in water [170]. For that reason, we can observe a significantly prolonged release from the hydrogel.

We demonstrated the possibility to use core-shell nanofibres with hydrogel filaments and hydrogel nanofilaments as a drug delivery system. Such a system is based on a hydrogel core delivery and shows a slower release and absence of burst release when compared to materials without hydrogel. It is also interesting to note that the change in proportions between the monomers which form the hydrogel is affecting the diffusion coefficient. These important results will make it possible to adjust the release profile by changing the hydrogel composition.

# Chapter 6: Conclusions

The behaviour of micro and nanoobjects suspended in fluids is a widely studied issue, in the context of both basic research and potential applications. Without a doubt, the current achievements of nanotechnologies have led to their extensive application studies in biology, medicine, and material engineering. In order to be able to discuss the future applications of these materials, it is necessary to be familiar with all their characteristics.

The research conducted on the mobility of spherical nanoparticles under the influence of thermal fluctuations has confirmed that there are numerous factors affecting this mobility. The ionic strength of the medium is one of the most important factors that have a significant impact on the hydrodynamic diameter of nanoparticles. The impact of the environment is essential for estimating the diffusion of nanoparticles and biological macromolecules. It is also important for evaluating the so called "slip velocity", an apparent deviation from the sticky kinematic boundary conditions in nanoscale experiments. Knowing the impact that the environment of biological particles has on the value of the hydrodynamic diameter, it will be possible to estimate the actual size of these molecules and understand their diffusion process.

The second part of the research concerned more complex structures in terms of shape and behaviour – hydrogel nanofilaments. These objects are characterized by high flexibility, while their mechanical behaviour can mimic long biological molecules. We studied our hydrogel nanofilaments for Brownian motion, bending dynamics, and migration. The results we obtained showed that the diffusion coefficients of our flexible hydrogel nanofilaments differ from the theoretical predictions based on a drag force for stiff ellipsoidal nanoobjects. We have also shown that hydrogel nanofilaments are characterized by a great flexibility, which is an essential parameter in the context of future applications. Therefore, for future models, the application of a better approach that would take into account long and deformable objects is necessary. The creation of models of filaments with variable stiffness and dimensions is a great challenge for future theoreticians. The biocompatibility of hydrogel materials, as well as the mechanical properties mentioned above, opens up a number of possible biomedical applications for our nanofilaments.

Depending on their typical in-flow behaviour and shape change, we divided nanofilaments into three groups: bent-like, U-shape backed, and U-shape stretched filaments. Studies on the influence of the oscillatory flow on their dynamics have shown that nanofilaments can be used as models of elastic biopolymers, such as actin filaments or DNA molecules. This

is related to the fact that hydrogel nanofilaments and biomolecules are characterized by similar hydrodynamic reactions. Another important result we obtained is the demonstration of the ability of hydrogel nanofilaments to migrate laterally. The direction of their migration depends on the group to which a nanofilament belongs, while their velocity is comparable to the bead-spring model, which was developed at IPPT PAN.

We showed that by changing the content of the hydrogel-forming crosslinking factor, the speed and efficiency of the marker release (for example drug) is affected. Furthermore, the presence of a hydrogel in the core-shell structure of nanofibre mats prevents the almost immediate release of all the drug it contains.

In the future, our electrospun hydrogel nanofilaments could be useful for more systematic studies which will be focused on the development and optimization of microfluidic devices for the sorting of biopolymer and lab-on-a-chip technologies. A particular interest is focused on the use of such flexible polymeric nanoobjects as specialized biomimetic networks for targeting drug delivery and local tissue regeneration. Hydrogel nanofilaments may also be a useful experimental model for elucidating the role of hydrodynamic interactions in describing the physical phenomena responsible for the processes of folding and bending of long molecular chains (e.g. proteins, DNA).

Based on the performed experiments I am in a position to discuss the theses of this dissertation:

1) We showed that the mobility of spherical nanoparticle depends on several factors that affect the hydrodynamic diameter value. Factors influencing the effective diffusivity of nanoparticles by changing the size of hydrodynamic diameter include: ionic strength of medium, valence of salt, size of ions and distance from the channel wall.
2) We presented that the oscillatory flow in microchannel is a very promising tool for investigating micro- and nanoobjects behaviours. A full understanding of this behaviour in a flow which simulates intercellular motion of biomolecules inside the body opened new possibilities for biomedical application as: systems for controlled release of drugs, nanocarriers capable to delivery drugs in specific body tissue, local tissue regeneration.
3) We confirmed that flexible hydrogel nanofilaments can be used as experimental model to elucidate the role of hydrodynamic interactions in describing physical phenomena responsible for the processes of folding and bending of long molecular chains (e.g. proteins, DNA).

# APPENDIX

## APPENDIX 1: Factors affecting the hydrodynamic size

### A1.1 Surface structure effect

The nature of the surface and the polymer, in addition to the ionic concentration of the medium, can affect polymer conformation, which in turn can change the apparent size by several nanometres. With any change in the surface structure of particles, an absorbed layer of polymer will correspondingly change the particle apparent size by influencing the diffusion speed. It is assumed that particles are surrounded by a hairy layer which is created by flexible and protruding chains of polymer. These chains may have been introduced during the synthesis of particles. This type of layer is very thin, typically around a few nanometres (even 11 nm), and this causes micrometre particles to be often undetectable [8].

Lisiecki et al. [171] found that the addition of a low concentration of surfactant (e.g. cetyltrimethylammonium chloride CTAC causes an unforeseen strong increase in the hydrodynamic size of the metallic copper particles. On the other hand, at higher concentrations they observed a decreased hydrodynamic size. They suggested that the addition of surfactant (CTAC) to 0.1 M AOT reverses micelles and causes the hydrodynamic radius to remain almost unchanged (within the experimental error range). Unchanged magnetic iron oxide nanoparticles are unstable when they aggregate, and this is the reason for the high free energy which is associated with the surface of nanoparticles. When nanoparticles start to come into contact with each other, aggregates are formed. Hence, particles are coated with a protective layer to prevent aggregation. Such a layer often consists of organic surfactant molecules. It also prevents nanoparticles from coming into contact and aggregating due to repulsive steric and/or electrostatic interactions [172]. The size of the chain of functional groups forming the shell affects the value of the hydrodynamic diameter (Fig. A1.1).

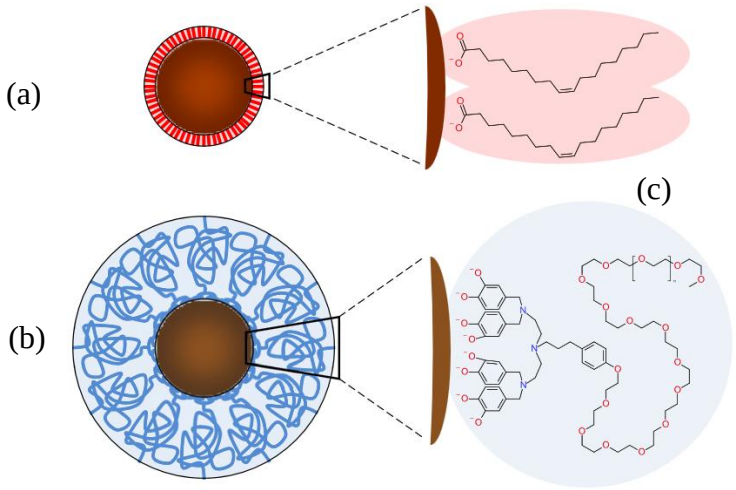


Fig. A1.1. Scheme of (a) FeOx nanoparticles coated with oleic acid and (b) FeOx nanoparticles coated with the title PEG-based tetra-catechol surfactant. (c) Surfactant molecular structure [172].

Dong et al. [173] also investigated the influence of the surfactant concentration on the thermal diffusion coefficient of polystyrene particles (Fig. A1.2). They found that the thermal diffusion coefficient of polystyrene particles (less polar group – hydrophobic PS) decreases as the surfactant concentration increases. The same situation was observed in the case of polystyrene particles with sulfonated surface (more polar group – hydrophilic PS).

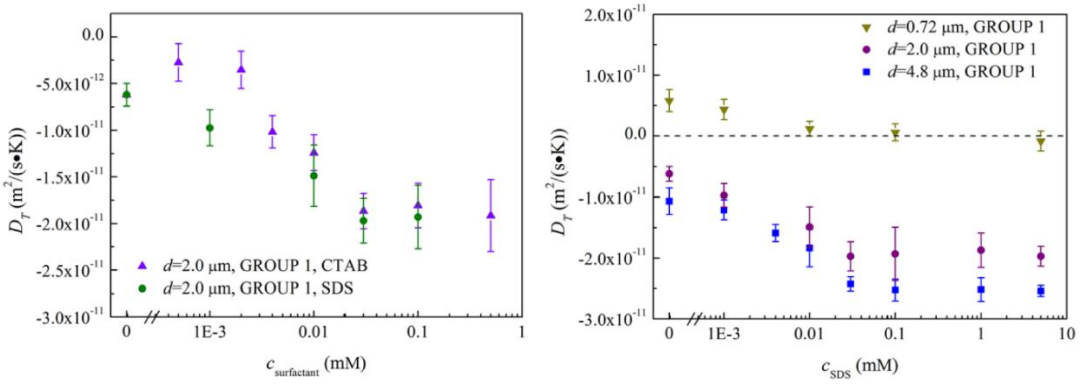


(a) (b)

Fig. A1.2. Thermal diffusion coefficient as a function of (a) the concentration of two different surfactants (for polystyrene particles 2 µm), and (b) the concentration of SDS surfactants (for three different polystyrene particle sizes). This was verified by the single-particle tracking method [173].

This effect depends on the adsorption of the surfactant molecules on the particle surface, and changes the interface properties. In the case of low concentrations of anionic surfactants, its nonpolar tails come into contact with the particle (e.g. polystyrene particle) colloid surface and mostly lie flat on the surface as a result of hydrophobic interaction

(Fig. A1.3 (a)). When the concentration of the anionic surfactant is high, its molecules align more vertically as a result of the sterically crowded particle surface (Fig. A1.3 (b)). At low cationic surfactant concentration (e.g. CTAB), polar heads are in contact with the particle surface. Consequently, nonpolar tails are facing outwards (towards the bulk liquid side) (Fig. A1.3 (c)). When the concentration of the cationic surfactant is high, and there is a neutralized charge on the colloid surface, another adsorption layer is formed. This is due to the hydrophobic interaction. The polar heads of the second layer are facing outwards (Fig. A1.3 (d)).

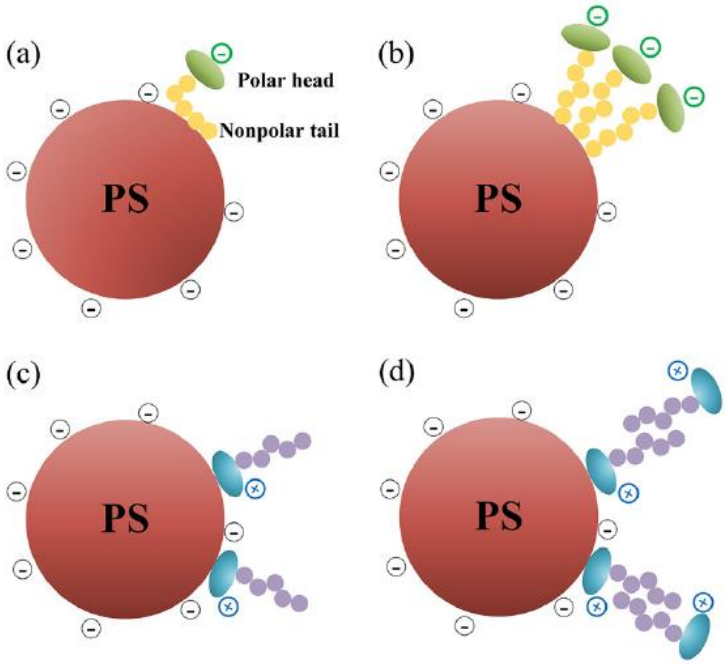


Fig. A1.3. Schematic illustration of anionic (SDS) and cationic (CTAB) surfactants on polystyrene particle surface [173].

It can be seen that as the concentration of SDS surfactants increases, the zeta potential is reduced. This is the result of increasing the number of polar head groups which are pointing outwards (from the colloid surface) with an increased surfactant concentration. When SDS was adsorbed on the colloid surface, a pronounced increase in the hydrodynamic radius of this structure was observed. This is possibly the result of colloid swelling when surfactant molecules move into the interior of particles [173, 174]. This is confirmed by several research reports showing that the presence of surfactants (anionic and cationic) affects the particle diffusion coefficient and that this effect depends on the different concentration of surfactants [173-175].

## A1.2 Agglomeration effect

According to the DLVO theory, increased particle size decreases the coagulation rate, while the total energy of interactions increases for such colloids. This particle size effect, however, was not verified through coagulation studies. It was considered that that the ratios of experimental stability are insensitive to the particle size [176].

Suttiponparnit et al. [177] examined the effect of primary particle size on dispersion properties by dispersing different-sized anatase TiO2 in deionized water. They showed that the average value of the hydrodynamic diameter depends on the ionic strength of solution and zeta potential, as well as on a primary particle size. The hydrodynamic diameter can reflect the primary particle size when attractive forces dominate over repulsive forces. In his study, Suttiponparnit pointed out that the particles of physical sizes from 6 nm to 104 nm increased their hydrodynamic diameter from 67 nm to 490 nm (Fig. A1.4). The particle-particle interaction (affected by the dispersion ionic strength and zeta potential) affects the observed nonlinear increment in the hydrodynamic diameter.

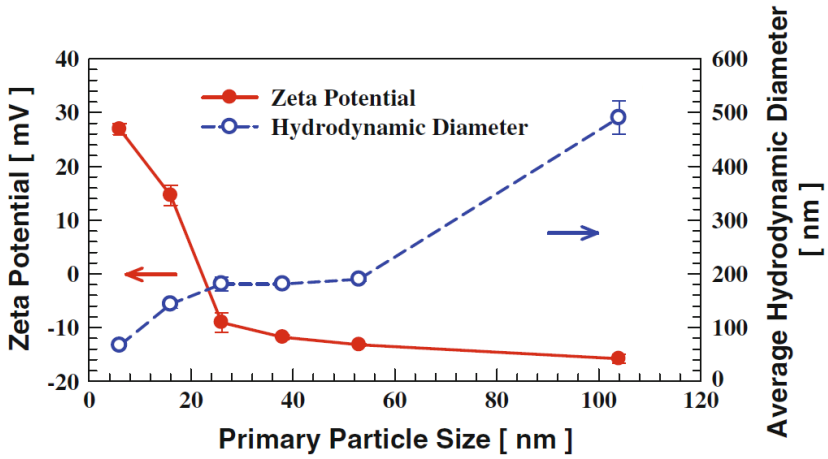


Fig. A1.4. Hydrodynamic diameter and Zeta Potential (evaluated by DLS measurement) as a function of TiO2 nanoparticle size (6 nm, 16 nm, 26 nm, 38 nm, 53 nm, 104 nm), dispersed in deionized water and mass concentration 50 µg/mL [177].

Suttiponparnit's study shows that the significant increase in hydrodynamic diameter is due to the formation of particle agglomerates. Jiang et al. came to a similar conclusion. They observed that nanoparticles in the dry state can be either agglomerated (held by weaker van der Waals forces) or aggregated (with hard bonds between primary particles). When nanoparticles are dispersed in a solution, they can either appear as singlets or form agglomerates, or they can also be aggregated and surrounded by an electrical double layer (Fig. A1.5). Typically, aggregated nanoparticles in a liquid cannot be separated, unlike agglomerated nanoparticles in a liquid. Their separation becomes possible by overcoming the weakest attractive forces [178].

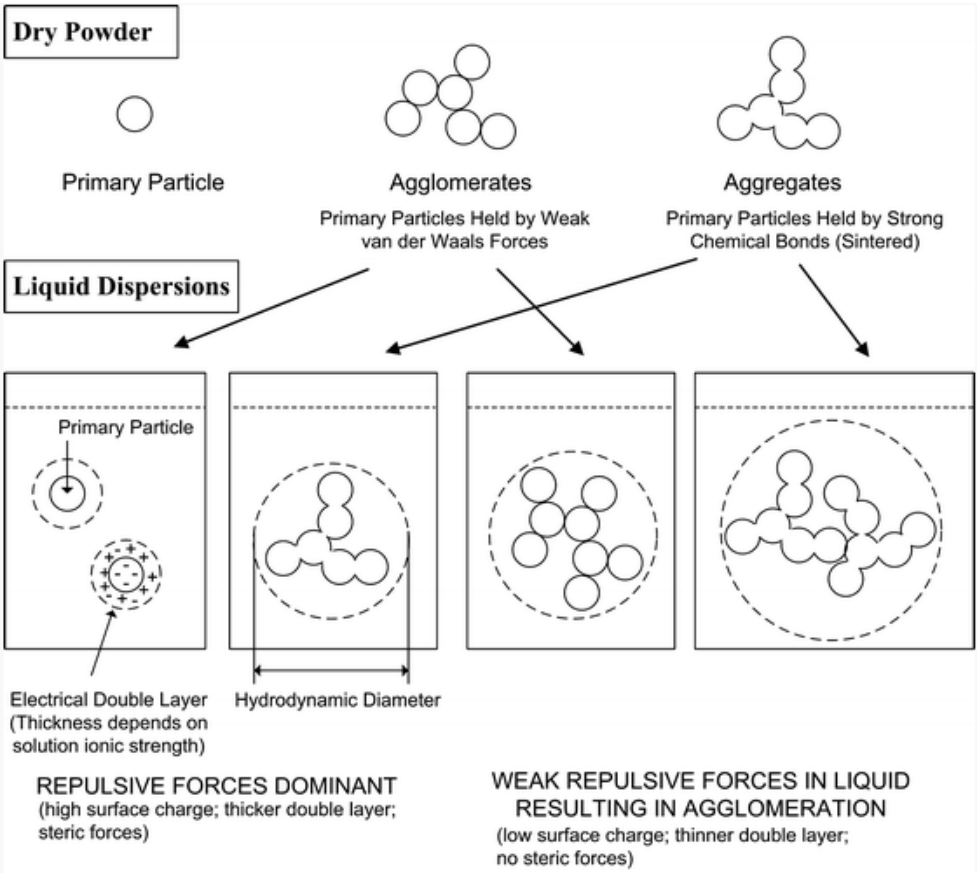


Fig. A1.5. Configuration of particles in dry and liquids state [178].

The clear definition of the actual physical size of nanoparticles based on their hydrodynamic value is a problem being studied by a number of researchers. As already mentioned several times in my thesis, this problem is related to many factors affecting the size of the layer surrounding the particle core, while their effect on the difference between the hydrodynamic and the physical size depends on the latter size.

### A1.3 Particle concentration

The particle concentration is a very important parameter affecting the value of the hydrodynamic diameter. Generally speaking, it should be kept low enough to ensure that the effects of interparticle interactions can be minimized. The effect of particle interaction is proportional to the average value of interparticle distance, as well as to particle concentration. At a fixed volume fraction, the average value of interparticle distance tends to decrease, along with the particle size. For this reason, the interaction effect will be less visible for particles with larger sizes. On the other hand, experimental methods using scattering light (like DLS) require sufficient particle concentration, especially if their diameter is less than 100 nm. At low volume fractions ($10^{-4}$-$10^{-5}$), the dispersions of such particles usually do not scatter sufficient light. In such a situation, the concentration of

the particles used is increased to volume fractions up to value 0.1, and particle interactions appear. Attractive (e.g. van der Waals) interactions cause diffusivity to decrease with concentration, while in the case of repulsive interactions (e.g. steric or electrostatic interactions), the collective diffusion coefficient increases with concentration. In such circumstances, the sizes of particles can be determined only by extrapolations to infinite dilution of the collective diffusion coefficient measurements, or by specific calibration procedures which make it possible to discriminate the parameters responsible for single particle mobility [179]. Fig. A1.6 shows examples of the dominant role of repulsive or attractive interactions on the diffusion coefficient measured for different volume fractions of thermodynamically stable dispersions [179].

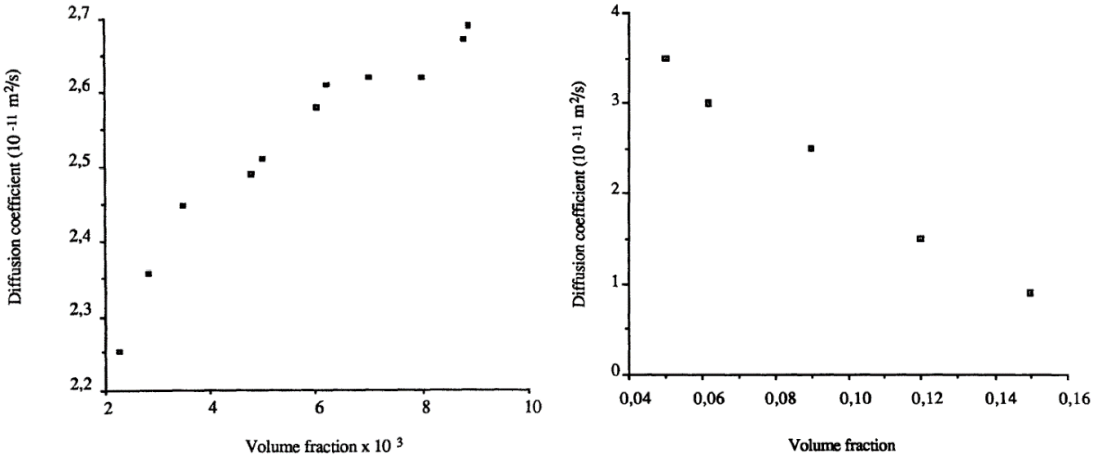


(a) (b)

Fig. A1.6. Diffusion coefficient of (a) silica dispersions (21.3 nm) and (b) a water-in-oil microemulsion (16 nm) as a function of volume fraction [179].

Chassagne et al. [10] analysed the correlation between particle concentration and hydrodynamic diameter. They have shown when the concentration of particles affects the results of the evaluated autocorrelation function. At too low a particle concentration, due to the fluctuating number of particles in the measuring volume, an additional fluctuation of the scattered light intensity occurs. In the case of high particle concentrations, interparticle effects may start to play a role, and additional multiple scatterings are present. Consequently, the estimated size of particles becomes smaller [10]. In the range 1-10 mg/L (corresponding roughly to $10^{-6}$ in volume fraction), these authors observed that the hydrodynamic diameter decreases as the particle concentration increases (Fig. A1.7). A similar trend was registered for pure water, and monovalent and divalent salts. At a particle concentration greater than 10 mg/L, the hydrodynamic size starts to increase.

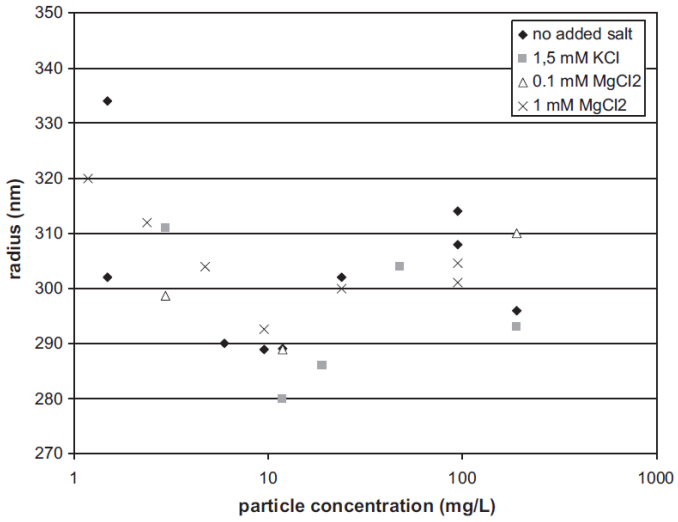


Fig. A1.7. The hydrodynamic size of particles as a function of particle concentration found using the dynamic light scattering technique (DLS) [10].

Similar conclusions have been reached with the experiments of Gittings and Saville [7] in the case of volume fraction in the range from $1.4 \cdot 10^{-6}$ to $5.7 \cdot 10^{-6}$ for particles in 1mM NaCl. As shown in Fig. A1.8, the measured diameter decreases linearly as the volume fraction increases. Ideally, a series of measurements at various volume fractions should be extrapolated to zero volume fraction to determine the hydrodynamic size. These changes, however, are not always monotonic. The difference in hydrodynamic size between measured and extrapolated values is estimated to be less than 3%. This linearity was observed by Lisiecki et al. [171].

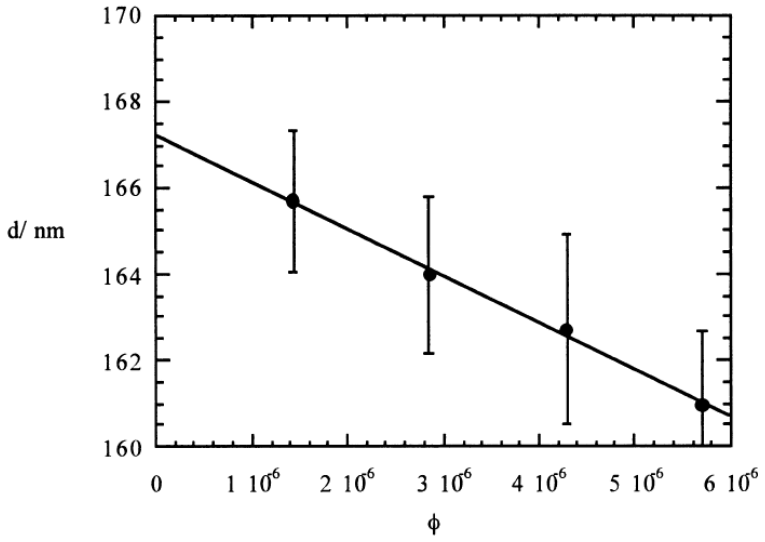


Fig. A1.8. The hydrodynamic diameter as a function of various volume fractions ($\phi$) determined by DLS [7].

Suttiponparnit et al. found very interesting results when they investigated the hydrodynamic diameter based on particle concentration for different ionic strengths of

the medium (IS). They showed that in the case of a low ionic solution strength, the dispersion hydrodynamic size does not change when the concentration of particles increases. This is due to the electrostatic repulsive force which helps to prevent agglomeration (Fig. A1.9). In high ionic strength solutions it can be observed that the increased particle concentration causes higher coagulation rates and greater hydrodynamic diameters [177].

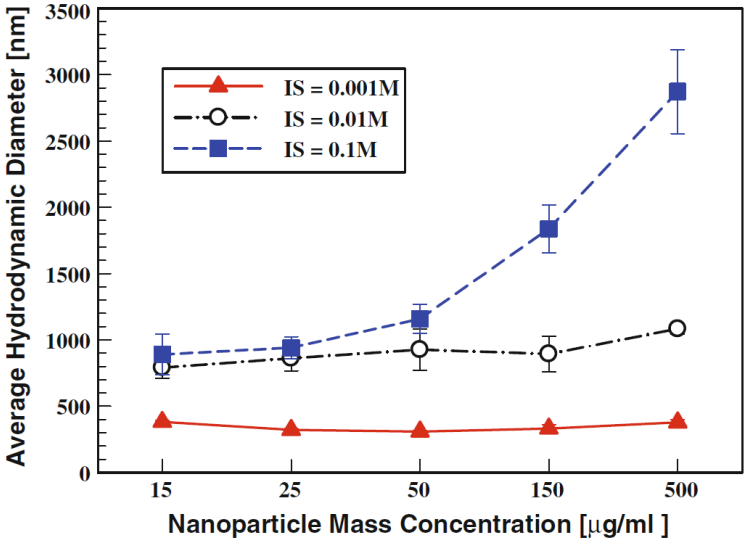


Fig. A1.9. $TiO_2$ particle (27 nm diameter) hydrodynamic diameter as a function of mass concentration of particles and depending on different ionic strengths of the medium (determined by DLS) [177].

In one case of 0.1 M ionic strength solution and 500 μg/mL particle mass concentration, large agglomerations of particles with hydrodynamic diameters of around 3000 nm were observed, where the physical diameter was equal to 27 nm.

It is very important, however, to note that many data on DLS particle size measurements in literature show that this technique is subject to considerable errors, depending on the applied particle concentration. *For this reason, in my opinion the nanoparticle tracking analysis (NTA) seems to be the most useful and reliable technique, with a low risk of errors*. Such a method was used in the present study.

**APPENDIX 2: Particle size analysis techniques**

The number of techniques used for particle size evaluation shows how important such an evaluation is. Moreover, it indicates how difficult it is to obtain this information. Briefly, these techniques can be broken down into several classes [180]:

- Microscopy methods: optical, scanning electron microscopy, transmission electron microscopy, atomic force microscopy, imaging analysis.

- Light interaction method: laser diffraction, single particle light scattering, photon correlation spectroscopy (dynamic light scattering, DLS), multi-angle light scattering, single laser Doppler velocimetry, particle light obscuration, fibre optic Doppler anemometry (FODA), time of flight.
- Sedimentation methods: X-ray sedimentation, centrifugal sedimentation, photo sedimentation.
- Electrical property methods: zeta potential, electrophoretic mobility, differential mobility analyser, coulter (electrozone) principle.
- Sorting and classification methods: air classification, field flow fractionation (FFF), fluorescence activated cell sorting, sieving and screening.

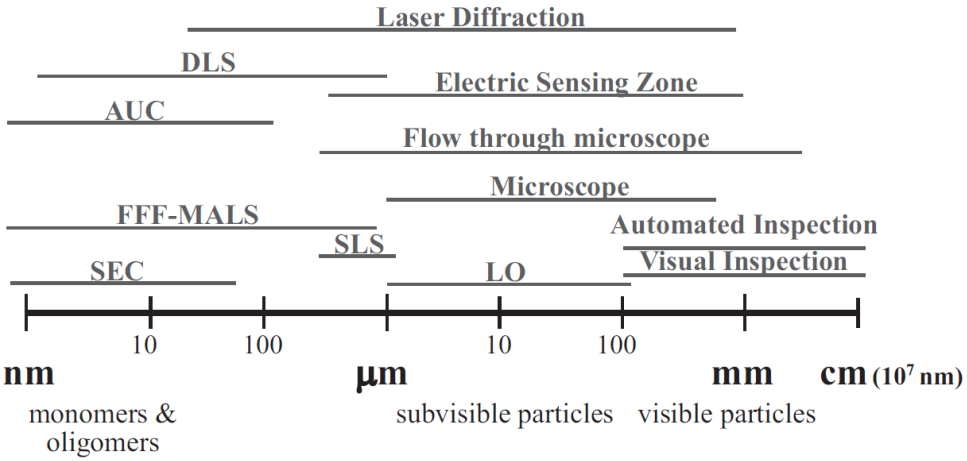


Fig. A2.1. Common method for particle/aggregate analysis: SEC – size-exclusion chromatography; AUC – analytical ultracentrifugation; SLS – static light scattering; LO – light obscuration; DLS – dynamic light scattering; FFF - field flow fractionation; MALS – multi-angle light scattering [181].

In our work we focused on just two of the techniques listed above: microscopy and light interaction methods.

## A2.1 Light Scattering

Light scattering is one of the most important techniques: it is useful for measuring the motion and diffusion of macromolecules, and also for studying macromolecular chemical reaction kinetics. This can be evaluated by observing the light scattering angle intensity [182].

The light scattering method is based on the research conducted by Richter, Tyndall, Rayleigh, Einstein, Mie, and Debye. The phenomenon of light-scattering from a sol of colloidal gold was observed by Richter for the first time in 1802. In 1869, Tyndall attempted to explain the reflection phenomena by studying a beam of light passing

through mixed vapours of butyl nitrate and hydrochloric acid. In 1881 Rayleigh began a study of the theoretical and practical aspects of light scattering based on electromagnetic theory. Some years later, Einstein devised the fluctuation theory. This theory could be successfully used to explain the light scattering of fluid systems. Mie developed a light scattering theory for particle sizes comparable to the light wavelength and refractive indices different from those of the dispersing medium. Debye was the first to show how to determine the molecular weight of weakly interacting particles by light scattering. The progress took many years to reach its present stage of development [183, 184].

Pecora et al. [185] showed that the time fluctuations of the intensity of light scattered by macromolecular solutions would give the macromolecular diffusion coefficient values and, in special conditions, these fluctuations might be used to study the flexing and rotational motion of macromolecules. Because of very small changes in these time fluctuations, the conventional monochromators could not be used to obtain a proper frequency distribution [184].

In a typical light scattering experiment, to define the polarization of the incident beam the light from a laser passes through a polarizer and then impinges on the scattering medium. Next, the scattered light passes through an analyser, and finally reaches the detector. The scattering angle $\theta$ is defined by the detector position. Furthermore, a scattering region of volume is defined by the intersection of the incident beam and the beam intercepted by the detector (Fig. A2.2) [184].

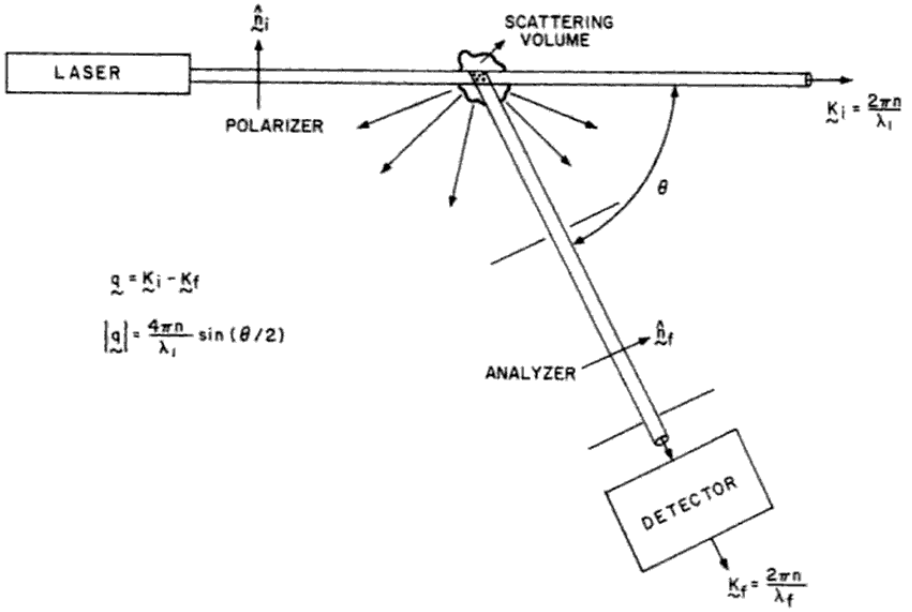


Fig. A2.2. A scheme of the light scattering experiment [184]

The light scattered by small particles is described depending on the ratio of the particle refractive index to the surrounding medium, the particle size, and their orientation and shape. Observation angle and polarization also determine the scattered light intensity [186]. A common dichotomy in light scattering terminology is dynamic light scattering versus static light scattering.

Dynamic Light Scattering (also known as Photon Correlation Spectroscopy) is one of the most popular methods used to determine the particle hydrodynamic size. This method is based on the measurement of changes in the speckle pattern produced by the scattering light of particles during Brownian motion. An intensity autocorrelation function $G_2(\tau)$, is produced by monodisperse suspensions, and can be described by the equation [180]:

$$G_2(\tau) = A\left[1 + Be^{\left(-2Dq^2\tau\right)}\right]$$

$$q = (4\pi n/\lambda)sin(\theta/2)$$

where: $\tau$ - the time delay between intensity measurements; $A$, $B$ – the baseline and intercept of the correlation function; $D$ – diffusion coefficient; $n$ – the refractive index of the solvent; $\lambda$ - the laser wavelength; $\theta$ - the scattering angle.

In the case of a monodisperse system, the diffusion coefficient is related to the hydrodynamic diameter $d_h$, and is calculated by the Stokes-Einstein equation [180]:

$$d_h = \frac{k_B T}{3D\pi\eta}$$

where: $k_B$ – the Boltzmann constant, T – absolute temperature, $\eta$ - viscosity of the medium.

In the case of a polydisperse sample, the sum of the exponential decays of the different populations of particles (which are present in the sample) describes the correlation function. Due to the ill-posed nature of the Laplace inversion of this correlation function, the obtained decay rate distribution suffers from low resolution [179, 180].

When the light hits the moving Brownian particle, it changes its wavelength due to the Doppler Shift. This change is connected with the particle size. It is possible to calculate the size distribution for spheroidal particles by evaluating the particle diffusion coefficient from the autocorrelation function [187]. The size of particles is determined by the fluctuations of scattered light intensity due to the particles' Brownian movements. This technique is very sensitive to the presence of large particles, because the scattered light intensity is proportional to the sixth power of the particle diameter [180]. When the

goal is to detect small amounts of large particles this can be an advantage, but if we want to accurately determine their size, it can be a major disadvantage. Small amounts of large aggregates or even dust particles can make the size determination difficult, especially when the main component of the analysed colloid is characterized by a significantly smaller size [188]. However, its high throughput and its easy use has made DLS one of the simplest and most common techniques for the determination of particle size distribution [180].

### A2.2 Nanoparticle Tracking Analysis by commercial NanoSight equipment

NanoSight is a type of equipment used to measure nanoparticle sizes and concentrations based on nanoparticle tracking analysis (NTA). This nanoparticle analysis instrument generates videos of a population of nanoparticles moving in a liquid under Brownian motion when illuminated by laser light. Within a specially designed and constructed laser illumination device mounted under a microscope lens, particles dispersed in a liquid are detected by the instrument as bright spots of light moving rapidly under Brownian motion. Despite the movement speed of the particles (in the sub-100nm size range, in particular), such motion can be tracked using a conventional CCD camera operating at 20 to 60 frames per second. The videos obtained can then be analysed using the NanoSight NTA software, which can determine separately the size of each particle and the resulting particle size distribution profiles.

The software selects trajectories whose lifetimes are long enough to ensure statistically accurate results, ignoring those which are too short (e.g. less than 5 or 10 video frames). The simultaneous measurement of the mean squared displacement of each particle tracked makes it possible to determine the particle diffusion coefficient ($D_{th}$), and hence the sphere-equivalent, hydrodynamic diameter ($d_h$), using the Stokes-Einstein equation.

## APPENDIX 3: Hydrogel materials

Hydrogels are known as a water-insoluble crosslinked three-dimensional network of polymers with a water content of up to over 99 weight percent (wt%) [189]. They are defined as a water-swollen and crosslinked polymeric network produced by the simple reaction of one or more monomers. This polymer holds water within its structure, but will not dissolve in water [190]. Usually the mass fraction of water in a hydrogel in the swollen state is much higher than the mass fraction of the polymer [190]. Due to its high water content, the microstructure and degree of flexibility of the hydrogel material is similar to those of living tissues [189, 191]. The presence of hydrophilic functional groups which

are attached to the polymeric backbone determines the ability of hydrogels to absorb water. The resistance of hydrogel to dissolution depends on crosslinks among network chains. The hydrogel may contain various amounts of water, depending on several factors such as the properties of the polymers included in the hydrogel network, and the nature and density of the network joints. Depending on their origin, hydrogels may be further subdivided into two groups: natural and synthetic. Synthetic hydrogels have a shorter history, and over the past twenty years have begun to gradually replace natural hydrogels. Synthetic hydrogels are characterized by decent stability, high water absorption capacity, and high gel strength. They also have well-defined structures that can be modified to improve their functionality and degradation rate. Additionally, a synthetic hydrogel is more stable at conditions of strong temperature fluctuations [190, 192].

Hydrogel materials already have quite a long history and a wide range of applications, particularly in biology and medicine. They were first used in 1960 as a material for the production of contact lenses. The inventors of the method of crosslinked hydrophilic structure preparation are Wichterle and Lim [193]. Nowadays hydrogel biomaterials are widely used in pharmacy, medicine, and tissue engineering, and to produce the third generation of dressing materials [194]. These types of patches are normally used in the case of traumatic wounds, burns, and ulcers. Their great advantage lies in the possibility to use them anywhere in the body, due to their high degree of flexibility. Thanks to a dressing with hydrogel materials, the healing process and regeneration of damaged areas is much faster than with conventional dressings [195].

There are several advantages to the application of hydrogel materials in tissue engineering. These materials are ideal for growing human cells and microorganisms, thanks to the physical properties of hydrogels, the mechanical properties of which resemble those of soft tissues. Their high water content and structural similarities to the natural extracellular matrix are conducive to cell proliferation and survival. The ability to control the shape, porosity, surface morphology, and size of hydrogel scaffolds has created new opportunities for overcoming various bioengineering challenges, such as vascularization and tissue reconstruction. Particularly prevalent is the use of hydrogel matrices in drug delivery systems, allowing for a controlled and continuous delivery of drugs into the body fluids.

The wide range of biomedical applications of hydrogels is possible due to their special properties [194-196]:

- nontoxicity – lack of chemical damage to the cells: the material is harmless for the health of living bodies;
- biocompatibility – harmonious interaction with living matter, whereby such material does not cause any acute and chronic inflammatory reactions in surrounding tissues;
- biodegradability – the ability of the material to degrade after a certain prescribed period of time;
- good permeability for oxygen and metabolites dissolved in the water – such an environment improves the speed and efficiency of cell growth;
- flexibility – the ability to easily adjust to the surface on which the material is applied;
- high mechanical strength – the ability to withstand loads, even significant ones;
- chemical and thermal resistance – this involves the possibility of carrying out sterilization, by either heat or chemicals. Sterilization is necessary for applying the material onto or into a patient's body;
- low interfacial tension with water or biological fluids;
- high rate of fluid absorption in a reversible manner – the presence of functional groups and the degree of the polymer crosslinking determine the level of absorbency. This ability can reduce the presence of chemicals and electrolytes, which may react with functional groups.

Crosslinked polymers are formed by the crosslinking process, leading to the formation of a three-dimensional network through the formation of bridges among various chemical groups. The reactive-side groups of long linear polymer molecules can react with each other to form a three-dimensional network in which the original polymer chains are linked by chemicals.

The most commonly used crosslinking monomers are: divinylbenzene and N,N'-methylene bisacrylamide, ethylene glycol dimethacrylate, triethylene glycol dimethacrylate, and trimethylolpropane 2-ethyl-2-hydroxymethyl-1,3-propanediol [197]. There are two types of crosslinked copolymers: porous and gel. The gel structure is synthetised with a mixture of specific monomers in the absence of additional solvents.

The chemical structure and concentration of crosslinking monomers determine the properties of the resulting structures. Monomers are like chemical building bricks of a three-dimensional polymer network, e.g. a crosslinked polymer. Copolymers are polymeric materials which have at least two kinds of monomers in their structure [197, 198]. Copolymerization/crosslinking free-radical polymerization is helpful for producing hydrogels based on the reaction between hydrophilic monomers and multifunctional crosslinkers.

In general, three integral parts are necessary for the preparation of a hydrogel: monomer, crosslinker, and initiator. In solution copolymerization/crosslinking reactions, the polymerization is initiated thermally by either a redox initiator system or UV-irradiation [190, 199].

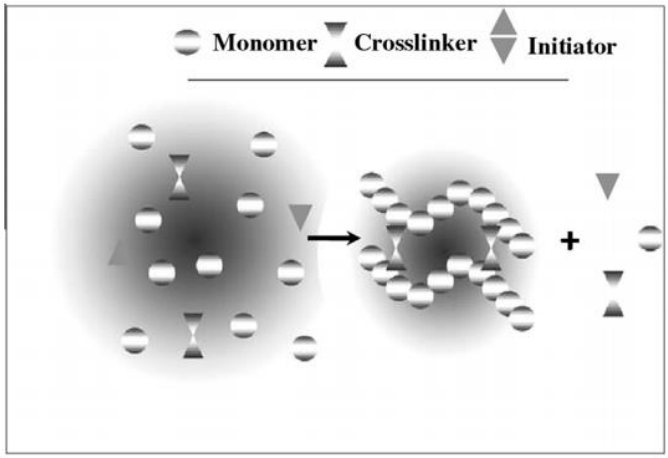


Fig. A3.1. Hydrogel preparation – schematic diagram [190].

The first monomer used to form hydrogels was hydroxyethyl methacrylate (HEMA), which was used by Wichterle and Lin [193]. Today, there are still some difficulties in using this hydrogel for implant devices because of its low mechanical strength [200]. Shin and co-workers [201] created a multicomponent nanocomposite hydrogel nanofibre from ferritin and polyvinyl alcohol (PVA). The addition of ferritin contributed to increasing the mechanical rigidity significantly, as well as to reducing creep during the cyclic deformation of nanocomposite hydrogels. Such hydrogel hybrid networks have a potential application in tissue engineering (for the preparation of scaffolds), drug release systems, and also as actuators. Another common synthetic polymeric material used to form hydrogel is polyethylene glycol (PEG). With its biocompatibility, flexibility, and stealth properties, it is an ideal material for pharmaceutical applications [202, 203].

*In this thesis, investigations are based on the use of polyacrylamide and its derivatives as hydrogel-forming polymer materials*. Monomers were crosslinked with N,N'-methylene

Bisacrylamide (BIS-AAm). Acrylamide monomers used for the production of polyacrylamide have been reported as toxic and carcinogenic for living organisms, possibly damaging their nervous systems [204]. Fortunately, this carcinogenicity disappears after the polymerization. A particular acrylamide derivative is N-isopropylacrylamide (NIPAAm). Poly(N-isopropylacrylamide) (PNIPAAm) belongs to a group of stimuli-responsive hydrogel polymeric materials, because it reacts to temperature changes. The balance between the fractions of hydrophobic and hydrophilic monomers of polymers is responsible for this phenomenon. Small temperature changes associated with changes in the hydrophobic and hydrophilic forces are the cause of the changed interaction between segments of the polymer and water. Such a polymer is defined as a smart polymer. Its structural features respond to a temperature variation similar to that of the human body [205]. The phase transition between hydrophilicity and hydrophobicity is sharp and reversible, and occurs at $32 \pm 1\text{-}2^{o}C$. PNIPAAm is a favourite biomaterial due to its high biocompatibility.

There are numerous reports on PNIPAAm applications, including drug delivery systems, tissue engineering, surfaces for cell culture, and actuator and sensor coatings [205-207]. Guan and co-workers demonstrated the possibility of using PNIPAAm microgels in the form of dispersed particles for biosensors, drug delivery, and enzyme encapsulation [196]. The significant disadvantage of PNIPAAm-based hydrogels lies in the fact that they are not biodegradable. Due to their high fragility, the surgical removal of the hydrogel material is also very problematic [205]. However, this concerns only the most classic, single-component hydrogels. In order to improve the mechanical strength of hydrogel materials, it is possible to use inorganic nanoparticles that are suspended in a network of crosslinked organic polymers, thereby forming nanocomposite hydrogels [208]. Skelton et al. [189] found that the addition of a crosslinking agent (dopamine methacrylamide) increases the stiffness and ability to dissipate energy, which can mimic the characteristics of the tissue elastomeric copolymers. Gaharwar et al. [208] reported that poly (N-isopropylacrylamide)-based nanoparticles/hydrogel were used in tissue engineering for designing therapeutic agents and as drug delivery systems. Up to the present time, however, the extreme fragility of hydrogel materials has limited their use to bulk structures, capsules, or films. *The casting of flexible nanosized hydrogel filaments appeared possible thanks to the implementation of our innovative technique of electrospinning a hydrogel core protected in a polymer shell*.

We may find the following hydrogel products formulated according to their polymeric composition:

1) Homopolymeric hydrogel – polymer network formed by a single species of monomer. This type may have a crosslinked skeletal structure. This structure depends on the polymerization technique and monomer nature [190].
2) Copolymeric hydrogel – made of more than one different species of monomer. These monomers must have at least one randomly arranged hydrophilic component, with an alternating or block configuration along the polymer network chain [190].
3) Multipolymer interpenetrating polymeric hydrogel – this is made of two independent crosslinked synthetic and/or natural polymer components, contained in network form. If one component is a crosslinked polymer but the other is a non-crosslinked polymer, the structure is called a semi-multipolymer interpenetrating hydrogel [190, 199].

According to Rosiak et al. [194], two basic groups of hydrogels may be identified:

1) Conventional hydrogels - hydrophilic polymers, which are crosslinked by light irradiation. They are free of ionic charges, undergo significant swelling in water and are not dissolved by it. The level of swelling in water does not change when the pH, temperature, present electric field, light, or other stimulation changes.
2) Stimuli responsive hydrogels – these show a significant change in volume as a response to small changes in temperature, pH, light, or electric field. They may be charged or not charged. Typically, they contain ionic groups which are sensitive to changes in pH and hydrophobic structure elements.

There are a few ways that water-soluble linear polymers can be crosslinked to form hydrogel [190]:

1) Ionizing radiation – used to generate main-chain free radical. This structure can recombine as cross-link junctions.
2) Linking polymer chains by chemical reaction.
3) Physical interactions – crystallite formation, entanglements, electrostatics.

Table A3.1. Monomers used for the synthesis of hydrogels [203].

| Monomer abbreviation | Monomer |
|---|---|
| HEMA | Hydroxyethyl methacrylate |
| HEEMA | Hydroxyethoxyethyl methacrylate |
| HDEEMA | Hydroxydiethoxyethyl methacrylate |
| MEMA | Methoxyethyl methacrylate |
| MEEMA | Methoxyethoxyethyl methacrylate |
| MDEEMA | Methoxydiethoxyethyl methacrylate |
| EGDMA | Ethylene glycol dimethacrylate |
| NVP | N-vinyl-2-pyrrolidone |
| NIPAAm | N-isopropylacrylamide |
| Vac | Vinyl acetate |
| AA | Acrylic acid |
| MAA | Methacrylic acid |
| HPMA | N-(2-hydroxypropyl) methacrylamide |
| EG | Ethylene glycol |
| PEGA | Polyethylene glycol acrylate acrylate |
| PEGMA | Polyethylene glycol acrylate methacrylate |
| PEGDA | Polyethylene glycol acrylate diacrylate |
| PEGDMA | Polyethylene glycol acrylate dimethacrylate |
| PNIPAAm | Poly(N-isopropylacrylamide) |

## APPENDIX 4: Alternative methods for nanofibre production

### A4.1 Melt spinning process

The melt spinning (MS) process has proved to be a simple method for producing non-woven webs of microfibres. The diameter of the fibres formed by this process is typically greater than 2 μm. It is the simplest fibre manufacture method, mostly because it does not involve problems associated with the use of solvents [209, 210]. MS entails drawing down extruded strands of the melted polymer to reduce the fibre diameter and to induce the polymer chain orientation. One of the limitations of melt spun fibre technology is that it is restricted to viscoelastic materials which can withstand the stresses developed during the drawing process [22].

Polymers, in the form of granules or pellets, are fed into an extruder, where they are melted and pumped by a displacement pump to the melt spin pack. The spin pack consists of filters and channels which supply the molten polymer to a multifilament spinneret. The molten filaments that exit the spinneret enter a cooling zone. During this step the filaments cool down and solidify. The cooling zone may be a chamber where the cooling environment should be strictly controlled. The molten fibres exiting the spinneret are simultaneously pinched to a smaller cross-sectional size by the drawing-down force applied [209, 211].

### A4.2 Solution blow spinning process

The solution blow spinning process (SBS) is a relatively new method for the production of nanofibres which is characterized by a high throughput [212]. It is used to fabricate polymer micro- and nanofibres with a rich variety of diameters ranging from a few tens of nanometres to several micrometres. SBS can be applied as solution or melt spinning, and combined with electrospinning. The fibres produced by SBS are at least one or two orders of magnitude smaller in diameter than those produced by conventional fibre production methods (e.g. melt spinning process) [213]. Solution blow spinning makes possible a mass production of nanofibres [22, 214]. SBS is based on the high speed of decompressed air leading to rapid stretching and solvent evaporation of a jet of polymeric solution issued from concentric nozzles of the system outlet. The high-pressure air applied allows the solution blow spinning to be easily scaled-up [215, 216].

The main part of the solution blow spinning apparatus is a system of specifically designed concentric nozzles. The polymer solution is supplied through the inner nozzle of this system via a syringe pump with a controlled injection rate, while compressed gas (e.g. air, nitrogen, argon) is supplied throughout the outer nozzle. Fine polymer nanofibres are collected on a rotating drum (collector). The collector is positioned at a fixed working distance from the nozzle. The geometry of nozzles generates a region of low pressure around the inner nozzle which helps to draw the polymer solution into a cone. Polymer nanofibres are dragged from the cone by the viscous forces of the flowing air which overcome surface tension forces [22, 216].

The solution blow spinning process is applied for the commercial production of non-woven polymer webs [22]. Due to the very small fibre diameter, the non-woven web has a high porosity and a large surface area. Such properties increase the commercial value of these materials for applications in membrane tissue engineering scaffolds, and sensors [212, 214, 217].

Melt blowing is a special form of melt spinning process which forms very fine but weak fibres [211]. It involves extruding molten polymers through a narrow orifice and into a stream of high-velocity hot air [218].

The drag of the hot air on the polymer melt surface causes the polymer to start to elongate into a fibre. This process can be controlled to produce fibres ranging in diameter from 1 μm to 50 μm [22]. These micrometre fibres are finding applications in a growing number of fields, such as absorbency, filtration, hygiene, and clothing [218].

## APPENDIX 5: Apparatus

### A5.1 Experimental setup for Brownian motion

Solutions of suspended particles were introduced between two parallel plates of quartz glass (depth 0.5 mm, Fig. A5.1 (a)) or PDMS chambers (15 mm of diameter and 3 mm of depth, Fig. A5.1 (b)), which were illuminated by laser or a Hg lamp.

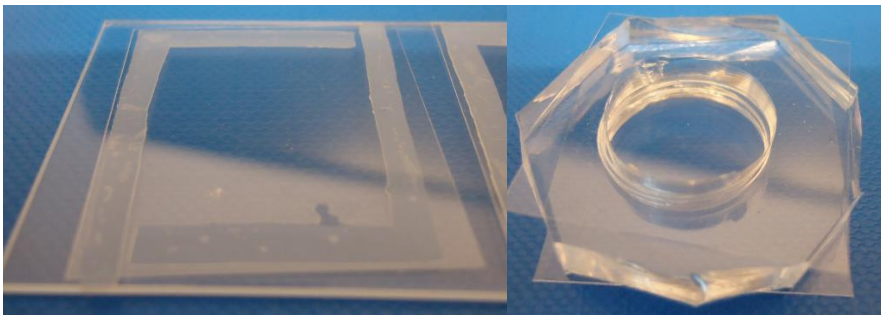

(a) (b)

Fig. A5.1. Chambers for Brownian motion analysis: (a) quartz glass chamber; (b) PDMS chamber.

A Lambert camera HiCAM-500 or Hamammatsu camera (C9100-2) and a fluorescent microscope (Leica) were used to capture images at a specific time rate used to detect particle displacements (Fig. A5.2). A Matlab script was used for data analysis.

Fig. A5.2. Photography of an experimental stand.

### A5.2 Electrospinning apparatus and process parameters

The core-shell nanomaterials for this study were produced using a designed electrospinning chamber made at the IPPT PAN (Fig. A5.3). This chamber enables the electrospinning process under controlled atmosphere and thermal conditions. The cooling

system makes it possible to run the process under controlled temperature (from -10°C to room temperature). The high-voltage power control system ensures that voltage can be adjusted to the process requirements ranging from 1 to 30 kV.

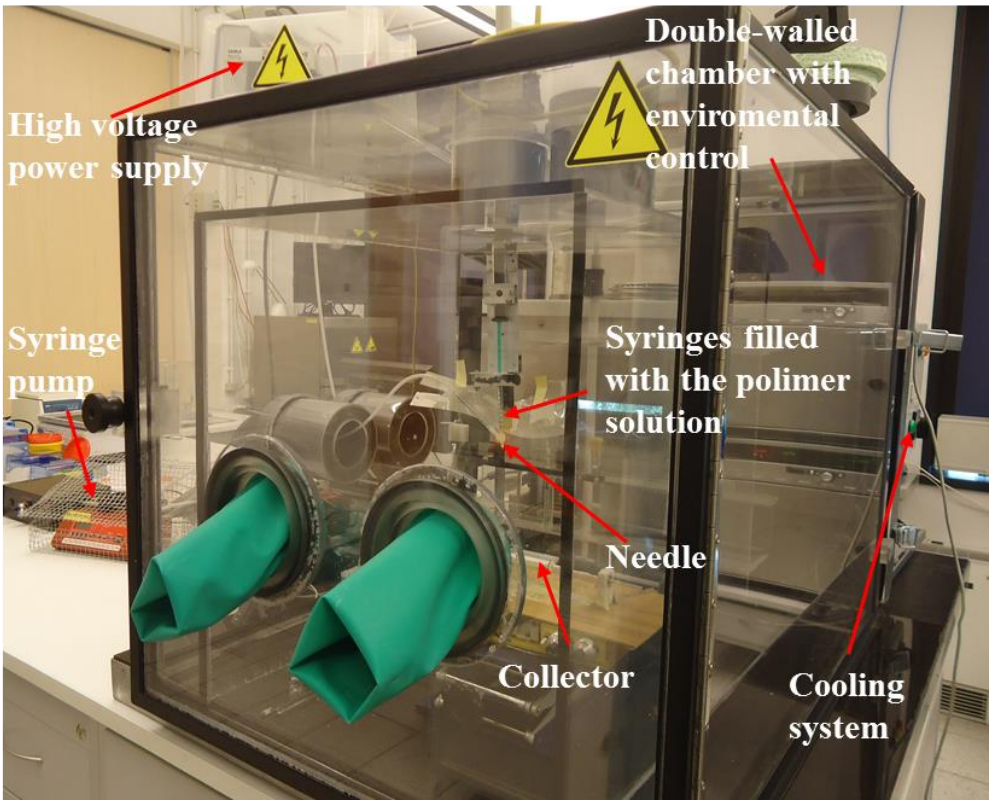


Fig. A5.3. Electrospinning chamber at IPPT PAN.

Two independent syringe pumps supply polymer solutions at selected flow rates. The polypropylene syringes (1 ml volume), filled with mixtures of core and shell polymers respectively, were connected to a co-axial nozzle, allowing the simultaneous dosing of both polymer mixtures. The handmade nozzle consisted of two needles. A 27-gauge needle was placed inside the 20-gauge needle to set the inner dimension for core-shell production (Fig. A5.4).

Fig. A5.4. Handmade nozzle, designed and manufactured at IPPT PAN.

The fibre collector is a rotating drum with a 9 mm diameter, which rotates at a speed of 2000 rpm and periodically moves in a direction perpendicular to the direction of polymeric nanofibre stretching. Such a collector movement makes it possible to improve the distribution of fibres in the mat.

Nanofibres were electrospun using a vertical co-axial setup with the outer layer flow rate $Q_{shell}$ set to 1500 μl/h. The core solution flow rate was set to $Q_{core}$ = 1500 μl/h. Electrospinning was performed at a positive voltage of V = 15 kV. Nanofibres were collected onto either a microscope slide or the rotating drum (2000 rpm), and covered with a 3 cm width grounded aluminium foil. Temperature and humidity during electrospinning were T = 25°C and h = 45%, respectively.

### A5.3 Fluorescent microscopy

The analysis of Brownian motion and the hydrodynamics of fluorescent solid particles and hydrogel nanofilaments were assessed by a Leica AM TIRF MC inverted epifluorescence microscope. Depending on the type of interrogated particles, we used different lens magnifications and sets of filters. For Brownian motion analysis high magnification is necessary, so HCX PL APO 100x/1.47 OIL was used. For studying the behaviour of particles and fibres under the flow we used a 20x/0.40 NA microscopic lens, with which it was possible to view the whole microchannel width. In the case of polystyrene particles dyed with rhodamine, a filter with excitation and emission wavelengths equal to 542 nm and 612 nm was needed. The observation of hydrogel nanofilaments dyed by BSA-FITC was possible thanks to the use of filters with excitation and emission wavelengths equal to 470 nm and 525 nm, respectively.

The experimental station was equipped with a Leica EL6000 mercury lamp for fluorescence excitation and a high-gain EM-CCD camera (C9100-2, Hamamatsu) for recording the nanoobjects' behaviour. Measurements were performed inside the microscopy environmental chamber, thus maintaining constant temperature conditions and protecting samples from the disturbing external light.

### A5.4 AFM and Optical Tweezers

Atomic force microscopy (AFM) is the most frequently used technique for measuring the interaction forces of nanomaterials and molecules [219]. AFM measures intermolecular forces between the sample and a probe. AFM is mainly used for imaging purposes: a topographical structure can be obtained by scanning the surface of samples using a tip fastened to a flexible cantilever. Some technical developments of AFM, such as the introduction of the piezo stage and microfabricated cantilevers, have made possible some

significant improvements in force measurements [220]. Atomic force microscopy, however, has a limited use for examining very small forces (e.g. in the range of femtonewtons). The reason for this is that its sensitivity is strictly dependent on the mechanical property of the probe [102, 221].

Optical Tweezers (OT) is a technique capable of trapping small particles using the forces generated by the laser radiation pressure. It can be used to manipulate and study the motion of microspheres and single molecules in the range of nanometres [222]. Optical Tweezers offers the possibility to detect forces with femtonewton resolution. A commercial AFM system (Ntegra Spectra, NT-MDT, Limerick, Ireland) has been coupled to an OT system at IPPT PAN (Fig. A5.5). This instrument helped us study the morphology of micro- and nanoobjects such as solid spheroidal particles and highly deformable hydrogel nanofilaments, as well as to evaluate the mechanical properties of these materials.

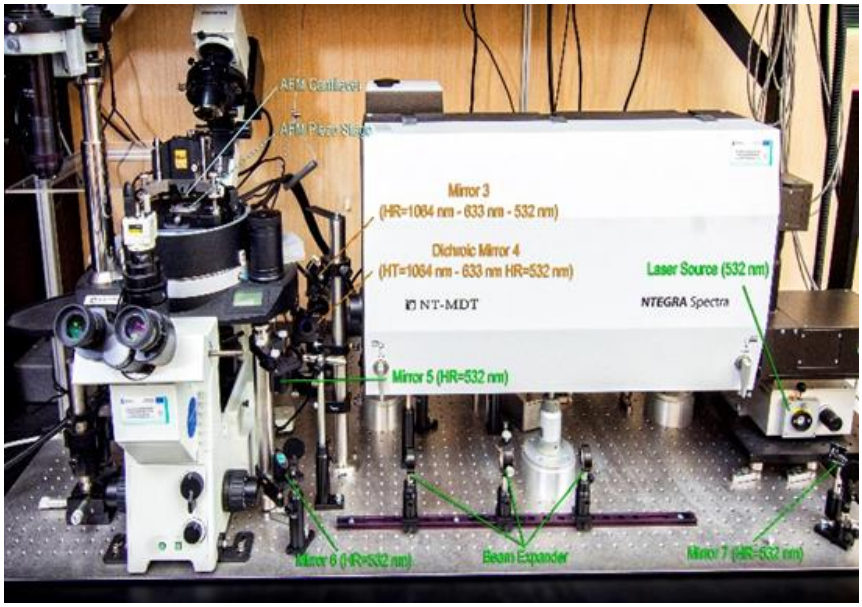


Fig. A5.5. Atomic force microscopy (AFM) and Optical Tweezers setup at IPPT PAN.

The Optical Tweezers instrument implemented at IPPT PAN is based on the inverted microscope (IX71, Olympus Optical Co. Ltd, Tokyo, Japan) which is part of a commercial AFM (Ntegra Spectra, NT-MDT, Limerick, Ireland) (Fig. A5.5). The system consists of three different lasers, each preforming a different task: a 1064 nm Nd:YAG diode-pumped solid state laser (which creates an optical trap that could confine single objects in colloidal systems); a 633 nm He-Ne laser (which is the core of the most sensitive detection system); a 532 nm wavelength pulsed laser (which is used to excite fluorescent materials for imaging purposes) [102].

For the visualization of the trapped objects and their surroundings in both fluorescent and white light, a high-speed camera (HiCAM 500, Lambert Instruments) is used. The sample moves in the X and Y directions thanks to the precision piezo-stage. These movements are perpendicular to each other as well as to the optical axis of the microscope.

In the present study the Optical Tweezers system makes it possible to investigate the interactions between particles and microchannel wall in different environments, as described in Chapter 3.

### A5.5 Pulse pump system

For the study of the behaviour of micro- and nanoobjects in an oscillating flow, a special pulse pump was designed and constructed. The principle of its operation is based on the use of a rotating disk, which is mounted excentrally on the stepper motor with a 0.44 Nm torque. As the disk (with a 6 cm diameter) rotates, it periodically presses the 22 cm-long arm of the pump (Fig. A5.6).

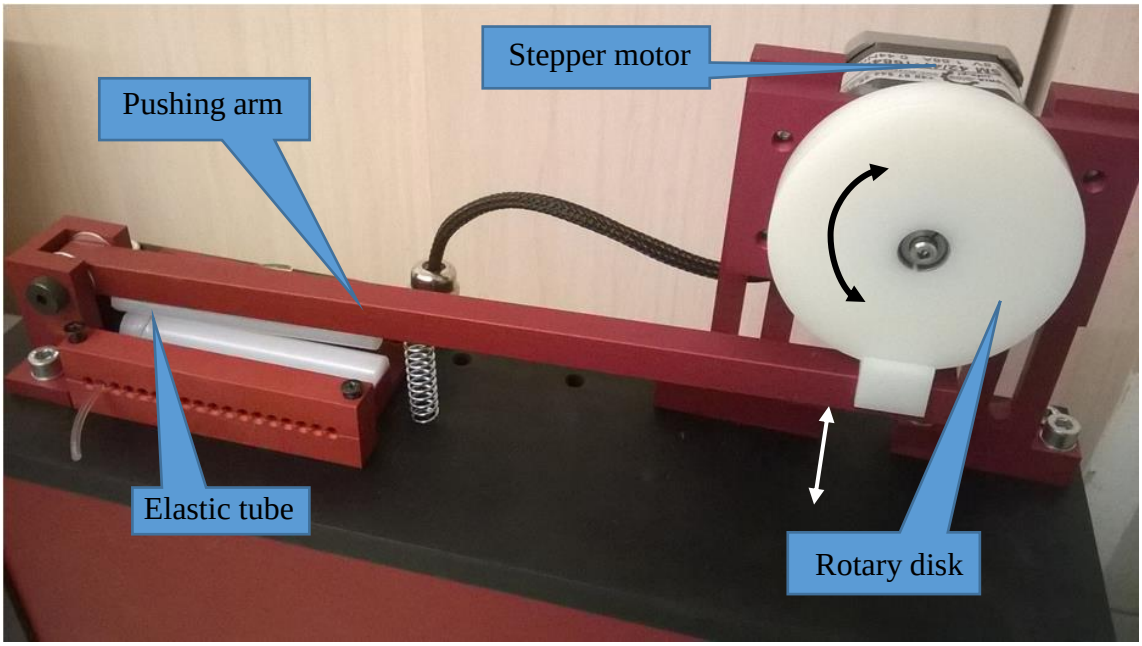


Fig. A5.6. Pulse pump for generating an oscillatory flow at IPPT PAN.

The pump arm bends where the cross-section of the elastic tube, filled with the working liquid (water), closes and opens. The elastic tube is connected at one end by a steel capillary tube connected with a microfluidic system, ending with a glass syringe filled with a solution of the analysed objects. At the other end the tube is closed, thus causing the flow generated by the compressed tube to move only towards the microchannel. Thanks to this, the liquid moves forward and backward, as a result of the compression and expansion of the elastic tubing when pressed by the pump arm (Fig. A5.7).

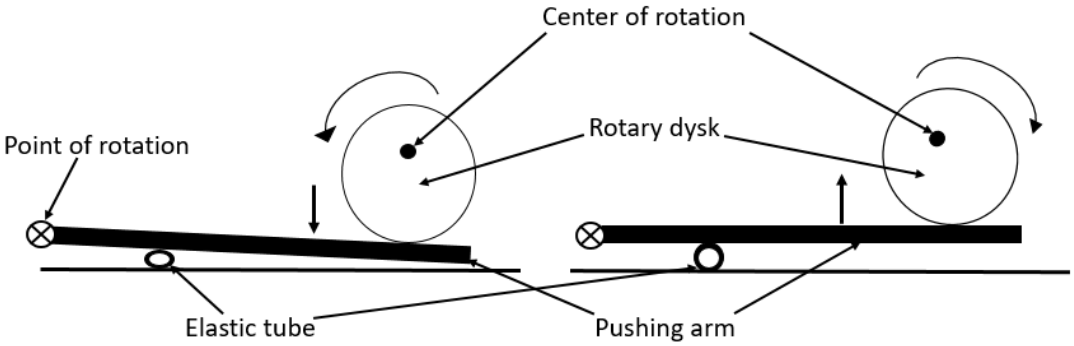


Fig. A5.7. Scheme of the work idea of the pulse pump.

The use of a pulse pump driven by a computer program permitted the automatic control of the selected oscillatory flow pattern. The speed and duration of one phase in the oscillatory flow cycle were controlled by motion amplitude and rotary disk speed.

## APPENDIX 6: Procedures

### A6.1 Experiments using a nanoparticle tracking commercial equipment (NanoSight)

NanoSight is a type of equipment used to measure nanoparticle sizes and concentrations based on NTA. This nanoparticle analysis instrument generates videos of a population of nanoparticles moving in a liquid under Brownian motion when illuminated by laser light. Within a specially designed and constructed laser illumination device mounted under a microscope lens, the particles dispersed in a liquid are detected by the instrument as small points of light moving rapidly under Brownian motion.

Despite the movement speed of the particles (in the sub-100nm size range, in particular), such motion can be tracked using a conventional CCD camera. When supported on a C-mount on the microscope and operating at 20 to 60 frames per second (fps), such cameras can be used to capture video images of particle suspensions when present in the device's approximately 80 micron-wide laser beam. Such videos can then be analysed using the NanoSight NTA analytical software program described herein, which is able to determine separately the size of each particle, as well as the accurate resulting particle size distribution profiles.

The software selects trajectories whose lifetimes are long enough to ensure statistically accurate results, ignoring those which are so short (e.g. less than 5 or 10 frames) that the estimation of their diffusion coefficient is statistically inaccurate. The possible occurrence of cross-trajectory measurements is automatically eliminated, thus minimising particle tracking errors. The simultaneous measurement of the mean squared displacement of each

particle tracked makes it possible to determine the particle diffusion coefficient and hence the sphere-equivalent, hydrodynamic diameter, using the Stokes-Einstein equation.

### A6.2 Preparation of microfluidic devices

The final procedure complies with the manufacturer's guidelines, and was selected so that the depth of the microchannels obtained in the end would be equal to 50-60 μm:

a) Cleaning of silicon wafer using plasma cleaner:

- plasma process parameters:
  - pumping down pressure to 10 Pa
  - gas supply period:
    - process length: 15 minutes
    - gas flow: 0.5 $cm^3$/min
    - process pressure: 10 Pa
  - plasma process:
    - length: 10 minutes
    - power: 100%

b) Spin-coating of photoresist (the process requires limited access to light):

- apply 2 ml of Su-8 to the central part of silicon wafer;
- spin at 500 rpm for 20 seconds and then at 2000 rpm for 30 seconds;
- remove excess Su-8 from the silicon wafer edge bead using a MicroChem Su-8 developer (for 10 seconds, starting 15 seconds before the end of the spin-coating process);
- Soft Bake step 1 – leave the silicon wafer with photoresist on a 65$^o$C hotplate for 3 minutes;
- Soft Bake step 1 – leave the silicon wafer with photoresist on a 95$^o$C hotplate for 9 minutes;
- Soft Bake step 1 – leave of the silicon wafer with photoresist on a 65$^o$C hotplate for 1 minute, and let cool down to room temperature;
- leave the silicon wafer with photo resist at room temperature in a dark place for 10 minutes for stabilisation.

c) Illumination with UV light through a mask:

- place the mask (negative, Fig. 2.10, made by the Computer to Film CtF technique), and long pass filter (LP360, to eliminate UV radiation below 350 nm, to obtain

vertical sidewalls in the photoresist) on the surface of the silicon wafer with photoresist;

- illuminate with UV light (density of power 225 mW/cm$^2$) for 5 seconds;
- leave the silicon wafer with photoresist at room temperature in a dark place for 10 minutes for stabilisation.

Fig. A6.1. Photography of a mask. The transparent areas of the mask presented the shape of future microchannel structures, through which the UV light during exposure was curing Su-8.

d) Master:

- Soft Bake step 2 – leave the silicon wafer with photoresist on a 65ºC hotplate for 2 minutes;
- Soft Bake step 2 – leave the silicon wafer with photoresist on a 95ºC hotplate for 7 minutes;
- Soft Bake step 2 – leave the silicon wafer with photoresist on a 65ºC hotplate for 1 minute, and let cool down to room temperature;
- Development - selectively remove a photoresist that has not been exposed to UVs. The development time for a 50-60 μm-thick layer of photoresist was equal to 7 minutes. After this time, the master should be washed with isopropanol alcohol. The absence of white blots denotes the complete removal of unexposed photoresist from the master. The last step was air drying.

e) PDMS poured on the master:

- The PDMS mixture is obtained by mixing two liquid components: dimethylsiloxane (monomer) and a crosslinker, in the proportion of 10:1, respectively;

- after mixing, the PDMS mixture must be degassed under reduced pressure (gradual reduction to 15 mbar);

f) Open microstructure in PDMS:

- PDMS is poured onto the master and put into the oven at a temperature of 60°C for 4 hours, to obtain crosslinked polysiloxane resin (Fig. A6.2).

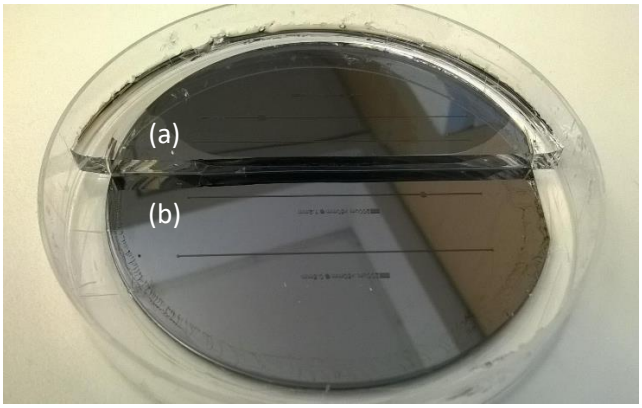


Fig. A6.2. Microstructures in PDMS (a) and master (b).

g) Microfluidic device (Fig. A6.3):

- PDMS is hydrophobic, but to attach it to the glass slide it is necessary to modify its surface properties using oxygen plasma;
- a piece of PDMS with microstructures and clean glass slide are attached using the plasma cleaner chamber;
- parameters of the plasma process:
  - pumping down pressure: 10 Pa
  - gas supply period:
    - length: 5 minutes
    - gas flow: 0.5 $cm^3$/min
    - process pressure: 10 Pa
  - plasma process:
    - length: 1 minute
    - power: 1%
- connect the microfluidic device with steel capillary or plastic tubes.

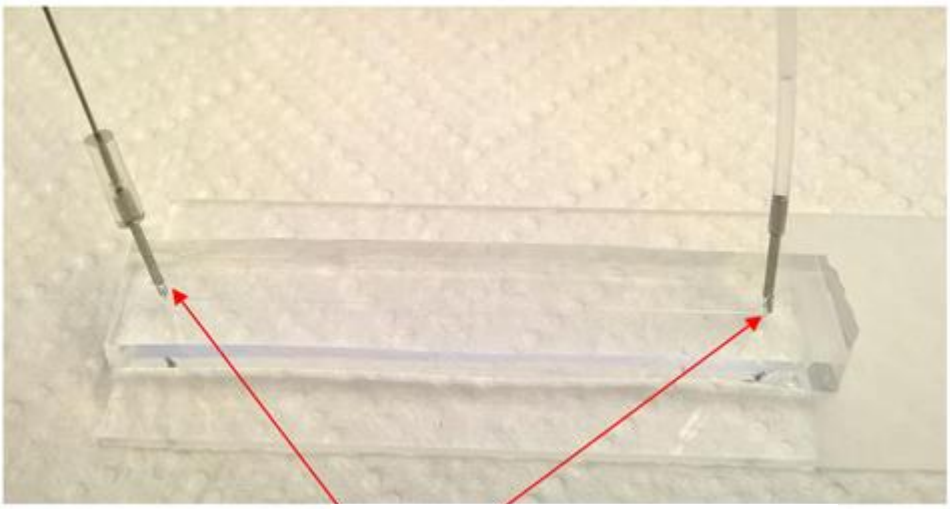

Inlet and outlet of the microchannel

Fig. A6.3. PDMS with microchannel attached to glass slide.

### A6.3 Sample preparation for spherical particle morphology analysis

Pieces of appropriately purified silica wafer were used as a substrate on which the analysed particle samples were placed. These were washed with solvents – deionized water, isopropanol, and acetone in succession – and then subjected to compressed air drying and oxygen plasma treatment (for about 10 minutes), thus obtaining an additional cleaning and increased hydrophilicity of the substrate.

The particles used for the analysis were suspended in different solutions with different dilutions:

- deionized water; particle concentration 1:1000, filtered before its application on the substrate;
- Triton X-100/methanol (1:5, 1:3, 1:1), particle concentration 1:100;
- SDS/Methanol (1:1), particle concentration 1:100;
- Tween/Methanol (1:1), particle concentration 1:100.

In order to obtain the thinnest layer (single particle layer), a spin coater was used. Spin coater process parameters:

- 200 rpm for 20 seconds;
- stop for 10 seconds;
- 1000 rpm for 20 seconds;
- stop for 10 seconds;
- 4000 rpm for 60 seconds.

After drying, samples were analysed using an AFM (Ntegra, NT-MDT), equipped with a rectangular silicon cantilever (CSG01, NT-MDT), which worked in contact mode to obtain the sample surface topography.

For SEM analysis, particle samples were sputtered with gold using a Polaron model SC7620 mini sputter coater (Quorum Technologies Ltd., Ashford, UK). Measurements were obtained using a SEM model JSM 6390 LV microscope (Jeol, Japan).

## APPENDIX 7: Biomedical application of micro and nanoobjects

### A7.1 Biomedical application of spherical particles

Colloidal gold nanoparticles are an especially promising platform of drug delivery for targeted cancer treatments. In recent years, nanomedicine preparations based on colloidal gold have been submitted to clinical trials as anticancer drugs [144]. For a successful outcome of this treatment, however, the multiple systemic administration must be safe. Furthermore, nanoparticles must be able to deliver drugs to cancer cells in a specific and effective way [223]. This is a completely new technology in the field of particle-based drug delivery to targeted tumours. Colloidal gold has also been used as an indicator for immunodiagnostics. Recently, gold nanoparticles have been combined into scaffolds to be used as biosensors and for DNA diagnostics [144]. Several therapeutic nanoparticles have been approved for clinical use. Up to now, however, there are only few clinically approved nanocarriers with molecules that selectively bind and target tumour cells [143]. In the past decades, researchers focused their attention on the development of very small metallic particles which are useful for biological and medical applications [135]. One of the first applications of metallic particles in diagnostics is magnetic resonance imaging. Today a new generation of biosensors called quantum dots has been created for implementation in medical imaging and diagnosis. The potentials of metal nanoparticles can be useful for time- and space-controlled drug release. In the case of drug delivery systems, metallic particles are presently used on either magnetically guided carriers or thermal responsive matrices. Recently, efforts have been made to develop metal nanoobjects to be used as nucleic acid vectors for vaccination and transfection [136].

Other metal-based colloids, such as iron oxide nanoparticles, are currently one of the most successful applications of nanotechnologies in medicine [136]. A second generation of iron oxide colloids has been applied to angiography, for the detection of vascular lesions associated with a disease, brain functional imaging, tumour angiogenesis imaging, and

kidney or heart perfusion. The new generation of this type of nanoparticles has made it possible to improve the MR imaging of tumours in animal models [136, 224].

Further innovative studies on the use of nanoparticles as drug carriers (vectors) focus on expanding the range of the drugs they can carry, and on testing the possibility to deliver multiple treatments on a single particle [144].

### A7.2 Biomedical application of elongated polymeric nanoobjects

Typically, polymers such as polylactic acid (PLA), poly-glycolic acid (PGA), or polycaprolactone (PCL) are used for this purpose. It appears that the best biomaterial used for this purpose is PCL. The scaffolds made of this substance have a high porosity and ratio of nanofiber surface area to occupied volume, and are morphologically similar to natural collagen fibres. It is also possible to produce them in any shape and size, and they are stable substrates. Scaffolds made from PLLA (poly-L-lactide), collagen, and PLGA (lactide-glycolide copolymer) have also been tested in vitro. It has been shown that under these conditions they are suitable for the regeneration of cartilage tissue. Their density is comparable to the density of natural tissue and they continually produce type II collagen [225].

Attempts are also being made to develop biodegradable materials capable of becoming wholesome bone replacers. They must have the appropriate mechanical properties at each stage of bone formation, be osteoconductive, and degrade at a certain rate, leaving room for the cells to form [226]. Moreover, polymers such as PCL, PGA, PLA, or PLGA, polymer composites, and biodegradable ceramics (hydroxyapatite, calcium triphosphate, calcium carbonate) are used to produce scaffolds which are used in bone tissue culture. As with the scaffolds for the development of cartilage tissue, it is important for the materials to be similar to the mineralized phase of the extracellular matrix of bone tissue. The polymer used as a matrix for ceramic particles allows for the free shaping of the implant, and solves the problem of the ceramic brittleness. What is more, this composite system has better osteoconductive properties than pure polymers. Polymer nanofibres with calcium carbonate particles exhibit a much better osteoblast adhesion than polymeric nanofibres.

Recent advances in nerve regeneration based on the application of the principles of tissue engineering have contributed to the development of a new perspective for nerve therapy. The success of neural tissue engineering is mostly based both on the tissue progression and on the regulation of cell behaviour through the development of a synthetic scaffold [227]. Scaffolds made of polymer nanofibres help regenerate the damaged central nervous

system. Their structure is similar to the extracellular substance of the central nervous system, and their porosity contributes to the inhibition of glial scars. Such synthetic scaffolds must also be a biocompatible, immunologically inert, biodegradable, infection-resistant biomaterial to support neurite outgrowth and electro-conducting [228]. Other very important properties needed for the successful graft uptake by host tissues is the compatibility and mechanical stability of scaffolds. The targeted structure of nanofibres, obtained by electrospinning, influences the behaviour of cultured cells which grow according to the orientation of the nanofibres, resulting in better nerve regeneration [229]. There is a wide choice of polymers available with the required properties. In various nerve regeneration approaches both natural (like alginate, collagen, chitosan, chitin, gelatin), and synthetic polymers have been used. The group of synthetic polymers includes: biodegradable polymers such as PLGA, poly (ε- caprolactone (PCL), poly L-lactic acid (PLLA), non-degradable polymers (silicone), and conducting polymers (polyaniline, polypyrrole). It is preferable, however, to use biodegradable materials to prevent the chronic inflammation and compression of nerves over time [227, 230].

Polymeric fibres are the best materials used for making scaffolds for the formation of blood vessels. These fibres, made of natural collagen, have poor mechanical properties. Those produced from biodegradable polymers (e.g. PGA) have better mechanical properties and high biocompatibility. PGA is easy to mould but it quickly dissolves and has little resistance to cyclic pressure changes. Polyurethane foam copolymers (PHA), PLA, and polyethylene glycol (PEG) are used to minimize the shortcomings of PGA, resulting in better mechanical properties and higher biocompatibility [226]. The polymer structure of nanometric fibres is similar to the basement membrane: therefore, some attempts have been made to use polymeric membranes (PLA or PCL) with collagen-coated fibres. The results indicate that collagen coverage improves endothelial cell viability, adhesion to the substrate, and mechanical properties, while furthermore, seeded cells do not require any additional growth factor stimulation.

A very interesting application of polymer fibre mats in surgical practice is the use of antibiotic-releasing scaffolds. Such scaffolds act as a barrier, while also controlling the delivery of the antibiotics, and could potentially decrease the frequency and severity of post-surgery adhesion (e.g. abdominal) formation [160].

One of the largest research areas in the field of drug delivery is the targeted and controlled delivery of anticancer drugs [161]. The surface area and dimensions of the fibres used as cancer drug carriers are very important. A very small nanofibre diameter provides a short

diffusion passage length [231], while the large surface area is helpful in transferring the mass and effective drug release [157]. The features of the drug release depend on the quality of the drug encapsulation in the fibres [156].

# Literature


[1] M. Kochańczyk, J. Jaruszewicz, T. Lipniacki, "Stochastic transitions in a bistable reaction system on the membrane", Journal of The Royal Society Interface, vol. 10, no. 84, pp. 1-12, 2013.

[2] J. Jaruszewicz, P. J. Żuk, T. Lipniacki, "Type of noise defines global attractors in bistable molecular regulatory systems", Journal of Theoretical Biology, vol. 317, pp. 140-151, 2013.

[3] S. Tay, J. J.Hughey, T. K. Lee, T. Lipniacki, S. R. Quake, M. W. Covert, "Single-cell NF-kB dynamics reveal digital activation and analogue information processing", Nature, vol. 466, pp. 267-271, 2010.

[4] R. A. Kellogg, C. Tian, T. Lipniacki, S. R. Quake, S. Tay, "Digital signaling decouples activation probability and population heterogeneity", eLIFE, vol. 4, pp. e08931-1-26, 2015.

[5] W. Pabst, E. Gregorova, "Characterization of particles and particle systems". ICT Prague, 2007.

[6] K. M. Krueger, A. M. Al-Somali, M. Mejia, V. L. Colvin, "The hydrodynamic size of polymer stabilized nanocrystals", Nanotechnology, vol. 18, pp. 475709-1-7, 2007.

[7] M. R. Gittings, D. A. Saville, "The determination of hydrodynamic size and zetapotential from electrophoretic mobility and light scattering measurements", Colloids Surf. A, vol. 141, pp. 111-117, 1998.

[8] R. Xu, "Shear plane and hydrodynamic diameter of microspheres in suspension", Langmuir, vol. 14, pp. 2593-2597, 1998.

[9] Ch.-H. Fischer, E. Kenndler, "Analysis of colloids IX. Investigation of the electrical double layer of colloidal inorganic nanometer-particles by size-exclusion chromatography", J. Chromatogr. A, vol. 773, pp. 179-187, 1997.

[10] C. Chassagne, M. Ibanez, "Hydrodynamic size and electrophoretic mobility of latex nanospheres in monovalent and divalent electrolytes", Colloids and Surfaces A: Physicochem. Eng. Aspects, vol. 440, pp. 208-216, 2014.

[11] Y. Sun, "New interpretation for laser light scattering, arXiv:physics/0511159v1, 2005.

[12] J. Gross, S. Sayle, A. R. Karow, U. Bakowsky, P. Garidel, "Nanoparticle tracking analysis of particle size and concentration detection in suspensions of polymer and protein samples: influence of experimental and data evaluation parameters", European Journal of Pharmaceutics and Biopharmaceutics, vol. 104, pp. 30-41, 2016.

[13] M. Carboni, "Nanostructures for protection and vehiculation of bioactive molecules". PhD thesis, University of Cagliari, Cagliari, 2012.

[14] K. Bohinc, V. Kralj-Iglic, A. Iglic, "Thickness of electrical double layer. Effect of ion size", Electrochimica Acta, vol. 46, pp. 3033-3040, 2001.

[15] A. Drechsler, K. Grundke, "The influence of electrolyte ions on the interaction forces between polystyrene surfaces", Colloids and Surfaces A: Physicochem. Eng. Aspects, vol. 264, pp. 157–165, 2005.

[16] B. V. Derjaguin, N. V. Churaev, V. M. Muller, "Surface forces: The Derjaguin—Landau—Verwey—Overbeek (DLVO) theory of stability of lyophobic colloids", Springer Science + Business Media New York, pp. 293-310, 1987.

[17] D. H. Everett, "Basic principles of colloid science", The Royal Society of Chemistry, pp. 130-134, 1988.

[18] S. Birner, C. Uhl, M. Bayer, P. Vogl, "Theoretical model for the detection of charged proteins with a silicon-on-insulator sensor", J. Phys.: Conf. Ser., vol. 107, pp. 012002-1-15, 2008.

[19] P. Jurney, R. Agarwal, V. Singh, K. Roy, S. V. Sreenivasan, L. Shi, "Size-dependent nanoparticle margination and adhesion propensity in a microchannel", Journal of Nanotechnology in Engineering and Medicine, vol. 4, pp. 031002-1-7, 2013.

[20] K. Zembrzycki, S. Błoński, T. A. Kowalewski, "Analysis of wall effect on the process of diffusion of nanoparticles in a microchannel", J. Phys.: Conf. Ser., vol. 392, pp. 012014, 2012.

[21] E. Lauga, T. M. Squires, "Brownian motion near a partial-slip boundary: A local probe of the no-slip condition", Phys. Fluids, vol. 17, pp. 103102-1-16, 2005.

[22] E. S. Medeiros, G. M. Glenn, A. P. Klamczynski, W. J. Orts, L. H. C. Mattoso, "Solution blow spinning: a new method to produce micro- and nanofibres from polymer solutions", Journal of Applied Polymer Science, vol. 113, pp. 2322-2330, 2009.

[23] T . Grafe, K. Graham, "Polymeric nanofibres and nanofibre webs: a new class of nonwovens", International Nonwovens Technical Conference, Atlanta, Georgia, 2002.

[24] A. Formalas, "Process and apparatus for preparing artificial threads", US patent 1,975,504, 1934.

[25] D. Li, Y. Xia, "Electrospinning of nanofibres: reinventing the wheel?", Adv. Mater., vol. 16, no. 14, pp. 1151-1170, 2004.

[26] A. Greiner, J. H. Wendorff, "Electrospinning: A fascinating method for the preparation of ultrathin fibres", Angew. Chem. Int. Ed., vol. 46, pp. 5670-5703, 2007.

[27] P. Nakielski, **S. Pawlowska**, F. Pierini, V. Liwinska, P. Hejduk, K. Zembrzycki, E. Zabost, T. A. Kowalewski, "Hydrogel nanofilaments via core-shell electrospinning", PLOS ONE, vol. 10, no. 6, pp. 1-16, 2015.

[28] T. A. Kowalewski, S. Błoński, S. Barral, "Experiments and modelling of electrospinning process", Bulletin Of The Polish Academy Of Sciences Technical Sciences, vol. 53, no. 4, pp. 385-394, 2005.

[29] P. Nakielski, "Systemy uwalniania leków oparte na nanowłóknach", IPPT Reports on Fundamental Technological Research, vol. 1, pp. 1-216, 2015.

[30] J. Stanger, N. Tucker, A. Wallace, N. Larsen, M. Staiger, R. Reeves, "The effect of electrode configuration and substrate material on the mass deposition rate of electrospinning", Journal of Applied Polymer Science, vol. 112, pp. 1729-1737, 2009.

[31] P. Kumar, "Effect of collector on electrospinning to fabricate aligned nanofiber", Bachelor thesis, National Institute of Technology, Rourkela, 2012.

[32] M. M. Hohman, M. Shin, G. Rutledge, M. P. Brenner, "Electrospinning and electrically forced jets. I. Stability theory", Physics of Fluids, vol. 13, no.8, pp. 2201-2220, 2001.

[33] F. Pierini, M. Lanzi, P. Nakielski, **S. Pawłowska**, O. Urbanek, K. Zembrzycki, T. A. Kowalewski, "Single-material organic solar cells based on electrospun fullerene-grafted polythiophene nanofibers", Macromolecules, vol. 50, no. 13, pp. 4972-4981, 2017.

[34] F. Pierini, M. Lanzi, P. Nakielski, **S. Pawłowska**, K. Zembrzycki, T. A. Kowalewski, "Electrospun poly(3-hexylthiophene)/poly(ethylene

oxide)/graphene oxide composite nanofibers: effects of graphene oxide reduction", Polymers for Advanced Technologies, vol. 27, no. 11, pp. 1465-1475, 2016.

[35] A. V. Bazilevsky, A. L. Yarin, C. M. Megaridis, "Co-electrospinning of core−shell fibres using a single-nozzle technique", Langmuir, vol. 23, pp. 2311-2314, 2007.

[36] Ch. Wang, L. Wang, M. Wang, "Evolution of core-shell structure: from emulsions to ultrafine emulsion electrospun fibres", Materials Letters, vol. 124, pp. 192-196, 2014.

[37] H. Qu, S. Wei, Z. Guo, "Coaxial electrospun nanostructures and their applications", J. Mater. Chem. A, vol. 1, pp. 11513-11528, 2013.

[38] D.-G. Yu, J. H. Yu, L. Chen, G. R. Williams, X. Wang, "Modified coaxial electrospinning for the preparation of high-quality ketoprofen-loaded cellulose acetate nanofibers", Carbohydr Polym., vol. 90, pp. 1016-1023, 2012.

[39] M. F. Elahi, W. Lu, G. Guoping, F. Khan, "Core-shell fibres for biomedical applications - A review", J. Bioengineer and Biomedical Sci., vol. 3, no. 1, pp. 1-14, 2013.

[40] J. D´ıaz, A. Barrero, M. M´arquez, I. Loscertales, "Controlled encapsulation of hydrophobic liquids in hydrophilic polymer nanofibres by co-electrospinning", Adv. Funct. Mater., vol. 16, pp. 2110-2116, 2006.

[41] A. Ortega, J. Garcia de la Torre, "Hydrodynamic properties of rodlike and disklike particles in dilute solution", J Chem Phys., vol. 119, no. 18, pp. 9914-9919, 2003.

[42] J. Philibert, "One and a half century of diffusion: Fick, Einstein, before and beyond", Diffusion Fundamentals, vol. 4, pp. 6.1-6.19, 2006.

[43] S. R. de Groot, P. Mazur, "Nonequilibrium thermodynamics", North Holland Publishing Company, Amsterdam, 1962.

[44] M. A. Charsooghi, E. A. Akhlaghi, S. Tavaddod, H. R. Khalesifard, "A MATLAB program to calculate translational and rotational diffusion coefficients of a single particle", Computer Physics Communications, vol. 182, pp. 400-408, 2011.

[45] A. J. Levine, T. B. Liverpool, F. C. MacKintosh, "Mobility of extended bodies in viscous films and membranes", Phys. Rev. E, vol. 69, pp. 021503-1-10, 2004.

[46] A. Einstein, "Investigations on the theory of the Brownian movement, Dover, New York, 1956.

[47] A. Loman, I. Gregor, C. Stutz, M. Mundb, J. Enderlein, "Measuring rotational diffusion of macromolecules by fluorescence correlation spectroscopy", Photochem. Photobiol. Sci., vol. 9, pp. 627-636, 2010.

[48] O. Kratky, G. Porod, "Röntgenuntersuchung gelöster Fadenmoleküle", Rec. Trav. Chim. Pays-Bas., vol. 68, pp. 1106-1122, 1949.

[49] H. Yamakawa, "Modern theory of polymer solutions", Harper & Row Publishers, New York, 1971.

[50] A. M. Słowicka, M. L. Ekiel-Jeżewska, K. Sadlej, E. Wajnryb, "Dynamics of fibres in a wide microchannel", J. Chemical Physics, vol. 136, pp. 044904-1-8, 2012.

[51] K. Sadlej, E. Wajnryb, M. L. Ekiel-Jezewska, D. Lamparska, T. A. Kowalewski, "Dynamics of nanofibres conveyed by low Reynolds number flow in a microchannel", Int. J. Heat Fluid Flow, vol. 31, pp. 996-1004, 2010.

[52] L. Dai, Y. Mu, L. Nordenskio, J. R. C. van der Maarel, "Molecular dynamics simulation of multivalent-ion mediated attraction between DNA molecules", Phys. Rev. Lett., vol. 100, pp. 118301-1-4, 2008.

[53] A. M. Słowicka, E. Wajnryb, M. L. Ekiel-Jeżewska, "Lateral migration of flexible fibres in Poiseuille flow between two parallel planar solid walls", Eur. Phys. J. E, vol. 36, no. 31, pp. 1-12, 2013.

[54] P. Szymczak, M. Cieplak, "Influence of hydrodynamic interactions on mechanical unfolding of proteins", J. Phys.: Condens. Matter, vol. 19, pp. 285224-1-12, 2007.

[55] D. R. Steinhauser, "Actin filaments and bundles in flow", PhD thesis, Georg August University of Göttingen, Göttingen, 2008.

[56] R. G. Larson, "The rheology of dilute solutions of flexible polymers: progress and problems", Journal of Rheology, vol. 49, no. 1, pp. 1-70, 2005.

[57] A.-K. Tornberg, M. J. Shelley, "Simulation the dynamics and interactions of flexible fibres in Stokes flow", Journal of Computational Physics, vol. 196, pp. 8-40, 2004.

[58] B. Delmotte, E. Climent, F. Plouraboue, "A general formulation of Bead Models applied to flexible fibres and active filaments at low Reynolds number", Journal of Computational Physics, vol. 286, pp. 14-37, 2015.

[59] S. Reddig, H. Stark, "Cross-streamline migration of a semiflexible polymer in a pressure driven flow", J. Chem. Phys., vol. 135, pp. 165101-1-11, 2011.

[60] R. Khare, M. D. Graham, J. J. de Pablo, "Cross-stream migration of flexible molecules in a nanochannel", Physical Review Letters, vol. 96, pp. 224505-1-4, 2006.

[61] P. S. Doyle, B. Ladoux, J.-L. Viovy, "Dynamics of a tethered polymer in shear flow", Physical Review Letters, vol. 84, no. 20, pp. 4769-4772, 2000.

[62] D. E. Smith, H. P. Babcock, S. Chu, "Single-polymer dynamics in steady shear flow", Science, vol. 283, pp. 1724-1727, 1999.

[63] K. Jo, Y. L. Chen., J. J. de Pablo, D. C. Schwartz, "Elongation and migration of single DNA molecules in microchannels using oscillatory shear flows", Lab on a Chip, vol. 9, no. 16, pp. 2348-2355, 2009.

[64] M. Harasim, B. Wunderlich, O. Peleg, M. Kröger, A. R. Bausch, "Direct observation of the dynamics of semiflexible polymers in shear flow", Physical Review Letters, vol. 110, pp. 108302-1-5, 2013.

[65] R. Herczynski, "Fåhræus effect revisited", Arch. Mech., vol. 68, no. 1, pp. 81–93, 2016.

[66] G. Segre, A. Silberberg, "Radial particle displacements in Poiseuille flow of suspensions", Nature, vol. 189, pp. 209-210, 1961.

[67] G. Segre, A. Silberberg, "Behaviour of macroscopic rigid spheres in Poiseuille flow. Part2. Experimental results and interpretation", J. Fluid Mech., vol. 14, pp. 136-157, 1962.

[68] F. J. Gauthier, H. L. Goldsmith, S. G. Mason, "Flow of suspensions through tubes – X. Liquid drops as models of erythrocytes", Biorheology, vol. 9, pp. 205-224, 1972.

[69] P. C. H. Chan, L. G. Leal, "Motion of a deformable drop in a second order fluid", J. Fluid Mech., vol. 92, pp. 131-170, 1979.

[70] W. Hiller, T. A. Kowalewski, "An experimental study of the lateral migration of a droplet in a creeping flow", Exp. in Fluids, vol. 5, pp. 43-48, 1987.

[71] H. A. Stone, "Dynamics of drop deformation and breakup in viscous fluids", Annu. Rev. Fluid Mech., vol. 26, pp. 65-102, 1994.

[72] S. Mortazavi, G. Tryggvason, "A numerical study of the motion of drops in Poiseuille flow. Part1. Lateral migration of one drop", J. Fluid Mech., vol. 411, pp. 325-350, 2000.
[73] X. Chen, Ch. Xue, L. Zhang, G. Hu., X. Jiang, J. Sun, "Inertial migration of deformable droplets in a microchannel", Phys. Fluids, vol. 26, pp. 112003-1-25, 2014.
[74] C. A. Stan, L. Guglielmini, A. K. Ellerbee, D. Caviezel, H. A. Stone, G. M. Whitesides, "Sheathless hydrodynamic positioning of buoyant drops and bubbles inside microchannels", Phys. Rev. E, vol. 84, pp. 036302-1-19, 2011.
[75] K. Chaudhury, S. Mandal, S. Chakraborty, "Droplet migration characteristics in confined oscillatory microflows", Phys. Rev. E, vol. 93, pp. 023106-1-18, 2016.
[76] T. V. Starkey, "The laminar flow of streams of suspended particles", Brit. J. Appl. Phys., vol. 7, no. 2, pp. 52-55, 1956.
[77] A. Brandt, G. Bugliarello, "Concentration redistribution phenomena in the shear flow of monolayers of suspended particles", Trans. Soc. Rheo., vol. 10, no. 1, pp. 229-251, 1966.
[78] A. D. Maude, J. A. Yearn, "Particle migrations in suspension flows", J. Fluid Mech., vol. 30, pp. 601-621, 1967.
[79] B. P. Ho, L. G. Leal, "Inertial migration of rigid spheres in two-dimensional unidirectional flows", J. Fluid Mech., vol. 65, no. 2, pp. 365-400, 1974.
[80] G. B. Jeffery, "The motion of ellipsoidal particles immersed in a viscous fluid", Proc. Roy. Soc. A, vol. 102, pp. 161-179, 1922.
[81] L. C. Nitsche, E. J. Hinch, "Shear-induced lateral migration of Brownian rigid rods in parabolic channel flow", J. Fluid Mech., vol. 332, pp. 1-21, 1997.
[82] H. Amini, W. Lee, D. Di Carlo, "Inertial microfluidic physics", Lab on the Chip, vol. 14, pp. 2739-2761, 2014.
[83] S. Yang, G. Dou, "Drag reduction in a flat-plate turbulent boundary layer flow by polymer additives", Physics of Fluids, vol. 17, no. 6, pp. 065104-1-13, 2005.
[84] G. H. Michler, F. J. Balta-Calleja, "Mechanical properties of polymers based on nanostructure and morphology", Taylor &Francis Group, 2005.
[85] N. Mücke, K. Klenin, R. Kirmse, M. Bussiek, H. Herrmann, M. Hafner, J. Langowski, "Filamentous biopolymers on surfaces: atomic force microscopy images compared with brownian dynamics simulation of filament deposition", PLOS ONE, vol. 4, no. 11, e7756-1-7, 2009.
[86] S. E. Bresler, Y. I. Frenkel, "The character of thermal motion of long organic chains with reference to the elastic properties of rubber", Zh. Eksp. Teor. Fiz., vol. 9, pp. 1094-1106, 1939.
[87] Z. Florjańczyk, S. Penczek (ed.), "Chemia polimerów. Makrocząstki i metody ich otrzymywania", Oficyna Wydawnicza Politechniki Warszawskiej, 1995.
[88] J. S. Graham, B. R. McCullough, H. Kang, W. A. Elam, W. Cao, E. M. De La Cruz, "Multi-platform compatible software for analysis of polymer bending mechanics", PLOS ONE, vol. 9, no. 4, pp. e94766-1-6, 2014.
[89] T. B. Liverpool, "Active gels: where polymer physics meets cytoskeletal dynamics", Phil. Trans. R. Soc. A, vol. 364, pp. 3335-3355, 2006.
[90] F. Gittes, B. Mickey, J. Nettleton, J. Howard, "Flexural rigidity of microtubules and actin filaments measured from thermal fluctuations in shape", The Journal of Cell Biology, vol. 120, no. 4, pp. 923–934, 1993.

[91] E. J. Janson, M. Dogterom, "A bending mode analysis for growing microtubules: evidence for a velocity-dependent rigidity", Biophys. J., vol. 87, pp. 2723-2736, 2004.
[92] A. Ott, M. Magnasco, A. Simon, A. Libchaber, "Measurement of the persistence length of polymerized actin using fluorescence microscopy", Physical Review E, vol. 48, no. 3, pp. R1642-R1645, 1993.
[93] M. Doi, S. F. Edwards, "The theory of polymer dynamics. International series of monographs on physics", Clarendon Press, 1986.
[94] Z. Maolin, L. Jun, Y. Min, H. Hongfei, "The swelling behavior of radiation prepared semi-interpenetrating polymer networks composed of polyNIPAAm and hydrophilic polymers", Radiation Physics and Chemistry, vol. 58, pp. 397-400, 2000.
[95] F. Sabbagh, I. I. Muhamad, "Acrylamide-based hydrogel drug delivery systems: release of acyclovir from MgO nanocomposite hydrogel", Journal of the Taiwan Institute of Chemical Engineers, vol. 72, pp. 182-193, 2017.
[96] M. Kurečič, M. Sfiligoj-Smole, K. Stana-Kleinschek, "UV polymerization of poly (N-isopropylacrylamide) hydrogel", Materials and Technology, vol. 46, no. 1, pp. 87-91, 2012.
[97] J. R. Tse, A. J. Engler, "Current protocols in cell biology: preparation of hydrogel substrates with tunable mechanical properties", John Wiley & Sons, Inc., supplement 47, 10.161-16, 2010.
[98] T. Kanai, D. Lee, H. C. Shum, D. A. Weitz, "Fabrication of tunable spherical colloidal crystals immobilized in soft hydrogels", Small Journal, vol. 6, no. 7, pp. 807-810, 2010.
[99] Z. Wei, Z. Jia, J. Athas, C. Wang, S. R. Raghavan, T. Li, Z. Nie, "Hybrid hydrogel sheets that undergo pre-programmed shape transformations", Royal Society of Chemistry Soft Matter, vol. 10, pp. 8157-8162, 2014.
[100] Y. Ono, T. Shikata, "Hydration and dynamic behavior of poly(n-isopropylacrylamide)s in aqueous solution: a sharp phase transition at the lower critical solution temperature", J. Am. Chem. Soc., vol. 128, no. 31, pp. 10030–10031, 2006.
[101] J. H. Priest, S. L. Murray, R. J. Nelson, A. S. Hoffma, "Reversible polymeric gels and related systems: lower critical solution temperatures of aqueous copolymers of N-isopropylacrylamide and other N-substituted acrylamides", American Chemical Society, Washington, DC, pp. 255-264, 1987.
[102] K. Zembrzycki, **S. Pawłowska**, P. Nakielski, F. Pierini, "Development of a hybrid Atomic Force Microscope and Optical Tweezers apparatus", IPPT Reports on Fundamental Technological Research, vol. 2, pp.1-58, 2016.
[103] www.therom.com/particletechnology
[104] M. L. Bleam, C. F. Anderson, M. T. J. Record, "Relative binding affinities of monovalent cations for double-stranded DNA", Proc. Natl Acad. Sci. USA, vol. 77, no. 6, pp. 3085-3089, 1980.
[105] Y. Wang, I. A. Weinstock, "Polyoxometalate-decorated nanoparticles. Chem. Soc. Rev., vol. 41, pp. 7479-7496, 2012.
[106] A. E. Larsen, D. G. Grier, "Like-charge attractions in metastable colloidal crystallites", Nature, vol. 385, pp. 230-233, 1997.
[107] C. A. Murray, "When like charges attract", Nature news and views, vol. 385, pp. 203-204, 1997.
[108] S. Assemi, J. Nalaskowski, W. P. Johnson, "Direct force measurements between carboxylate-modified latex microspheres and glass using atomic force

microscopy", Colloids and Surfaces A: Physicochem. Eng. Aspects, vol. 286, pp. 70-77, 2006.

[109] F. Pierini, K. Zembrzycki, P. Nakielski, **S. Pawłowska**, T. A. Kowalewski, "Atomic force microscopy combined with optical tweezers (AFM/OT)", Meas. Sci. Technol., vol. 27, pp. 025904-1-11, 2016.

[110] W. S. Rasband, ImageJ, U. S. National Institutes of Health, Bethesda, Maryland, USA, 1997-2014, 2014. Available: http://www.imagej.nih.gov/ij.

[111] Matlab, Mathworks, www.mathworks.com, 2014

[112] B. Bhaduri, A. Neild, T. W. Ng, "Directional Brownian diffusion dynamics with variable magnitudes", Appl. Phys. Lett., vol. 92, no. 8, pp. 084105-1-3, 2008.

[113] E. P. Tan, C. T. Lim, "Mechanical characterization of nanofibers - A review", Compos Sci Technol., vol. 66, pp. 1102-1111, 2006.

[114] M. Ahearne, Y. Yang, A. J. El Haj, K. Y. Then, K.-K. Liu, "Characterizing the viscoelastic properties of thin hydrogel-based constructs for tissue engineering applications", Journal of The Royal Society Interface, vol. 2, pp. 455-463, 2005.

[115] S. Kasas, G. Longo, G. Dietler, "Mechanical properties of biological specimens explored by atomic force microscopy", J. Phys. D: Appl. Phys., vol. 46, pp. 133001-1-12, 2013.

[116] M. Kikumoto, M. Kurachi, V. Tosa, H. Tashiro, "Flexural rigidity of individual microtubules measured by a buckling force with optical traps", Biophysical Journal, vol. 90, pp. 1687-1696, 2006.

[117] V. Kantsler, R. E. Goldstein, "Fluctuations, dynamics, and the stretch-coil transition of single actin filaments in extensional flows", Phys. Rev. Lett., vol. 108, no. 3, pp. 038103-1-5, 2012.

[118] L. Li, H. Manikantan, D. Saintillan, S. E. Spagnolie, "The sedimentation of flexible filaments", J. Fluid Mech., vol. 735, pp. 705-736, 2013.

[119] H. M. Lopez, J.-P. Hulin, H. Auradou, M. D'Angelo, "Deformation of a flexible fiber in a viscous flow past an obstacle", Phys. Fluids, vol. 27, pp. 013102-1-12, 2015.

[120] G. A. Evingür, Ö. Pekcan, "Elastic properties of a swollen PAAm-NIPA copolymer with various NIPA contents", Polymer-Plastics Technology and Engineering, vol. 53, pp. 834-839, 2014.

[121] O. San, A. E. Staples, "An improved model for reduced-order physiological fluid flows", J. Mech. Med. Biol., vol. 12, no. 3, pp. 1250052-1-28, 2012.

[122] **S. Pawłowska**, "Highly deformable nanofilaments in flow", Journal Of Physics: Conference Series, vol. 760, pp. 1-10, 2016.

[123] D. Steinhauser, S. Köster, T. Pfohl, "Mobility gradient induces cross-streamline migration of semiflexible polymers", ACS Macro Lett., vol. 1, pp. 541-545, 2012.

[124] B. Nöding, S. Köster, "Intermediate filaments in small configuration spaces", Phys. Rev. Lett., vol. 108, no. 8, pp. 088101-1-4, 2012.

[125] K.S. Bloom, "Beyond the code: the mechanical properties of DNA as they relate to mitosis", Chromosoma, vol. 117, no. 2, pp. 103-110, 2008.

[126] **S. Pawłowska**, P. Nakielski, F. Pierini, I. K. Piechocka, K. Zembrzycki, T. A. Kowalewski, "Lateral migration of electrospun hydrogel nanofilaments in an oscillatory flow", PLOS ONE, vol. 12, no. 11, pp. 1-21, 2017.

[127] N. Quennouz, M. Shelley, O. du Roure, A. Lindner, "Transport and buckling dynamics of an elastic fibre in a viscous cellular flow", J. Fluid Mech., vol. 769, pp. 387-402, 2015.
[128] E. Wandersman, N. Quennouz, M. Fermigier, A. Lindner, O. du Roure, "Buckled in translation", Soft Matter., vol. 6, pp. 5715-5719, 2010.
[129] P. LeDuc, C. Haber, G. Bao, D. Wirtz, "Dynamics of individual flexible polymers in a shear flow", Nature., vol. 399, pp. 564-566, 1999.
[130] Y.J. Chen, S. Johnson, P. Mulligan, A.J. Spakowitz, R. Phillips, "Modulation of DNA loop lifetimes by the free energy of loop formation", Proc. Natl. Acad. Sci., vol. 111, no. 49, pp. 17396-17401, 2014.
[131] A. Izmitli, D.C. Schwartz, M.D. Graham, J.J. de Pablo, "The effect of hydrodynamic interactions on the dynamics of DNA translocation through pores", J. Chem. Phys., vol. 128, no. 8 pp. 085102-1-7, 2008.
[132] A. Farutin, T. Piasecki, A.M. Słowicka, Ch. Misbah, E. Wajnryb, M.L. Ekiel-Jezewska, "Dynamics of flexible fibers and vesicles in Poiseuille flow at low Reynolds number", Soft Matter., vol. 12, no. 35, pp. 7307-23, 2016.
[133] R. Chelakkot, R.G. Winkler, G. Gompper, "Migration of semiflexible polymers in microcapillary flow", EPL., vol. 91, no. 1, pp. 14001-1-6, 2010.
[134] J.J. de Pablo, H.C. Ottinger, Y. Rabin, "Hydrodynamic changes of the depletion layer of dilute polymer solutions near a wall", AIChE J., vol. 38, no. 2, pp. 273-283, 1992.
[135] K. Bogunia-Kubik, M. Suguisaka, "From molecular biology to nanotechnology and nanomedicine", BioSystems, vol. 65, pp. 123-138, 2002.
[136] F. Sonvico, C. Dubernet, P. Colombo, P. Couvreur, "Metallic based nanotechnology, applications in diagnosis and therapeutics", Curr. Pharm. Des., vol. 11, no. 16, pp. 2091-2105, 2005.
[137] Z. Wang, "Imaging nanotherapeutics in inflamed vasculature by intravital microscopy", Theranostics, vol. 6, no. 13, pp. 2431-2438, 2016.
[138] A. Samborski, P. Jankowski, J. Węgrzyn, J. A. Michalski, **S. Pawłowska**, S. Jakieła, P. Garstecki, "Blood diagnostics using sedimentation to extract plasma on a fully integrated point-of-care microfluidic system", Engineering in Life Sciences, vol. 15, no. 3, pp. 333-339, 2015.
[139] O. C. Farokhzad, R. Langer, "Impact of nanotechnology on drug delivery", ACS Nano, vol. 3, no. 1, pp. 16-20, 2009.
[140] P. Decuzzi, R. Pasqualini, W. Arap, M. Ferrari., "Intravascular delivery of paniculate systems: does geometry really matter?", Pharm. Res., vol. 26, no. 1, pp. 235-243, 2009.
[141] S. S. Davis, "Biomedical applications of nanotechnologysimplications for drug targeting and gene therapy", Trends Biotechnol. 15, 217-224, 1997.
[142] T. M. Allen, P. R. Cullis, "Drug delivery systems: entering the mainstream", Science, vol. 303, no. 5665, pp. 1818-1822, 2004.
[143] D. Peer, J. M. Karp, S. Hong, , O. C. Farokhzad, R. Margalit, R. Langer, , "Nanocarriers as an emerging platform for cancer therapy", Nat. Nanotechnol., vol. 2, no. 12, pp. 751-760, 2007.
[144] G. F. Paciotti, L. Myer, D. Weinreich, D. Goia, N. Pavel, R. E. McLaughlin, L. Tamarkin, "Colloidal gold: a novel nanoparticle vector for tumour directed drug delivery", Drug Delivery, vol. 11, pp. 169-183, 2004
[145] J. Kreuter, "Nanoparticulate systems for brain delivery of drugs", Adv. Drug Delivery Rev., vol. 47, pp. 65-81, 2001.

[146] A. Daddi-Moussa-Ider, S. Gekle, "Hydrodynamic mobility of a solid particle near a spherical elastic membrane: Axisymmetric motion", Physical Review E, vol. 95, 013108-1-16, 2017.
[147] D. Chu, J. Gao, Z. Wang, "Neutrophil-mediated delivery of therapeutic nanoparticles across blood vessel barrier for treatment of inflammation and infection", ACS Nano, vol. 9, pp. 11800-11, 2015.
[148] A. Moore, J. P. Basilion, E. A. Chiocca, R. Weissleder, "Measuring transferrin receptor gene expression by NMR imaging", Biochim Biophys Acta, vol. 1402, pp. 239-249, 1998.
[149] P. Erbacher, S. Zou, T. Bettinger, A. M. Steffan, J. S. Remy, "Chitosan-based vector/DNA complexes for gene delivery: biophysical characteristics and transfection ability", Pharm. Res., vol. 15, no. 9, pp. 1332-1339, 1998.
[150] S. Agarwal, J. H. Wendorff, A. Greiner, "Use of electrospinning technique for biomedical applications", Polymer, vol. 49, pp. 5603-5621, 2008.
[151] N. Khan, "Applications of electrospun nanofibers in the biomedical field", Studies by Undergraduate Researchers at Guelph, vol. 5, no. 2, pp. 63-73, 2012.
[152] D. Kołbuk, S. Guimond-Lischer, P. Sajkiewicz, K. Maniura-Weber, G. Fortunato, "Morphology and surface chemistry of bicomponent scaffolds in terms of mesenchymal stromal cell viability", Journal of Bioactive and Compatible Polymers, vol. 1, pp. 1-14, 2016.
[153] J. Dulnik, P. Denis, P. Sajkiewicz, D. Kołbuk, E. Choińska, "Biodegradation of bicomponent PCL/gelatin and PCL/collagen nanofibers electrospun from alternative solvent system", Polymer Degradation and Stability, vol. 130, pp. 10-21, 2016.
[154] M. M. Stevens, J. H. George, "Exploring and engineering the cell surface interface", Science, vol. 310, pp. 1135-1138, 2005.
[155] S. Grad, L. Kupsik, K. Gorna, S. Gogolewski, M. Alini, "The use of biodegradable polyurethane scaffolds for cartilage tissue engineering: potential and limitations", Biomaterials, vol. 24, pp. 5163-5171, 2003.
[156] Y. Z. Zhang, C.T. Lim, S. Ramakrishna, Z.-M. Huang, "Recent development of polymer nanofibers for biomedical and biotechnological applications", J Mater Science Mater Med., vol. 16, no. 10, pp. 933-946, 2005.
[157] G. Verreck, I. Chun, J. Rosenblatt, J. Peeters, A. V. Dijck, J. Mensch, M. Noppe, M. E. Brewster, "Incorporation of drugs in an amorphous state into electrospun nanofibers composed of a waterinsoluble, nonbiodegradable polymer", J. Controlled Release, vol. 92, pp. 349-360, 2003.
[158] W. Cui, Y. Zhou, J. Chang, "Electrospun nanofibrous materials for tissue engineering and drug delivery", Sci. Technol. Adv. Mater., vol. 11, pp. 014108-1-11, 2010.
[159] Z. M. Huang, C. L. He, A. Yang, Y. Zhang, X. J. Han, J. Yin, Q. Wu, "Encapsulating drugs in biodegradable ultrafine fibers through co-axial electrospinning", J. Biomed. Mater. Res. A, vol. 77, no. 1, pp. 169-179, 2006.
[160] N. Bölgen, I. Vargel, P. Korkusuz, Y. Z. Menceloğlu, E. Pişkin, "In vivo performance of antibiotic embedded electrospun PCL membranes for prevention of abdominal adhesions", J. Biomed. Mater. Res. B Appl. Biomater., vol. 81, no. 2, pp. 530-543, 2007.
[161] J. Xie, C. H. Wang, "Electrospun micro- and nanofibers for sustained delivery of paclitaxel to treat C6 glioma in vitro", Pharm Res., vol. 23, no. 8, pp. 1817-1826, 2006.

[162] H. Nie, C. H. Wang, "Fabrication and characterization of PLGA/Hap composite scaffolds for delivery of BMP-2 plasmid DNA", J. Control Release, vol. 120, pp. 111-121, 2007.
[163] H. Jiang, Y. Hu, P. Zhao, Y. Li, K. Zhu, "Modulation of protein release frombiodegradable core-shell structured fibers prepared by coaxial electrospinning", J. Biomed. Mater. Res. B Appl. Biomater., vol.79, no. 1, pp. 50-57, 2006.
[164] D. Liang, Y. K. Luu, K. Kim, B. S. Hsiao, M. Hadjiargyrou, B. Chu, "In vitro non-viral gene delivery with nanofibrous scaffolds", Nucleic Acids Res, vol. 33, no. 19, pp. e170-1-8, 2005.
[165] T. J. Sill, H. A. von Recum, "Electrospinning: applications in drug delivery and tissue engineering", Biomaterials, vol. 29, pp. 1989-2006, 2008.
[166] Z. Sun, E. Zussman, A. L. Yarin, J. H. Wendorff, A. Greiner, "Compound core-shell polymer nanofibers by co-electrospinning", Adv. Mater., vol. 22, no. 22, pp. 1929-1932, 2003.
[167] I. G. Loscertales, A. Barrero, M. Marquez, R. Spretz, R. Verlarde-Ortiz, G. Larsen, "Electrically forced coaxial nanojets for one-step hollow nanofiber design", J. Am. Chem. Soc., vol. 126, pp. 5376–5377, 2004.
[168] T. Kowalczyk, A. Nowicka, D. Elbaum, T. A. Kowalewski, "Electrospinning of bovine serum albumin. Optimization and the use for production of biosensors", Biomacromolecules, vol. 9, no. 7, pp. 2087-2090, 2008.
[169] P. Nakielski, T. Kowalczyk, K. Zembrzycki, T. A. Kowalewski, "Experimental and numerical evaluation of drug release from nanofiber mats to brain tissue", J. Biomed. Mater. Res. B: Applied Biomaterials, vol. 103, no. 2, pp. 282-291, 2015.
[170] A. Shkilnyya, P. Proulxb, J. Sharpa, M. Lepagec, P. Vermette, "Diffusion of rhodamine B and bovine serum albumin in fibrin gels seeded with primary endothelial cells", Colloids and Surfaces B: Biointerfaces, vol. 93, pp. 202-207, 2012.
[171] I. Lisiecki, M . Björling, L. Motte, B. Ninham, M. P. Pileni, "Synthesis of copper nanosize particles in anionic reverse micelles: effect of the addition of a cationic surfactant on the size of the crystallites", Langmuir, vol. 11, no. 7, pp. 2385-2392, 1995.
[172] S. Mondini, C. Drago, A. M. Ferretti, A. Puglisi, A. Ponti, "Colloidal stability of iron oxide nanocrystals coated with a PEG-based tetra-catechol surfactant", Nanotechnology, vol. 24, pp. 105702-1-14, 2013.
[173] R.-Y. Dong, Y. Zhou, C. Yang, B.-Y. Cao, "Experimental study on thermophoresis of colloids in aqueous surfactant solutions", J. Phys.: Condens. Matter, vol. 2, 495102-1-9, 2015.
[174] W. Brown, J. Zhao, "Adsorption of sodium dodecyl sulfate on polystyrene latex particles using dynamic light scattering and zeta potential measurements", Macromolecules, vol. 26, no. 11, pp. 2711-2715, 1993.
[175] L. K. Koopal, E. M. Lee, M. R. Bohmer, "Adsorption of cationic and anionic surfactants on charged metal-oxide surfaces", J. Colloid Interface Sci., vol. 170, pp. 85-97, 1995.
[176] M. Elimelech, C. R. O'Melia, "Effect of particle size on collision efficiency in the deposition of brownian particles with electrostatic energy barriers", Langmuir, vol. 6, no. 6, pp. 1153-1163, 1990.
[177] K. Suttiponparnit, J. Jiang, M. Sahu, S. Suvachittanont, T. Charinpanitkul, P. Biswas, "Role of surface area, primary particle size, and crystal phase on

titanium dioxide nanoparticle dispersion properties", Nanoscale Res. Lett., vol. 6, no. 27, pp. 1-8, 2011.

[178] J. Jiang, G. Oberdörster, P. Biswas, "Characterization of size, surface charge, and agglomeration state of nanoparticle dispersions for toxicological studies", J. Nanopart. Res., vol. 11, pp. 77-89, 2009.

[179] R. Finsy, "Particle sizing by quasi-elastic light scattering", Advances in Colloid and Interface Science, vol. 52, pp. 79-143, 1994.

[180] W. Anderson, D. Kozak, V. A. Coleman, Å. K. Jämting, M. Trau, "A comparative study of submicron particle sizing platforms: accuracy, precision and resolution analysis of polydisperse particle size distributions", Journal of Colloid and Interface Science, vol. 405, pp. 322-330, 2013.

[181] L. O. Narhi, Y. Jiang, S. Cao, K. Benedek, D. Shnek, "A critical review of analytical methods for subvisible and visible particles", Curr. Pharm. Biotechnol., vol. 10, no. 4, pp. 373–381, 2009.

[182] R. Pecora, "Laser Light Scattering and macromolecular Brownian motion", Nature Physical Science, vol. 231, pp. 73-75, 1971.

[183] W. I. Goldburg, "Dynamic light scattering", Am. J. Phys., vol. 67, no. 12, pp. 1152-1160, 1999.

[184] B. J. Berne, R. Pecora, "Dynamic Light scattering, with applications to chemistry, biology, and physics", John Wiley & Sons, Inc., 2000.

[185] R. Pecora, **"**Doppler shifts in light scattering from pure liquids and polymer solutions", J. Chem. Phys., vol. 40, no. 6, pp. 1604-1614, 1964.

[186] M. Raffel, C. Willert, J. Kompenhans, "Particle image velocimetry: a practical guide", Springer, 1998.

[187] R. A. Dragovic, C. Gardiner, A. S. Brooks, D. S. Tannetta, D. J. Ferguson, P. Hole, B. Carr, C. W. Redman, A. L. Harris, P. J. Dobson, P. Harrison, I. L. Sargent, "Sizing and phenotyping of cellular vesicles using nanoparticle tracking analysis", Nanomedicine: Nanotechnology, Biology, and Medicine, vol. 7, pp. 780-788, 2011.

[188] V. Filipe, A. Hawe, W. Jiskoot, "Critical evaluation of Nanoparticle Tracking Analysis (NTA) by NanoSight for the measurement of nanoparticles and protein aggregates", Pharm. Res., vol. 27, no. 5, pp. 796–810, 2010.

[189] S. Skelton, M. Bostwick, K. O'Connor, S. Konst, S. Casey, B. P. Lee, "Biomimetic adhesive containing nanocomposite hydrogel with enhanced materials properties", Soft Matter, vol. 9, no. 14, pp. 3825–3833, 2013.

[190] E. M. Ahmed, "Hydrogel: preparation, characterization, and applications: A review", J. Advanced Research, vol. 6, pp.105–121, 2015.

[191] J. Kopeček, "Polymer chemistry: Swell gels", Nature news and views, vol. 417, pp. 388-391, 2002.

[192] S. Kiatkamjornwong, "Superabsorbent polymers and superabsorbent polymer composites", Science Asia, vol. 33, supplement 1, pp. 39-43, 2007.

[193] O. Wichterle, D. Lim, "Hydrophilic gels for biological use", Nature, vol. 185, no. 4706, pp. 117-118, 1960.

[194] J. M. Rosiak, F. Yoshii, "Hydrogels and their medical applications", Nucl. Instr. and Meth. in Phys. Res., vol. 151, pp. 56-64, 1999.

[195] B. Tyliszczak, K. Pielichowski, "Charakterystyka matryc hydrożelowych – zastosowania biomedyczne superabsorbentów polimerowych. Czasopismo techniczne", Wydawnictwo Politechniki Krakowskiej, z. 1-Ch, pp. 161-167, 2007.

[196] Y. Guan, Y. Zhang, "PNIPAM microgels for biomedical applications: from dispersed particles to 3D assemblies", Soft Matter, vol. 7, pp. 6375-6384, 2011.
[197] A. Hamerska-Dudra, "Termoczułe polimery usieciowane – synteza i wybrane właściwości", PhD thesis, Wroclaw University of Technology, Wrocław,2007.
[198] C. E. Carraher Jr, "Polymer Chemistry. Marcel Dekker", Inc., New York, 2003.
[199] Z. Maolin, L. Jun, Y. Min, H. Hongfei, "The swelling behaviour of radiation prepared semi-interpenetrating polymer networks composed of polyNIPAAm and hydrophilic polymers", Radiation Physics and Chemistry, vol. 58, pp. 397-400, 2000.
[200] J. M. Seidel, S. M. Malmonge, "Synthesis of PolyHEMA hydrogels for using as biomaterials. Bulk and solution radical-initiated polymerization techniques", Mat. Res., vol. 3, no. 3, pp. 79-83, 2000.
[201] M. K. Shin, G. M. Spinks, S. R. Shin, S. I. Kim, S. J. Kim, "Nanocomposite hydrogel with high toughness for bioactuators", A dv. Mater., vol. 21, no. 17, pp. 1712-1715, 2009.
[202] A. Datta, "Characterization of polyethylene glycol hydrogels for biomedical applications", PhD thesis, Louisiana State University, 2007.
[203] N. A. Peppas, P. Bures, W. Leobandung, H. Ichikawa, "Hydrogels in pharmaceutical formulations", European Journal of Pharmaceutics and Biopharmaceutics, vol. 50, no. 1, pp. 27-46, 2000.
[204] A. Sapota, M. Skrzypińska-Gawrysiak, "Akrylamid. Dokumentacja proponowanych dopuszczalnych wielkości narażenia zawodowego", Podstawy i Metody Oceny Środowiska Pracy, vol. 2, no. 80, pp. 5-71, 2014.
[205] M. A. Haq, Y. Su, D. Wang, "Mechanical properties of PNIPAM based hydrogels: A review", Mater. Sci. Eng., C, vol. 70, pp. 842–855, 2017.
[206] M. Chen, M. Dong, R. Havelund, V. R. Regina, R. L. Meyer, F. Besenbacher, P. Kingshott, "Thermo-responsive core-sheath electrospun nanofibres from poly(N-isopropylacrylamide)/polycaprolactone blends", Chem. Mater., vol. 22, no. 14, pp. 4214-4221, 2010.
[207] D. L. Huber, R. P. Manginell, M. A. Samara, B. I. Kim, B. C. Bunker, "Programmed adsorption and release of proteins in a microfluidic device", Science, vol. 301, pp. 352–354, 2003.
[208] A. K. Gaharwar, S. A. Dammu, J. M. Canter, C. J. Wu, G. Schmidt, "Highly extensible, tough, and elastomeric nanocomposite hydrogels from poly(ethylene glycol) and hydroxyapatite nanoparticles", Biomacromolecules, vol. 12, pp. 1641-1650, 2011.
[209] V. B. Gupta, V. K. Kothari (ed.), "Manufactured fibre technology: melt-spinning processes", Chapman & Hall, pp. 67-97, 1997.
[210] K. Katayama, T. Amano, K. Nakamura, "Structural formation during melt spinning process", Kolloid-Zeitschrift und Zeitschrift fur Polymere, vol. 226, no. 2, pp. 125-134, 1967.
[211] I. E. Spruiell, E. Bond, J. Karger-Kocsis (ed.), "Polypropylene: an A-Z reference: melt spinning of polypropylene", Kluwer Publishers, pp. 427-439, 1999.
[212] X. Zhuang, L. Shi, K. Jia, B. Cheng, W. Kang, "Solution blown nanofibrous membrane for microfiltration", Journal of Membrane Science, vol. 429, pp. 66-70, 2013.
[213] B. Eling, S. Gogolewski, A. Pennings, "Biodegradable materials of poly(L-lactic acid): 1. Melt-spun and solution-spun fibres", J. Polymer, vol. 23, pp. 1587-1593, 1982.

[214] D. D. da Silva Parize, M. M. Foschini, J. E. de Oliveira,. A. P. Klamczynski, G. M. Glenn, J. M. Marconcini, L. H. Capparelli Mattoso, "Solution blow spinning: parameters optimization and effects on the properties of nanofibres from poly(lactic acid)/dimethyl carbonate solutions", J. Mater. Sci., vol. 51, no. 9, pp. 4627-4638, 2016.

[215] J. E. Oliveira, E. A. Moraes, R. G. F. Costa, A. S. Afonso, L. H. C. Mattoso, W. J. Orts, E. S. Medeiros, "Nano and submicrometric fibres of poly(D,L-lactide) obtained by solution blow spinning: process and solution variables", Journal of Applied Polymer Science, vol. 122, no. 5, pp. 3396-3405, 2011.

[216] M. Wojasiński, M. Pilarek, T. Ciach, "Comparative studies of electrospinning and solution blow spinning processes for the production of nanofibrous poly(L-lactic acid) materials for biomedical engineering", Pol. J. Chem. Tech., vol. 16, no. 2, pp. 43-50, 2014.

[217] A. M. Behrens, B. J. Casey, M. J. Sikorski, K. L. Wu, W. Tutak, A. D. Sandler, P. Kofinas, "In situ deposition of PLGA nanofibres via solution blow spinning", ACS Macro Lett., vol. 3, pp. 249-254, 2014.

[218] R. Zhao, L. C. Wadsworth, "Attenuating PP/PET biocomponent melt blown microfibres", Polymer Engineering And Science, vol. 43, no. 2, pp. 463-469, 2003.

[219] A. Janshoff, M. Neitzert, Y. Oberdorfer, H. Fuchs, "Force spectroscopy of molecular systems – Single molecule spectroscopy of polymers and biomolecules", Angew Chem. Int. Ed., vol. 39, no. 18, pp. 3212-3237, 2000.

[220] A. Beyder, C. Spagnoli, F. Sachs, "Reducing probe dependent drift in atomic force microscope with symmetrically supported torsion levers", Rev. Sci. Instrum., vol. 77, pp. 056105-1-3, 2006.

[221] N. K. Voulgarakis, A. Redondo, A. R. Bishop, K. Ø. Rasmussen, "Sequencing DNA by dynamic force spectroscopy: limitations and prospects", Nano Lett., vol. 6, no. 7, pp. 1483-1486, 2006.

[222] W. Nasalski, "Optical beams at dielectric interfaces – fundamentals", Trends in Mechanics of Materials, IPPT PAN, Warszawa, pp. 1-282, 2007.

[223] M. A. Dobrovolskaia, A. K. Patri, J. Zheng, J. D. Clogston, N. Ayub, P. Aggarwal, B. W. Neun, J. B. Hall, S. E. McNeil, "Interaction of colloidal gold nanoparticles with human blood: effects on particle size and analysis of plasma protein binding profiles", Nanomedicine: Nanotechnology, Biology, and Medicine, vol. 5, pp. 106-117, 2009.

[224] D. Artemov, N. Mori, B. Okollie, Z. M. Bhujwalla, "MR molecular imaging of the Her-2/neu receptor in breast cancer cells using targeted iron oxide nanoparticles", Magn. Reson. Med. Vol. 49, pp. 403-408, 2003.

[225] D. A. Grande, C. Halberstadt, R. Schwarz, R. Manji, "Evaluation of matrix scaffolds for tissue engineering of articular cartilage grafts, J. Biomem. Mater. Res., vol. 34, pp. 211-220, 1997.

[226] K. Kurzydłowski, M. Lewandowska, "Nanomateriały inżynierskie, konstrukcyjne i funkcjonalne: Zastosowanie nanowłókien w medycynie", PWN, Warszawa, pp. 277-284, 2010.

[227] A. Subramanian, U. M. Krishnan, S. Sethuraman, "Development of biomaterial scaffold for nerve tissue engineering: Biomaterial mediated neural regeneration", Journal of Biomedical Science, vol. 16, pp. 108-1-11, 2009.

[228] C. E. Schmidt, J. B. Leach, "Neural tissue engineering: strategies for repair and regeneration", Annu Rev Biomed Eng, vol. 5, pp. 293-347, 2003.

[229] F. Yang, R. Murugan, S. Wang, S. Ramakrishna, "Electrospinning of nano/micro scale poly(L-lactis acid) aligned fibers and their potential in neural tissue engineering", Biomateriale, vol. 26, pp. 2603-2610, 2005.

[230] L. E. Freed, G. Vunjak-Novakovic, R. J. Biron, D. B. Eagles, D. C. Lesnoy, S. K. Barlow, R. Langer, "Biodegradable polymer scaffolds for tissue engineering", Nat Biotechnol, vol. 12, pp. 689-693, 1994.

[231] L. S. Nair, S. Bhattacharyya, C. T. Laurencin, "Development of novel tissue engineering scaffolds via electrospinning", Expert Opin. Biol. Ther., vol. 4, no. 5, pp. 659-668, 2004.